UNIVERSITY OF WARMIA AND MAZURY IN OLSZTYN

Technical Sciences

12

PUBLISHER UWM

OLSZTYN 2009

EDITORIAL BOARD
Stefan Cenkowski – University of Manitoba, Canada, Adam Chrzanowski – University of New Brunswick, Canada, Janusz Laskowski – Uniwersity of Agriculture in Lublin, Lech Tadeusz Polkowski – University of Warmia and Mazury in Olsztyn, Vladimir Tilipalov – Kaliningrad State Technical University, Russia, Alojzy Wasilewski – University of Warmia and Mazury in Olsztyn

EDITORIAL COMMITTEE
Marek Markowski (Editor-in-Chief), Piotr Artiemjew, Ireneusz Białobrzewski, Tomasz Lipiński, Wojciech Sobieski

Executive Editor
Mariola Jezierska

The Journal is also available in electronic form.
The online edition is hosted by MetaPress (www.metapress.com) in partnership with Versita (www.versita.com)

PL ISSN 1505-4675

© Copyright by Wydawnictwo UWM • Olsztyn 2009

Address
ul. Jana Heweliusza 14
10-718 Olsztyn-Kortowo, Poland
tel.: (48) (089) 523 36 61
fax: (48) (089) 523 34 38
e-mail: wydawca@uwm.edu.pl

Ark. wyd. 22,5, ark. druk. 18,25
Druk – Zakład Poligraficzny UWM w Olsztynie
zam. nr 599

Contents

Biosystems Engineering

B. Gładyszewska, A. Ciupak – *Changes in the Mechanical Properties of the Greenhouse Tomato Fruit Skins During Storage* 1
J. Bieranowski, T. Olkowski – *Comparison of Combustion Gas Emission by Low Power Boilers Fired by Biomass Obtained from Wood – Pellets* 9
R. Myhan – *Airflow Modeling in a Grain Silo* 17
K. Gołacki, P. Rowiński, Z. Stropek – *The Determination of Apples Bruise Resistance by the Multiple Impact Method* 29

Environmental Engineering

L.M. Kaczmarek – *Hydro- and Lithodynamic Aspects of Constructing a Navigable Canal Through the Vistula Spit* 40

Civil Engineering

M. Zagroba – *Aspects of Designing Education Buildings in a Conservation Area: a Case Study of a Building Designed for the School of Civil Engineering at the University of Warmia and Mazury in Olsztyn* 57
M. Knauff, K. Klempka – *Effective Lengths of Reinforced Concrete Columns in Single-Storey Frame Structures in the Light of the Eurocode* 71
S. Dominikowski, P. Bogacz – *Determination of Internal Forces in end Plates of Simple end Plate Joints* 83
J. Zabielski, P. Bogacz – *Aspects of Cost-Estimate for Construction Work in Listed Buildings* 95

Geodesy and Cartography

A. Bobojć – *Selected Accelerations and Orbital Elements of the Goce Satellite in the Time Domain* 104
A. Łyszkowicz – *Assessment of Accuracy of EGM08 Model Over the Area of Poland* 118
R. Duchnowski – *Geodetic Application of R-Estimation – Levelling Network Examples* 135

K. Kowalczyk, M. Bednarczyk – *Relational Database of Three Precise Levelling Campaigns in Poland* 145
K. Pająk – *Analysis of Compilation Technology of Digital Terrain Model Based on Satellite, Tacheometric and Photogrametric Data* 165

Informatics

H. Tańska – *Enterprise Architect and Magic Draw UML – Comparing the Abilities of CASE Tools* 181

Mechanical Engineering

J. Pelc – *Numerical Aspects of a Pneumatic Tyre Model Analysis* 190
P. Pietkiewicz – *Algorithms Applied in Turbomachine Modeling with Variable Input Data* 204
P. Pietkiewicz – *Typical Failures of Gear Pumps. Defects Classification* 219
K. Nalepa, P. Pietkiewicz, G. Żywica – *Development of the Foil Bearing Technology* 229
W. Miąskowski, P. Pietkiewicz, G. Żywica – *Modeling Foil Bearings* 241
W. Miąskowski, K. Nalepa, G. Żywica – *Foil Micro-Bearing Tests* 249
W. Sobieski – *Numerical Analysis of Flow Bifurcations in a Closed-Off Channel* 259
W. Sobieski – *Numerical and Experimental Analyses of Hopf Bifurcations in a Locally Expanded Channel* 272

Spis treści

Inżynieria rolnicza

B. Gładyszewska, A. Ciupak – *Zmiany mechanicznych właściwości skórki owoców pomidora szklarniowego podczas przechowywania* 1
J. Bieranowski, T. Olkowski – *Porównanie emisyjności spalin kotłów małej mocy opalanych biomasą drewnopochodną – pelety* 9
R. Myhan – *Modelowanie przepływu powietrza w silosie zbożowym* 17
K. Gołacki, P. Rowiński, Z. Stropek – *Wyznaczanie odporności na obicie jabłek metodą wielokrotnego udaru* 29

Inżynieria środowiska

L.M. Kaczmarek – *Hydro- i litodynamiczne aspekty budowy kanału żeglugowego przez Mierzeję Wiślaną* 40

Inżynieria lądowa i wodna

M. Zagroba – *Problematyka projektowania obiektów dydaktycznych w strefach ochrony konserwatorskiej na przykładzie budynku dla kierunku budownictwo Uniwersytetu Warmińsko-Mazurskiego w Olsztynie* 57
M. Knauff, K. Klempka – *Długości obliczeniowe słupów żelbetowych w parterowych układach ramowych w świetle przepisów Eurokodu* 71
S. Dominikowski, P. Bogacz – *Wyznaczenie wartości sił wewnętrznych w blachach czołowych połączeń doczołowych zwykłych* 83
J. Zabielski, P. Bogacz – *Problematyka kosztorysowania robót budowlanych w obiektach zabytkowych* 95

Geodezja i kartografia

A. Bobojć – *Wybrane przyśpieszenia i elementy orbitalne satelity GOCE w dziedzinie czasu* 104
A. Łyszkowicz – *Ocena dokładności modelu EMG08 na obszarze Polski* 118
R. Duchnowski – *Geodezyjne zastosowania R-estymacji – przykłady dla sieci niwelacyjnych* 135
K. Kowalczyk, M. Bednarczyk – *Relacyjna baza danych sieci niwelacji precyzyjnej obszaru Polski z kolejnych kampanii* 145
K. Pająk – *Analiza technologii opracowania numerycznego modelu terenu na podstawie danych satelitarnych, tachimetrycznych i fotogrametrycznych* 165

Informatyka

H. Tańska – *Enterprise Architect a Magicdraw UML – porównanie możliwości narzędzi CASE* 181

Inżynieria mechaniczna

J. Pelc – *Numeryczne aspekty analizy modelu opony pneumatycznej* 191
P. Pietkiewicz – *Algorytmy stosowane w modelowaniu maszyn wirnikowych z uwzględnieniem zmienności danych wejściowych* 204
P. Pietkiewicz – *Typowe uszkodzenia pomp zębatych. Klasyfikacja defektów* 219
K. Nalepa, P. Pietkiewicz, G. Żywica – *Rozwój technologii łożyskowania foliowego* 229
W. Miąskowski, P. Pietkiewicz, G. Żywica – *Modelowanie łożysk foliowych* 241
W. Miąskowski, K. Nalepa, G. Żywica – *Badanie łożysk foliowych* 249
W. Sobieski – *Numeryczna analiza zjawiska bifurkacji w przepływie płynu przez ślepo zakończony kanał* 159
W. Sobieski – *Analiza numeryczna i eksperymentalna bifurkacji Hopfa w kanale z lokalnym rozszerzeniem* 272

TECHNICAL SCIENCES
Abbrev.: Techn. Sc., No 12, Y 2009

DOI 10.2478/v10022-009-0001-z

CHANGES IN THE MECHANICAL PROPERTIES OF THE GREENHOUSE TOMATO FRUIT SKINS DURING STORAGE

Bożena Gładyszewska, Anna Ciupak

Faculty of Physics
University of Life Sciences in Lublin

K e y w o r d s: tomato skin, storage period, Young's modulus, Poisson's ratio.

A b s t r a c t

This study investigates the effect of the period of storage of greenhouse tomato (*Lycopersicon Esculentum* Mill) c.v. Admiro on changes in the selected mechanical properties of tomato skin. Changes in the value of Young's modulus and Poisson's ratio were determined in tomato fruit harvested from the maternal plant at the initial phase of skin ripeness, stored in a controlled environment chamber with limited light access at a temperature of 14°C. A decrease in the value of Young's modulus and Poisson's ratio was observed.

ZMIANY MECHANICZNYCH WŁAŚCIWOŚCI SKÓRKI OWOCÓW POMIDORA SZKLARNIOWEGO PODCZAS PRZECHOWYWANIA

Bożena Gładyszewska, Anna Ciupak

Katedra Fizyki
Uniwersytet Przyrodniczy w Lublinie

S ł o w a k l u c z o w e: skórka owoców pomidora, czas przechowywania, moduł Younga, współczynnik Poissona.

A b s t r a k t

W pracy przedstawiono wyniki badań nad wpływem czasu przechowywania owoców pomidora szklarniowego (*Lycopersicon Esculentum* Mill) odmiany Admiro na zmianę wybranych mechanicznych właściwości skórki. Zbadano zmienność modułu sprężystości podłużnej oraz współczynnika Poissona podczas przechowywania owoców pomidora zebranych bezpośrednio z rośliny macierzystej w początkowym stadium dojrzałości skórki, a następnie przechowywanych w komorze klimatycznej z ograniczonym dostępem światła w temperaturze 14°C. Zaobserwowano zmniejszenie wartości modułu Younga, a także współczynnika Poissona.

Introduction and objective of the study

Plant production (including fruit and vegetable growing) is oriented towards individual consumers and the processing industry. For specific target groups to be identified, qualitative standards have to be met as regards the product's safety, nutritional value, storage and processing requirements. During collection, packaging, transport and even storage, tomato fruits are often subjected to breaking load and breaking stress. Surface damage directly lowers the product's commercial value. Physiological changes during the ripening process also contribute to the fruit's susceptibility to damage (GONLEY, EGAN 1978, HANKINSON, RAO 1979, MOSHENIN 1970, RAMANA 1991). The mechanical properties of tomato skins which are directly exposed to external damaging factors are, therefore, an important consideration. The basic physical indicators which describe the mechanical properties of the investigated plant material are Young's modulus E and Poisson's ratio ν (DOBRZAŃSKI 1998, GŁADYSZEWSKA 2007, MOSHENIN 1970). Strength tests of tomato skins are also carried out with the use of rheological methods supporting the development of mathematical models (PETRACEK, BUKOVAC 1995, THOMPSON 2001). BARGEL and NEINHUIS (2005) performed a detailed study investigating the relationship between the biochemical properties of tomato skins and the process of fruit growth and ripening. They carried out a combined analysis of SEM (scanning electron microscopy) images and uniaxial tensile tests. KABAS et al. (2008) determined Poisson's ratio by measuring the transverse and longitudinal strain of a tomato during compression between two plates.

Published sources quote the values of Young's modulus E obtained from uniaxial tensile tests of tomato skins (HAMAN, BURGES 1986, HERSHKO et al. 1994, MATAS et al. 2005, RAJABIPOUR et al. 2004, VOISEY, LYALL 1986, WIDEMANN, NEINHUIS 1998). The value of Young's modulus is determined with the use of popular measuring devices such as Instron testing machines. Poisson's ratio ν may be very difficult or impossible to determine as transverse strain cannot be measured with the use of a standard strength testing device.

The objective of this study was to determine the basic mechanical properties of tomato skins, i.e. Young's modulus and Poisson's ratio, during uniaxial tensile tests, subject to the period of fruit storage.

Method

Greenhouse tomato fruits (*Lycopersicon Esculentum* Mill) cv. Admiro grown by the Kwietniewski Gardening Production Company in Chodel, Lublin Province, were subjected to laboratory analyses in September 2007. Tomato

fruits were harvested directly from the maternal plant at the initial ripening stage (orange skin color) and stored in a controlled environment chamber with limited light access at a temperature of 14°C. The applied storage temperature is consistent with Polish Standard requirements (1993) and the recommendations of the Main Inspectorate of Plant Health and Seed Production (Państwowa Inspekcja Ochrony Roślin i Nasiennictwa).

The mechanical properties of thin-layer biological materials such as tomato fruit skins were investigated by image analysis and an analysis of the mutual position of markers randomly applied to the studied material (GŁADYSZEWSKA 2007). Young's modulus and Poisson's ratio are computed with the use of a tensometric platform and specialist software. This method supports skin peeling tests and strain observations. By applying the random marking method in strength tests, the authors were able to disregard boundary conditions which made the produced results independent from material strain in the area of critical cross-sections (GŁADYSZEWSKA 2006).

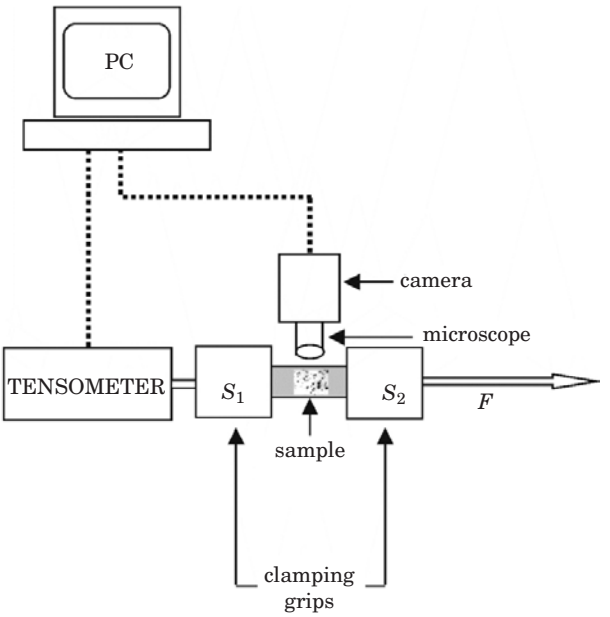

Fig. 1. Specimen mounted in clamps. S_1 and S_2 – clamping grips, F – force

Graphite markers were randomly sprayed on the surface of the specimen. The direction of force F ensured that the specimen was stretched precisely in its plane. The applied markers did not affect the specimen's properties and they did not come into contact, therefore, the studied material's natural

mechanical properties were preserved. The specimen was placed in clamping grips S_1 and S_2. Grip S_1 was connected to a Megaton Electronic AG&Co. KT-1400 tensometer with a force measurement range of 0-100 N. S_2 was a moving grip. After the strength test began, the specimen image generated by a camera equipped with a microscope lens was transmitted to computer memory with information on the current value of the tensile force corresponding to the given image. With the use of a microscope lens, the specimen was viewed at 240×320 pixel resolution and 5× magnification. The signal from the tensometer was transferred by an analogue-to-digital converter to computer memory, and the observed image – to video input. The tensile strength value was later correlated with specimen strain.

The first measurements were performed directly after harvest, and follow-up measurements were carried out as scheduled. Measurements were taken every 2–3 days for 26 days. Tomatoes were removed from the controlled environment chamber and kept in a laboratory until fruit temperature became equal to ambient temperature. The surface of tomatoes was washed and a specially profiled knife was used to cut 30 mm long and 9–13 mm wide skin strips. The incision was made from the base of the tomato to the stalk. A third dimension (thickness) had to be specified as part of the applied method. Skin thickness was measured at 10 points with the use of an optical microscope. The specimen prepared in this way was placed in clamping grips S_1 and S_2. Prior to measurement, powdered graphite markers were applied to the specimen with a special brush.

The image of the skin surface with the marked points was transferred from the camera to a computer analyzing the changes between the points during a tensile strength test. The cosine of the angle between the grid axis and the image edge, and the force exerted on a given specimen were determined. The relative distance shift between selected points before and after strain and the value of angle cosines were used to determine stress values. The value of Young's modulus E for each of the 30 specimens was determined based on the tangent of the inclination angle of a straight line describing a single dependence: $\varepsilon_x = f(\sigma)$, (Fig. 2 and Fig. 3), where:

$$\sigma = \frac{F}{S} \tag{1}$$

σ – stress value [MPa],
F – value of force exerted on the specimen [N],
S – cross-sectional area of the specimen [mm^2].

The value of Poisson's ratio ν was calculated based on the following formula:

$$\nu = \frac{\varepsilon_y}{\varepsilon_x} \tag{2}$$

where:
ε_x – strain in the direction of the x-axis,
ε_y – strain in the direction of the y-axis.

The process of data collection during measurement and the calculations applied to determine the required parameters were controlled by the Videoo software (GŁADYSZEWSKA, CHOCYK 2005).

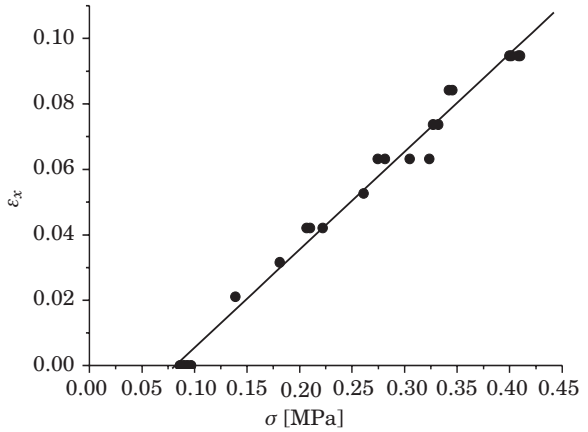

Fig. 2. Example of a dependence ε_x (σ) for the stretched specimen

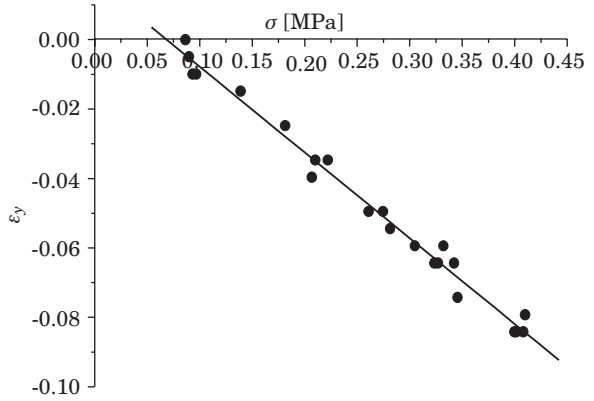

Fig. 3. Example of a dependence ε_y (σ) for the stretched specimen

Results and discussion

Figure 4 presents the dependence of an average values of Young's modulus E determined for tomato fruit skin samples on every day of the storage period. A decrease in the value of the elasticity modulus E of tomato skins was observed during the analyses from about 4.5 MPa on harvest day down to about 2.35 MPa after 26 days of storage at a temperature of 14°C. The obtained values of Young's modulus can be considered as rather low in comparison with other values reported in the literature. Hankinson and Rao have found for different tomato cultivars Young's modulus varying from 17.16 up to 24.67 MPa (HANKINSON, RAO 1979). BARGEL, NEINHUIS collected results revealing much higher spread of Young's modulus, from 14.1 even up to 600 MPa for different tomato cultivars (BARGEL, NEINHUIS 2004). Matas et al. have performed experiments for different relative humidities of tomato peels. A clear increase of Young's modulus has been found with a decrease of the relative humidity (MATAS et al. 2005). In our storage experiment Young's modulus decreases with the time of storage therefore this effect cannot be connected with eventual decrease of relative humidity. Moreover, such low values of Young's modulus as observed in our work has also been reported by Matas et al. when tensile force ranged from 0.1 N up to 0.2 N (MATAS et al. 2004).

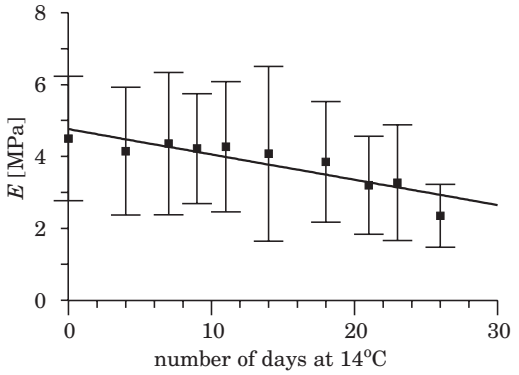

Fig. 4. Average values of Young's modulus E determined for tomato fruit skin samples on every day of the storage period

The values of Poisson's ratio ν determined for individual skin samples varied widely due to the specific properties of the investigated material. For average values (calculated from 30 repetitions), a drop in Poisson's ratio ν was noted over storage time from around 0.74 on harvest day to 0.55 after 26 days of storage at 14°C (see Fig. 5). One could be surprised by these large Poisson's ratio values, however quite similar values (up to 0.72) have already been

reported by Thompson (THOMPSON 2001). Moreover it is necessary to stress that "0.5 limit" for Poisson's ratio is valid only for isotropic 3D materials, whereas tomato peel structure is not isotropic at all and the tested samples should be considered rather as 2D than 3D samples.

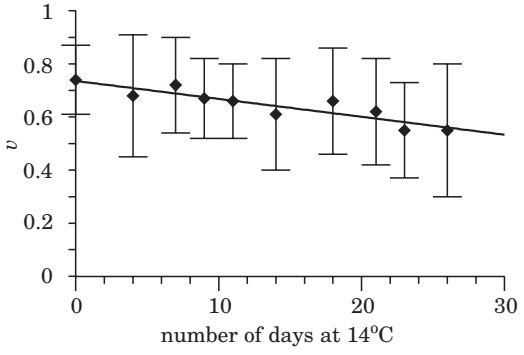

Fig. 5. Average values of Poisson's ratio ν determined for tomato fruit skin samples on every day of the storage period

Conclusions

Significant changes in the analyzed parameters were observed during long-term storage of tomatoes as the anticipated consequence of ripening progress and biochemical changes occurring in the fruit.

The following conclusions can be drawn from the conducted study:

1. The value of Young's modulus for tomato fruit skins (Admiro) stored at a temperature of 14°C decreased from 4.5 MPa to 2.35 MPa on day 26 of the experiment.

2. Poisson's ratio ν was also characterized by a decreasing trend from 0.74 to 0.55 on the last measurement day.

3. The values of Young's modulus E and Poisson's ratio ν varied widely due to the specific properties of the investigated plant material, i.e. tomato fruit skins.

Accepted for print 27.03.2009

References

BARGEL H., NEINHUIS C. 2005. *Tomato (Lycopersicon esculentum Mill.) fruit growth and ripening as related to the biomechanical properties of fruit skin and isolated cuticle*. J. Exp. Bot., 56 (413): 1049–1060.

DOBRZANSKI B. jr. 1998. *Mechanizmy powstawania uszkodzeń nasion roślin strączkowych*. Acta Agrophys., 13: 1–96.

GORNLEY R., EGAN S. 1978. *Firmness and colour of the fruit of some tomato cultivars from various sources during storage*. J. Sci. Food Agric., 29: 534–538.

GŁADYSZEWSKA B. 2006. *Testing machine for assessing the mechanical properties of ąbiological materials*. Technical Sciences, 9: 21–31.

GŁADYSZEWSKA B. 2007. *Metoda badania wybranych mechanicznych właściwości cienkowarstwowych materiałów biologicznych*. Rozprawy naukowe AR w Lublinie, 325.

GŁADYSZEWSKA B., CHOCYK D. 2005. *Program „Videoo" – testy wytrzymałościowe*. Opis i obsługa programu.

HAMAN D.Z., BURGESS G.J. 1986. *Theoretical development for measuring the elastic properties of spherical cuticular membranes*. Trans. ASAE, 29: 1470–1476.

HANKINSON B., RAO V.N.M. 1979. *Histological and physical behavior of tomato skins susceptible to cracking*. J. Amer. Hort. Sci., 104(5): 577–581.

HERSHKO V., RABINOWITCH H.D., NUSSINOVITCH A. 1994. *Tensile characteristics of ripe tomato skin*. Lebensm.-Wiss.u.-Technol., 27: 386–389.

KABAS O., CELIK H.K., OZMERZI A., AKINCI I. 2008. *Drop test simulation of a sample tomato with finite element method*. J. Sci. Food Agic., 88: 1537–1541.

MATAS A.J., COBB E.D., BARTSCH J.A., PAOLILLO D.J., NIKLAS K.J. 2004. *Biomechanics and anatomy of Lycopersicon Esculentum fruit peels and enzyme – treated samples*. Am. J. Bot., 91(3): 352–360.

MATAS A.J., LOPEZ-CASADO G., CUARTERO J.S. HEREDIA A. 2005. *Relative humidity and temperature modify the mechanical properties of isolated tomato fruit cuticles*. Am. J. Bot., 92(3): 462–468.

MOSHENIN N.N. 1970. *Physical properties of plant and animals*. I. *Structure, physical characteristics and mechanical properties*. Gordon and Breach Sci. Publ., New York, London, Paris.

Państwowa Inspekcja Ochrony Roślin i Nasiennictwa. www.piorin.gov.pl.

PETRACEK P.D., BUKOVAC M.J. 1995. *Rheological properties of enzymatically isolated tomato fruit cuticle*. Plant Physiol., 109: 675–679.

Pomidory – Wytyczne przechowywania i transportu chłodniczego. 1993. PN-R-75416.

RAJABIPOUR A., ZARIEFARD M.R., DODD G.T., NORRIS E.R. 2004. *Tensile strength and relaxation skin by a loop technique*. Int. Agrophys., 18: 1–5.

RAMANA K.V.R. 1991. *Effect of evaporative cooling storage on ripening and quality of tomato*. J. Food Quality, 14: 127–144.

THOMPSON D.S. 2001. *Extensiometric determination of the rheological properties of the epidermis of growing tomato fruit*. J. Exp. Bot., 52(359): 1291–1301.

VOISEY P.W., LYALL L.H. 1986. *Methods of determining the strength of tomato skins in relation to fruits cracking*. J. Am. Soc. Hort. Sci., 111: 597–609.

WIEDEMANN P., NEINHUIS C. 1998. *Biomechanics of isolated plant cuticles*. Bot. Acta, 111: 28–34.

TECHNICAL SCIENCES
Abbrev.: Techn. Sc., No 12, Y 2009

DOI 10.2478/v10022-009-0002-y

COMPARISON OF COMBUSTION GAS EMISSION BY LOW POWER BOILERS FIRED BY BIOMASS OBTAINED FROM WOOD – PELLETS

Jacek Bieranowski, Tomasz Olkowski

Chair of Electrical Engineering and Power Engineering
University of Warmia and Mazury in Olsztyn

K e y w o r d s : wood derived biomass, combustion gas composition, emissivity of low power boilers, furnace structure.

A b s t r a c t

This paper discusses the relationship between the furnace structure in low power boilers fired by biomass and the composition of combustion gas emitted to the atmosphere. The emissivity of the boilers was also assessed by determination of a generalised criterial parameter of a boiler evaluation and a ranking of boiler emissivity was drawn up. A significant correlation was found to exist between the content of nitrogen oxides and carbon monoxide in the combustion gas. The carbon dioxide content was also found to affect CO and NO_x content in the emitted combustion gas.

PORÓWNANIE EMISYJNOŚCI SPALIN KOTŁÓW MAŁEJ MOCY OPALANYCH BIOMASĄ DREWNOPOCHODNĄ – PELETY

Jacek Bieranowski, Tomasz Olkowski
Katedra Elektrotechniki i Energetyki
Uniwersytet Warmińsko-Mazurski w Olsztynie

S ł o w a k l u c z o w e: biomasa drewnopochodna, skład spalin, emisyjność kotłów małej mocy, konstrukcja paleniska.

A b s t r a k t

W artykule zbadano zależności między konstrukcją paleniska w kotłach małej mocy opalanych biomasą a składem spalin emitowanych do atmosfery. Określono również emisyjność badanych kotłów przez wyznaczenie uogólnionego parametru kryterialnego oceny kotła i wykonano ranking emisyjności badanych kotłów. Stwierdzono istotną korelację między zawartością tlenków azotu i tlenku węgla w spalinach. Wykazano również wpływ zawartości dwutlenku węgla w emitowanych spalinach na zawartość CO i NO_x.

Introduction

Owing to the development of technology of renewable energy production, it is possible to use such energy to replenish the national energy balance, in which primary energy accounts for about 95% of the entire energy consumption. There is high energy potential in Poland contained in biomass, which can be used as a substitute for primary fuels. Using biomass for energy production more positively affects the natural environment than primary energy carriers because, according to BIERANOWSKI and PIECHOCKI (2005), each megawatt hour (MWh_{el}) produced from such primary energy carriers as hard or brown coal is accompanied by 15 kg of sulphur dioxide, 7 kg of nitrogen oxides and 150 kg of fly ash emitted to the environment.

The benefits from substituting primary energy with renewable energy have been pointed out by BIERANOWSKI and OLKOWSKI (2007), who claim that by producing biogas from waste biomass in individual farms and by using the biogas for energy production in co-generation, the energy demands of such a farm can be satisfied:

- 27% of the current consumption of primary thermal energy can be replaced – which makes possible the complete substitution of heating oil and coal as well as partial substitution of another renewable energy carrier – firewood;
- energy obtained from co-generation with electrical energy may satisfy the demand for such energy in a selected household. This electrical energy surplus may reach 150% of the energy supplied from the power network and may provide additional income for the household.

Substituting solid fossil fuels with biomass fuels aims at reducing emissions to the atmosphere of noxious gases which are produced during the combustion process. However, the problem of hazardous substances in combustion gas cannot be eliminated by mere substitution of primary energy carriers with biomass. To make biomass combustion more efficient, devices are needed which – owing to their structure – will provide appropriate conditions for complete combustion of the gas and dust produced in the process. Hence, studies have been conducted into the effect of the structure of commercially available heating equipment (low power water boilers) on the combustion gas composition.

Aim of the study

– To examine the effect of the furnace structure in selected low power boilers, fired with biomass (wood pellets) and manufactured in Poland, on the amount of substances emitted in the combustion gas.

– To examine the emissivity of the boilers by determination of a generalised criterial parameter of a boiler assessment and drawing up a ranking of emissivity of the boilers under study.

Object of the study

The nine boilers fired with pellet fuel used in the study are shown in Table 1. The boilers differ in the structure of the burner and the amount of thermal achieved in them. All are equipped with automatic fuel dispensers, which helps to carry out the burning process in a precise manner. In addition, one of the boilers (see Table 1, item 7) is equipped with a lambda probe to precisely regulate the air excess index. The study was based on the results of measure-

Table 1

Characteristics of the boilers under study

No.	Marked in figures as	Boiler manufacturer	Furnace structure	Boiler power (kW)	Type of fuel
1	*A*	Fu-Wi	Grate furnace with drawer, amount of air for combustion – adjusted manually, fuel dispensed automatically.	30	Wood pellets
2	*B*	HKS Lazar	Furnace with rotating retort, amount of air for combustion – adjusted manually, fuel dispensed automatically.	38	Wood pellets
3	*C*	Fu-Wi	Grate furnace with drawer, amount of air for combustion – adjusted manually, fuel dispensed automatically.	15	Wood pellets
4	*D*	HKS Lazar	Furnace with rotating retort, amount of air for combustion – adjusted manually, fuel dispensed automatically.	72	Wood Pellets
5	*E*	Klimosz	Retort furnace, amount of air for combustion – adjusted manually, fuel dispensed automatically.	72	Wood pellets
6	*F*	Klimosz	Retort furnace, amount of air for combustion – adjusted manually, fuel dispensed automatically.	25	Wood pellets
7	*G*	PPH Kostrzewa	Retort furnace, regulation of amount of air for combustion – lambda probe, fuel dispensed automatically.	25	Wood pellets
8	*H*	HKS Lazar	Furnace with rotating retort, amount of air for combustion – adjusted manually, fuel dispensed automatically.	18	Wood pellets
9	*I*	ZGM Zębiec	Retort furnace, amount of air for combustion – adjusted manually, fuel dispensed automatically.	20	Wood pellets

ments made and supplied by Instytut Energetyki (2009). Fuel (wood pellets) of the same quality parameters were used for each of the boilers under study.

Study results

The noxious substances found in combustion gas include mainly:
– sulphur dioxide (SO_2),
– nitrogen oxides (NO_x),
– carbon monoxide (CO),
– polycyclic aromatic hydrocarbons (PAH) (KUBICA 2007).

Due to the type of fuel applied in the boilers under study – wood pellets – sulphur dioxide and PAH were not taken into account for the result analysis as only traces of them are found in combustion gases. The gases were only analysed for the content of CO_2, as well as that of noxious gases, such as CO and NO_x.

The results of measurements carried out by Instytut Energetyki (2009) are presented in Figure 1. The names of boilers on the *X*-axis are replaced with capital letters (*A*-*I*), referred to in Table 1.

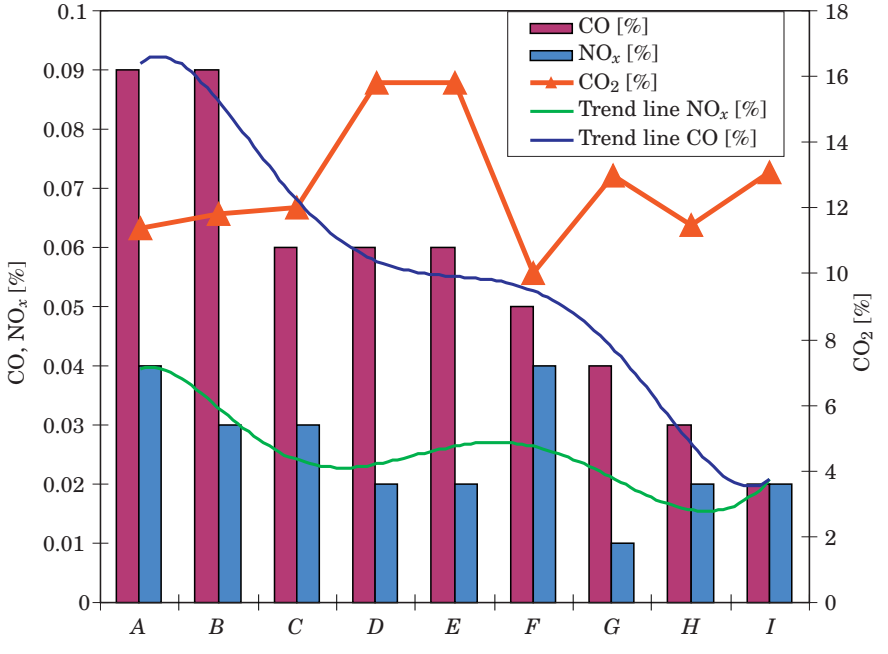

Fig. 1. Comparison of noxious gas emission from the boilers under study, according to the results of Instytut Energetyki measurements (2009)

The diagram in Figure 1 shows that an increase in NO_x content is accompanied by a strong increase in CO content, which is clearly indicated by the trend lines.

ALBERS et al. (2007) claim that too high NO_x content suggests too high temperature in the combustion chamber (>1200°C) and too long time that the air for combustion spends in it, which facilitates formation of so-called "thermal" NO_x. An increase in CO content is favoured by disturbances in the operation of a combustion gas runoff system or an insufficient amount of air supplied for combustion (too low value of λ coefficient).

The desired amount of air for combustion and the maximal reduction of NO_x concentration in combustion gas seems to be ensured by controlling the furnace by a lambda probe. This solution is applied in the *G* boiler furnace.

A significant relationship has also been found to exist between NO_x, CO and CO_2 content in gas combustion – an increase in CO_2 content is accompanied by a decrease in NO_x and CO content (see: *A* and *B* boilers as compared to *C* and *D*).

A ranking of emissivity for the boilers under study was prepared based on the methodology presented below of the generalised criteria parameters of boiler emissivity, as proposed by KUBICA and SZLĘK (2007). In order to determine the parameters, they adopted the energy (thermal) efficiency of the boiler and the level of emission of CO, NO_x and total dust – the substances that pollute the environment. The generalised criteria parameters of a boiler evaluation are calculated from the following formula:

$$O_i = 3.75\ Ws_i + 1.25\ We_i \tag{1}$$

where:

O_i – evaluation criterion index for the i-th boiler, where $i \in \{A, B, C, D, E, F, G, H, I\}$,

Ws_i – determinant characterising the efficiency of the i-th boiler,

We_i – determinant characterising emission of noxious substances from the i-th.

The determinants are described by the following formulae:

$$Ws_i = \frac{\eta_i - \eta_{\min}}{\eta_{\max} - \eta_{\min}},\ Ws_i \in (0,1) \tag{2}$$

$$We_i = \frac{e_{\max} - e_i}{e_{\max} - e_{\min}},\ We_i \in (0,1) \tag{3}$$

where:

η_i – the actual efficiency achieved by the i-th boiler, expressed in percentage,

e_i – the actual equivalent emission, expressed in mg/m^3, achieved by the i-th boiler at the rated power,

$\eta_{\min}$ – the minimal boiler efficiency, expressed in percentage, below which the boiler is not included in the ranking list,

$\eta_{\max}$ – the maximal boiler efficiency, expressed in percentage, depending on the current state of technology and physical limitations,

$e_{\min}$ – the minimal equivalent emission, expressed in mg/m^3, depending on the current state of technology,

$e_{\max}$ – the maximal equivalent energy, expressed in mg/m^3, which cannot be exceeded due to the standards of environment protection and standards of heating device testing.

The following values for low power water boilers with automatic fuel dispensing were adopted after KUBICA and SZLĘK (2007): $\eta_{\min} = 74\%$; $\eta_{\max} = 92\%$; $e_{\min} = 119$ mg/m^3; $e_{\max} = 518$ mg/m^3.

The actual equivalent emission e_i for the i-th boiler is calculated from the following formula:

$$e_i = k_{NO_x} e_{NO_x} + k_{CO} e_{CO} + k_p e_p \tag{4}$$

where:

k_{NO_x} – coefficient of harmfulness of NO_x, determined from the threshold limit value for a workplace, according to current regulations,

k_{CO} – coefficient of harmfulness of CO, determined from the threshold limit value for a workplace, according to current regulations,

k_p – coefficient of harmfulness of total dust, determined from the threshold limit value for a workplace, according to current regulations,

e_{NO_x} – emission of NO_x, expressed in mg/m^3, converted to the comparable oxygen content in combustion gas,

e_{CO} – emission of CO, expressed in mg/m^3, converted to the comparable oxygen content in combustion gas,

e_p – emission of total dust, expressed in mg/m^3, converted to the comparable oxygen content in combustion gas.

The emission of SO_2 is not taken into account in calculations of the actual equivalent emission e_i because it depends on the fuel quality rather than on the boiler structure.

The ranking of emissivity of the boilers under study is presented in Table 2. The position in the ranking is determined by the value of O_i – the generalised criteria parameter of evaluation of the i-th boiler.

Table 2

Ranking of emissivity of the boilers under study

No.	Boiler manufacturer	Boiler power (kW)	CO (mg/m^3)	NO_x (mg/m^3)	η_i (%)	Dust (mg/m^3)	Ws_i	e_i	We_i	O_i	Place in the ranking
A	Fu-Wi	30	1125	821.6	88.0	7	0.78	443.89	0.19	3.15	**3**
B	HKS Lazar	38	1125	616.2	74.5	4	0.03	355.73	0.41	0.61	**9**
C	Fu-Wi	15	750	616.2	85.8	6	0.66	325.98	0.48	3.06	**4**
D	HKS Lazar	72	750	410.8	77.8	5	0.21	241.82	0.69	1.66	**7**
E	Klimosz	72	750	410.8	78.0	5.1	0.22	242.02	0.69	1.70	**6**
F	Klimosz	25	625	821.6	82.0	133	0.44	650.89	-0.33	1.25	**8**
G	PPH Kostrzewa	25	500	205.4	87.0	89	0.72	305.16	0.53	3.38	**2**
H	HKS Lazar	18	375	410.8	77.8	1.35	0.21	200.77	0.80	1.79	**5**
I	ZGM Zębiec	20	250	410.8	88.7	94	0.82	374.82	0.36	3.51	**1**

Results and conclusions

1. The greatest effect on CO_2 content in the combustion gas was exerted by the furnaces in the HKS Lazar (72 kW) and Klimosz (72 kW) boilers. As the results and calculations show, the boilers are similar in terms of most parameters.

2. The lowest NO_x content was found in the combustion gas produced in the retort furnace with a lambda probe (the boiler manufactured by PPH Kostrzewa).

3. The lowest CO content was found in the combustion gas produced in the HKS Lazar (18 kW) and ZGM Zębiec (20 kW) boilers.

4. The lowest emissivity was determined for the ZGM Zębiec (20 kW), PPH Kostrzewa (25 kW) and Fu-Wi (30 kW) boilers; the first two are equipped with retort furnaces and the third – with a grate furnace with a drawer.

5. The highest emissivity was determined for the following boilers: HKS Lazar (38 kW) – 9th in the ranking of emissivity, Klimosz (25 kW) – 8th, HKS Lazar (72 kW) – 7th.

Accepted for print 28.09.2009

Reference

ALBERS J., DOMMEL R., MONTALDO-VENTSAM H., NEDO H. 2007. *Systemy centralnego ogrzewania i wentylacji. Poradnik dla projektantów instalatorów*. WNT, Warszawa.

BIERANOWSKI J., OLKOWSKI T. 2007. *Koncepcja substytucji energii pierwotnej energią odnawialną z odpadowej biomasy w wybranym gospodarstwie rolnym*. Inżynieria Rolnicza, 7(95): s. 23–30.

BIERANOWSKI J., PIECHOCKI J. 2005. *Program ekoenergetyczny dla województwa warmińsko-mazurskiego na lata 2005–2010*.

Instytut Energetyki. 2009. Wyniki pomiarów udostępnione grzecznościowo przez Instytut Energetyki, Zakład Kotłów i Urządzeń Grzewczych, 93-231 Łódź, ul. Dostawcza 1.

KUBICA K. 2007. *Efektywne i przyjazne środowisku źródła ciepła – ograniczenie niskiej emisji. Poradnik*. Polski Klub Ekologiczny – Okręg Górnośląski, Katowice.

KUBICA K., SZLĘK A. 2007. *Zasady wyznaczania parametru kryterialnego oceny energetyczno-ekologicznej kotłów małej mocy*. Projekt PBR-16/RIE-6/2007 finansowany z NFOŚiGW.

TECHNICAL SCIENCES
Abbrev.: Techn. Sc., No 12, Y 2009

DOI 10.2478/v10022-009-0003-x

AIRFLOW MODELING IN A GRAIN SILO

Ryszard Myhan

Department of Agricultural Process Engineering
University of Warmia and Mazury in Olsztyn

K e y w o r d s: silo, airflow, distribution of airflow velocity, discretization, model, process simulation.

A b s t r a c t

Grain storage in a silo requires the passage of a forced air stream through grain layers for the purpose of airing, cooling and drying the stored product. The intensity of the observed processes is determined by, among others, the distribution of airflow velocity throughout the silo which, in turn, is affected by the silo's structural characteristics and the parameters of the plant material. The objective of this study was to develop a model of airflow through the grain layer, subject to the above parameters. The study involved the development and the formal presentation of a mathematical model and its implementation in a chosen programming environment. For the needs of the modeling process, the part of the silo filled with grain was divided into a finite number of elements with the use of strictly formalized discretization principles.

MODELOWANIE PRZEPŁYWU POWIETRZA W SILOSIE ZBOŻOWYM

Ryszard Myhan

Katedra Inżynierii Procesów Rolniczych
Uniwersytet Warmińsko-Mazurski w Olsztynie

S ł o w a k l u c z o w e: silos, przepływ powietrza, rozkład prędkości przepływu, dyskretyzacja, model, symulacja procesu.

A b s t r a k t

Podczas przechowywania ziarna w silosach zbożowych wskazane jest wymuszenie przepływu strumienia powietrza przez warstwę. Wymuszony przepływ powietrza jest wykorzystywany do wietrzenia, schładzania lub dosuszania magazynowanego ziarna. Intensywność zachodzących procesów zależy między innymi od rozkładu prędkości przepływu strumienia powietrza w całej objętości silosu. Ta z kolei zależy od parametrów konstrukcyjnych silosu i parametrów materiału roślinnego.

Celem pracy było opracowanie modelu przepływu powietrza w warstwie ziarna w zależności od tych parametrów. Zakres pracy obejmował opracowanie i formalizację modelu matematycznego oraz jego implementację w wybranym środowisku programistycznym. Na potrzeby modelu wypełnioną ziarnem objętość silosu podzielono na skończoną liczbę elementów, stosując własne ściśle sformalizowane zasady dyskretyzacji.

Symbols

D	– silo diameter	m
F	– area	m^2
H	– silo height	m
J, N, K	– discretization parameters	
Re	– Reynolds number	
T. ΔT	– temperature	K
V	– volume	m^3
c	– drag coefficient	
p, Δp	– pressure, pressure loss	Pa
t. Δt	– time	s
Q	– fan output	$m^3\ s^{-1}$
q	– volumetric flow rate	$m^3\ s^{-1}$
v	– velocity	$m\ s^{-1}$
κ	– local drag coefficient (empirical constant)	
θ	– porosity	
ρ	– density	$kg\ m^{-3}$

Introduction

Theory and practical experience indicate that the storage of grain in a silo requires the passage of a forced air stream through grain layers. Subject to the volume and the temperature of the airflow, the purpose of this procedure is to air, cool or dry the stored grain. The intensity and quality of the observed processes are determined by, among others, the distribution of airflow velocity throughout the silo which, in turn, is affected by:

- structural parameters of the silo, such as: shape, dimensions, perforation of the walls, point and method of airflow supply;
- parameters of plant material, such as: shape and size of seeds, moisture content, layer porosity (KUSIŃSKA 2006), non-homogeneity of parameter distribution as the result of self-segregation during silo filling (ŁUKASZUK 2005).

In view of the number and the variability of the discussed parameters, their effect on the distribution of airflow velocity is very difficult to determine by way of a natural experiment in an actual site as such a procedure would be very time consuming, costly and impossible to replicate. The effect of those factors

could be minimized by performing the experiment in a laboratory, yet this would lead to dimensional analysis problems related to the scale of the experiment (MÜLLER 1983). In view of the above, a simulation experiment based on the mathematical model of the process and a formalized description of partial phenomena seems to offer a sound solution.

Objective and scope of the study

The objective of this study was to develop a model of airflow through the grain layer, subject to the discussed parameters. The model should:
- provide information on the velocity and direction of flow at any point of the stored grain volume;
- support the selection of an optimal airflow supply method;
- provide input data for modeling grain airing, cooling and drying in a silo.

As part of the study, a mathematical model has been developed, formalized and implemented in a selected programming environment. A process simulation has been performed, and the obtained data was validated in view of the results of published empirical studies.

Mathematical model

The mathematical model has been formulated on the following assumptions:
- the modeled process takes place in a set environment;
- to account for the purpose of the modeling process, the characteristic parameters of the studied plant material were layer porosity and the drag coefficient;
- the value of the investigated parameters varies in the volume of stored grain;
- the grain silo has a cylindrical shape with a circular cross-section.

Discretization

For the purpose of discretizing the silo volume filled with grain, this region is divided into thin, horizontal layers, subject to the purpose of modeling and the adopted simplifications (CARVALLO et al. 2006). Alternatively, the layers may be further sub-divided into concentric rings (IGAUZ et al. 2004). Both methods are deployed on the assumption that the observed phenomena and processes are axially symmetric. In the proposed solution, the silo volume filled with grain was

regarded as a cylinder with diameter equal to the silo diameter D and height equal to bed height H. Silo volume was divided into a finite number of elements on the following discretization principles:
– the cylinder was equally divided by horizontal planes into a K number of layers;
– each layer was divided into an N number of rings, with a J number of elements in each ring;
– it has been assumed that the core of the layer is divided into four elements, and the number of elements in each successive ring is doubled;

$$\underset{n=1,N}{\wedge} J = (n + 1)^2 \tag{1}$$

– the radii r_n of successive rings were selected to ensure that the upper and lower areas of all elements, including their volume, are identical.

$$\underset{n=1,N}{\wedge} r_n = \frac{D \cdot \sqrt{(2^n - 1)}}{2 \cdot \sqrt{(2^N - 1)}} \tag{2}$$

A model division at $N = 4$ and $K = 8$ is presented in Figure 1.

Element

The identified element $E_{i,j,k}$ is part of a ring with flat upper, lower and side walls which are sections of the cylinder's internal and external walls. Unless limited by boundary conditions, airflow takes place through those walls from or in the direction of all adjacent elements (Fig. 2).

Having made the assumption that under the established conditions, air pressure inside the element does not change over time ($p(t)$ = const.), and that relative temperature change $d(\Delta T/T)/dt$ is irrelevant for instantaneous airflow density, the balance equation for the volumetric flow rate in the region of any element takes on the following form:

$$\Sigma\, q_i = q_d + q_g + q_l + q_p + q_w + q_{zl} + q_{zp} = 0 \tag{3}$$

where the applied symbols indicate the following flows: d – lower, g – upper, l – left, p – right, w – internal, zl – external left, zp – external right.

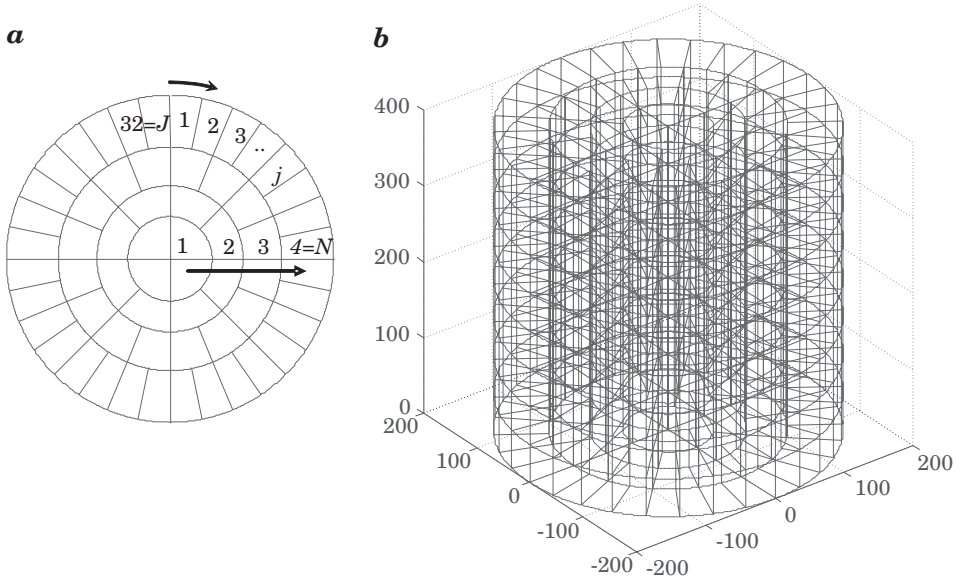

Fig. 1. Discretization of a silo with a diameter of $D = 4$ m and height of $H = 4$ at $N = 4$ and $K = 8$: *a* – division into elements in a layer, *b* – division into layers

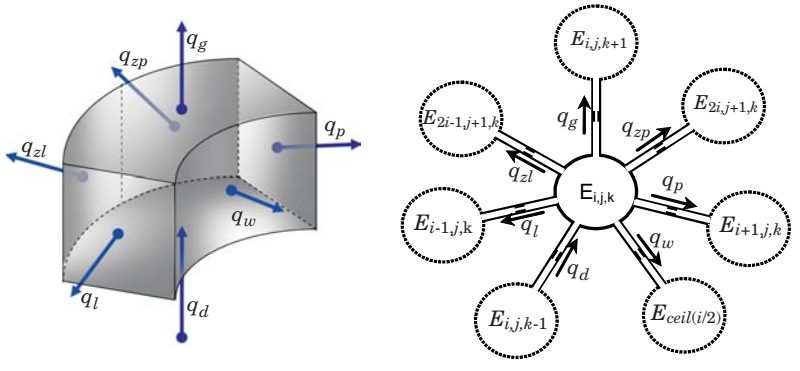

Fig. 2. Airflow model: *a* – geometric model, *b* – physical model

Each flow can be expressed in the form of a product of average airflow velocity v_i and effective airflow area F_{ei}:

$$q_i = v_i \cdot F_{ei} \tag{4}$$

The effective airflow area is the product of the area of the i^{th} wall of the element and the porosity θ of the grain layer for the element tangential to the element analyzed in the region of that wall.

$$\theta = \frac{V_e}{V} \qquad \rightarrow \qquad F_{ei} = \theta_i^{\frac{2}{3}} \cdot F_i \tag{5}$$

The geometric surface area of element walls will reach, respectively:

$$F_d = F_g = \frac{\pi \cdot D^2}{16 \cdot (2^N - 1)} \tag{6}$$

$$\underset{n=1,N}{\wedge} F_w = \frac{\pi \cdot \sqrt{2^{(n-1)} - 1}}{2} \cdot \frac{D}{2 \cdot \sqrt{2^N - 1}} \cdot \frac{H}{K}$$

$$\underset{n=1,N}{\wedge} F_l = F_p = (\sqrt{2^n - 1} - \sqrt{2^{(n-1)} - 1}) \cdot \frac{D}{2 \cdot \sqrt{2^N - 1}} \cdot \frac{H}{K}$$

$$\underset{n=1,N}{\wedge} F_{zl} = F_{zp} = \frac{\pi \cdot \sqrt{2^n - 1}}{2^{(n=1)}} \cdot \frac{D}{2 \cdot \sqrt{2^N - 1}} \cdot \frac{H}{K}$$

Flow split

The splitting of the airflow that reaches the element into evacuated flows is determined by the value of the drag coefficient Δp and the correlation between individual drags. The drags are directly proportional to the square of average flow velocity:

$$\Delta p_i = \frac{c \cdot \rho}{2} \cdot v_i^2 = \frac{c \cdot \rho}{2} \cdot \left(\frac{q_i}{F_{ei}}\right)^2 = \frac{c \cdot \rho}{2} \cdot \frac{q_i^2}{\theta_i^{\frac{4}{3}} \cdot F_i^2} \tag{7a}$$

where: c – drag coefficient

The results of measurements of the actual air drag in a grain layer (KUSIŃSKA 2006, 2007) indicate that for low flow velocity (laminar flow), i.e. for low Reynolds numbers Re, the loss will be proportional to velocity:

$$\Delta p_i = \kappa \cdot \rho \cdot v_i = \frac{\kappa \cdot \rho \cdot q_i}{F_{ei}} = \frac{\kappa \cdot \rho \cdot q_i}{F_i} \cdot \theta_i^{-\frac{2}{3}} \tag{7b}$$

where: κ – is an empirical coefficient whose value can be estimated with the use of the Ergun equation (ERGUN 1952) or Shedd's equation (SHEDD 1953).

The splitting of the evacuated flows can be described in view of the system's specific properties – the incoming flows will be split in such a way as to minimize hydraulic flow loss in an element. Having assumed that density ρ is constant and that coefficient κ is not modified, this function will take on the following form:

$$\min \left[f(\Sigma \Delta p_i) = f\left(\Sigma \left(\frac{q_i}{F_i} \cdot \theta_i^{-\frac{2}{3}} \right) \right); \quad q_i \geq 0 \right] \tag{8}$$

Boundary conditions

In the analyzed model, boundary conditions concern the region where the silo is supplied with air, the walls of the silo, including any perforated wall sections, as well as the free, upper surface of the grain layer. In all cases, those conditions were determined by identifying the porosity θ of the grain layer and the effective area of airflow F_{ei} through the walls of the boundary zone element. As regards the elements in the air supply zone (Fig. 3), boundary conditions are expressed by the following equation:

$$q_i = Q \cdot \frac{F_{ei} \cdot \theta_i^{\frac{-2}{3}}}{\Sigma \left(F_{ei} \cdot \theta_i^{\frac{-2}{3}} \right)} \tag{9}$$

where Q is the fan output.

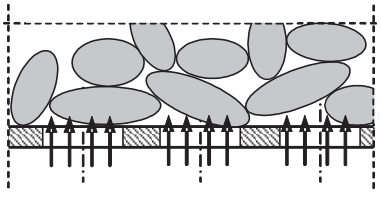

Fig. 3. Silo supply zone

Operating model

Three groups of variables have been determined in the operating model:
– the geometric dimensions of the silo and the filling method,
– selected attributes of plant material and its spatial distribution in a layer,
– the method of supplying the silo with air and airflow volume.

The calculations were preceded by a silo filling simulation to account for the distribution of plant material values (MYHAN 2003). The model has been implemented in the MATLAB 7.1 (MathWorks) programming environment using the sparse matrix presentation option which lowers the memory requirement and significantly speeds up calculations.

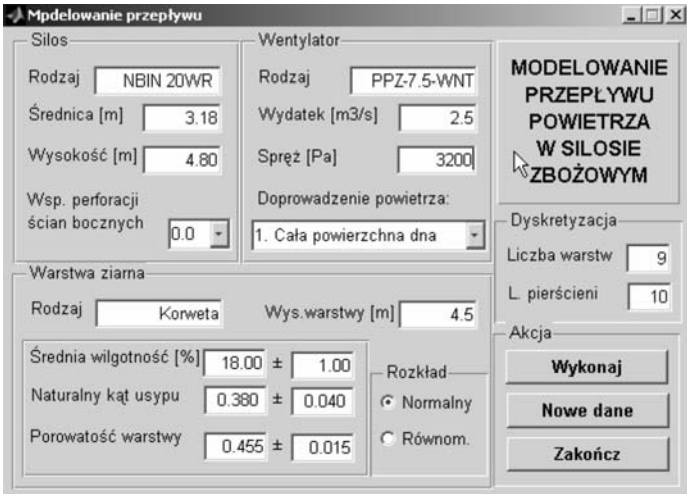

Fig. 4. Input data interface

Preliminary verification of the model

Full model verification requires a complex and a costly experimental procedure. Since the objective of modeling was not only to determine the distribution of airflow velocity but also the effect of that distribution on the evenness of grain drying in the silo, the preliminary verification relied on the results of an experiment carried out by GU et al. (2000). The experiment was performed in a laboratory, and the cited results concern moisture distribution in a grain bed after grain with initial moisture content of 22.5% had been air dried for 91 h at the temperature of 25.3°C and relative humidity of 32%. The

average velocity of the supplied airflow was 0.04 m/s. A simulation experiment was carried out under identical initial conditions and in accordance with the proposed model. The results of both experiments are presented in Figure 5. A comparison of the obtained data indicates that when the remaining process parameters are constant, moisture distribution in a grain bed is highly correlated with the distribution of airflow velocity.

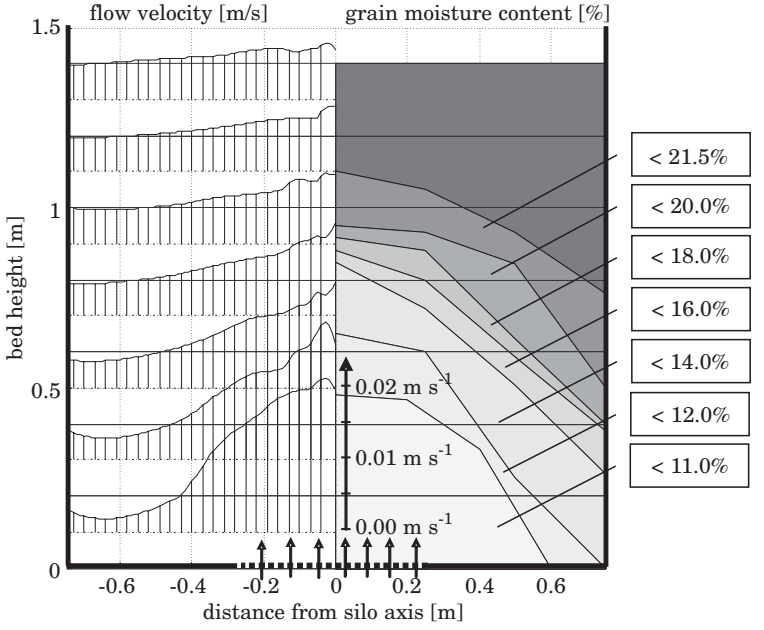

Fig. 5. Comparison of airflow velocity distribution in a silo (simulation) and the distribution of grain moisture content (GU 2000)

Process simulation – examples

The process of airflow through a grain layer in an NBIN 20WR silo with the diameter of $D = 3.18$ m (www.bin.agro.pl) was simulated. It was assumed that the silo was filled with wheat grain to the height of 4.5 m using the center, gravitational fill method. Bed porosity was set at 0.455 ± 0.015 (ŁUKASZUK et al. 2004) and the natural dumping angle was adopted at 0.38 ± 0.04 (HORABIK et al. 2000). In line with the manufacturer's recommendations, it was assumed that airflow through the grain layer was forced by a fan with volumetric output of 2.5 m^3/s, and air was supplied evenly through the silo's perforated bottom.

The distribution of velocity components in the entire layer volume is presented in Figure 6.

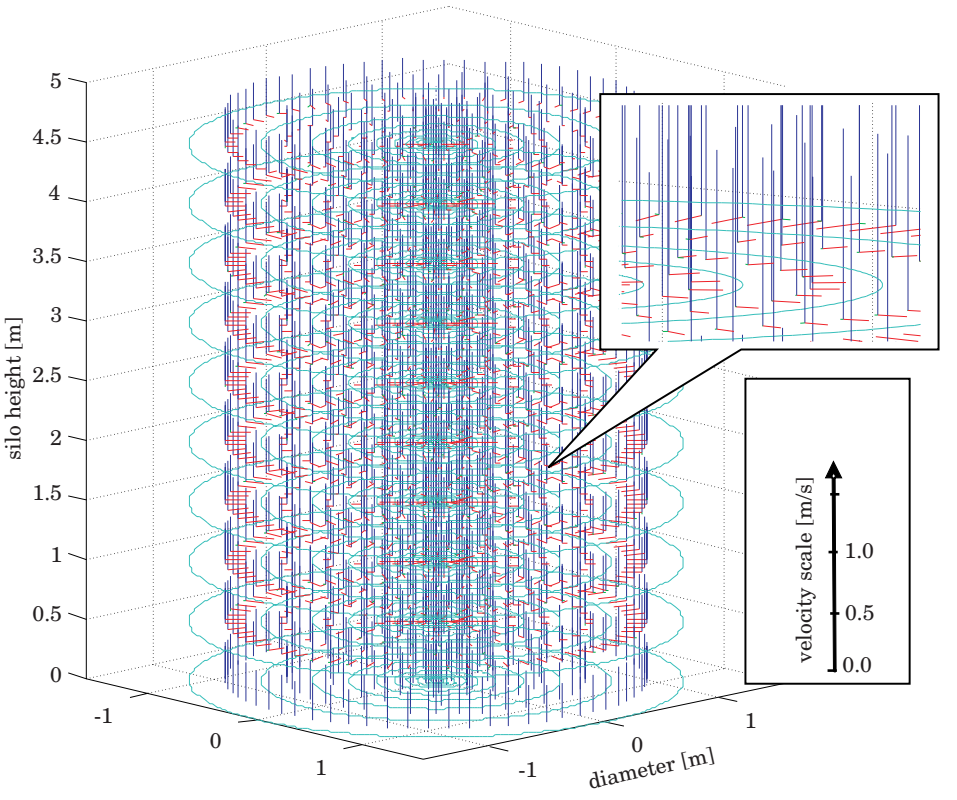

Fig. 6. Distribution of airflow velocity in a grain bed

The experiment was replicated. The only modified parameter was the method of air supply which was changed to:
– axial to $^1/_2$ D of the silo bottom;
– ring shaped to $^1/_2$ $D \div D$ of the silo bottom;
– a central duct with the diameter of 0.4 m, immersed in the bed at the depth of 1.75 m.

Each variant was analyzed with solid and perforated side walls of the silo. Averaged values of airflow velocity distribution in the bed are presented in Figure 7.

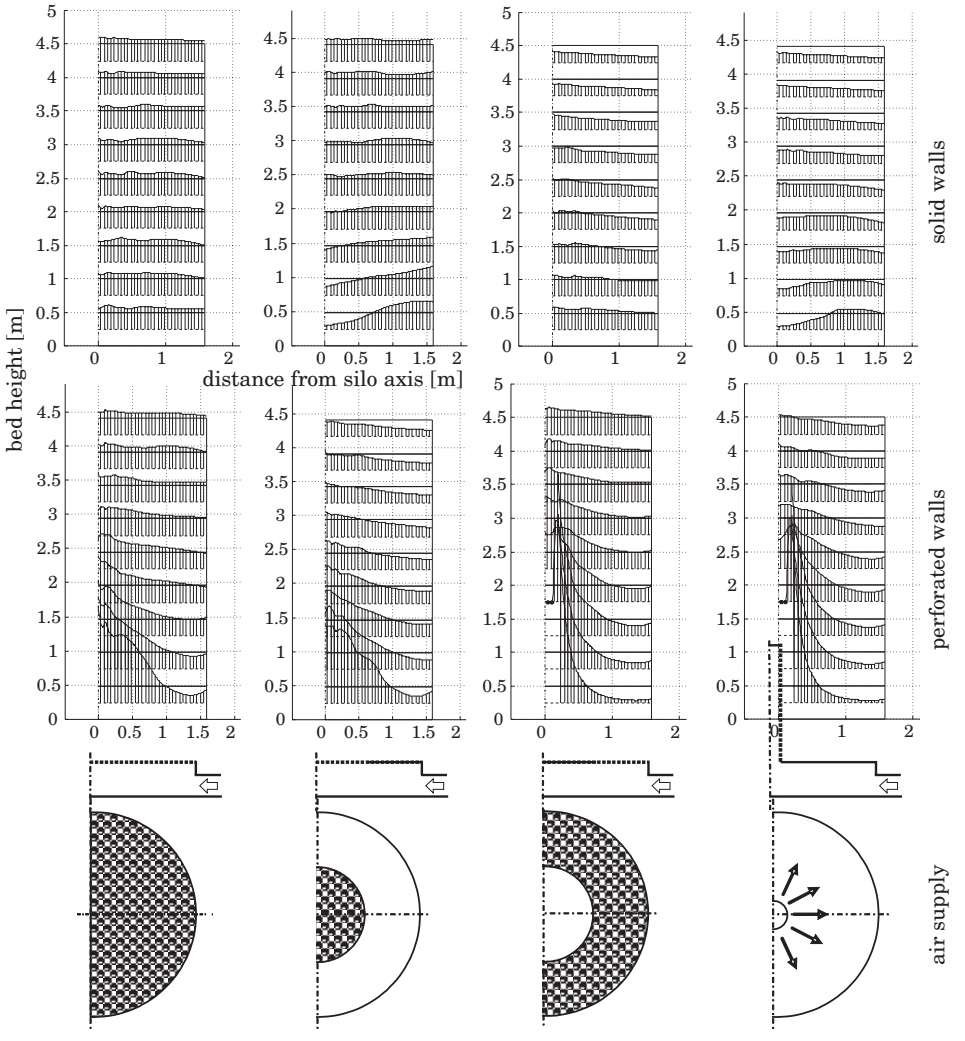

Fig. 7. Averaged distribution of the axial airflow velocity component subject to the supply method and the perforation of the silo's side walls

Conclusions

1. A preliminary verification and the performed simulations indicate that the proposed method and the resulting model may be applied to simulate the distribution of airflow velocity in a silo.

2. The obtained results suggest that the distribution of airflow velocity is strongly correlated with the method of air supply and the ratio of the silo's

diameter to bed height, and it is weakly correlated with fan output when airflow is laminar.

3. The presented model should be regarded as a preliminary stage in modeling the process of grain airing, drying and cooling in a silo. It can be fully verified after heat and mass exchange processes have been modeled in the region of finite elements discretizing the grain bed.

Accepted for print 27.07.2009

References

Carvallo Lopes D. De, Martins J.H., Casrtro Melo E. De, Barros Monteiro P.M. De. 2006. *Aeration simulation of stored grain under variable air ambient conditions*. Postharvest Biology and Technology, 42: 115–120.

Ergun S. 1952. *Fluid flow through packed columns.* Chemical Engineering Progress, 48: 89–94.

Gu D., Sokhansanj S., Haghighi K. 2000. *Influence of floor air entry on grain moisture content, temperature, and bulk shrinkage during ambient air in-bin drying of wheat.* Canadian Agricultural Engineering, 42(4): 185–193.

Horabik J., Łukaszuk J., Grochowicz M. 2000. *Formation of shear band in a granular material during triaxial compression test.* International Agrophysics, 14(4): 273–279.

Iguaz A., Arroqui C., Esnoz A., Virseda P. 2004. *Modelling and Validation of Heat Transfer in Stored Rough Rice without Aeration.* Biosystem Engineering, 88(4): 429–439.

Łukaszuk J., Molenda M., Szwed G. 2004. *Zależność oporu przepływu powietrza od gęstości złoża nasion.* Acta Agrophysica, 4(1): 77–83.

Łukaszuk J. 2005. *Wstępna ocena wpływu sposobu formowania złoża ziarna pszenicy na opór przepływu powietrza.* Acta Agrophysica, 6(3): 709–714.

Kusińska E. 2006. *Ocena wpływu prędkości przepływu powietrza i gęstości upakowania ziarna żyta na opór hydrauliczny.* Inżynieria Rolnicza, 11(86): 277–284.

Kusińska E. 2007. *Wpływ porowatości ziarna owsa na opór przepływu powietrza.* Inżynieria Rolnicza, 8(96): 149–155.

Müller L. 1983. *Zastosowanie analizy wymiarowej w badaniach modeli.* PWN, Warszawa.

Myhan R. 2003. *Modelowanie procesu napełniania silosu zbożowego*. Inżynieria Rolnicza, 13(55): 27–34.

Shedd C.K. 1953. *Resistance of grain and seeds to airflow*. Agric. Eng., 34(9): 616–619.

TECHNICAL SCIENCES
Abbrev.: Techn. Sc., No 12, Y 2009

DOI 10.2478/v10022-009-0004-9

THE DETERMINATION OF APPLES BRUISE RESISTANCE BY THE MULTIPLE IMPACT METHOD

Krzysztof Gołacki, Paweł Rowiński, Zbigniew Stropek

Department of Machine Theory and Automatics
University of Life Sciences in Lublin

Key words: bruise resistance, impact, apple.

Abstract

In this paper an attempt was undertaken aiming at establishing a methodology determining bruise resistance and the influence of apple storage time on its value and variability. The bruise resistance is a quotient bruise energy to bruise volume. The method applied to determine bruise resistance is the method of multiple drop at a constant height. It consists in multiple dropping of a tested fruit at a constant height up to stabilizing of a rebound height. The research was carried out in two time limits. The first time limit directly after the harvest and the second time limit after a four-month storage period. The measurements were performed on Melrose variety apples. On the basis of the experimental studies of apples mechanical properties under impact loading conditions, the small variability of the bruise volume in the separate research time limits was obtained. In connection with it, the main factor of the bruise resistance variability is the bruise energy.

WYZNACZANIE ODPORNOŚCI NA OBICIE JABŁEK METODĄ WIELOKROTNEGO UDARU

Krzysztof Gołacki, Paweł Rowiński, Zbigniew Stropek

Katedra Podstaw Techniki,
Zakład Teorii Maszyn i Automatyki
Uniwersytet Przyrodniczy w Lublinie

Słowa kluczowe: odporność na obicie, uderzenie, jabłko.

Abstrakt

W pracy podjęto próbę określenia metodyki wyznaczenia odporności na obicie oraz wpływu czasu przechowywania jabłek na jej wartość oraz zmienność. Odporność na obicie jest to stosunek energii obicia do objętości obicia. Metoda stosowana do wyznaczania odporności na obicie to metoda wielokrotnego zrzutu ze stałej wysokości. Polega na kilkukrotnym zrzucaniu badanego owocu ze

stałej wysokości aż do ustabilizowania się wysokości odbicia. Badania wykonano w dwóch terminach: termin pierwszy – bezpośrednio po zbiorze, termin drugi – po czteromiesięcznym okresie przechowywania. Pomiary przeprowadzono na jabłkach odmiany Melrose. Na podstawie badań eksperymentalnych właściwości mechanicznych jabłek w warunkach obciążeń udarowych uzyskano małą zmienność objętości obicia w poszczególnych terminach badań. W związku z tym głównym czynnikiem zmienności odporności na obicie jest energia obicia.

Introduction

In Poland every year on average about 2 million tons of apples are picked up (KIERCZYŃSKA 2005, DOBRZAŃSKI 2006). According to the Central Office of Statistics data in apple production, which Poland is a leading global producer, the losses caused by impacts, are estimated at the level of 15 %. It is a quotient of apples mass picked up in an orchard to apples mass placed in a storehouse. At this harvest size and level of generated losses, assuming an average price for 1 kilo of apples around 1 zloty, financial losses of several hundred million zlotys are developed. To quantitative losses it should be also added lightly damaged' apples, which were allowed to further production stages and whose quality and market value fell considerably. Apart from economical aspects there is still another equally important, aspect connected with the environment protection. It should be emphasized that such a large mass of damaged, rotten apples effects the natural environment. During putrefaction a lot of toxic substances are produced, of which liquid ones land in soil and gaseous ones mix in the air. This substances are responsible for degradation of the environment and are also the cause of many diseases and allergies among people and animals.

Above mentioned consequences of mechanical damage became a reason for researching and describing the phenomenon of fruit and vegetables susceptibility to mechanical loading. Not only is it important to explain the phenomenon of strain arising, causing apple tissue destruction but also to undertake some attempts connected with minimalization of the damage effects.

Correct determination of apple susceptibility under impact loading requires an application of indicators, whose values will be not dependent on physiological changes in tissue (KNEE 2002, AMIOT 1992, SAMIM 1993), and will be determined rather on the basis of the material strength. From among them it can be singled out a bruise resistance. The bruise resistance is a quotient bruise energy to bruise volume. There was developed a lot of research techniques to determine this indicator (CHEN 1991, ZHANG 1994, BAJEMA 1995, CHEN 1995, MATHEW 1997, MCGLONE 1997, BARITELLE 2001, VAN ZEEBROECK 2007). The method applied to determine bruise resistance and more accurate one of its components – bruise energy is the method of multiple drop at

a constant height. It consists in multiple dropping of a tested fruit at a constant height up to stabilizing of a rebound height. The stabilizing of a rebound height takes place, when separate drops caused such damage to apple tissue and increasing of contact surface area, that the next drops do not cause any further, additional damage. On the basis of obtained rebound height are determined elastic deformation energy, viscous deformations energy and bruise energy (plastic) (HOLT 1977, BAJEMA 1998). To establish bruise resistance it is also essential determining bruise volume. The total bruise volume is the sum of bruise volume above and below the contact surface (HOLT 1977).

In this paper an attempt was undertaken aiming at establishing a methodology determining bruise resistance, which describes apple susceptibility on mechanical damage, and the influence of apple storage time on its value and variability.

Materials and methods

The research was carried out in two time limits. The first time limit directly after the harvest and the second time limit after four-month storage period. The measurements were performed on Melrose variety apples. 50 apples in total were tested. Measuring series were every 7 days at 10 apples for 28 days. In the second time limit, the research period, the amount of measuring series and the amount of apples in separate series was analogous to the first research time limit. In the both time limit the apples chosen for the studies were not selected. Before the right impact test mass fruit and maximum diameter fruit measurements were carried out. The temperature in the research room changed in the 18–21degree range. It is the temperature, in which apples often are stored in retail both on a shop shelf and at consumer's home (DOBRZAŃSKI 2006).

The impact test was carried out on the measuring stand acting on the rule of pendulum, in which an impacting element was an apple dropped on a plate attached to an undeformable steel sheet. The measuring stand was also fitted with the scale with marked quantities corresponding to specific free fall height values. An apple placed at a definite drop height and held by means of a suction pump was next released through its shutdown.

Bruise resistance measurement

Bruise energy was determined by the multiple drop method at a constant height. The most important element of the technique is recording rebound height, which was made by means of an angle scale and a digital camera (Fig. 1).

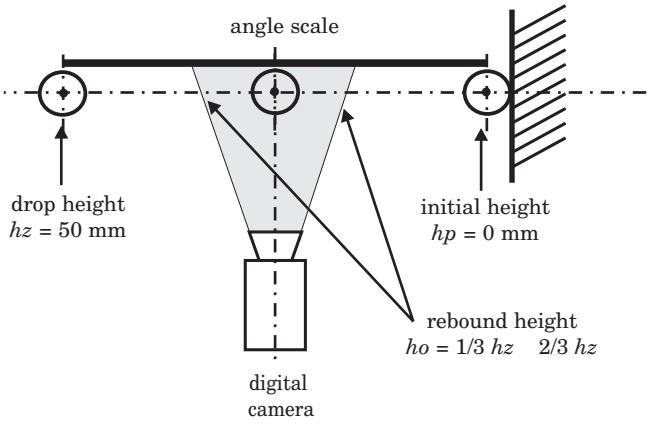

Fig. 1. The diagram of apple movement recording by the camera – view from above

Each apple was dropped six times at the same height. Stabilizing of rebound height took place already at the fourth drop. To make sure, that the rebound height stabilized , two drops were still recorded. During the preliminary research the drop height was so selected that the height of the first rebound was equal of the 1/3 drop height (BAJEMA 1998). It was stated, that over 90% of apples meets this criterion for the 50 mm drop height. The recorded film of the drop and rebound courses was transferred to a PC computer. By means of a specialist video software the recording was analyzed and the rebound height was read out for separate drops. On the basis of the data from the experiences for an each apple were created the graphs representing energy distribution in separate drops (Fig. 2.).

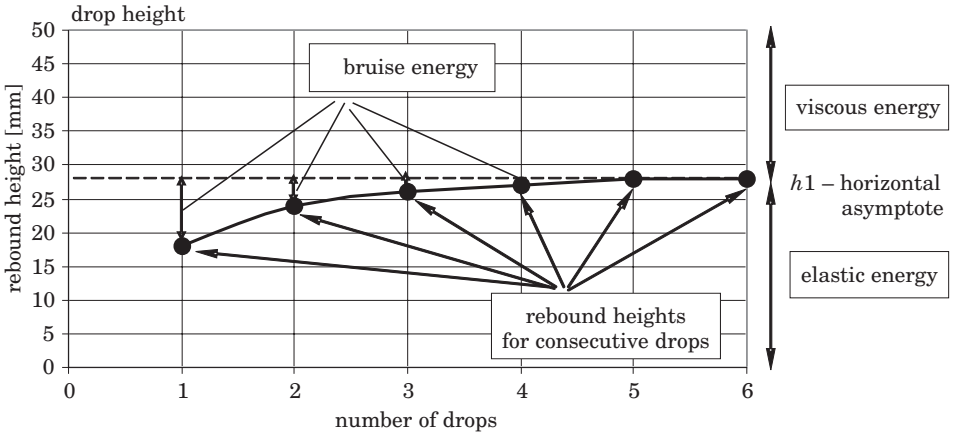

Fig. 2. Determining the rebound energy on the basis of the rebound height

The appropriate energy values, which are marked in the figure, are obtained by multiplying suitable heights by apple mass and gravitational acceleration.

The graph is formed through marking rebound height for consecutive drops. As it is seen in figure 2 after the first impact the rebound height of an apple is the lowest in comparison with other impacts. It shows, that during the first drop a large part of the impact energy is dissipated on permanent tissue deformation. During the consecutive rebounds the participation of elastic energy in total impact energy increases. After the fourth impact the rebound height stabilizes, which was marked by $h1$ horizontal asymptote. From this impact the consecutive drops trigger fewer and fewer permanent deformations of apple tissue. It can be stated, that for separate impacts the rebound height value represents elastic deformations energy. However, the segment from the height determined through the $h1$ asymptote to the drops height represents viscous deformations energy for a single impact. Irreversible deformation energy (plastic energy) that is permanent destruction of tissues represents the middle segment between the rebound height and the $h1$ asymptote. Thus the sum of segments between the rebound height value for the consecutive impacts and the $h1$ asymptote presents a total plastic deformation energy that is bruise energy.

The second element essential to determining bruise resistance is bruise volume. For this purpose after carrying out the research, bruised apples were left up to the moment of bruise discoloration. The manner of determining bruise volume of spherical shaped material represents Figure 3 (HOLT 1977).

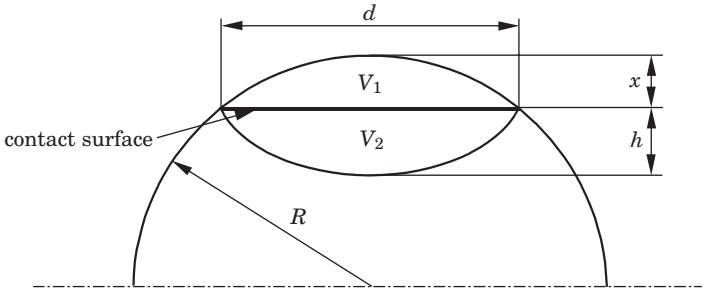

Fig. 3. Determining bruise volume

On the basis of d and h measured quantities V_1 bruise volume below contact surface can be determined:

$$V_1 = \frac{\pi h}{24}(3d^2 + 4h^2) \tag{1}$$

where: h is the bruise depth below the contact surface and d is the diameter of the contact surface area.

The diameter d was estimated on the basis of the contact surface area, established as a circle, reflected on a piece of paper. It was performed by means of a colouring substance, which was put on an apple in the place of an expected bruise before carrying out the last impact.

Similarly to the equation (1) bruise volume V_2 above the contact surface can be calculated:

$$V_2 = \frac{\pi x}{24}(3d^2 + 4h^2) \tag{2}$$

where: x is the bruise depth above the contact surface

The total bruise volume is therefore the sum of volumes below and above the contact surface

$$V = V_1 + V_2 \tag{3}$$

Results and discussion

Bruise energy is a part of the total impact energy, which triggers off tissue and plant cells damage that is irreversible changes. The curves of the energy distribution for a single apple were determined by recording the rebound heights in the consecutive drops at a constant height of 50 mm (Fig. 4).

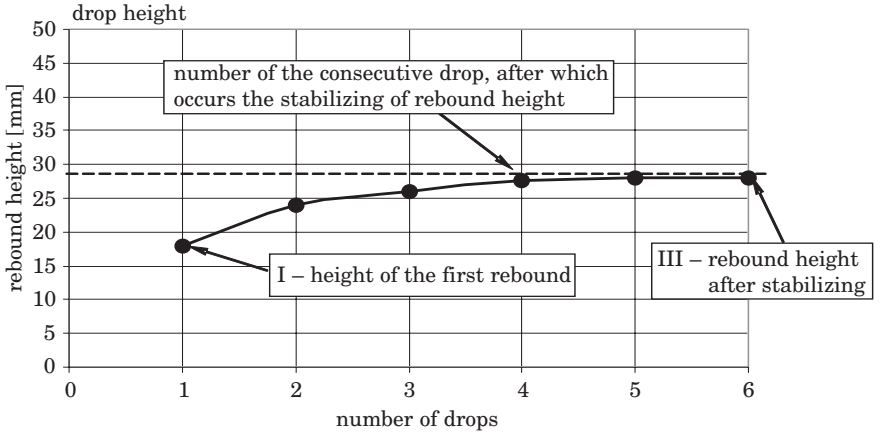

Fig. 4. The illustrative curve of the rebound stabilization process for Melrose variety apple directly after the harvest

The sum of segments between the individual rebound heights and the rebound height after stabilizing is bruise energy. The analysis of energy distributions shows size of permanent apple damage after consecutive impacts. For further analyses three characteristic points on the graph of energy distribution were selected (Tab. 1):

I – the height of the first rebound;

II – the number of the consecutive drop, after which occurs stabilizing of the rebound height;

III – the rebound height after stabilizing.

Table 1

Average values describing characteristic points for Melrose variety apples

Specification	Characteristic points	Consecutive research weeks				
		week 1	week 2	week 3	week 4	week 5
Apples directly after harvest	I [mm]	14	15	17	19	20
	II	5	5	5	5	5
	III [mm]	27	27	27	28	28
	average bruise energy [J]	**0.027**	**0.019**	**0.016**	**0.012**	**0.010**
Apples after four-month storage period	I [mm]	17	18	18	19	18
	II	2	2	2	2	2
	III [mm]	24	24	22	22	20
	average bruise energy [J]	**0.014**	**0.013**	**0.007**	**0.008**	**0.005**

The bruise energy value is determined directly through the above mentioned characteristic points. The bigger the difference between the first rebound height and the rebound height after stabilizing and the later stabilizes rebound height the higher value reaches the bruise energy.

Also the bigger value of the rebound height after stabilizing at the same height of the first rebound the bigger will be the rebound energy.

Collected in Table 1 data shows how long-term storage influences bruise susceptibility of apples. The bruise energy is closely connected with plastic deformations energy and elastic deformations energy. During the consecutive impacts the nature of deformations change. To the moment of rebound height stabilizing in consecutive impacts occur plastic deformations, which trigger off the permanent change of apple tissue structure. After four impacts occurs stabilizing of the rebound height which shows, that in an apple takes place only viscous and elastic deformations. The consecutive drops after stabilizing do not cause further permanent deformations. The bruise energy reaches the biggest value for apples, which require a larger number of drops for stabilizing the rebound height.

The bruise volume was determined on the basis of the contact surface area for the last drop and the bruise depth after discoloration that is about 24 hours after the measurement.

The bruise depths x and h were measured by calliper with accuracy of 0.1 mm after cutting an apple in the perpendicular plane to contact surface and going through the middle of the apple.

The total bruise volume is the sum of the volume above and below the contact surface (equation 3). For the studies were selected apples, whose shape was similar to the sphere, hence the curvature radius depends on an apple size that is also on its mass. In relation to it the bruise energy was higher for the apples with a larger mass. The storage time depended more on bruise discoloration than its size, because average values of the bruise volume during this period changed to a small degree. It results from the fact, that in the consecutive weeks of the storage, the apple skin is more and more creased and becomes a natural protective barrier for apple tissue more and more susceptible to bruise.

Apples directly after the harvest

In Figure 5 were presented the average energy distributions in the separate research weeks for apples directly after the harvest.

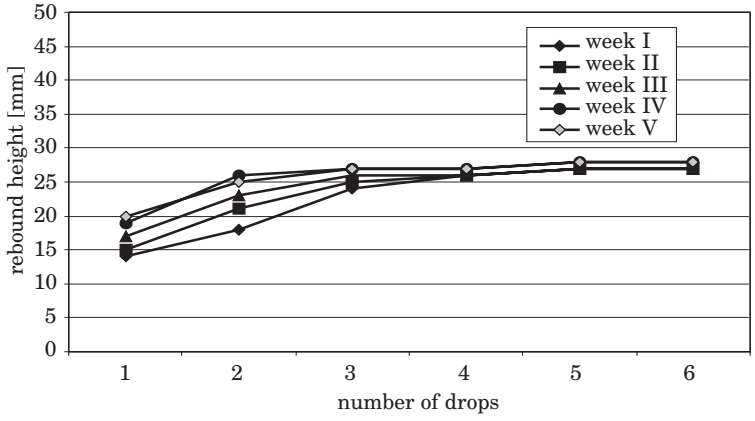

Fig. 5. The average values of rebound height in the consecutive research weeks for Melrose variety apples directly after the harvest

The energy distributions in the separate research weeks for the three first drops showed, that the plastic deformations energy for the consecutive drops decreases, thereby the elastic deformations energy increases. However, in the three consecutive drops permanent deformations energy value reaches already small values close to 0, which causes elastic deformations energy to remain of the same level in practice. The curves approach asymptote, showing that contact

surface area reaches such a size, which determines the occurrence of the stress values not causing already subsequent tissue damage.

Apples after the four-month storage period

The data analysis was carried out similarly to apples directly after the harvest. The average bruise distributions in the consecutive research weeks were showed in Figure 6.

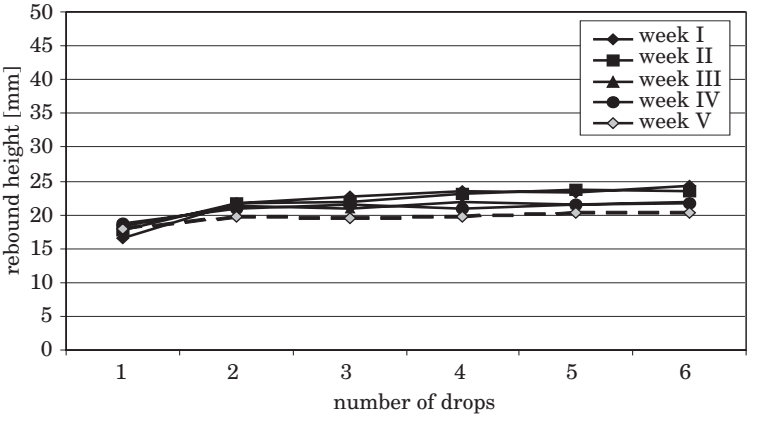

Fig. 6. The average values of rebound height in the consecutive research weeks for Melrose variety apples after the four-month storage period

In comparison to apples directly after the harvest (Fig. 5) it can be noticed, that the tested apples are noted for smaller plastic deformations energy values during the consecutive drops, because the height of the first rebound in each research week is higher. Moreover, the stabilizing of the rebound height in all research weeks occurs already after the second drop, which shows that the contact surface area quickly increases. In the fifth week apples partly rotted. Hence in figure 6 the fifth week marked by the dotted line, was not taken into consideration in the final results analysis

The influence of research time limit on bruise resistance

The next stage of the analysis was describing the bruise resistance and determining the influence of the research time limit on its variability. The comparison of the measurements results for the apples directly after the harvest

and after the four-month storage period was carried out. The bruise energy is directly proportional and the bruise volume inversely proportional to the bruise resistance. The average bruise volume value did not change significantly during the tests in the consecutive research weeks. In case when the bruise volume is subject to small changes, variability of the bruise energy determines the changes of bruise resistance. In case of the apples directly after the harvest the bruise energy decreases with the storage time, hence the bruise resistance also decreases.

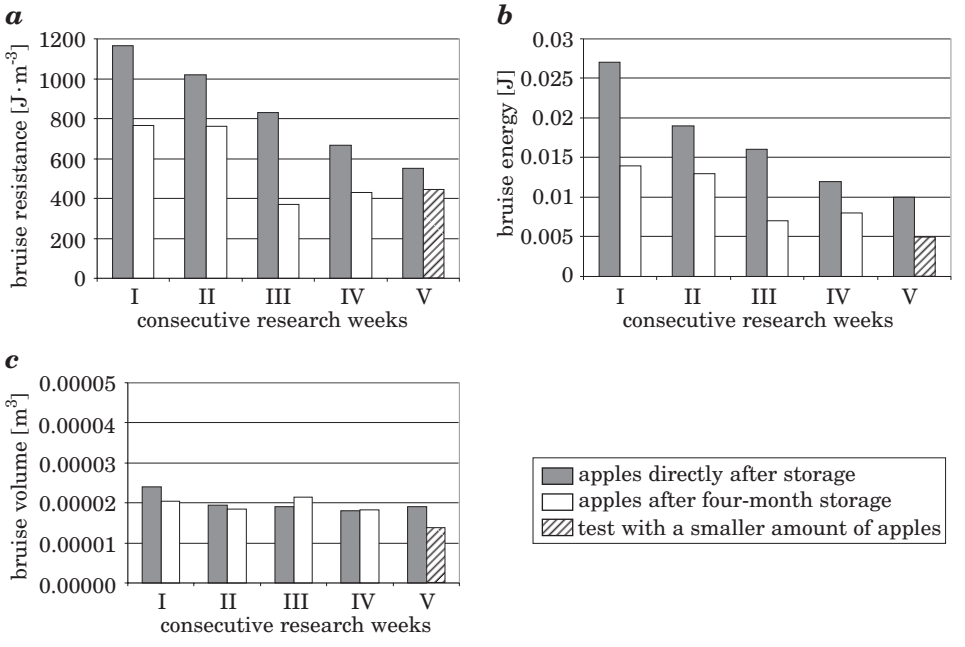

Fig. 7. Comparison of the average values: *a* – bruise resistance, *b* – bruise energy, *c* – bruise volume in the consecutive weeks for two research time limits

Figure 7 shows the average values of the bruise resistance and its components in separate research weeks for the apples directly after the harvest and after the four-month storage. In each graph (Fig. 7*a, b* and *c*) the fifth week in case of the apples after the four-month storage was filled with a pattern. In this way the trial with a smaller amount of the tested apples was marked. Figure 7*c* confirms the independence of the bruise volume from the length of the storage period and from the research time limits.

Conclusions

1. The bruise resistance of the apples subjected to the four-week storage directly after the harvest decreased with time.

2. There was stated a small variability of the bruise volume in the consecutive weeks for two research time limits. Hence also the main factor of the bruise resistance variability is the bruise energy.

3. The analysis of characteristic points location allows for comparative estimation of bruise stabilization phenomenon course for different apple varieties.

Accepted for print 12.10.2009

References

AMIOT M. J., TACCHINI M., AUBERT S., NICOLAS J. 1992. *Phenolic composition and browning susceptibility of various apple cultivars at maturity*. J. Food Sci., 57: 958–962.

BAJEMA R.W., HYDE G.M. 1995. *Packing line bruise evaluation for :Walla Walla; summer sweet onions*. Transactions of the ASAE, 38(4): 1167–1171.

BAJEMA R.W., HYDE G.M. 1998. *Instrumented pendulum for impact characterization of whole fruit and vegetable specimens*. Transactions of the ASAE, 41(3): 1399–1405.

BARITELLE A.L., HYDE G.M. 2001. *Commodity conditioning to reduce impact bruising*. Postharvest Biol. Technol., 21(3): 331–339.

CHEN H., BAERDEMAEKER J. DE 1995. *Optimization of impact parameters for reliable excitation of apples during firmness monitoring*. J. Agri. Eng. Res., 61(4): 275–282.

DOBRZAŃSKI B. jr., RABCEWICZ J., RYBCZYŃSKI R. 2006. *Handling of apple*. B. Dobrzański Institute of Agrophysics Polish Academy of Science.

HOLT J.E., SCHOORL D. 1977. *Bruising and energy dissipation in apples*. Journal of Textures Studies, 7: 421–432.

KIERCZYŃSKA S., WAWRZYNIAK J. 2005. *Ekonomika produkcji jabłek w różnych typach sadu*. AR, Poznań.

KNEE M., MILLER A.R. 2002. *Mechanical injury*. W: *Fruit Quality and its Biological basis*. Ed. M. KNEE. Sheffield Academic Press, Sheffield, pp. 157–179.

MATHEW R., HYDE G.M. 1997. *Potato impact damage thresholds*. Transactions of the ASAE, 40(3): 705–709.

MCGLONE V.A., JORDAN R.B., SCHAARE P.N. 1997. *Mass and drop-height influence on kiwifruit firmness by impact force*. Transactions of the ASAE, 40(5): 1421–1428.

SAMIM W., BANKS N.H. 1993. *Effect of fruit water status on bruise susceptibility and bruise color of apples*. N.Z.J. Crop. Hortic. Sci., 21: 373–376.

SCHOORL D., HOLT J.E. 1980. *Bruise resistance measurements in apples*. Journal of Textures Studies, 11: 389–394.

VAN ZEEBROCK M., VAN LINDEN V., RAMON H., DE BAERDEMAEKER J., NICOLAÏ B.M., TIJSKENS E. 2007. *Impact damage of apples during transport and handling*. Postharvest Biology and Technology, 45: 157–167.

ZHANG X., STONE M.L., CHEN D., MANESS N.O., BRUSEWITZ G.H. 1994. *Peach firmness determination by puncture resistance, drop impact, and sonic impulse*. Transactions of the ASAE, 37(2): 495–500.

TECHNICAL SCIENCES
Abbrev.: Techn. Sc., No 12, Y 2009

DOI 10.2478/v10022-009-0005-8

HYDRO- AND LITHODYNAMIC ASPECTS OF CONSTRUCTING A NAVIGABLE CANAL THROUGH THE VISTULA SPIT

Leszek M. Kaczmarek

Institute of Hydroengineering of the Polish Academy of Sciences (IBW PAN) in Gdańsk
Department of Civil Eugineering and Building Constructions
University of Warmia and Mazury in Olsztyn

K e y w o r d s: the Vistula Spit, the Vistula Lagoon, cutting, navigable canal, fairway, breakwater, sediment transport, silting up of fairways, changes in the shoreline, non-homogenous sediments.

A b s t r a c t

The paper presents hydro- and lithodynamic aspects of the intended construction of a navigable canal across the Vistula Spit. The discussion is based on the results of a study funded by a research and development grant carried out in 2007/2008 at the Institute of Hydro-Engineering of the Polish Academy of Sciences in Gdańsk in collaboration with the Chair of Civil Engineering and Building Constructions, Faculty of Technical Sciences, the University of Warmia and Mazury in Olsztyn. The paper also contains an analysis of the effect of planned breakwaters protecting the entrance to the canal from the Gulf of Gdańsk on the seaward shores of the Vistula Lagoon and the effect of their length on the silting up of the fairway. Some recommendations have been suggested regarding the optimal length of planned breakwaters.

HYDRO- I LITODYNAMICZNE ASPEKTY BUDOWY KANAŁU ŻEGLUGOWEGO PRZEZ MIERZEJĘ WIŚLANĄ

Leszek M. Kaczmarek

Instytut Budownictwa Wodnego PAN w Gdańsku
Katedra Budownictwa i Konstrukcji Budowlanych
Uniwersytet Warmińsko-Mazurski w Olsztynie

S ł o w a k l u c z o w e: Mierzeja Wiślana, Zalew Wiślany, przekop, kanał żeglugowy, tor wodny, falochrony, transport osadów, zapiaszczanie torów, zmiany linii brzegowej, osady niejednorodne granulometrycznie.

Abstrakt

W artykule przedstawiono aspekty hydro- i litodynamiczne planowanej budowy kanału żeglugowego przez Mierzeję Wiślaną. Dyskusję wyników przeprowadzono na podstawie rezultatów uzyskanych w ramach grantu badawczego rozwojowego realizowanego w latach 2007/2008 przez Instytut Budownictwa Wodnego PAN w Gdańsku we współpracy z Katedrą Budownictwa i Konstrukcji Budowlanych Wydziału Nauk Technicznych Uniwersytetu Warmińsko-Mazurskiego w Olsztynie. Przedstawiono analizę dotyczącą oddziaływania projektowanych falochronów osłaniających wejście do przekopu od strony Zatoki Gdańskiej na odmorskie brzegi Mierzei Wiślanej oraz wpływu ich długości na zapiaszczanie toru wodnego. Analizę wykonano na podstawie autorskiej metody uwzględniającej zmienność uziarnienia osadów. Sformułowano zalecenia optymalizacyjne dotyczące długości projektowanych falochronów.

Introduction

Constructing a new fairway on the Vistula Lagoon and a canal across the Vistula Spit raises high emotions (cf. DUBRAWSKI, ZACHOWICZ 1997). Supporters emphasize the economic benefits to be gained by the Polish economy, should the canal and a new fairway be opened that would connect the Gulf of Gdańsk with the port in Elbląg. Those against the idea speak about catastrophic impact of the planned construction on environment and emphasize huge costs of maintaining a fairway across the Lagoon and an approach fairway from the Gulf of Gdańsk.

At this point, it is worth reminding the reader that the concept of cutting the Vistula Spit is not a new one. On the contrary, it goes back to the times of King Stefan Batory. In brief, the history of plans to dig a canal across the Vistula Spit is as follows:

- 1577 (a riot in Gdańsk), King Stefan Batory plans to dig up a canal across the Spit and build a seaport on the seaward coast. The plan fails due to a war with Moscow,
- the 17th century, following the Swedish Deluge, a plan to cut the Spit between the villages of Przebrno and Skowronki appeared. In order to protect the canal, two forts were planned to be raised – for land and water defence,
- 1695 (the time of King Jan III Sobieski), the Lord Castellan of Chełm, Kazimierz Rogala Zawadzki, proposed to build a town and a seaport on the Hel Spit or the Vistula Lagoon,
- 1766–68, Andrzej Stanisław Młodziejowski, the Chancellor of the Crown and a bishop, presented a plan to cut through the Vistula Spit,
- 1847, a concept of digging up a canal near the vilage of Kąty Rybackie appeared,
- after 1945, Eugeniusz Kwiatkowski, head of the government delegates for

the reconstruction of the Polish Seacoast, expressed his hope that the problem of the Vistula Lagoon narrows would be solved successfully,
- 1983, prof. T, Jednorał completed a plan for the construction of a navigable canal across the Vistula Lagoon,
- 1994–96, a three-volume report "Principles for activation of the Elbląg region in terms of sea and river transport, recreation and fisheries" was published,
- 2007/2008, the Sea Office in Gdynia commissioned *The Feasibility Study for the Construction of a Navigable Canal across the Vistula Lagoon*. The feasibility study was prepared by the consortium of Polbud Pomorze, GEOSYNTEX Ltd and Fundacja Naukowo-Techniczna Gdańsk.

Despite so many attempts to build a canal which would cut across the Vistula Spit, the actual hydrotechnical works performed up to this day are limited to two undertakings: a permanent cutting across the Spit near Piława (in 1497) and, in the 1960s, the broadening and deepening of the narrows leading to the war port Baltijsk to about 460 m in width and 12 m in depth.

However, it should be kept in mind that the Spit is a geologically young formation and back in the Middle Ages it was intersected by single cuttings, including one near Krynica Morska present before the year 1300 and the so-called Elbląg Depth near the village of Skowronki between 1426 and 1431.

The concept of constructing a navigable canal consists of the following works:
- construction of a canal across the Spit, 1100 m long, 60 m wide at the depth (locally 100 m at the depth along a 200-meter-long section), 150 m wide at the water level and 5 m deep including the embankments,
- construction of a lock, 200 m long, 25 m wide and 5 m deep, with gates on each end,
- construction of breakwaters protecting the port and the approach to the canal from the sea,
- construction of a fairway on the side of the Vistula Lagoon along the section from the canal to buoy ELB10, about 13 km long, 60 m wide and 4 m deep in the first stage of the construction,
- construction of two low draw bridges and access roads.

Objectives of the research and development work conducted in the area of the intended canal

The article is a summary of the papers (KACZMAREK L.M. et al. 2008, KACZMAREK J. et al. 2008) which presented the results of the research completed under R&D grant no R04 017 03, called "Analysis of hydro- and

lithodynamic processes in the area of the planned cutting across the Vistula Spit and prediction of the effect of the cutting on the seashore, along with the evaluation of the intensity of silting up of the fairway from the cutting to the port in Elbląg". At the same time, this paper is an extension of the presentation the Author gave during the ceremony of the 60th anniversary of the Olsztyn Branch of the Polish Association of Civil Engineers and Technologists (PZITB).

The outcome of the study, carried out at the Institute of Hydro-Engineering, Polish Academy of Sciences, in Gdańsk in collaboration with a subcontractor, the University of Warmia and Mazury in Olsztyn (Chair of Civil Engineering and Building Constructions), consisted of an evaluation of the effect produced by the intended cutting across the Vistula Spit in the village of Skowronki (3 km away from Kąty Rybackie, situated at the base of the Spit, cf. Fig. 1) on the seashore on each side of the cutting. Another, equally important aim of the project has been to evaluate (predict) sedimentation processes in the fairway from the planned cutting to the port in Elbląg and on the approach fairway to the cutting from the Gulf of Gdańsk. Additionally, recommendations have been proposed regarding optimum length of entrance breakwaters on the side of the Gulf as well as suggestions concerning neutralization of possible erosion processes occurring on the shore near the aforementioned breakwaters.

Fig. 1. Location of the planned navigable canal across the Vistula Lagoon

Numerical calculations as well as field and laboratory measurements have been performed in order to achieve the above aims. The calculations (theoretical modelling) comprised the following physical processes: wind waves, wave-generated currents and sediment motion in the Gulf of Gdańsk and Vistula Lagoon, wind and gradient currents on the Vistula Lagoon, the morphodynamics of the seashore near the planned cutting on each side of the Vistula Lagoon, with particular attention paid to the effect produced by the entrance breakwaters on the side of the Gulf of Gdańsk as well as the intensity of the silting up of the fairway. For the calculations concerning the wave field, a third generation spectral model WAM4 was applied, whereas the calculations of the parameters defining the sediment motion were performed using a Dutch numerical software package UNBEST-LT and a novel Polish method, which takes into account the non-uniform grain size structure of sediments. Finally, mathematical modelling of water flow velocities in the Vistula Lagoon was performed using a Dutch software package DELFT-3D.

The field testes included measurements of the concentration of suspended sediments in the Vistula Lagoon, analyses of ground samples taken from the seabed near the shores of the Gulf of Gdańsk and detailed tachymetric and bathymetric measurements on the waters and shores of the Gulf of Gdańsk and Vistula Lagoon. For the measurements of the concentration of sediments suspended in the Vistula Lagoon, a laser device LISST-100 (version C) was used, which can measure volume concentration of sediments in 32 diameter classes, from 2.5 to 500 μm. The measurements were conducted within the area of the planned Elbląg-Skowronki fairway, at the sites where core samples from the seabed were taken. The bathymetric measurements were accomplished with an aid of a single-beam echo sounder coupled with a GPS receiver. One of the subcontractors, the University of Warmia and Mazury in Olsztyn, performed the field studies comprising collection of surface ground samples from the seabed of the Gulf of Gdańsk and Vistula Lagoon in the area of the planned approach fairways. The other subcontractor, the UNIGEO Ltd., carried out the sampling and analysis of core ground samples from the seabed of the Vistula Lagoon.

The laboratory tests consisted of the measurements of the speed of "washing away" of a seabed composed of both sandy sediments and cohesive ones, characteristic of the seabed in the Vistula Lagoon. In addition, deploying a LISST-100C device, turbidity time, i.e. time required for sedimentation of the sediments from the bottom of the Vistula Lagoon, was measured. These tests enabled us to estimate the maximum time it takes for sediment particles raised up during the future dredging works to fall down.

The present article is limited to the presentation of the results concerning two aspects, i.e. estimated effect of the planned breakwaters protecting the

approach to the cutting from the side of the Gulf of Gdańsk on the seaward shores of the Vistula Lagoon and determination of their influence on the silting up of the fairway. The rationale behind these research areas is the following principle: the longer the breakwaters (in this case, the ones protecting the entrance to the planned cutting), the lesser the problems caused by silting. However, when the breakwaters are longer, they are more expensive to construct and can generate more severe negative impact on the nearby stretches of seashores. When breakwaters are short, the costs incurred by their construction are reduced and their negative influence on the seashore is minimized. At the same time, however, it can become more difficult to enter and leave the canal due to the excessive silting up of the fairway.

For the purpose of our calculations, it has been assumed that the breakwaters will be perpendicular to the coast, which means the least positive solution regarding their effect on the shores. The breakwaters consisted of single, impenetrable, perpendicular groynes, measuring 100, 200, 300 and 400 m in length. Apart from the length of the breakwaters, the volume and rate of the silting up of the fairway has been analyzed depending on the assumed six variants of lengths of breakwaters protecting the entrance to the cutting. In the basic variant, recommended by KACZMAREK et al. (2008), the minimum distance between the heads of the breakwaters and the coast is 400 m, and the depth of the fairway, according to the Feasibility Study (1007/1008) is no less than 5.5 m. Five other variants have been analyzed, i.e. the distance between the breakwater heads and the shore is 150 m and the assumed depth is 6 and 5,5 m, or when the distance is 300 m and the depth is 6 and 5.5 m, and when the distance is 400 m and the depth is 6 m. The analysis of sedimentation processes within the fairway (in each of the six variants) leading from the Gulf of Gdańsk to the planned cutting was conducted for three types of grain size distribution, i.e. for sediments with a large amount of fine fractions, with a relatively small amount of such fractions and with homogenous distributions of a grain diameter $d = 0.22$ mm.

Hydrologic, bathymetric and ground conditions in the area of the planned canal

Measurements of wind waves on the Baltic Sea are conducted irregularly and only in a few places. For the water reservoir situated in the Gulf of Gdańsk near the Vistula Spit, no historic measurements are available. Thus, in order to re-create wind waves, a prognostic model was applied, which calculates wind wave parameters, such as height, period and angle (azimuth) of waves approaching the shore on the basis of speeds and directions of winds as well as the extent of their influence.

These computations have been done using the WAM4 model. In this model, the basic equation is the so-called equation of the wave effect balance, in which the following are included: energy transfer from wind to sea, formation of whitewater waves, i.e. whitecapping, bottom friction and mutual resonance interactions between wave components. The resolution of the computational space grid was 5' × 5' (about 9 × 9 km).

In order to determine the parameters of the wind waves occurring in an average statistical year in the forefield of the Vistula Lagoon near the planned cutting, the data obtained from a 44-year-long reconstruction of wind waves in the Baltic Sea based on wave sets from prognostic points situated in the eastern part of the Gulf of Gdańsk were analyzed. The point located closest to the analyzed region was found at the coordinates 54°25' N and 19°18' E and the depth $h \approx 45$ m, situated about 6 km off the shore. In order to establish periods of duration of certain wind wave heights for each direction, wave intervals at 0.5m were assumed, and for each interval the following were determined: significent wave heights H_s, peak times T_p, wave radius azimuths A_z and periods of duration.

The results of the calculations indicate that in an average statistical year wind waves approach the shores for a nearly identical time period from both sectors. The highest waves occur at winds blowing from NNW and N, when they reach the parameters: $\bar{H}_s = 4.72$ m, $T_p = 11.2$ s and duration time about 3 hours.

In 2007, bathymetric and tachymetric measurements were performed in the site of the planned cutting (KM 27, near Skowronki), on the side of the Gulf of Gdańsk. The field measurements included tachymetry of the beach (from the base of the dune) and bathymetry of the shore zone belt 800 m wide and 2 km long. The cutting was planned to be made in the centre of the analyzed area. The measurements were made in profiles located 100 m from one another and perpendicular to the averaged shoreline. Based on the results of these measurements, the seacoast near the planned cutting was classified as dissipative, that is the one whose near-shore profile favours gradual and gentle dispersion of energy generated by waves. The bathymetric profile of the seabed (Fig. 2) in this area is characterized by the presence of two bars (I – about 80 m and II about 250 m away from the shoreline). The average bed incline is about 1%.

In 2007, samples of sediments from the seabed of the Gulf of Gdańsk were taken in the analyzed area. Based on the grain size distribution analyses, it has been determined that the bottom in the analyzed area is composed of sandy sediments characterized by varied grain size along the crosswise profile of the shore (Fig. 3). The cumulative grain size distributions shown in Figure 3 indicate that further away from the shore (at depths of 4–9 m) the sediments

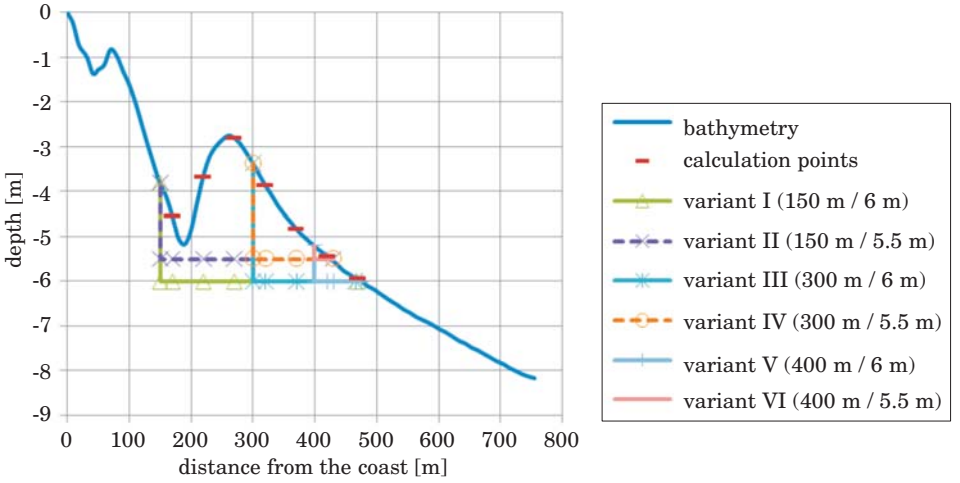

Fig. 2. The Gulf of Gdańsk – the bathymetry used for the calculations

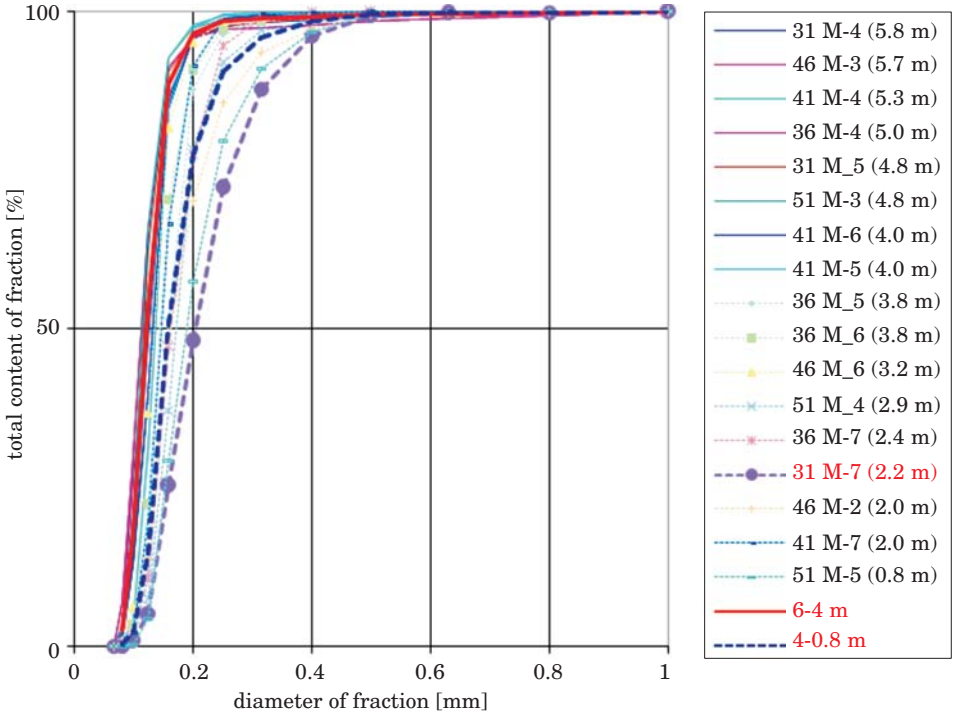

Fig. 3. Cumulative curves of grain size distributions of the seiment sampled from different depths near Skowronki

consist of fine sand of a median D_{50} = 0.12 to 0.15 mm and in the shore zone (at depths of 1-4 m) the sediments are slightly coarser of a median D_{50} = 0.17 to 0.25 mm. Closets to the shoreline and on the beach is sand of non-uniform grain size and a median in the interval from 0.21 to 0.38 mm.

The influence of the planned breakwaters on the seaside coasts of the Vistula Lagoon

The force responsible for transport of sediments and, consequently, the evolution of the see shore and bed consists of waves and currents, and in particular the so-called currents generated by waves breaking as they approach the coast. The volume of sediment transport depends on the intensity of hydrodynamic processes which occur, mainly during storms, in the shoreline zone and on the bathymetric conditions as much as on the type and supply of rubble lying on the sea bottom.

The calculations concerning the longshore sediment transport were performed using a licensed numerical programme from Holland *UNIBEST-LT* (version 4.0), which is part of the numerical package *UNIBEST*. The calculations in this programme were carried out on one, selected, representative bathymetric profile (cf. Fig. 2). The diameters of the sediments occurring in the shore zone were averaged for the calculations, by assuming in the numerical simulations the median D_{50} = 0.22 mm. In the *UNIBEST-LT* programme, the calculations regarding the volume of longshore sediment transported were performed using van Rijn's formula (1993). The results thus obtained were compared with the results generated by Kaczmarek's model (cf. KACZMAREK et al. 2004, KACZMAREK 2008) for homogenous sand (d = 0.22 mm) and very good agreement between the two sets of results was revealed.

The calculated distributions of the size of transported rubble as a function of the distance to the coast for particular directions of wind waves as well as the total resultant transport are presented in Figure 4. When comparing the calculated distributions of sediment transport intensity, as shown in Figure 4, with the shape of the bathymetric profile, illustrated in Figure 2, three streams of transport sediment are observable. The first one, relatively small, occurs very close to the coast, in a 50-m wide belt; the strongest one appears on the seaward slope of the first bar from the land; the third stream, a small one, occurs along the second bar on the seaward slope. The maximum width of the shore zone where sediment transport takes place is about 400 meters, but most of the sediment is transported within 160 meters from the coast.

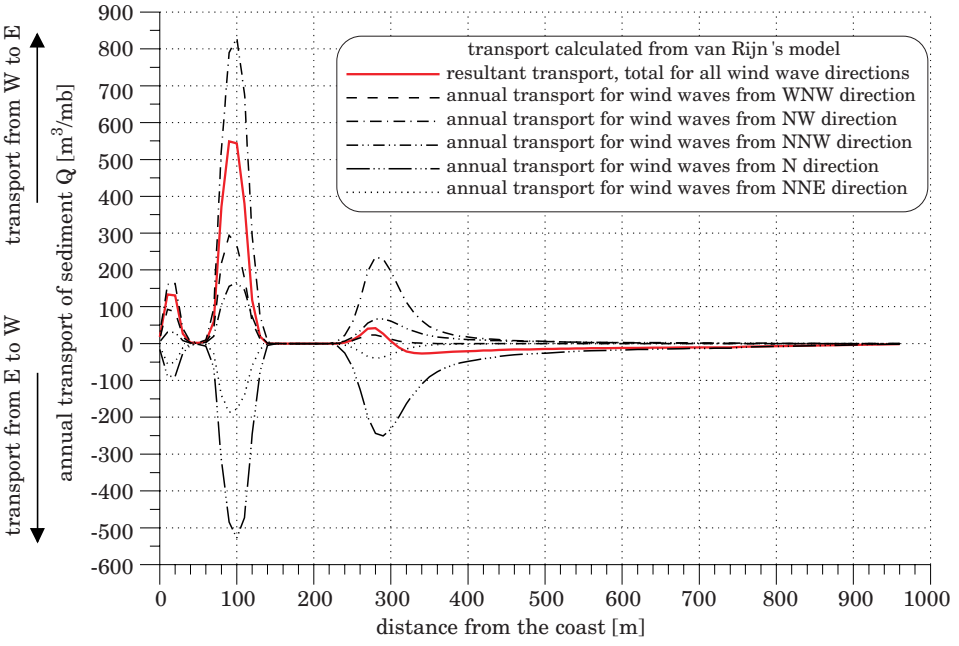

Fig. 4. Calculated distributions of sediment transport in an average statistical year on the seaward side of the Vistula Lagoon near Skowronki

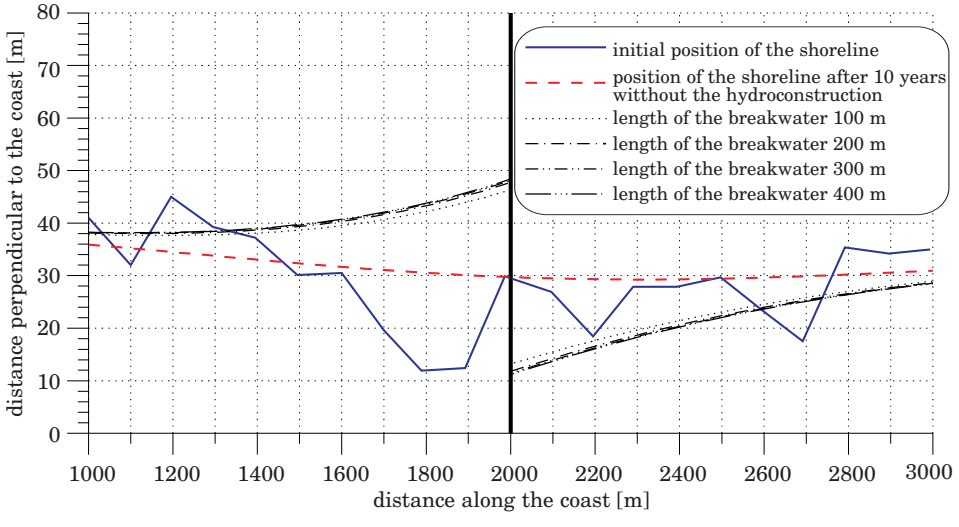

Fig. 5. Calculated changes in the position of the shoreline after 10 years, depending on the length of breakwaters near Skowronki on the seaward side of the Vistula Lagoon

Figure 5 shows the calculated changes in the position of the shoreline ten years after constructing the breakwaters provided that the breakwaters block all longshore sediment transport. In the simulations, the breakwaters are represented by a single, impenetrable groyne, situated perpendicularly to the coast and measuring 100, 200, 300 and 400 m in length. The starting point consisted of previously calculated resultant intensities of sediment transport in an average statistical year. This figure proves that, irrespective of the length of the breakwaters, both maximum changes in the position of the shoreline as well as the extent of such changes along the coast are nearly identical. This is due to the fact that most of the sediments transported along the coast travel very close to the shore.

Effect of the length of breakwaters on the silting up of the fairway from the Gulf of Gdańsk to the cutting

The calculations deployed a model for transport of non-uniform sediments that has been developed for a few years now (cf. KACZMAREK et al. 2004, KACZMREK 2008). This model enables one to calculate transport of sediments including all sandy fractions present in sediments since, as it turns out, it may be insufficient to know only one parameter, i.e. median D_{50}, to attain reliable evaluation of sediment transport and analysis of the silting up of fairways (cf. KACZMAREK, SAWCZYŃSKI 2007). Apart from the value of D_{50}, the shape of the grain size distribution is crucial. It becomes even more important when the amount of fine fractions in sediment is high.

This model distinguishes the bedload layer, the contact layer and the outside area where sediments are transported as suspension. The nature of interactions between water and sediments is different in each of the layers and therefore they are described using different equations, whereas at the contact area between these layers the solutions are "sewn" together, ensuring a complete description of the structure of transport of sandy sediments.

The mathematical modelling takes into account the fact that the most intensive vertical sorting out of grains occurs when they are raised up in the contact layer above the seabed. In the contact layer, pulse turbulences and chaotic collisions between grains cause very strong differentiation in the transport of particular size fractions of the sediment. Very close to the seabed – in the sub-layer where bedload flow features very strongly in the distributions of the velocity of i^{th} fraction of sediments – there is a very strong interaction between particular fractions, caused by mutual chaotic collisions. Further upwards from the bed, these interactions between the fractions weaken. However, the concentration of i^{th} fraction is big enough to cause

suppression of turbulences, with the actual suppression depending on the grain diameter d_i. It can be, therefore, expected that each i^{th} fraction, due to mutual interactions, moves at its own speed and is characterized by its individual concentration.

The velocities and concentrations of coarser fractions calculated in the contact layer are larger than the values obtainable should the bed be uniform and consisted of one corresponding fraction. Such acceleration of speed in a mixture results from mutual interactions between fractions, where coarser fractions are accelerated by finer ones.

In the outside layer, above the contact one, it is assumed that grain size distribution of transported sediment remains unchanged. The vertical concentration distribution in this layer is described by a power function.

It has been assumed, for the purpose of the calculations, that each wave characterized by the parameters H_{rms} and T_p can be described via the Stokes second approximation, with the crest made steeper and the flattened trough. This assumption has limited the area for the calculations to the waters near the second bar (cf. Fig. 2).

It has also been assumed (cf. KACZMAREK 2008) that along the windward edge (away from the current) of the approach fairway, sediments are transported during the wave crest phase in the bedload and contact layers and in the outside layer under the effect of the resultant current. On the edge away from the wind (under the current), sediments are transported only during the wave trough phase in the bedload and contact layers.

As mentioned above, this model enables inclusion of the effect of all fractions on sediment transport. The calculations were completed for two grain size distributions, shown in Figure 3, i.e. for the distributions designated with the symbol 31M-7 (collected from the depth of 2.2 m) and an averaged distribution from samples taken from depths 6 ± 4 m or the depths 4–8 m.

It is worth noticing that the measured sediment grain size distribution marked as 31M-7 resembles in its shape the distributions collected from the edge of the approach fairway to the port in Łeba (cf. KACZMAREK, SAWCZYŃSKI 2007, DUBRAWSKI 2003). Thus, although at the moment the contribution of fine fractions in averaged grain size distributions in the crosswise profile of the shore near Skowronki is larger than the 31M-7 distribution, it can be expected that following the exploitation (dredging) of the planned entrance fairway the presence of fine fractions will stabilize at a level similar to the one found in the sediments on the edge of the approach fairway in Łeba.

The results of the calculations pertaining to the distribution along the crosswise profile of the average annual volumes (cubic capacities) of sediments retained annually at 50-m long sections of the fairway, for the three presupposed "entrance" grain size distributions (including one homogenous distribution characterized by the diameter d =0.22 mm) are shown in Figures 6, 7 and 8.

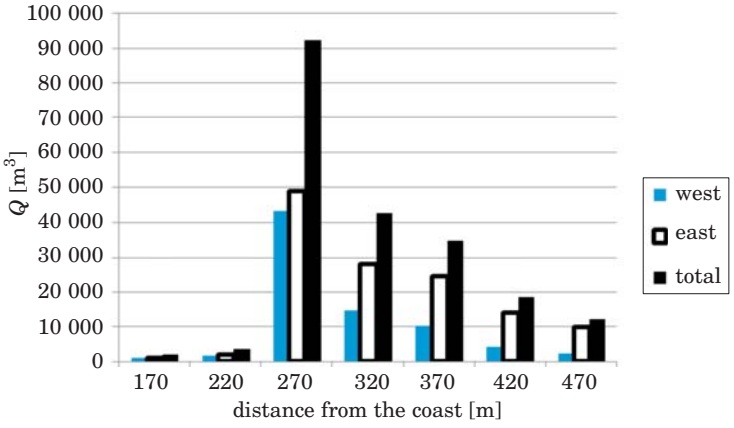

Fig. 6. Results of the calculations of the year average silting up along the fairway for the real grain size distribution, i.e. averaged from the depth 0.8–4 m or 4–6 m

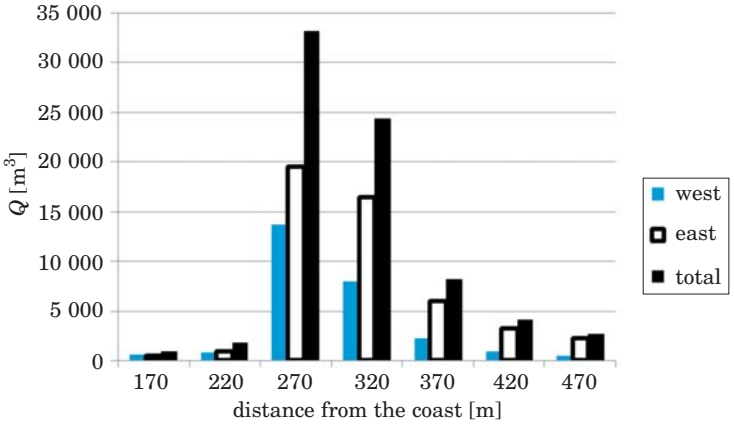

Fig. 7. Results of the calculations of the year average silting up along the fairway for the distribution 31M-7

It should be noticed here, however, that the contribution of wave situations to the silting up of the fairway is considerably large from both directions, i.e. from the west side as well as the eastern edge of the fairway. Nevertheless, it is evident that near the second bar, where the above calculations were made, the contribution of wind waves from the east to the silting up of the fairway is larger than the analogous influence from the western direction.

It needs to be emphasized that the largest intensity of silting up along the crosswise profile will occur at the top of the bar, i.e. at a calculation point distant about 270 m from the coast. This means that if we should decide to build shorter breakwaters, the future administrator of the fairway at the entrance to the canal from the Gulf of Gdańsk would be constantly in need of

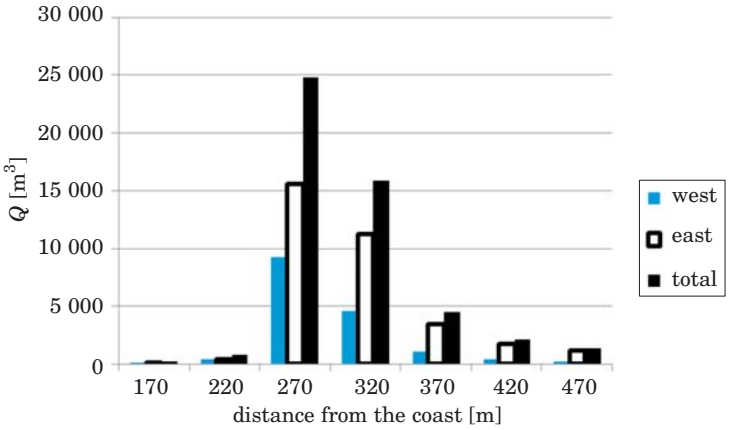

Fig. 8. Results of the calculations of the year average silting up along the fairway for homogenous distribution $d = 0.22$ mm

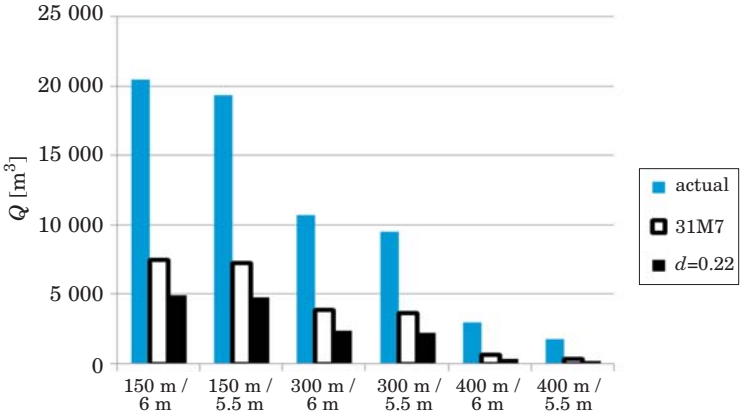

Fig. 9. Results of the calculations of the year average silting up along the fairway for different types of sediments and six variants of the fairway

using dredgers in order to maintain this entrance in good working order. The problems caused by accumulation of sand in this area will be graver when amounts of fine fractions in sediments lying on the edges of the future fairway increase.

The effect of grain size distribution on the total (sum) volume of sand built-up in the fairway is illustrated in Fig. 9. The calculations were performed for six variants of the fairway. It can be seen that the highest year average silting up will appear in the fairway in variant 1, i.e. where breakwater heads are 150 m away from the coastline and the intended depth is 6 meters. By extending the breakwaters, and consequently moving the

fairway further away from the coast, we can decrease the rate of silting up. In the most optimum situation (variant VI), where the breakwater heads are 400 m away from the coast and the depth of the fairway is 5.5 m, the total amount of sand accumulated due to silting will be 18.5 thousand m^3/year provided the amount of fine fractions in sediments remains considerably large. Should less fine fractions be deposited on the edges of the fairway (distribution 31M-7 and uniform distribution d = 0.22 mm), it can be expected that the year average silting up will reach, respectively, 4.1 and 2.1 thousand m^3/year, which means that the entrance fairway will have to be cleaned every 1-3 years.

Summary

The article contains a discussion on the influence of planned breakwaters on the seaward shores of the Vistula Spit and the effect of the length of these breakwaters on sedimentation processes in the fairway from the Gulf of Gdańsk to the planned cutting across the Vistula Spit. The analysis of the hydro- and lithodynamic aspects was conducted using a licensed Dutch programme *UNIBEST* and an original, Polish method which includes varied grain size distribution of sediments. In our simulations, the breakwaters consisted of a single, impenetrable groyne, perpendicular to the coast, which was 100, 200, 300 and 400 m long. The volume and rate of the silting up of the fairway were analyzed depending on the six variants of the lengths of the breakwaters. In the basic variant, the minimum distance from the breakwater heads to the coast was 400 m and the depth of the fairway was no less than 5.5 m. Additionally, five other variants were considered, i.e. the distance from the heads of the breakwaters to the coast was 150 m and the assumed depth of the fairway was 6 and 5.5 m, the distance was 300 m and the depth was 6 and 5.5 m and, finally, the distance was 400 m and the depth 6 m. The results are discussed in terms of three grain size distributions of the sediments, i.e. sediments with a large amount of fine fractions, with a relatively small amount of such fractions and uniform sediments characterized by the diameter d = 0.22 mm.

Owing to the fact that most of the sediments transported along the coast travel very close to the shore, within a belt measuring 160 m from the coast, the calculated changes in the position of the shoreline 10 years after constructing the breakwaters, for the analyzed lengths of these constructions: 100, 200, 300 and 400 m, are nearly identical.

The maximum increments of the shoreline, appearing at the same time, immediately near the western side of the breakwaters and losses on the

eastern side are about 20 m. However, considering all the errors made while calculating parameters of waves, water flow rates, intensities of sediment transport, it has to be assumed that an error in the evaluation of changes to the shorelines can be as high as 100%. This means that the maximum changes in the position of the shoreline are within the range of 10 and 40 m.

The extent of the changes to the shoreline 10 years after constructing the breakwaters, calculated from the outside edges of the breakwaters along the shore in both directions is about 1000 meters.

The above analysis verified that the optimum variant of a length of the breakwaters is the basic variant, i.e. when the distance from the breakwater heads to the coast is 400 m and the depth of the fairway if 5.5 m. In that case, the maximum volume of silting up will reach about 18.5 thousand m^3/year provided that the contribution of fine fractions in the sediment will remain high. This volume means that the fairway will have to be dredged every year. Should less fine fractions persist in sediments on the edges of the fairway (distribution 31M-7 and homogenous distribution d = 0.22 mm), the average annual volume of silting up could be expected to reach, respectively, 4.1 and 2.1 thousand m^3/year, which means that the approach fairway would have to be cleaned just every 1-3 year.

Accepted for print 1.10.2009

References

DELFT3D holenderski pakiet programów obliczeniowych, wersja 3.14.

DUBRAWSKI R., ZACHOWICZ J. 1997. *Kanał żeglugowy na Mierzei Wiślanej – pozytywy i negatywy dla środowiska morskiego.* Inżynieria Morska i Geotechnika, 5: 301–307.

DUBRAWSKI R. 2003. *Ocena oddziaływania na środowisko prac czerpalno-konserwacyjnych w porcie Łeba. Opracowanie wewnętrzne.* Instytut Morski, Gdańsk.

KACZMAREK L.M., SAWCZYŃSKI SZ. 2007. *Zastosowanie modelu transportu osadów niejednorodnych granulometrycznie do analizy zapiaszczania toru podejściowego do portu w Łebie*. Inżynieria Morska i Geotechnika, 6: 364-374.

KACZMAREK L.M. 2008. *Modelling of the silting up of navigation channels.* Technical Sciences, 11: 175–188.

KACZMAREK J., SAWCZYŃSKI SZ., DOMINIKOWSKI S., PAWŁOWICZ J., GRZYB G. 2008. *Podatność na zapiaszczanie i zamulanie planowanego toru wodnego z Zatoki Gdańskiej do portu w Elblągu w świetle wyników badań terenowych i analizy teoretycznej*. Raport z wykonania zlecenia wewnętrznego nr 523-0612.0301. Uniwersytet Warmińsko-Mazurski, Olsztyn.

KACZMAREK L.M., BIEGOWSKI J., OSTROWSKI R. 2004. *Modelling cross-shore intensive sand transport and changes of bed grain size distribution versus field data.* Coastal Engineering, Elsevier Science B.V., 51(5–6): 501–529.

KACZMAREK L.M., BIEGOWSKI J., GACA K., GĄSIOROWSKI D., KAŹMIERSKI J., OSTROWSKI R., PERFUMOWICZ T., PRUSZAK Z., SCHÖNHOFER J., SKAJA M., SZMYTKIEWICZ M., SZMYTKIEWICZ P. 2008. *Analiza procesów hydro- i litodynamicznych w rejonie planowanego przekopu przez Mierzeję Wiślaną i predykcja*

wpływu przekopu na brzeg morski wraz z oceną intensywności zapiaszczania (zamulania) toru wodnego na odcinku od przekopu do portu w Elblągu. Raport końcowy z realizacji projektu badawczego rozwojowego – na zlecenie Ministerstwa Nauki i Szkolnictwa Wyższego. IBW PAN, Gdańsk.

Studium wykonalności inwestycji (2007/2008): Budowa kanału żeglugowego przez Mierzeję Wiślaną. Konsorcjum: Polbud Pomorze, Geosyntex Sp. z o.o. i Fundacja Na-u-kowo-Techniczna - wykonane na zlecenie Urzędu Morskiego w Gdyni.

UNIBEST-LT Version 4.0. 1993. User;s manual MS-DOS PC-program. Delft Hydraulics, The Netherlands.

VAN RIJN L.C. 1993. *Principles of sediment transport in rivers, estuaries and coastal seas*. Aqua Publications, the Netherlands.

TECHNICAL SCIENCES
Abbrev.: Techn. Sc., No 12, Y 2009

DOI 10.2478/v10022-009-0006-7

ASPECTS OF DESIGNING EDUCATION BUILDINGS IN A CONSERVATION AREA: A CASE STUDY OF A BUILDING DESIGNED FOR THE SCHOOL OF CIVIL ENGINEERING AT THE UNIVERSITY OF WARMIA AND MAZURY IN OLSZTYN

Marek Zagroba

Department of Civil Engineering and Building Constructions
University of Warmia and Mazury in Olsztyn

K e y w o r d s: architecture, urbanism, building permit design, spatial composition, conservation area, campus, Kortowo.

A b s t r a c t

Designing architectural objects in a conservation area usually involves many problems, whose solution most often means complying with a series of restrictions, which pertain to elements of urban and architectural design. Creating spatial connections between the new and the existing, listed architecture is not an easy task. Many historic locations experience architectural chaos, which ensues from inapt attempts at combining these two types of architecture and the historic part of the academic campus in Kortowo is a good example in this resepct.

This paper presents the architectural, structural and services design problems encountered while working on a design of an education and laboratory building localized in a conservation area. The building in question is to replace the existing, one-storey and flat-roofed building, which will be demolished. The main obstacles to designing the building caused by the conservation requirements were how to adapt the new building's functions to the specific character of the civil engineering course of study and how to create an architectural form that would fuse with the historic shape of this part of the academic campus.

The oldest part of the campus, which has been designated as a conservation area, in practice excludes construction of larger buildings on undeveloped land. This, however, does not mean that the area is completely closed to possible and, in some cases, necessary investment projects. New constructions, in compliance with the local development plan, should eliminate the buildings whose form, plan and architecture introduce discord to the historically defined space.

PROBLEMATYKA PROJEKTOWANIA OBIEKTÓW DYDAKTYCZNYCH W STREFACH OCHRONY KONSERWATORSKIEJ NA PRZYKŁADZIE BUDYNKU DLA KIERUNKU BUDOWNICTWO UNIWERSYTETU WARMIŃSKO-MAZURSKIEGO W OLSZTYNIE

Marek Zagroba

Katedra Budownictwa i Konstrukcji Budowlanych
Uniwersytet Warmińsko-Mazurski w Olsztynie

S ł o w a k l u c z o w e: architektura, urbanistyka, projekt budowlany, kompozycja przestrzenna, strefa ochrony konserwatorskiej, miasteczko akademickie, Kortowo.

A b s t r a k t

Projektowanie obiektów architektonicznych w strefie ochrony konserwatorskiej wiąże się najczęściej z wieloma problemami, których rozwiązanie wynika z wielu obostrzeń. Dotyczy to elementów projektowania urbanistycznego oraz architektonicznego. Przestrzenne powiązanie projektowanej architektury z istniejącą – objętą ochroną, nie jest zagadnieniem łatwym. W wielu miejscach o historycznym rodowodzie można zaobserwować chaotyczne skutki takich działań. Za przykład posłużyć może historyczna część kampusu uniwersyteckiego w Olsztynie.

Artykuł przedstawia architektoniczne, konstrukcyjne i instalacyjne problemy związane z projektowaniem budynku dydaktyczno-laboratoryjnego, położonego w strefie ochrony konserwatorskiej. Obiekt ma zastąpić istniejący parterowy, płaski pawilon przeznaczony do rozbiórki. Główne trudności projektowe wynikające z warunków konserwatorskich skupiły się wokół dostosowania funkcji do potrzeb związanych ze specyfiką kształcenia na kierunku budownictwo oraz stworzenia formy architektonicznej odpowiadającej zagospodarowaniu historycznej części miasteczka akademickiego.

Objęta ochroną konserwatorską najstarsza część kampusu uniwersyteckiego nie nadaje się praktycznie do wznoszenia obiektów kubaturowych na niezabudowanym terenie. Nie oznacza to jednak, że jest to strefa pozbawiona możliwości czy nawet konieczności prowadzenia działań inwestycyjnych. Nowe inwestycje, zgodnie z zapisami planu miejscowego, powinny eliminować obiekty, które swą formą, układem i architekturą dysharmonizują przestrzeń historycznie zdefiniowaną.

Introduction

Designing architectural constructions in a conservation area will typically involve many problems, which must be solved without violating numerous restrictions. The actual restrictions vary depending on the binding form of conservation[1]. They can pertain to elements of urban design – adjustment of a new structure to the existing composition, which is contained in the development plan, as well as to architectural design, namely the functional layout, form and material, found in particular technical drawings.

[1] Historic buildings can be listed in a national heritage register, which in consequence means quite strict restrictions regarding possible investment changes. Another, more lenient form of protection is when a building or a complex of buildings are under the Conservation Officer's protection.

Creating spatial connection between the architecture in the process of being designed with the existing buildings, under conservation, is not an easy task. Many historic locations experience chaotic results of inapt solutions. The historic part of the academic campus in Kortowo, Olsztyn, is a good example, and the present spatial management of this area calls for some serious, planned and executed changes. However, any decision about raising a new building at a site already occupied by another construction is difficult to implement due to the economic considerations alone, and often remains as a study plan. The historic part of Kortowo is different in this respect. The idea of demolishing the one-storey, light-construction building, topped with a flat roof, and replacing it with a new building, which will resemble the historic buildings in its plan and form is a rare but certainly executable example of such construction projects[2]. This can also be the beginning of further actions aiming at the elimination of the chaos present in a historically defined space.

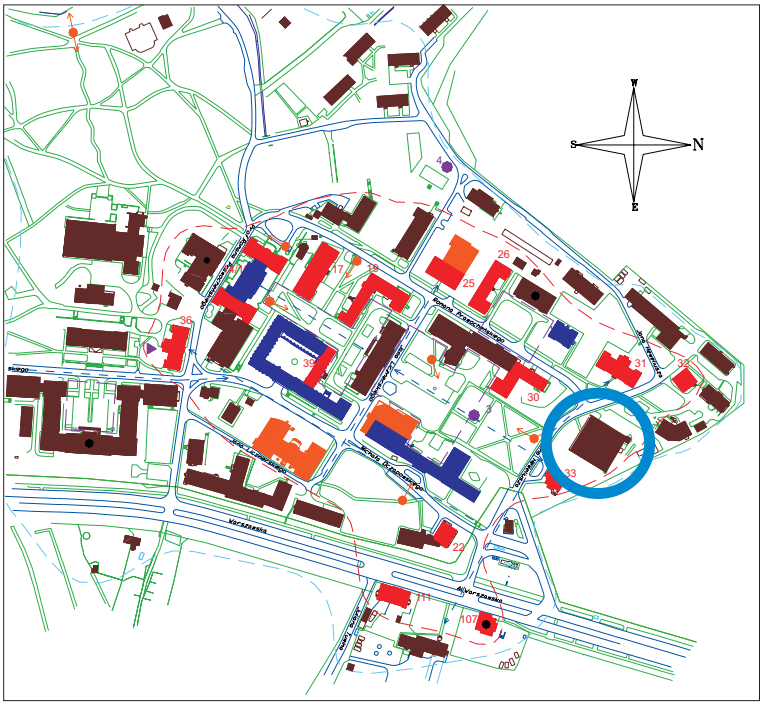

Fig. 1. The historic part of the university campus in Olsztyn (the blue circle marks the localization of a new building which will replace the existing one-storey building)
Source: Study on cultural values of Kortowo, by M. ZAGROBA.

[2] When this article was being written, the multi-branch building design for the education and laboratory building for the School of Civil Engineering at the University of Warmia and Mazury in Olsztyn had already been given administrative approval – a building permit.

The issues connected with designing a building to house classrooms and laboratories for the School of Civil Engineering at the University of Warmia and Mazury in Olsztyn, situated in a clearly defined space, are the subject of this paper. The designer's task was difficult not only because of the complicated functional plan, which needed to accommodate the specific functions of the school, but also because the new form was to be created in a way that would enhance and emphasize the historic part of the campus[3] – a conservation area.

The oldest buildings on campus are the remains of a psychiatric hospital compound, dating back to the late 19th century. The preserved urban and architectural pattern is composed of material culture objects which create spatial interactions between one another and, from the designer's point of view, have added to the difficulty of making a design. These consist of:
– archaeological objects – archaeological sites,
– urban objects – the compositional pattern, interiors, viewing axes,
– architectural objects – single buildings and their compounds,
– nature – nature monuments, green areas,
– landscape assets – landscape interiors, scenic overlooks.

Space management

The urban pattern of Kortowo has only partially retained its original layout. The changes took place at the end of World War Two, when some of the buildings were destroyed. Although the preserved foundations of the pre-war buildings were used to raise new edifices, the form and architecture of the post-war buildings has been in sharp contrast to the historic buildings until the present day. The one-storey, flat-roofed building at 4 Heweliusza Street, where the newly designed building will stand, is an evident example (Fig. 2). The existing one, located in the conservation area, with its form, layout and used building materials contrasts sharply with the historic buildings, typical for Kortowo (Figs. 3, 4)

The location of the present building has for many years been violating the recommendations contained in the relevant urban development plans, including the most current legal document, such as the binding local development plan for Kortowo[4]. According to the extract from the above plan, the one-storey building violates the rules of the historic conservation, with the concern raised by its architectural appearance, size and proportions. The document recom-

[3] Dr Marek Zagroba, BSc in Civil Engineering, MSc in Architecture, is the author of the building design, the architectural branch.

[4] The local development plan for the grounds of the University of Warmia and Mazury in Kortowo, the town of Olsztyn, was passed by the Act of the City Council of 17the January 2004

Fig. 2. The one-storey building at 4 Heweliusza Street. Photo: M. ZAGROBA

Fig. 3. The psychiatric hospital ward for women, block no 31. Photo: M. ZAGROBA

mends demolishing this building. The solutions included in the local plan comply with the conservator's decision to list Kortowo compound as a heritage site.

When approaching the task of creating a conceptual design for a new building, based on the prepared functional and services program, we encountered difficulties due to the detailed conservation restrictions for the new investment project. The conditions in the local plan specify quite precisely the scale, height and footprint of a new building, its shape, wall elevation and the building materials. To what extent that has been a complicated task is made

Fig. 4. The historic building of a post office in Heweliusza Street. Photo: M. ZAGROBA

evident by the fact that the Historic Conservation Office required a compliance assessment of the design documentation not once but twice[5] (which happens very rarely). Another problem to solve was how to adapt the new building to the size of the parcel of land without destroying any of the trees there, which are also protected. Complying with the Building Law meant not only designing properly the paths, drives and emergency exits, etc., but also the localization of the technical equipment, needed for the building's fittings (air intake vents and exhaust terminals)[6].

The extensive division of the building's floor plan enabled us to draw on the historic buildings in Kortowo. In addition, it provided the interiors with enough sunlight, made it easier to organize the public space in front of the entrance and design appropriate street furniture.

The functional and services programme for the building, or more precisely, the specific nature of a general building engineering laboratory, forced us to divide the building into two parts, with a glazed patio[7] connecting both parts and used for holding exhibitions and seminars.

---

[5] The design underwent a compliance assessment with the Municipal Historic Conservation Officer during the architectural conceptual stage and during the stage of making the building design.

[6] The restrictions formulated by the Conservation Officer forced us to place the air intake and exhaust vents on the ground rather than on the roof, which in turn needed to be approved by the Sanitary Hygiene Inspector for the District of Olsztyn.

[7] It was planned to place a resistance testing machine in the general laboratory, and the parameters of this machine forced us to design a special floor (80 cm in thickness) and some technical service space under the floor. The whole building was divided into two sections so as to protect the other part of the building from vibrations and noises from the laboratory.

Fig. 5. The conceptual plan for managing the grounds. Elaborated by M. ZAGROBA

The functional plan of the building

The work on the conceptual architectural design for the building began the moment the previously commissioned functional and services plan was ready and the usable floor space had been determined[8]. From the point of view of the designer, it was rather difficult to verify the actual additional floorage, which in the above plan was mentioned only in general terms. This aspect is associated with the relations between the expected number of users and the required parameters of communication passages, toilets, the width of staircases, etc.[9]

[8] The usable floor of the building is nearly 3.500 m^2. The footprint is over 1.500 m^2 and the cubage is 21.238 m^3.

[9] The parameters ensuing from adjusting elements of buildings to human anatomy and number of users are established in the Ordinance of the Minister for Infrastructure of 12th April 2002, on the technical conditions to be fulfilled by buildings and their location (Journal of Laws of 15th June 2002, No 75, item 690) as well as some more specific regulations.

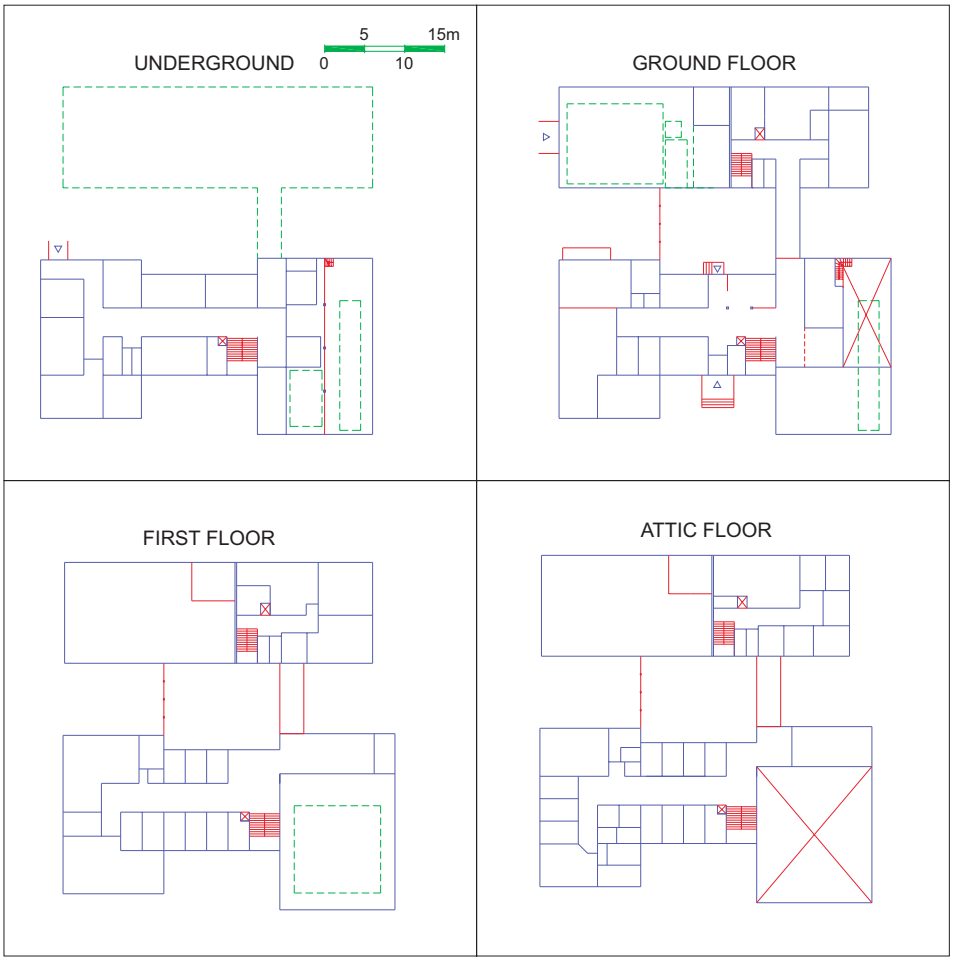

Fig. 6. The conceptual design of the functional layout of the building. Author: M. ZAGROBA

The changes introduced to the functional plan of the building were a consequence of the many meetings with the future users of the building, with ensuing eight concept design versions. This aspect reflects the sociological role of an architect but can be highly undesirable when working for a tender bid, with very strict deadlines, particularly for the other participants of the designing process, who are unable to begin their work on particular branch solutions until the general design is "finalized".

Buildings which combine education and laboratory functions are among very difficult objects to design. Classrooms, staff offices, specialist laboratories, workshops or utility rooms either have to be interconnected or separated, and

this means that the designer must engage much imagination and produce a huge number of sketches which will contain multi-plane aspects such as, for example, proper sunlight, good floor space and indoor capacity, integrity with the building's shape and wall elevation, adjustment to the adopted construction and fittings solutions or compliance with the Building Law in terms of work safety regulations, ergonomics, hygiene and health, fire protection, etc. One of the biggest challenges for the designer, caused by the complicated functional plan of the building, was to work out the technological solutions for particular laboratories and workshops. This aspect has largely added to the design's complexity.

Some other engineering problems were associated with the fact that the building needed to be furnished with specialist equipment, and some elements of the building had to be adjusted to the equipment's parameters. The length

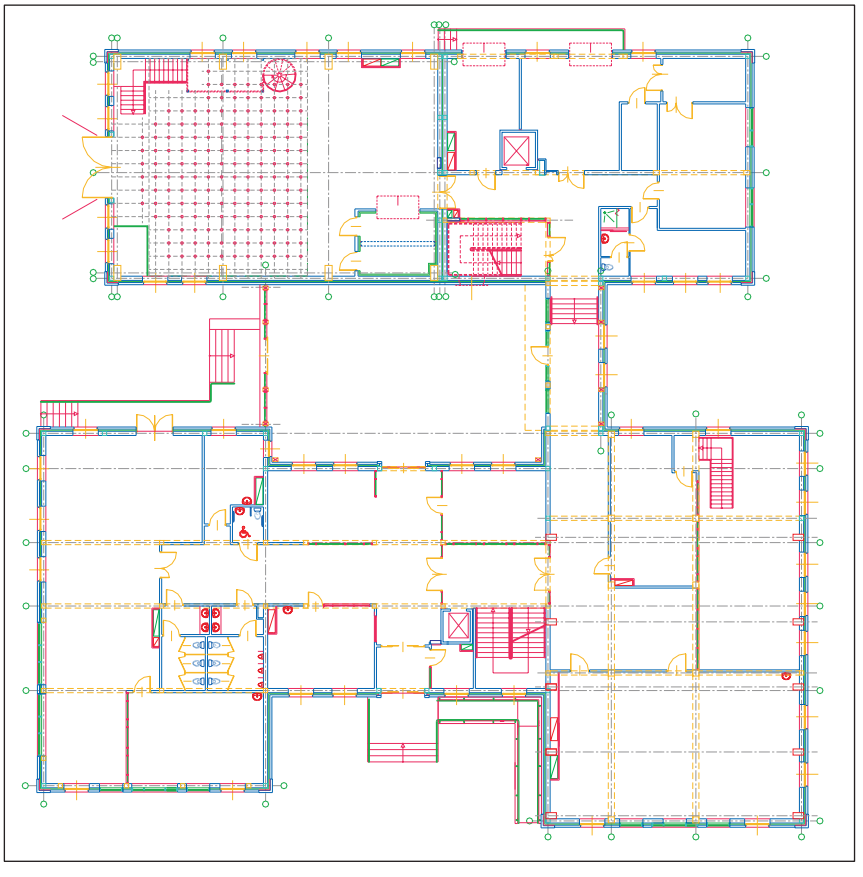

Fig. 7. The ground floor plan. Author: M. ZAGROBA

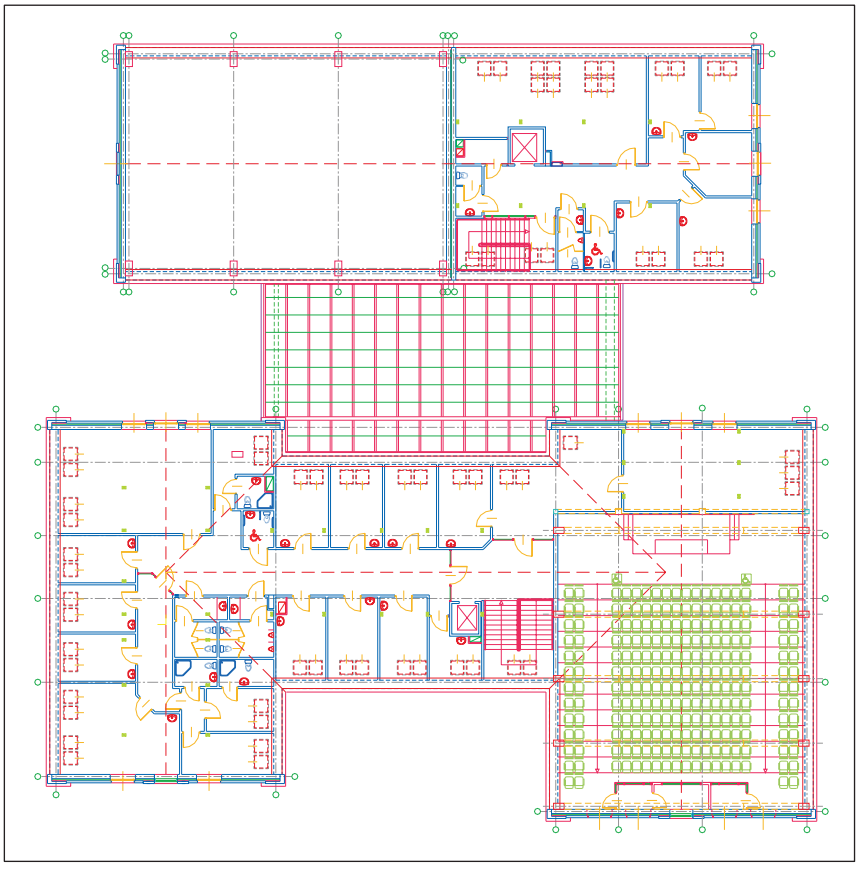

Fig. 8. The attic floor plan. Author: M. ZAGROBA

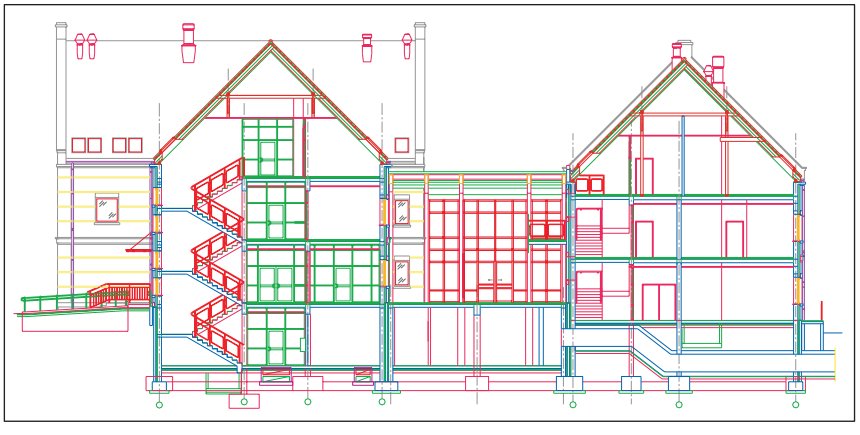

Fig. 9. The vertical cross-section of the building. Author: M. ZAGROBA

and height of a rubble-overflow channel imposed certain functional and space-management solutions. The parameters of a resistance testing machine in the civil engineering laboratory forced us to divide the building into two parts and to design a specially strengthened floor as well as some technical service space underneath. Another big challenge was to design a roof construction over a lecture theatre seating 238 persons, which because of the incline between rows of seats occupies the height of two storeys. The problem of finding support for the pillars holding the roof had to be solved by searching for a compromise between the architecture and the construction. The attention given to the energy-saving solutions made us reject gravitational ventilation, replacing it with a mechanical system including forced air intake and exhaust. This it turn meant finding additional surface area (on a small land parcel) to place large ventilation and A/C equipment (which needed over 190 m^2 of land surface).

The changes introduced to the design solutions, which are unavoidable when creating a multi-branch design, were on the one hand suggested by branch designers. On the other hand, they were a consequence of hearing suggestions and opinions of individuals and institutions involved in the process of the design's approval. Since the binding law forces designers to take into consideration such remarks, the preparation of the documentation took more time[10].

The architecture of the building

The preserved historic buildings in Kortowo possess characteristics typical for the regional architecture, namely they are red-brick buildings, with gable roofs covered with clay roofing tiles. Their facades are typically divided with risalits and the walls show some interesting architectural detail, for example brick cornices and tops of risalits or timber elements of the roof construction.

The Conservation Officer's recommendations dealing with the new building to replace the one-storey light-construction building were very strict[11]. The documentation prepared for the design of a new building underwent twice a compliance assessment at the Municipal Historic Conservation Office, which proves how important the building is for the whole conservation area.

[10] The compliance assessment procedure by the Design Documentation Assessment Unit or by the Historic Conservation Officer is an administrative procedure, which is time consuming, and designers have no influence on the length of the process.

[11] According to the Conservation Officer's recommendations, the scale, height and footprint of a new building should be adjusted to the historic urban composition. The building's shape, the shape of its roof, the composition of the wall elevation, including risalits, pattern, proportions, shapes of windows and doors should correspond to the architecture of the existing buildings.

Fig. 10. The south wall elevation. Author: M. ZAGROBA

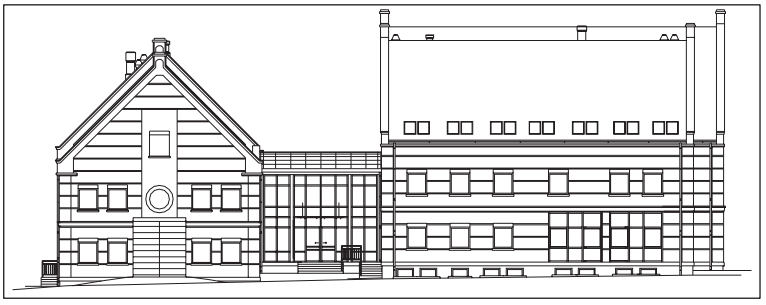

Fig. 11. The west wall elevation. Author: M. ZAGROBA

The new architecture is set in the spatial context of the historic part of the academic campus. The divisions of the building's shape, its scale, layout and roof angle, the divisions on the outside wall elevation, the proportions and the materials (brick and clay roofing tiles) correspond to the architecture of the historic buildings. The glazed elements in the wall elevation, the square shape of the windows and doors as well as the exposed aluminium and glass elements of the patio are a expression of the modern aspect of the building, a toned down expression because of the proximity of historic buildings.

One of the most difficult stages in our work on the design was associated with our attempt at preserving a pure shape of the building, undisturbed by technical solutions. Considering the fact that we often had to adapt the building to housing some specialist equipment, this aspect created a great challenge for the designers[12]. It was not uncommon for us to look for a compromise between particular branch designers.

[12] It is far too often that we can spot ugly A/C boxes or other devices which are components of fittings on walls of buildings (including historic ones).

Fig. 12. The visualization of the building. Author: M. ZAGROBA

Fig. 13. The visualization of the building. Author: M. ZAGROBA

Conclusions

Many buildings constructed in the historic part of Kortowo after World War Two largely depreciate the value of this conservation area. Their shapes, forms and structural solutions as well as the materials and techniques used for finishing their wall elevations are highly divergent from the harmonious historic architecture. The zoning documents, such as the local development plan, have for years been trying, rather unsuccessfully, to direct new invest-

ment projects (construction, expansion, addition of storeys, re-construction, and even demolition) so that they agree with the form, cubage and architectural expression of the historic buildings.

The design presented in this article proves that such attempts bordering between restoration and revitalization in a historically defined space can go beyond an analytical study stage. However, this has not been an easy task. Many solutions were dictated by the need to attain the contemporary standards set for buildings and meet the requirements imposed by the specific character of an education building while complying with the stricter regulations connected with the designated conservation area.

While discussing the presented design of a building for the School of Civil Engineering at the University of Warmia and Mazury in Olszyn, it can be concluded that the spatial development of the historic part of Kortowo should focus on restoration, namely on re-organisation of the form and surroundings of the buildings and on liquidation of the buildings which depreciate the value of this historically rooted space. However difficult it is, the contents of this article demonstrate that it is possible to achieve such aims[13].

Accepted for print 6.10.2009

References

Cielątkowska R. 2003. *Miasteczko Akademickie Uniwersytetu Warmińsko-Mazurskiego w Olsztynie w kontekście funkcjonowania campusów uniwersyteckich w świeci,* W: *Kortowo – Miasteczko Akademickie Uniwersytetu Warmińsko-Mazurskiego w Olsztynie. Kontekst-Historia-Stan obecny,* Red. R. Cielątkowska, Olsztyn.

Piechocki S. 1993. *Czyściec zwany Kortau.* Książnica Polska, Olsztyn.

Rozporządzenie Ministra Infrastruktury z dnia 12 kwietnia 2002 r. w sprawie warunków technicznych, jakim powinny odpowiadać budynki i ich usytuowanie. Dz.U. z 15 czerwca 2002 r. nr 75, poz. 690.

Ustawa z dnia 7 lipca 1994 r. – Prawo budowlane. Dz.U. z 2003 r. nr 207, poz. 2016, z późn. zmianami.

[13] When this article was being written, the building design already had a building permit. The decision when the existing building will be demolished and the new one will be constructed depends on the university's investment strategy.

TECHNICAL SCIENCES
Abbrev.: Techn. Sc., No 12, Y 2009

DOI 10.2478/v10022-009-0007-6

EFFECTIVE LENGTHS OF REINFORCED CONCRETE COLUMNS IN SINGLE-STOREY FRAME STRUCTURES IN THE LIGHT OF THE EUROCODE

***Michał Knauff*[1], *Krzysztof Klempka*[2]**

[1] Institute of Building Structures
Warsaw University of Technology
[2] Department of Civil Engineering and Building Structures
University of Warmia and Mazury in Olsztyn

K e y w o r d s: effective length of column, method based on nominal stiffness, second order effects, reinforced concrete buildings, reinforced concrete structures.

A b s t r a c t

In the following article we present the application of the Eurocode rules for calculating the effective length of columns in single-storey buildings. Assuming the same effective lengths for cantilevers (i.e. $l_0 = 2l_{col}$) and the construction columns, as in the example, will not always be correct. The problem of calculating the effective length mostly presents itself when using the simplified method. In the exact method it is not required to determine the effective lengths. This is why it is advisable while designing to use the exact method based on second order analysis and taking into account the nominal stiffness.

DŁUGOŚCI OBLICZENIOWE SŁUPÓW ŻELBETOWYCH W PARTEROWYCH UKŁADACH RAMOWYCH W ŚWIETLE PRZEPISÓW EUROKODU

***Michał Knauff*[1], *Krzysztof Klempka*[2]**

[1] Instytut Konstrukcji Budowlanych
Politechnika Warszawska
[2] Katedra Budownictwa i Konstrukcji Budowlanych
Uniwersytet Warmińsko-Mazurski w Olsztynie

S ł o w a k l u c z o w e: długość obliczeniowa słupa, metoda nominalnej sztywności, efekty drugiego rzędu, hale żelbetowe, konstrukcje żelbetowe.

A b s t r a k t

Rozpatrzono zastosowanie zasad Eurokodu do wyznaczania długości obliczeniowych słupów w jednokondygnacyjnych budynkach halowych. Przyjmowanie długości obliczeniowych l_0 jak dla

wsporników (tzn. $l_0 = 2l_{col}$) dla słupów w takich halach, jak w przykładzie, nie zawsze będzie prawidłowe. Problem wyznaczania długości obliczeniowej dotyczy przede wszystkim metody uproszczonej. Zastosowanie metody ścisłej nie wymaga określania długości obliczeniowych, dlatego do projektowania zaleca się stosowanie metody ścisłej polegającej na analizie II rzędu z uwzględnieniem sztywności nominalnych.

Introduction

In 2010, Eurocode EN 1992-1-1 (abbr: EN) will replace the Polish norm PN-B-03264 (abbr: PN) for designing reinforced concrete and pre-stressed constructions, which will in turn lead to many other changes in the design process. The EN calculating methods differ in many ways from the PN methods, and one of the differences are the principles for calculating the effective lengths of columns. The EN contains extensive rules referring to the effective length of isolated elements, but it does not contain any rules corresponding to the Polish rules for calculating single-storey structures according to the Appendix C of the PN. According to the PN, it can be assumed that $l_0 = 1{,}6l_{col}$ (when the roof construction is rigid), while according to the older versions of the PN even $l_0 = 1{,}2l_{col}$ "when there are four or more columns". After implementing the EN the recommendations regarding the effective lengths enclosed in the Appendix C of the PN will no longer act as rules of the norm. While calculating columns for single-storey buildings, as in the example, according to the EN it is required to assume that the effective length is the same as for the cantilevers (i.e. $l_0 = 2l_{col}$) – the EN has no rules which would allow engineers to assume any other effective length. We are thus faced with a question whether the assumptions of the EN referring to the effective lengths are correct. To answer this question we compared the values of bending moments for columns in a single-storey building obtained according to the method based on nominal stiffness (a simplified method in the EN) with the values obtained according to the exact method based on the second order analysis and taking into account the nominal stiffness. Later on in the article we present a short description of the method based on nominal stiffness and a derivation of the formula for a coefficient increasing the moment. We finish with examples of calculating a single-storey building.

Method based on nominal stiffness

This method is based on the fact that in the second order analysis are applied constant (i.e. load independent) values of stiffness, also called nominal stiffness, obtained from simple approximations of the flexural stiffness, smaller than the initial stiffness, calculated taking into account the influence of

cracking, non-linear qualities of materials and creep. In order to apply this method to the whole framed structure it is necessary to carry out static calculations according to the first order theory taking into account the nominal stiffness of columns and then to increase the derived bending moments M_{0Ed} according to the following formula:

$$M_{Ed} = \eta M_{0Ed} \qquad \eta = \left(1 + \frac{\beta}{\frac{N_B}{N_{Ed}} - 1}\right) \tag{1}$$

where

$$\beta = \frac{\pi^2}{c_0},$$

c_0 is a coefficient which depends on the distribution of first order moment (for instance, $c_0 = 8$ for a constant first order moment, $c_0 = 9{,}6$ for a parabolic and 12 for a symmetric triangular distribution etc.).

Formula (1) takes into account the second order effects and was derived for a column like in Figure 1 loaded with the longitudinal force N_{Ed} and any transverse load. w_0 is a deflection calculated according to the first order theory and w is a total deflection of column. The deflection half way through the length of the element $w_{\max}$ is a sum of the deflection according to the first order theory $w_{0\max}$ and the increment Δw caused by the moment of force N_{Ed} towards the deformed axis of the element. It was assumed that the deflection can be approximately calculated from the formula

$$w = w_{\max} \sin \frac{\pi x}{l_o}$$

After applying the Maxwell-Mohr formula we obtained:

$$\Delta w = \frac{N_{Ed}\, w_{\max} l_o^2}{\pi^2 EI} = N_{Ed} \frac{w_{\max}}{N_B}$$

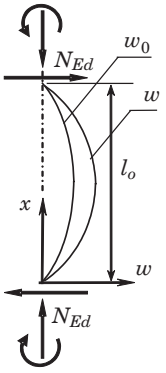

Fig. 1. A diagram of a column

In the above formula EI is the flexural rigidity of a compressed element (nominal stiffness), and N_B is a buckling load obtained from the Euler's formula

$$N_B = \frac{\pi^2 EI}{l_o^2} \tag{2}$$

Total deflection

$$w_{\max} = w_{0\max} + \Delta w = w_{0\max} + \frac{N_{Ed}}{N_B} w_{\max}$$

thus

$$w_{\max} = w_{0\max} \frac{1}{1 - \dfrac{N_{Ed}}{N_B}} \tag{3}$$

Half way through the length of the element the bending moment according to the second order theory

$$M_{Ed} = M_{0Ed} + N_{Ed} w_{\max} \tag{4}$$

Substituting in (3) $w_{\max}$ derived from (4) we obtain

$$\frac{M_{Ed} - M_{0Ed}}{N_{Ed}} = w_{0\max} \frac{N_B}{N_B - N_{Ed}},$$

$$M_{Ed} = M_{0Ed} + w_{0\max} \frac{N_B}{\frac{N_B}{N_{Ed}} - 1} = M_{0Ed} \left(1 + \frac{\frac{w_{0\max} N_B}{M_{0Ed}}}{\frac{N_B}{N_{Ed}} - 1} \right) \tag{5}$$

The deflection $w_{0\max}$ may be expressed by the following formula

$$w_{0\max} = \frac{M_{0\max} l_o^2}{c_0 B} \tag{6}$$

Placing (6) in (5) we obtain formula (1) recommended by the norm. The derivation of formula (1) was also presented in other articles, e.g. KLEMPKA, KNAUFF (2005).

The effective length of a column according to the EN may be derived by transfroming formula (2) to the following form

$$l_0 = \pi \sqrt{\frac{EI}{N_B}} \tag{7}$$

Then substituting N_B derived from (3) in formula (7) we obtain:

$$l_0 = \pi \sqrt{\frac{EI}{N_{Ed}} \left(1 - \frac{w_{0\max}}{w_{\max}} \right)}$$

Using the above formula we can derive the buckling coefficient

$$\mu = \frac{\pi}{l_0} \sqrt{\frac{EI}{N_{Ed}} \left(1 - \frac{w_{0\max}}{w_{\max}} \right)} \tag{8}$$

The examples of calculations

In the following examples the values of bending moments were calculated in columns of two-nave buildings using the method based on nominal stiffness and the exact method. We assumed that the horizontal force caused by wind

pressure and suction equals $H = 30$ kN. We also assumed that the rigid construction of the roof forces equal horizontal shifts of the top ends of columns. The columns have identical cross-sections $b = 40$ cm, $h = 45$ cm, concrete C40/50, and steel A-III. The edge columns' reinforcement is 4 ϕ 16 ($A_s = 8{,}04$ cm^2), and the internal columns' reinforcement is 7 ϕ 16 ($A_s = 14{,}07$ cm^2) on each side of the cross-section, $a = 3{,}5$ cm.

The calculations were carried out for two different longitudinal loads:
Case 1

$P_1 = 200$ kN in edge columns,

$P_2 = 900$ kN in internal column.

Case 2

$P_1 = 450$ kN in edge columns,

$P_2 = 790$ kN in internal column.

The calculations for case 1 are presented below.
Imperfections according to point 5.2 of the EN

$$\alpha_h = \frac{2}{\sqrt{l}} = \frac{2}{\sqrt{7{,}0}} = 0{,}756,\ \frac{2}{3} \le 0{,}756 \le 1{,}0,\ \alpha_m = \sqrt{0{,}5(1+1/\mathrm{m})} =$$

$$= \sqrt{0{,}5(1+1/3)} = 0{,}816,$$

$$\theta_h = \theta_0\, \alpha_h \alpha_m = \frac{1}{200}\, 0{,}756 \cdot 0{,}816 = 0{,}00308.$$

Horizontal forces caused by imerfections:
– In edge columns $H_1 = \theta_i\, P_1 = 0{,}00308 \cdot 200 = 0{,}616$ kN,
– In internal column $H_2 = \theta_i\, P_2 = 0{,}00308 \cdot 900 = 2{,}772$ kN.

Calculations according to the EN – the method based on nominal stiffness

Moments according to the first order theory caused by forces H_i, assuming that the stiffness of columns is identical, are presented in the diagram marked as $\mathrm{ENI}_{\mathrm{const}}$ (Fig. 2).

The nominal stiffness (point 5.8.7.2 of the EN) depends on the amount of reinforcement. While designing columns the reinforcement should always be taken into account because it allows us to calculate the increased bending moments, and based on these moments we can calculate the necessary reinforcement. The result is obtained through iteration after reaching a reasonable conformity between the assumed and calculated reinforcement.

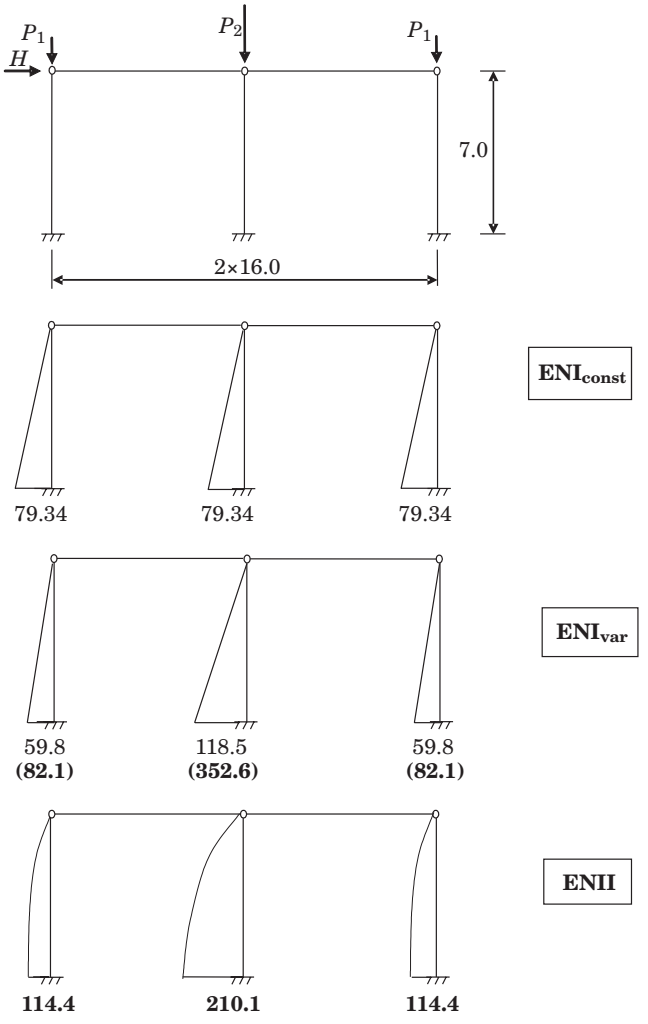

Fig.2. Static diagram and bending moments in columns [kNm]- case 1, the values in brackets were determined using formula (1), the abbreviations ENI_{const}, ENI_{var}, ENII are explained in the text

The design value of modulus of elasticity of concrete E_{cd} = 29170 MPa, the moment of inertia $I_c = 3{,}038 \times 10^{-3}$ m^4. Coefficients k_1 and k_2 according to point 5.8.7.2 of the EN:
$k_1 = \sqrt{f_{ck}/20} = \sqrt{40/20} = 1{,}414$. For $l_0 = 2l_{col} = 2 \cdot 7 = 14{,}0$ m, the radius of inertia $i = \dfrac{h}{2\sqrt{3}} = \dfrac{0{,}45}{2\sqrt{3}} = 0{,}1299$ m. Slenderness $\lambda = l_0 / i = 14{,}0 / 0{,}1299 = 107{,}8$. We assumed the effective creep ratio $\varphi_{ef} = 1{,}945$. The coefficient k_2 for the edge columns

$$n = N_{Ed} / (A_c f_{cd}) = 200/(0{,}40 \times 0{,}45 \times 26{,}7 \times 10^3) = 0{,}0416,$$

$$k_2 = n \cdot \frac{\lambda}{170} = 0{,}0416 \frac{107.77}{170} = 0{,}0264 \leq 0{,}20.$$

The moment of inertia of the reinforcement

$$I_s = 2A_s(h/2 - a_1)^2 = 2 \times 8{,}04 \times 10^{-4}(0{,}45/2 - 0{,}035)^2 = 5{,}8 \times 10^{-5}\ \mathrm{m}^4.$$

Coefficient $K_c = k_1 k_2 / (1 + \phi_{ef}) = 1{,}414 \times 0{,}0264 / (1 + 1{,}945) = 0{,}0127$ i $K_s = 1$

Nominal stiffness of the edge columns:

$$EI = K_c E_{cd} I_c + K_s E_s I_s = 0{,}0127 \times 29170 \times 10^3 \times 3{,}0375 \times 10^{-3} + 1{,}0 \times \\ \times 200 \times 10^6 \times 5{,}8 \times 10^{-5} = 12{,}73\ \mathrm{MNm}^2.$$

In the internal column

$$n = N_{\mathrm{Ed}} / (A_c f_{cd}) = 900/(0{,}40 \times 0{,}45 \times 26{,}7 \times 103) = 0{,}1873,$$

$$k_2 = n \cdot \frac{\lambda}{170} = 0{,}1873 \frac{107.77}{170} = 0{,}118 \leq 0{,}20,$$

$K_c = k_1 k_2 / (1 + \varphi_{ef}) = 1{,}414 \times 0{,}118 / (1 + 1{,}945) = 0{,}0566$ i $K_s = 1$.

Moment of inertia of the reinforcement

$$I_s = 2A_s(h/2 - a_1)^2 = 2 \times 14{,}07 \times 10^{-4}(0{,}45/2 - 0{,}035)^2 = 10{,}15 \times 10^{-5}\ \mathrm{m}^4.$$

Nominal stifffness of the internal column:

$$EI = K_c E_{cd} I_c + K_s E_s I_s = 0{,}0566 \times 29170 \times 10^3 \times 3{,}0375 \times 10^{-3} + 1{,}0 \times \\ \times 200 \times 10^6 \times 10{,}15 \times 10^5 = 25{,}31\ \mathrm{MNm}^2.$$

The result of calculations carried out according to the first order theory with nominal stiffness of columns is presented in Figure 2 – the diagram marked as $\mathrm{ENI}_{\mathrm{var}}$.

Incresed bending moments:

a) In the edge column:

$$\text{Buckling load } N_B = \frac{\pi^2}{l_0^2} EI = \frac{\pi^2}{14^2} 12{,}73 = 0{,}64077 \text{ MN},$$

$$M_{Ed} = M_{0Ed}\left(1 + \frac{\frac{\pi^2}{12}}{\frac{N_B}{N_{\text{Ed}}} - 1}\right) = 59{,}8\left(1 + \frac{0{,}8225}{\frac{640{,}77}{200} - 1}\right) = 82{,}1 \text{ kNm}.$$

b) In the internal column:

$$\text{Buckling load } N_B = \frac{\pi^2}{l_0^2} EI = \frac{\pi^2}{14^2} 25{,}31 = 1{,}27471 \text{ MN},$$

$$M_{Ed} = M_{0Ed}\left(1 + \frac{\frac{\pi^2}{12}}{\frac{N_B}{N_{Ed}} - 1}\right) = 118{,}515\left(1 + \frac{0{,}8225}{\frac{1274{,}71}{900} - 1}\right) = 352{,}6 \text{ kNm}.$$

Calculations according to the EN – second order theory, nominal stiffness

Using the stiffness derived in the previous point we carry out static calculations according to the second order theory – the result diagram marked as ENII is presented in Figure 2.

Additionally, the buckling coefficients were calculated using formula (8) for the edge columns

$$\mu = \frac{\pi}{l_0}\sqrt{\frac{EI}{N_{Ed}}\left(1 - \frac{w_{0\max}}{w_{\max}}\right)} = \frac{\pi}{7}\sqrt{\frac{12725{,}14}{200}\left(1 - \frac{0{,}0765}{0{,}1546}\right)} = 2{,}5$$

and the internal column

$$\mu = \frac{\pi}{l_0}\sqrt{\frac{EI}{N_{Ed}}\left(1 - \frac{w_{0\max}}{w_{\max}}\right)} = \frac{\pi}{7}\sqrt{\frac{25314{,}41}{900}\left(1 - \frac{0{,}0765}{0{,}1546}\right)} = 1{,}69$$

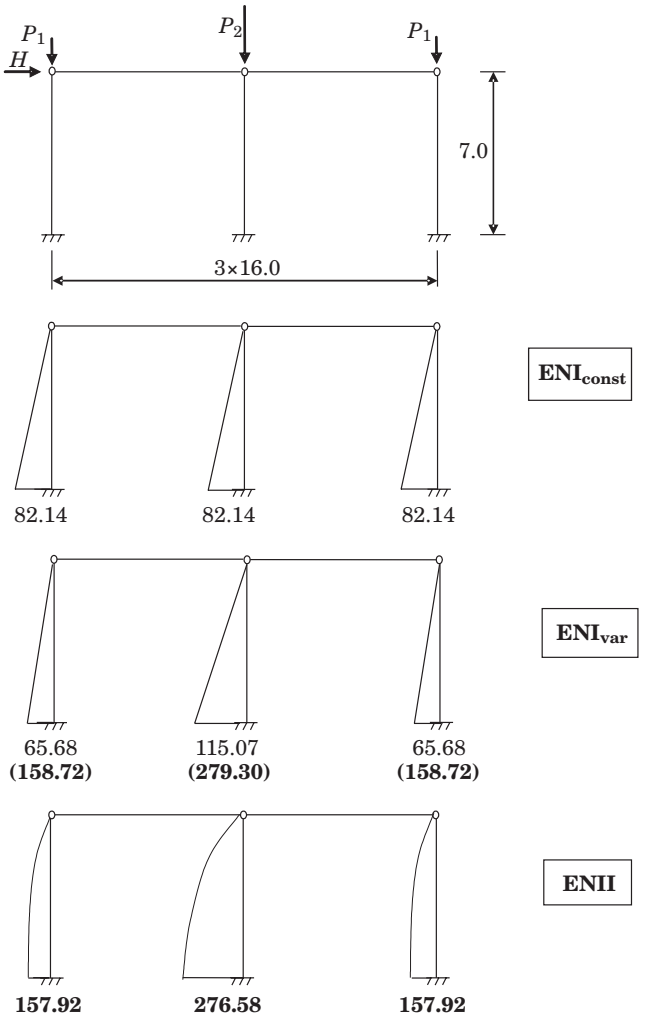

Fig. 3. A static diagram and bending moments in columns [kNm]- case 2, the values in brackets were determined using formula (1), the abbreviations ENI_{const}, ENI_{var}, ENII are explained in the text

Values of w_{0max} and w_{max} were obtained using the exact method.
The result of calculations for case 2 are presented in Figure 3.
The buckling coefficients for the edge columns:

$$\mu = \frac{\pi}{l_0}\sqrt{\frac{EI}{N_{Ed}}\left(1-\frac{w_{0\max}}{w_{\max}}\right)} = \frac{\pi}{7}\sqrt{\frac{14124{,}92}{450}\left(1-\frac{0{,}0759}{0{,}2047}\right)} = 2{,}0$$

and the internal column:

$$\mu = \frac{\pi}{l_0}\sqrt{\frac{EI}{N_{Ed}}\left(1-\frac{w_{0\max}}{w_{\max}}\right)} = \frac{\pi}{7}\sqrt{\frac{24729{,}69}{790}\left(1-\frac{0{,}0759}{0{,}2047}\right)} = 2{,}0$$

In the second case the reliable moments are similar to the reliable moments calculated using the method of increasing the moment, while in the first case these values are different. This diffeerence results from a false assumption that in case 1 each of the columns in the frame behaves in the same way as an isolated cantilever, which means that identical effective lengths were assumed for all the columns and the cantilevers ($\mu = 2$). Such an assumption can only be made when the ratios of the columns' stiffness EI to the longitudinal forces acting in them N_{Ed} are identical, which results from formula (8). This conclusion refers to cases in which the roof construction forces equal horizontal shifts of the top ends of columns, i.e. cases in which the ratio $\frac{w_{0\max}}{w_{\max}}$ is identical for each column.

Conclusions

Considering the presented analyses, we can conclude that:

1. In a single-storey building with columns joined monolithically with the foundations and via hinges with the roof construction the buckling coefficient for each column is 2,0 only when the ratios of the columns' stiffness EI to the longitudinal forces acting in them N_{Ed} are identical. It may not always be possible to meet such a condition, so assuming that $\mu = 2{,}0$ for each column will not always be correct.

2. The problem of calculating the effective length mostly refers to the simplified method. While applying the exact method it is not required to define the effective lengths – the shape of deflection and the resulting increase of the moments are calculated directly. This is why while designing it is advisable to use the exact method based on the second order analysis and taking into account the nominal stiffness.

Accepted for print 12.10.2009

References

Eurocode 2: Design of Concrete Structures. Part 1-1. General Rules and Rules for Buildings. EN 1992-1-1: 2008.

JASTRZĘBSKI P., MUTERMILCH J., ORŁOWSKI W. 1986. *Wytrzymałość materiałów*. Arkady, Warszawa.

KLEMPKA K., KNAUFF M. 2005. *Design of slender RC columns according to Eurocode and polish code compared with the improved numerical model*. Archives of Civil Engineering. LI, 4.

Konstrukcje betonowe, żelbetowe i sprężone. Obliczenia statyczne i projektowanie. PN-B-03264: 2002.

KORZENIOWSKI P. 1997. *Effectiveness of increasing load bearing capacity of rc columns by raising the strength of concrete and amount og reinforcement*. Archives of Civil Engineering, XLIII, 2.

KUKULSKI W., SULIMOWSKI W. 2006. *Stan graniczny nośności z udziałem efektów odkształceń konstrukcji*.W: *Podstawy projektowania konstrukcji żelbetowych i sprężonych według Eurokodu 2*. Dolnośląskie Wydawnictwo Edukacyjne, Wrocław.

TECHNICAL SCIENCES
Abbrev.: Techn. Sc., No 12, Y 2009

DOI 10.2478/v10022-009-0008-5

DETERMINATION OF INTERNAL FORCES IN END PLATES OF SIMPLE END PLATE JOINTS

Stefan Dominikowski, Piotr Bogacz

Department of Civil Engineering and Building Structures
University of Warmia and Mazury in Olsztyn

K e y w o r d s: end plate joints, internal forces, end plate.

A b s t r a c t

In the paper the authors propose computer simulation of simple end plate joints. A computer model has been elaborated using the Autodesk Robot Structural Analysis Professional 2010 software programme. Maps of internal forces and stresses on end plates of a joint have been analysed. The analysis of the maps enabled the authors to determine the course of variation of bending moments in any cross-section of the joint and to compare the obtained diagram with a diagram of moments cited in the literature (ŻÓŁTOWSKI et al. 2000, BIEGUS 1997), which serves the purpose of determination of the minimum thickness of end plates needed due to the lever effect. The paper also determines the dependence between the loading force acting on the joint and the thickness of end plates on the assumption of maximum stresses damaging the steel of the end plates, as this is one of the criteria for dimensioning end plate joints. In addition, effort of joint bolts was determined in relation to a value of the loading force.

WYZNACZENIE WARTOŚCI SIŁ WEWNĘTRZNYCH W BLACHACH CZOŁOWYCH POŁĄCZEŃ DOCZOŁOWYCH ZWYKŁYCH

Stefan Dominikowski, Piotr Bogacz

Katedra Budownictwa i Konstrukcji Budowlanych
Uniwersytet Warmińsko-Mazurski w Olsztynie

S ł o w a k l u c z o w e: połączenie doczołowe, siły wewnętrzne, blacha czołowa.

A b s t r a k t

W pracy zaproponowano symulację komputerową połączenia doczołowego zwykłego. Model komputerowy opracowano na podstawie programu Autodesk Robot Structural Analysis Professional 2010. Przeanalizowano mapy sił wewnętrznych i naprężeń na blachach czołowych połączenia. Analiza map pozwoliła określić przebieg zmienności momentów zginających w dowolnym przekroju

połączenia oraz porównać uzyskany wykres momentów z wykresem momentów podanym w literaturze (ŻÓŁTOWSKI i in. 2000, BIEGUS 1997), służącym do określenia minimalnej grubości blach czołowych ze względu na efekt dźwigni. W pracy określono również zależność siły obciążającej połączenie od grubości blach czołowych, z założeniem maksymalnych naprężeń niszczących stal blach czołowych. Jest to jedno z kryteriów wymiarowania połączeń doczołowych.

We wzorcowym połączeniu wyznaczono również wytężenie śrub połączenia w zależności od wartości siły obciążającej.

Introduction

In contemporary steel constructions, bolt joints are mainly used for joining shipping or assemblage elements. End plate joints, either non-bolted or bolted with high strength bolts, are a modern way of joining stretched or bent elements of metal constructions, in which the main component of the load is parallel to the axis of the bolts. These joints can be made easily and quickly at a construction site under any atmospheric conditions and without any heavy or specialist equipment. With such joints, it is also possible to assemble and, if necessary, dismantle a steel construction easily.

This paper discusses the problem of the effort of bolts and end plates in simple, strechted end plate joints. Among the most important issues which have not been solved satisfactorily until present day are distribution of internal forces in a joint (in end plates and in bolts), the way the edges of end plates interact with one another, the lever effect on the actual bearing capacity of a joint and the minimum thickness of end plates. Moreover, the nature of the work performed by bolts and the effect of the thickness of end plates on the character of work performed on end plates in end plate joints still await complete clarification.

Description of a computer model

In order to improve our understanding of the above problems, a computer-based simulation of a simple end plate joint subject to stretching has been completed using the software programme called Autodesk Robot Structural Analysis Professional 2010 licence 3251. A stretched end plate joint was designed in the form of two plate girder double-tee bars joined through end plates with M16 bolts fixed in ϕ 18 holes (Fig. 1).

The connection of the end plates was modelled as a joint of plates restrained at the sites where bolts joining the plates were fitted. The end plate joint was made using a fixed connection with a ϕ 16 rod, which simulated the properties of a grade 8.8 M16 bolt with all degrees of freedom being blocked (Fig. 2).

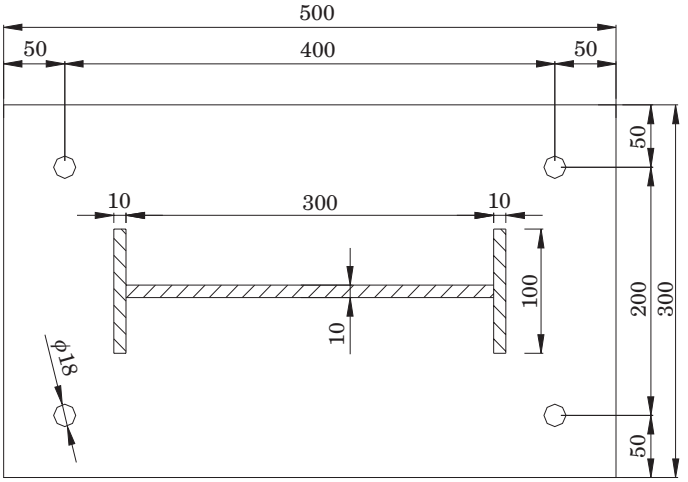

Fig. 1. A model of an end plate in a joint. Thickness of the end plates in the end plate joint is g_b = 16 mm. Thickness of the plates of the connected rods is g_p = 10 mm
Source: own elaboration.

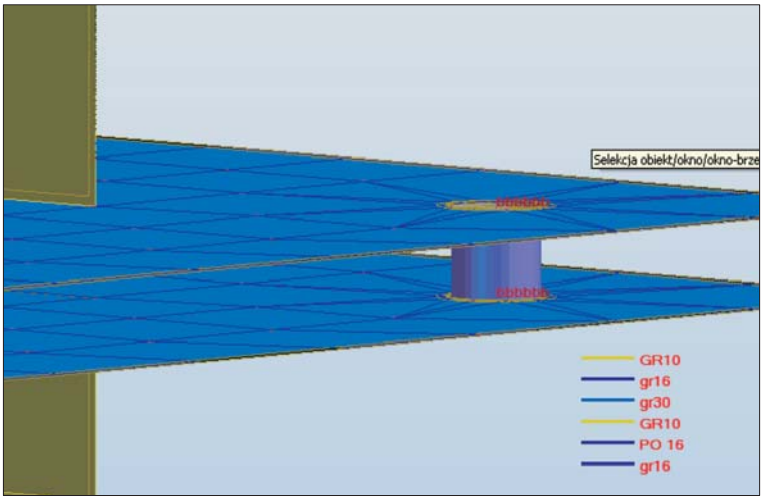

Fig. 2. Model of the bolted joint of end plates: rod ϕ 16. Steel in the bolt simulating grade 8.8 steel.
Source: Autodesk Structural Analysis Professional 2010 licence 3251.

It was assumed that the end plates and connected rods were made of S235 grade steel. The bolts were modelled from steel of mechanical properties close to those of grade 8.8 bolt steel. The bottom part of the joint was supported by articulated line supports. To the upper one, the connected plate girder rod, concentrated transmitted load was applied. The load was applied to the middle

node of a FEM grid at the upper edge of the plate girder web. A Finite Element Method grid was established according to Coonse's method, allowing for adjustment of FEM grids. Around the joints there were visible codes of blocked degrees of freedom.

In the subsequent stage of the simulation, thicknesses of end plates were changed, thus determining the dependences between the force causing normal damaging stresses and the thicknes of the end plates. In addition, the value of the load on the joint was determined at which the efforts of the bolt steel were close to one.

Analysis of the results

The following were obtained: a map of normal stresses on the upper surfaces of end plates (Fig. 3), a map of bending moments M_y (Fig. 4) and a map of translocations of the FEM grid centres (Fig. 5).

At the same time, in the vicinity of the effect produced by the bolts, a diagram of variation of bending moments was made, which verified diagrams of bending moments accepted in the literature (ŻÓŁTOWSKI et al. 2000) (cross-section A–A) (Fig. 6). Żółtowski presents a diagram of bending moments at the contact edge of end plates assuming a zero value of bending moments at the longitudinal edges of the end plates (Fig. 7).

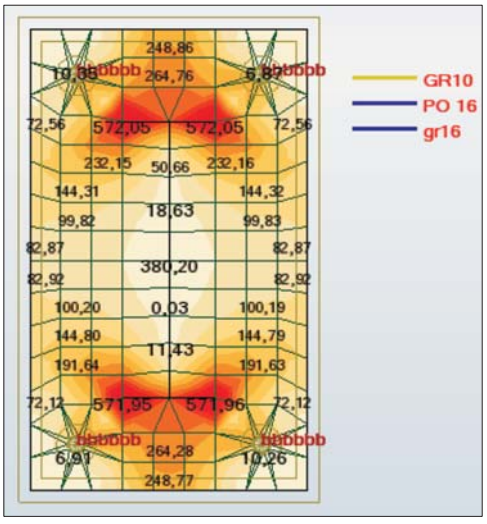

Fig. 3. Map of normal stresses in upper fibers of end plates in the joint
Source: Autodesk Structural Analysis Professional 2010 licence 3251.

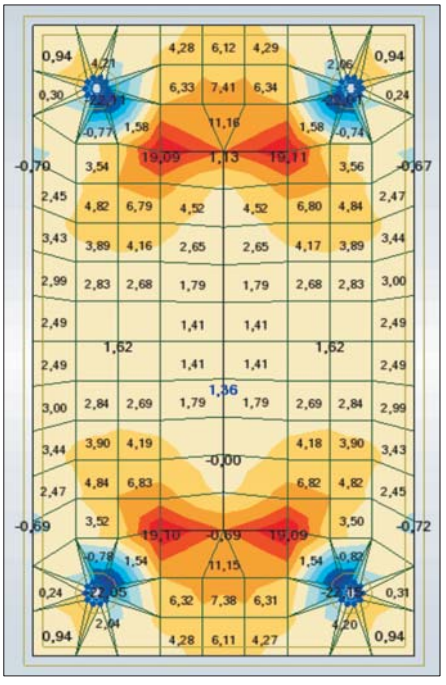

Fig. 4. Map of bending moments in upper fibers of end plates in the joint
Source: Autodesk Structural Analysis Professional 2010 licence 3251.

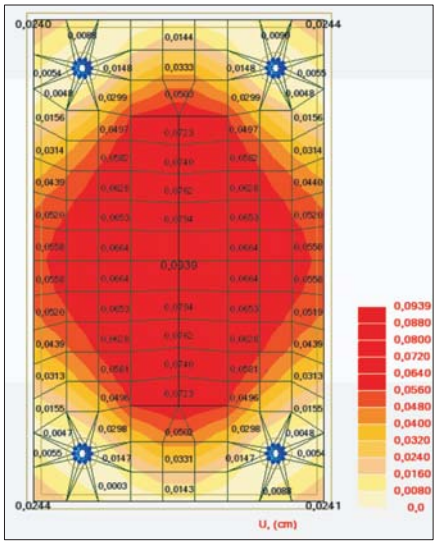

Fig. 5. Map of translocations of the FEM grid nodes in end plates of the joint
Source: Autodesk Structural Analysis Professional 2010 licence 3251.

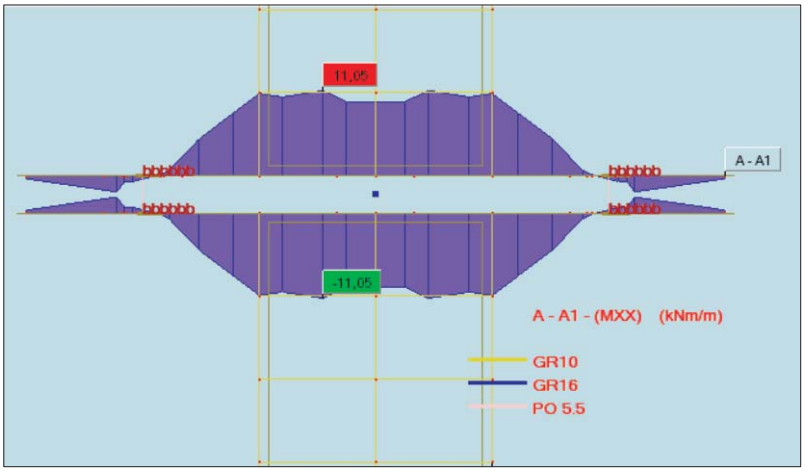

Fig. 6. Diagrams of bending moments M on end plates of the joint
Source: Autodesk Structural Analysis Professional 2010 licence 3251.

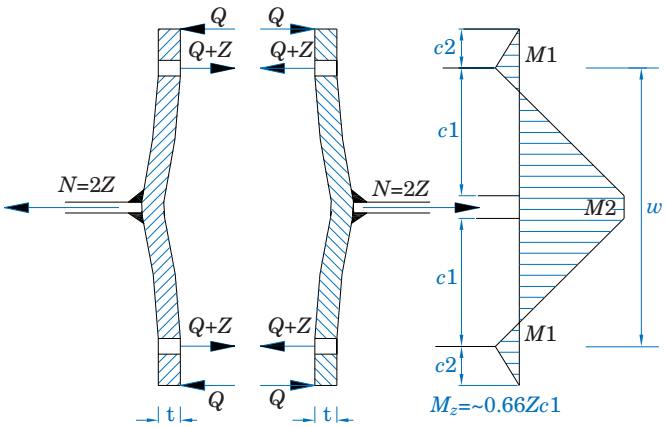

Fig. 7. The lever effect and diagram of moments on the surface of an end plate in an end plate joint
Source: own elaboration.

Taking advantage of such a diagram of moments, he derives a known standard dependence for the minimum thickness of end plates. It assumes that moment $M_z = \sim 0.66\, Z \cdot c_1$ (Fig. 8, 9). By distinguishing mentally a strip of the endplate of the width b_s (Fig. 10), one can determine the value of moment M_z (DOMINIKOWSKI et al. 2005).

$$M = 0.66 \cdot c \cdot Z = W \cdot f_d \Rightarrow \frac{M}{W} \leq f_d \tag{1}$$

$$W = \frac{1}{6} \cdot b_z \cdot t^2 \tag{2}$$

$$0.66c \cdot Z = 0.167 \cdot b_z \cdot t^2 \cdot f_d \tag{3}$$

$$t = \sqrt{\frac{0.66 \cdot c \cdot S_{Rt}}{0.167 \cdot b_z \cdot f_d}} = \sqrt{\frac{c \cdot S_{Rt}}{b_z \cdot f_d}} \tag{4}$$

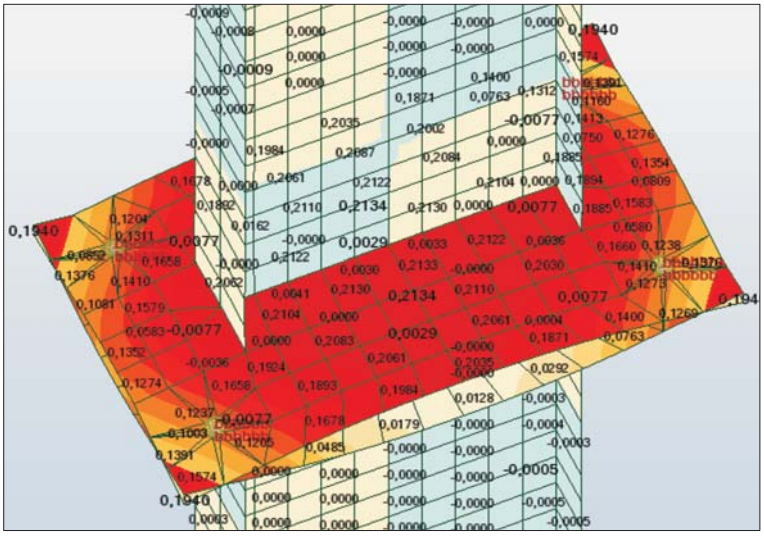

Fig. 8. Deformation of end plates in the joint
Source: Autodesk Structural Analysis Professional 2010 licence 3251.

Due to the limited increase in the value of the force in a bolt caused by the lever effect, it is assumed that the minimum thickness of the plate in the joint is $t_{\min} = 0.6$ t.

Then, the minimum thickness of the plate is:

$$t_{\min} = 0.6 \text{ t} = 1.2 \sqrt{\frac{c \cdot S_{Rt}}{b_z \cdot f_d}} \tag{5}$$

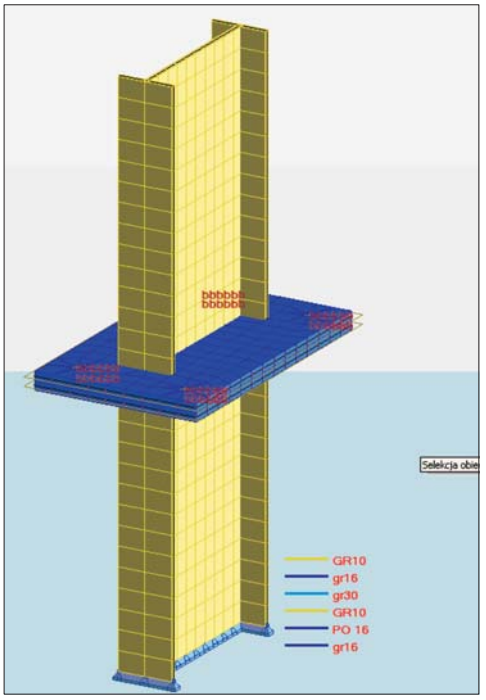

Fig. 9. Computer model of the analysed joint
Source: Autodesk Structural Analysis Professional 2010 licence 3251.

The above dependence is valid as long as the bending moment at the edges of the end plates is assumed as zero (PN-90/B-03200). In reality, at the endplate edges are there are non-zero, residual bending moments and normal stresses (Fig. 3, 9). The assumption that bending moments at end plate edges are equal zero is quite a good approximation in the light of the analysis of the diagram of moments (Fig. 3, 9). The diagram of moments (Fig. 7) is close to the diagram of moments (Fig. 6), but the assumed values M_2 are higher than the actual ones (Fig. 6). The flattening of the diagram (Fig. 6) is caused by the stiffening of the plate along the *x–x* axis. Paradoxically, the presence of factor *bz* in the denominator of the fraction (Fig. 10) should diminish the thickness of endplates as the spacing of bolts in the joint increases (PN-90/B-03200).

The cases described in (ŻÓŁTOWSKI et al. 2000, BIEGUS 1997, MAREK et al. 2003) are applicable to relatively thin end plates stiffened along one direction. The computer-based simulation presented in this paper accounts for the bracing of end plates along both directions. The *y–y* axis is braced with the webs of the connecting rods, whereas the *x–x* direction is braced with shelves of connected rods.

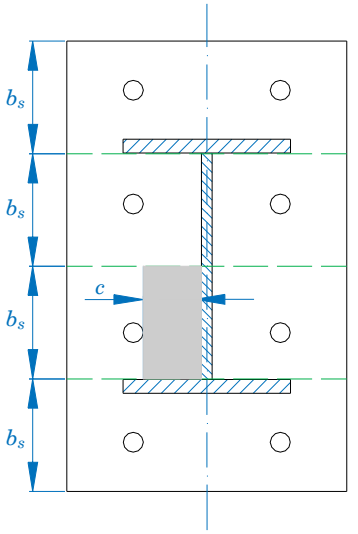

Fig. 10. Width of interaction of plate b_s per one bolt and distance c from the edge of the hole to the outer edge of the weld

Source: own elaboration.

MAREK et al. (2003) describes a computer-based simulation of a joint based on the SBRA (Simulation-Based Reliability Assessment) method, assuming that supports at bolts are elastic and articulated at edges (the edge of one end plate is supported on the edge of the other plate). Both methods attain zero moments at edges of end plates and assume that plates have articulated supports. At the same time, Marek compares the SBRA results with the EC3 recommendations (prEN 1993-1-1:2002), repeated in later publications of eurocodes (PN-EN 1993-1-8:2006).

The results of the SBRA simulations are close to the results of the simulation reported in this paper and cited in (ŻÓŁTOWSKI et al. 2000, BIEGUS 1997). They are also approximately the same as the ones given in EC3. The formula for the minimum thickness of an end plate should also include non-zero valeus of moments at edges of end plates (Fig. 4).

Moreover the applied computer-based simulation allowed for determination of the dependence of the load on the joint on the thickness of the end plates in the joint, assuming that there appear normal stresses in the end plates which damage the joint. It was assumed that the steel in the end plates was S235 grade steel. For different thicknesses of the end plates, the joint was loaded with a force which caused the appearance in the end plate steel of normal stresses close to damaging ones. The assumed values of the axial force were such as to attain the value of extreme stresses in end plates close to the

values causing damage to their steel. For S235 steel, the value was f_d = 375 MPa (PN-90/B-03200). These dependences are illustrated in figure 10. With such dependences, it is possible to determine the value of loads damaging the end plates in a joint. For a given thickness of an end plate, one can read the value of a force at which the values of stresses in end plates are nearly R_m.

The computations were performed for the thickness of end plates between 10 and 24 mm. The regression curve represents foreseen results of thickness of end plates up to 30 mm. At the same time, the value of a force was measured at which the efforts of the steel in the bolts are close to 1. The force which causes the break of grade 8.8 M16 bolts in the modelled joint is P = 320 kN. The load per 1 bolt is P_1 = 80 kN ≅ S_{Rt} 81.3 kN (PN-90/B-03200). The load capacity of a bolt in a joint also depends on the thickness of plates (the lever effect) and is lower for less thick plates (e.g. for a plate 16 mm in thickness, the load capacity of bolts is ~ 55 kN).

Conclusions

The currently available computer methods applied to analysis of constructions enable us to analyse more precisely how joints, including semi-rigid ones, work. Analysis of maps of bending moments (Fig. 4) makes it possible to verify the accepted static models of work of end plates. The assumption of zero bending moments at edges of plates is close to the distribution of bending moments (vector of moments along axis y) obtained in a computer-based simulation. At the edges of end plates there are moments whose values can be neglected while analysing how a joint works. They are residual in nature.

In bolts which join end plates, apart from tensile forces, there are also bending moments (Fig. 4). Values of bending moments on joining bolts decrease as the thickness of end plates of the joints rise. Diagrams of bending moments in a cross-sections in the vicinity of bolts obtained in our computer simulation are very close to the diagrams of moments presented in articles (ŻÓŁTOWSKI et al. 2000, BIEGUS 1997, DOMINIKOWSKI et al. 2005, MAREK et al. 2003). Little changes in the character of the distribution of stresses and bending moments on end plates were observed when different types of support given to edges of plates were assumed.

For any load on a joint, the question of mutual support of edges of end plates seems to be negligible because under the influence of loads there appears a gap between the end plates, as a result of which there is no mutual support of their edges.

In the simulation discussed in this paper, the maximum value of normal stresses on surfaces of end plates was achieved in the vicinity of the joint

connecting ends of shelves of plate girders joined (welded) with end plates. This confirms the principle of concentration of stresses in these places.

The computer-based simulation presented in this article enabled the authors to determine the dependence of the load on a joint on the thickness of end plates, assuming that there are normal stresses on end plates close to R_m (Fig. 11).

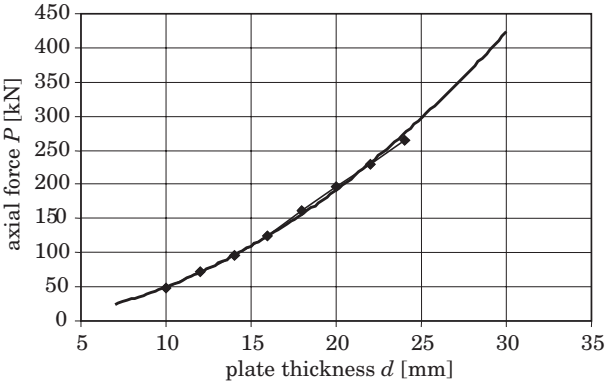

Fig. 11. Dependence of the axial force in the joint on the thickness of the end plates in the joint, on assumption of attaining stresses in the end plates that damage the joint
Source: own elaboration.

The simulation also made it possible to determine the values of forces which damage the joint by breaking the bolts. It turned out that on assumption that the joint would be braced with a rod modelled from steel whose mechanical properties were close to the steel from which the bolts were made, the obtained damaging forces were nearly identical to values S_{Rt} (PN-90/B-03200). At the same time, the authors observed a change in the value of axial forces P in the bolts depending on the thickness of the end plates. Therefore, the commonly accepted assumption about a reversely proportional dependence between thickness of end plates and the norm multiplier b_s (Fig. 10) seems questionable. Paradoxically, an increase in value *bz* diminished the minimum thickness of end plates.

The authors of this paper are fully aware of how fragmentary this analysis of semi-rigid joints is and are now working on expanding their analysis so as to cover more complex issues (greater density of bolts, analysis of welds) and on analysis of bent end plate joints.

Accepted for print 12.10.2009

References

BIEGUS A. 1997. *Połączenia śrubowe*. PWN, Warszawa.
DOMINIKOWSKI S., BOGACZ P. 2005. *Konstrukcje stalowe.*
Konstrukcje stalowe. Obliczenia statyczne i projektowanie. PN-90/B-03200,
Eurocode 3 Design of steel structures, part 1–1: General rules and rules for buildings CEN may 2002. prEN 1993-1-1:2002,
Eurokod 3: Projektowanie konstrukcji stalowych – Część 1–8: Projektowanie węzłów. PN-EN 1993-1-8:2006.
MAREK P., KRIVY V. 2003. *Reliability assessment of semi-rigid partial- strength steel joints and structures*, Konstrukcje stalowe, 5 (63).
ŻÓŁTOWSKI W., FILIPOWICZ A., ŁUBIŃSKI M. 2000. *Konstrukcje metalowe.* Część 1. *Podstawy projektowania*. Arkady, Warszawa.

TECHNICAL SCIENCES
Abbrev.: Techn. Sc., No 12, Y 2009

DOI 10.2478/v10022-009-0009-4

ASPECTS OF COST-ESTIMATE FOR CONSTRUCTION WORK IN LISTED BUILDINGS

***Jacek Zabielski*[1], *Piotr Bogacz*[2]**

[1] Department of Construction Engineering Processes
[2] Department of Civil Engineering and Building Structures
University of Warmia and Mazury in Olsztyn

K e y w o r d s: listed buildings, renovation work, owner/client cost estimate, public contracts.

A b s t r a c t

The paper discusses the aspects of estimating costs of construction work in historic buildings. An analysis of the unit prices for renovation and refitting an old building found in market available price lists has been completed. The results were compared with the prices attained through a detailed cost estimate. It has been demonstrated that at present the limited accessibility to price lists containing unit prices for redecoration work in historic buildings is a serious obstacle to estimating costs of such type of building work, as a result of which cost estimates must be performed several times using the detailed unit method.

PROBLEMATYKA KOSZTORYSOWANIA ROBÓT BUDOWLANYCH W OBIEKTACH ZABYTKOWYCH

***Jacek Zabielski*[1], *Piotr Bogacz*[2]**

[1] Zakład Inżynierii Procesów Budowlanych
[2] Katedra Budownictwa i Konstrukcji Budowlanych
Uniwersytet Warmińsko-Mazurski w Olsztynie

S ł o w a k l u c z o w e: obiekty zabytkowe, roboty remontowe, kosztorys inwestorski, zamówienia publiczne.

A b s t r a k t

W pracy przedstawiono problematykę związaną z kosztorysowaniem robót budowlanych w obiektach zabytkowych. Przeprowadzono analizę dostępnych na rynku cenników cen jednostkowych robót remontowych w porównaniu z cenami wyliczonymi w kalkulacji szczegółowej. Wykazano, że poważnym problemem kosztorysowania tego rodzaju robót jest ograniczony zakres dostępnych na rynku cenników cen jednostkowych robót remontowych w obiektach zabytkowych, co powoduje wielokrotną konieczność dokonywania kalkulacji ceny jednostkowej metodą szczegółową.

Introduction

Construction work in listed historic buildings requires a customized approach to the issues connected with conservation research, design making and cost estimate. The technical condition of such buildings often necessities complex restoration so as to revive their former splendour. Prolonged lack of ongoing maintenance repairs or redecoration work in historic buildings often leads to extensive damage of their structural and decorative components. When many elements of an old building are worn out, the whole construction poses a threat to its users and other persons. In addition, the aesthetic value of the building suffers too.

Construction work in historic buildings

The most common types of renovation work in historic buildings include:
– drying up damp cellars,
– redecoration of stairwells,
– redecoration of wall elevation,
– roof renovation,
– replacement of old fittings.

Each construction activity planned in a historic building needs to be assessed and approved of by the Conservation Officer. The scope of the work as well as the materials to use are agreed upon separately for each historic construction. Many solutions are unique and the materials to be used are unavailable on the Polish market. All this creates big problems while working out a detailed cost estimate. A cost estimator must complete a customized detailed cost estimate as well as suggest alternative material and technology solutions. The labour and material outlay norms in the published catalogues of in-kind outlays do not reflect the actual costs of restoration work.

Methods for cost estimating

Cost estimate methods are defined by the ways of cost estimating building work. They are specified in relevant legal regulations or in model case studies.

The current laws on cost estimating construction work contain regulations which are binding only to those owners/clients who act in accordance with the Act of 29th January 2004, the Act on Public Contracts (Journal of Laws no 223, item 1655 and later amendments). Public investors should possess an owner/client cost estimate drawn up in compliance with the executive acts

passed on the basis of the Law on Public Contracts, i.e. the Ordinance of the Minister for Infrastructure of 18th May 2004, on determination of cost estimate methods and basic information for elaborating an owner/client cost estimate, calculation of planned costs of designing work and planned costs of construction work as defined in the functional and services programme (Journal of Laws No 130, item 1389) and the Ordinance of the Minister for Infrastructure of 2nd September 2004, on detailed scope and form of design documentation, technical specification of completing and commissioning construction work, and the functional and services programme (Journal of Laws No 202, item 2072). With respect to other investors, there are no binding legal regulations which enforce and specify cost estimating. Most cost estimates are worked out on the basis of the now invalid Ordinance of the Minister for Regional Development and Civil Engineering of 13th July 2001 on cost estimate methods for construction projects (Journal of Laws No 80, item 876) or according to published materials, for example "Polish standards for cost estimates", prepared and published by the Association of Construction Industry Cost Estimators.

Following the above guidelines and the binding legal regulations in Poland, there are two cost estimate methods:
– detailed cost estimate,
– simplified cost estimate.

The choice of a cost estimate method depends on the type of a cost estimate and its purpose as well as the source of financing the building project. The way of performing an owner/client cost estimate, as required for public contracts, is legally regulated. The choice of a cost-estimate method is made by the contracting party and the contractor while negotiating the terms of the contract, when the scope and complexity of the construction work is taken into consideration alongside repeatability of certain jobs as well as availability of information on construction work prices, etc.

The generally applicable basis for making detailed cost estimates for building work in listed historic buildings consists of in-kind outlays, cited in In-kind Outlays Catalogues (in Polish, Katalogi Nakładów Rzeczowych, KNR) or Temporary Branch Catalogues of Outlays in Historic Conservation Work (in Polish, Tymczasowe Zakładowe Katalogi Nakładów Budownictwa Konserwatorskiego, TZKNBK). In turn, simplified cost estimating is based on the published price lists or unit prices for construction work available on the building industry market.

The detailed cost estimate method relies on determination of a cost-estimate value W_k by estimating the direct costs for all takeoff items and adding respective indirect costs, profit and VAT.

The indirect costs and profit can be estimated for the whole building or relative to every production unit. This in mind, the work cost-estimated value W_k is calculated from the formula:

$$W_k = \sum_i (L_i \cdot n \cdot c) + K_p + Z + P_V \tag{1}$$

or

$$W_k = \sum_i L_i \cdot (n \cdot c + K_{pj} + Z_j) + P_V \tag{2}$$

where:
L_i – number of takeoff units of the activity designated number i,
n – unit in-kind outlays of: n_r – labour, n_m – materials, n_s – equipment labour,
c – prices of production factors: C_r – labour rate, Cm – price of material purchase, C_s – price of equipment work,
$n \cdot c$ – direct costs of a takeoff unit, calculated from the formula:

$$n \cdot c = (\Sigma n_r \cdot C_r + \Sigma n_m \cdot C_m + \Sigma n_s \cdot C_s \tag{3}$$

where:
K_p – indirect costs for the whole range of the cost-estimated work,
Z – rofit for the whole project,
K_{pj} – indirect costs per takeoff unit,
Z_j – profit per takeoff unit,
P_v – value Added Tax (VAT).

Calculating the cost-estimated value from formula (1) means calculating direct costs of construction work activities and adding indirect costs, profit and VAT. When formula (2) is used, for each takeoff item, a unit price is calculated that includes direct costs, indirect costs and profit. Afterwards, the achieved value is multiplied by the number of the construction operations. When the values of all the operations are summed up, a VAT tax is added. The takeoff price for the calculations (C_j) (unit price) in formula (2) can also be written as:

$$C_j = R_j + M_j + S_j + K_{pj} + Z_j \tag{4}$$

where:
R_j – cost-estimate value of labour per takeoff unit,
M_j – cost-estimate value of materials per takeoff unit,
S_j – cost-estimate value of equipment work per takeoff unit, the remaining designations as in formula (2).

The direct cost breakdown elements: labour R_j, materials M_j and equipment work S_j are calculated from formula (3).

The simplified calculation means calculating the cost-estimated value of the construction operations as a sum of the multiplication products of takeoff units and their unit prices, with the VAT added afterwards.

According to this method, the cost-estimated value of construction work is:

$$C_k = \sum_i L_i \cdot C_j + P_v \tag{5}$$

where:

C_k – cost-estimate price,

L_i – number of takeoff units for a construction operation or element number i,

C_j – unit prices for determined takeoff units,

P_v – Value Added Tax (VAT).

The unit price C_j includes all calculation components of construction activities according to formula (4).

The simplified calculation method is applicable when the cost estimator has lists of unit prices for construction operations. Such sets of prices can be created by building industry companies for their own purposes or by owners/clients based on former contracts. Information on unit prices can also be obtained from tender bids and negotiations carried out when construction projects are commissioned, or found in specialist publications issued by institutions and firms which deal professionally with registration and publication of prices in the building industry.

Clients who open a public bid are obliged to have an owner/client cost-estimate. Such an estimate is used for determination of an estimated value of the planned building activities and for analysis and comparison of the offerers' estimates. The owner/client cost estimate is prepared with the detailed methods unless there are no grounds for using this method, in which case a simplified calculation method is used.

However, it is rather difficult to prepare a cost estimate for building work in a historic building based on the simplified method, using ready-made databases of unit prices, due to the limited range of published prices for a variety of construction work types. Besides, a client cost estimate for historic buildings is based on the design documentation, which imposes certain recommendations concerning the materials and technical solutions which will approximate the original ones. This means that cost estimators must adapt tailor-made calculation of labour and material consumption. Most often, such

Table 1

An example of a table of prices containing unit prices for renovation work in listed buildings

TZKNBK, part 15, Painting jobs

No	Statistical classification code	Job specification	Measure unit	Unit price (C_j) of work					Change in %	
				C_j min.	C_j max.	C_j mean	C_{juplud}	including materials M_{nj}	1st quarter 2009	4th quarter 2008
1	2	3	4	5	6	7	8	9	10	11
TZKNBK, part 15, Painting jobs										
Chapter 01 Plaster painting – code CPV 45442100-8										
1	0101-0110	Limewhiting of brick, stone or scored surfaces	m^2	2.95	4.86	**3.50**	3.84	1.01	-2.0	-1.1
2	0101-0120	Aas above, but twice	m^2	4.92	8.22	**5.88**	6.45	1.51	-1.8	-1.0
3	0102-0210	Limewhiting of previously soap grounded surfaces- once	m^2	4.02	6.77	**4.81**	5.27	1.07	-2.0	-1.2
4	0102-0220	As above, but twice	m^2	6.25	10.59	**7.51**	8.25	1.58	-1.8	-1.2
5	0103-0310	Limewhiting of plastered surfaces with adding colour and groundin – once	m^2	5.06	8.65	**6.09**	6.69	1.11	-2.1	-1.3
6	0103-0330	As above, but twice	m^2	6.28	11.59	**8.20**	9.01	1.65	-1.9	-1.2
7	0104-0410	Soap grounding of plastered walls	m^2	4.60	8.33	**5.68**	6.23	0.06	-2.2	-1.4
8	0105-0510	Painting elevation walls with so-called Swedish lime – once	m^2	6.12	10.58	**7.42**	8.15	1.18	-2.0	-1.3
9	0105-0520	As above, but twice	m^2	8.81	14.98	**10.61**	11.66	2.19	-1.9	-1.2
10	0106-0610	Painting previously colour grounded elevation walls with casein paint – once	m^2	12.51	22.20	**15.57**	17.11	2.48	-1.6	-1.6
11	1007-0710	Painting with "Swedish paint" of grounded drawn profiles max. length 5 cm	m^2	21.76	38.81	**26.69**	29.33	1.43	-2.1	-1.5
12	0107-0720	As above, but length 5 to 10 cm	m^2	18.06	32.54	**22.21**	24.40	1.01	-2.2	-1.4
13	0107-0730	As above, but length 10 to 20 cm	m^2	13.00	23.36	**15.98**	17.56	1.01	-2.1	-1.4
14	0107-0740	As above, but length over 20 cm	m^2	10.99	19.69	**13.49**	14.82	1.01	-2.0	-1.3
15	0108-0810	As above, but of simple ornamental plaster moulding	m^2	9.09	16.26	**11.16**	12.27	1.17	-1.8	-1.2

Source: Bulletin of Prices for Renovation and Construction Work in Listed Buildings, 3rd quarter of 2009; published by OWEOB Promocja Sp. z o.o. Warszawa.

a cost estimate is produced on the basis of published sets of norms and catalogues of in-kind outlays, taking into account the applied material solutions. In practice, it is not uncommon to consult companies which specialise in restoration and renovation of listed buildings.

The example of a price database shown in Tab. 1 is produced by firms which monitor price-creating factors on the building industry market and drawn up by the detailed calculation of unit prices (formula 4) according to the TKZNKN catalogues.

Below we present a cost-estimate of grounding 100 m^2 of walls in a listed building, calculated with the detailed method according to the KNR catalogues and the same estimation shown as a simplified position, using the value of unit price calculated with the detailed method (Tab. 3).

Table 2

Sample detailed calculation of wall grounding in a listed building

No	Base	Specification	Measure unit	Outlays	Unit cost	R	M	S
1	45442100-8	Wall surface grounding – detailed calculation						
1	KNR 10-01 1305-04 analogy	Grounding walls with the grounding preparation TAGOSIL G (once) quantity survey = 100 m^2	m^2	22.0000				
1*		**--R--** labour 0.22w-h/m^2 · 16,52PLN/w-h	w-h	33.0000	3.634	363.44		
2*		**--M--** TAGOSIL G – grounding agent and diluent for silicate paints and plasters 0.33 dm^3/m^2 · 22.14 PLN/dm^3	dm^3	33.0000	7.306		730.62	
3*		Additional materials 2% of M	%	2.0000	0.146		14.61	
Total direct costs: **Unit price:**		**1108.00** **14.31**				363.44 6.860	745.23 7.452	0.00

Source: Norma Pro, Athenasoft.

Table 3

Sample simplified calculation of wall grounding in a listed building

No	Base	Specification	Measure unit	Takeoff	Unit price	Value
1.	45442100-8	Wall surface grounding – detailed calculation				
1 d.1	KNR 19-01 1305-04 analogy	Wall surface grounding with TAGOSIL G (once)	m^2	100.000	14.31	1431.00

Source: Norma Pro, Athenasoft.

The cost estimate of this building activity – wall grounding – using the preparation suggested by the Conservation Officer is largely divergent from the cost-estimated value calculated according to a unit price found in one of the generally available price lists for renovation work in listed buildings (Tab. 4).

Table 4
Comparison of an item prepared according to the norms of R, M and S consumption, with a simplified item calculated according to a published bulletin of prices of renovation work in listed buildings

No	Base	Specification	Measure unit	Takeoff	Unit price	Value
1	45442100-8	Wall surface grounding – detailed calculation				
1 d.1	KNR 19-01 1305-04 analogy	Wall grounding with TAGOSIL G (once)	m^2	100.000	14.31	1431.00
2	45442100-8	Wall surface grounding – simplified calculation				
2 d.2	BRR 3/2009	Plaster painting – soap grounding of plastered walls	m^2	100.000	5.68	568.00

Source: Norma Pro, Athenasoft.

The cost of grounding walls calculated from the price list is just about 40% of the cost of grounding with the preparation recommended by the Conservation Officer (Fig. 1). This means that in practice it is impossible to produce a reliable cost estimate for renovation work in a listed building relying solely on unit prices in available published sources.

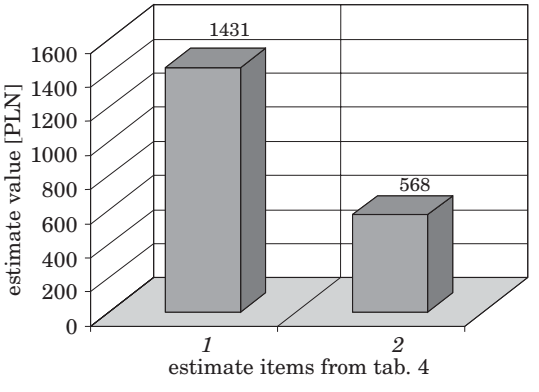

Fig. 1. Comparison of items from tab. 4. *1* – calculation item 1; *2* – calculation item 2
Source: Own elaboration.

Conclusion

Most of cost estimates for construction work in listed buildings are drawn up using the detailed method, based on the existing database of price catalogues, taking into consideration a whole variety of material and technological solutions. The fact that clients acting under the Act on Public Contracts must possess an owner/client cost estimate produced with the simplified method means that a detailed calculation of unit prices must be completed. The scope of construction activities and materials to be used suggested by an authorized conservation officer obliges the cost estimator to perform a customized analysis of labour consumption and cost of used materials.

Accepted for print 12.10.2009

References

KOWALCZYK Z., ZABIELSKI J. 2007. *Kosztorysowanie i normowanie w budownictwie*. WSiP, Warszawa.

Polskie standardy kosztorysowania robót budowlanych. 2005. SKB, Warszawa.

Ustawa z dnia 29 stycznia 2004 r. *Prawo zamówień publicznych* Dz.U. 2007 nr 223 poz. 1655 z późn. zm.

Rozporządzenie Ministra Infrastruktury z dnia 18 maja 2004 r. w sprawie określania metod i podstaw sporządzania kosztorysu inwestorskiego, obliczania planowanych kosztów prac projektowych oraz planowanych kosztów robót budowlanych określonych w programie funkcjonalno-użytkowym. Dz. U. nr 130, poz.1389.

Rozporządzenie Ministra Infrastruktury z dnia 2 września 2004 r. w sprawie szczegółowego zakresu i formy dokumentacji projektowej, specyfikacji technicznych wykonania i odbioru robót budowlanych oraz programu funkcjonalno-użytkowego. Dz.U. nr 202, poz. 2072; dotyczy robót budowlanych stanowiących zamówienie publiczne.

Rozporządzenie Ministra Rozwoju Regionalnego i Budownictwa z dnia 13 lipca 2001 r. w sprawie metod kosztorysowania obiektów i robót budowlanych Dz.U. nr 80, poz. 867.

TECHNICAL SCIENCES
Abbrev.: Techn. Sc., No 12, Y 2009

DOI 10.2478/v10022-009-0010-y

SELECTED ACCELERATIONS AND ORBITAL ELEMENTS OF THE GOCE SATELLITE IN THE TIME DOMAIN

Andrzej Bobojć
Institute of Geodesy
University of Warmia and Mazury in Olsztyn

K e y w o r d s: GOCE satellite orbit, satellite accelerations, orbital elements, geopotential.

A b s t r a c t

The work contains the results of the GOCE satellite orbit simulation. The GOCE satellite orbit was presented in the aspect of the temporary changes in selected accelerations and in selected keplerian elements. The satellite accelerations due to: the geopotential, the Earth tides and the ocean tides (the radial component for both), the gravitation of the Moon and the gravitation of the Sun, were presented in function of time. The showed changes in orbital elements include the semi-major axis, eccentricity, inclination, argument of perigee and right ascension of ascending node. For the orbit determination the Cowell numerical integration method of the eighth order was used. The geopotential was described by means of the EGM96 model. The mentioned temporary changes in the selected accelerations and orbital elements were described. Most of them contain the characteristic periodic components, which are close to the satellite orbital period, the Earth's rotation period and the Moon's synodic period.

WYBRANE PRZYŚPIESZENIA I ELEMENTY ORBITALNE SATELITY GOCE W DZIEDZINIE CZASU

Andrzej Bobojć
Instytut Geodezji
Uniwersytet Warmińsko-Mazurski w Olsztynie

S ł o w a k l u c z o w e: orbita satelity GOCE, przyśpieszenia satelity, elementy orbitalne, geopotencjał.

A b s t r a k t

Praca zawiera wyniki symulacji orbity satelity GOCE. Orbitę satelity GOCE przedstawiono w aspekcie zmian czasowych wybranych przyśpieszeń i elementów keplerowskich. Przyśpieszenia satelity spowodowane przez: geopotencjał, pływy skorupy, pływy oceaniczne (składowa radialna dla

obu), grawitację Słońca i grawitację Księżyca, przedstawiono w funkcji czasu. Pokazane zmiany w elementach orbity obejmują półoś wielką, mimośród, nachylenie, argument perygeum i rektascensję węzła wstępującego. Do wyznaczenia orbity użyto całkowania numerycznego metodą Cowella ósmego rzędu. Geopotencjał opisano modelem EGM96. Opisano wspomniane zmiany czasowe wybranych przyśpieszeń i elementów orbity. Większość z nich zawiera charakterystyczne składowe okresowe, które są zbliżone do okresu orbitalnego satelity, okresu rotacji Ziemi oraz okresu synodycznego Księżyca.

Introduction

One of the ESA's missions is the Gravity Field and Steady – State Ocean Circulation Explorer Mission (GOCE). The GOCE mission has been started on 17 March 2009. The main goal of this mission is to determine the geopotential model up to 200 degree and order of the spherical harmonic coefficients. The mentioned model will allow to obtain the gravity acceleration with an accuracy of 1 mGal and to estimate of the geoid with an accuracy of 1 cm. Such accuracies will be realized at spatial scales down to 100 km (*Gravity Field...* 1999, DRINKWATER et al. 2003, MEGIE, READINGS 2000).

A gradiometric satellite is a key component of the GOCE mission. This satellite is placed into almost circular and sun-synchronous orbit with an average altitude of about 250 km (*Gravity Field...* 1999). The non-gravitational forces acting on the satellite are compensated by a drag-free control system (DRINKWATER et al. 2003). The GOCE satellite is planned to provide two types of measurements: the gravity gradients (Satellite Gravity Gradiometry data – SGG data) and the high-low Satellite to Satellite tracking data (SST data). They will be obtained by two on-board devices: an electrostatic gravity gradiometer and a GPS/GLONASS receiver, respectively (JOHANESSEN et al. 2003). Both the SGG data and the SST data will be subject of a joint inversion to estimate the Earth's gravity field model (DITMAR, KLEES 2002, DITMAR et al. 2003).

The knowledge of the satellite orbit is one of the key factors in the estimation of Earth's gravity field. GPS measurements (SST data) are the basic data for the GOCE satellite orbit estimation. Advanced algorithms were prepared to determine the aforementioned orbit in the form of a reduced-dynamic and a kinematic orbit solution (BOCK et al. 2006, VISSER et al. 2006).

Basically, the SGG data (i.e. gravity gradients) will be used to obtain the Earth's gravity field model. However, these observations also carry the information about the position and velocity of a satellite. Thus they can be used in the process of satellite orbit improvement. This process requires the computation of approximated gravity gradients along a approximated orbit. The description of planned GOCE satellite orbit using the temporary changes in the selected accelerations and in keplerian elements, can be helpful in the computation of aforementioned approximated orbit.

Simulations

To obtain the GOCE satellite orbit, the Cowell numerical integration method of the eighth order was used. The computed orbit was expressed with respect to the J2000.0 reference frame (LAING 1991, ANDERSON et al. 2002). This frame can be described in the following way: the origin at the Earth's mass centre, the X-axis is directed towards the mean vernal equinox of the standard epoch J2000.0 (at noon on January 1, 2000), the Z-axis points out from the Earth's mass centre along the Earth's mean rotational axis of the standard epoch J2000.0, the Y-axis completes the frame to the right-handed frame. The following initial elements of the GOCE orbit were taken into the computation: the epoch: 54313.0 MJD, semi-major axis: 6634.7711 km, eccentricity: 0.001, inclination: 96.5 deg., argument of perigee: 0.00 deg., right ascension of ascending node: 45.00 deg., mean anomaly: 0.00 deg., the orbital period T = 89.64 min. (*Gravity Field...* 1999). The computations were performed using the TOP package (DROŻYNER 1995). The TOP package determines a satellite orbit in the Earth's gravity field taking into account selected perturbing forces. Several models were used to the orbit computation. The EGM96 model (LEMOINE et al. 1998) was taken for the geopotential. The Earth and ocean tides were modelled by the MERIT Standards (MELBOURNE et al. 1983). Both, the IAU1976 Theory of Precession and the IAU1980 Theory of Nutation (the Wahr nutation) were included to the computation. Additionally, the following data were taken into the computation: the Sun, Moon and planet ephemerides DE200/LE200 (epoch J2000.0). The pole coordinates were equal to zero.

It was assumed that the GOCE satellite motion is determined by the geopotential and by the following forces: the gravitation of the Moon, the gravitation of the Sun, the gravitation of the planets, the Earth tides and the ocean tides. Additionally, the relativity effects was taken into account in the satellite motion model. The relativity effects generate the corresponding satellite acceleration. Taking into account the aforementioned assumptions, a 30-day arc of the GOCE orbit with an integration step 60 s was obtained. The chosen satellite accelerations due to the mentioned above forces and the chosen keplerian elements, were computed along this orbit. The obtained temporary changes of the selected accelerations and keplerian elements were expressed with respect to the J2000.0 reference frame.

Description of the obtained temporary changes

The presented below graphs were prepared for the 30-day arc of the GOCE orbit. The initial epoch (denoted as 0) and the last given epoch (number 21600) correspond to 54313.0 MJD and 54343.0 MJD, respectively. A sampling

interval is 2 minutes. For most presented below figures, the main graph and additional small graphs were prepared. These small graphs zoom in the main graph in the chosen epoch ranges of the 30-day orbital arc. The width of these ranges is 400 minutes with the exception of Figure 9b, where the mentioned width is equal to 200 minutes.

The term "amplitude" used in this work, refers to the difference between a given maximum and a neighbouring minimum (so called peak-to-peak amplitude).

Changes in selected accelerations

The temporary changes of the satellite acceleration due to the geopotential are presented in Figure 1. The continuous oscillations of the mentioned acceleration result from this figure. The acceleration oscillates around the value of ~ 9.062 m s^{-2} (Fig. 1*a*). These oscillations have the periodic behavior with the increasing amplitude. At the start of the orbital arc, this amplitude is equal to about 0.04 m s^{-2}. Next, it decreases to approx. 0.03 m s^{-2} (at ~ one-fifth of the orbital arc) and increases to about 0.09 m s^{-2} at the end of the orbital arc. An occurrence of the oscillation of the geopotential-derived acceleration is in relation with the non-zero value of eccentricity (for the initial epoch 0.001). As the additional research showed, the increasing trend of the eccentricity appears together with the mentioned increase of the oscillating amplitude of the acceleration. Two periods of the acceleration changes can be seen in Figure 1. The first period visible in four small graphs of Figure 1 is equal to about 90 minutes and coincides with the satellite orbital period. The second period is equal to about 1 day and is close to the Earth's rotation period. This period concerns the changes of the maximum values of acceleration and is visible in Figure 1*a*. The occurrence of the aforementioned period is in relation with the Earth's rotation with respect to the used J2000.0 frame.

In the first three small graphs (Fig. 1*b*-1*d*), the characteristic small peaks between the main peaks of the oscillating acceleration, are shown. The mentioned peaks appear in the middle of the satellite orbital period. Taking into account Figure 1*b*, the explanation of such acceleration changes can be performed. The satellite experiences the maximum acceleration at the perigee, being simultaneously at the equatorial plane, near the equatorial bulge (the acceleration at the epoch 0 in Fig. 1*b*). Next, the acceleration decreases when the satellite moves around the Earth. When the satellite reaches the maximum altitude above the equatorial plane, after the quarter of the orbital period, the acceleration decreases to the minimum value. From this point, the experienced acceleration increases when the satellite returns to the equatorial plane. After half the orbital period, the satellite is again at the equatorial plane, near the

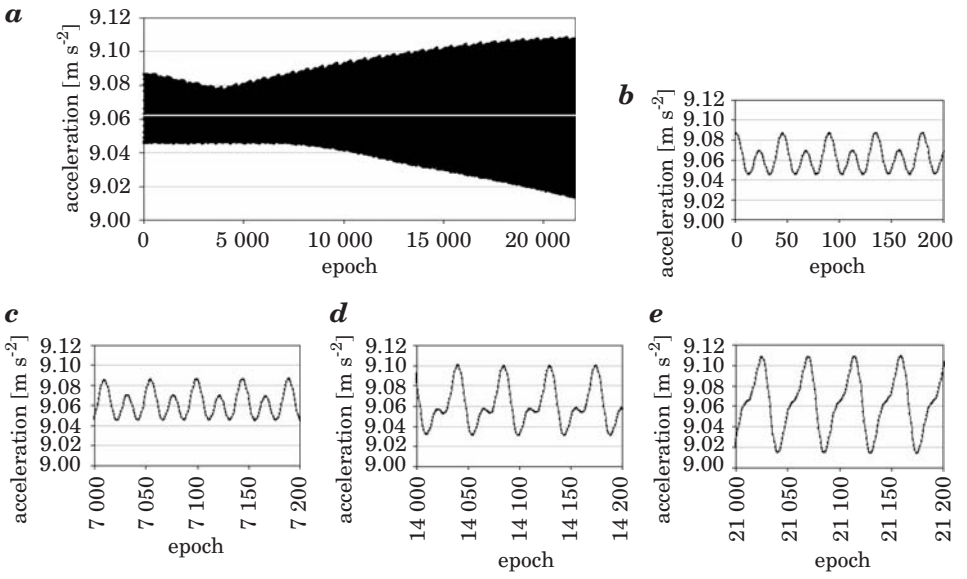

Fig. 1. The acceleration due to the geopotential along the 30-day orbit with the 2 minute sample interval. The epoch 0 and the last showed epoch correspond to 54313.0 MJD and 54343.0 MJD, respectively. The group of the small graphs presents the parts of the main graph in the chosen epoch ranges

equatorial bulge. At this point, the acceleration reaches the maximum value (the mentioned small peak, Fig. 1*b*). However, this maximum is smaller than the former one due to the apogee of the orbit. Then, the acceleration again decreases during the satellite travel under the equatorial plane. It reaches the minimum when the distance between the satellite and the equatorial plane has the maximum value. This point of the orbit corresponds to three-quarters the orbital period. Next, the acceleration increases – the satellite approaches again the equatorial plane. After the orbital period, the satellite is at the perigee and the acceleration has again the maximum value. The similar changes of acceleration (as in Fig. 1*b*) are given in Figure 1*c*. In two remaining Figures 1*d* and 1*e*, the acceleration changes differ from those showed in Figures 1*b* and 1*c*. The oscillation amplitude is greater and the small peaks of the acceleration are less clear in Figures 1*d* and 1*e*. Especially in Figure 1*e*, where only the remains of these peaks can be noticed. Such acceleration changes indicate an evolution of the orbit in the inhomogeneous gravity field of the oblated Earth and under the influence of other perturbing forces. As mentioned above, the increasing oscillation amplitude of acceleration is connected with the increasing eccentricity trend, whereas the change of the small peaks of acceleration in Figures 1*b*–1*e*, is in relation with the change of the argument of perigee.

The radial component of acceleration generated by the Earth tides is given in Figure 2. This component oscillates with a period of about 45 minutes (Fig. 2*b*–2*e*), which is close to half the orbital period of the satellite. Such period can be related to the Earth's oblateness. The satellite passess through the equatorial plane every approx. 45 minutes (half the orbital period). When the satellite is near this plane, the radial acceleration induced by the Earth tides reaches the minimum value. Additionally, the main graph (Fig. 2a) presents the maximum and minimum acceleration changes with the period of about 0.5 day and the oscillation amplitude changes with the period of about 29–30 days (close to the Moon's synodic period). This reflects the impact of an Earth--Moon-Sun configuration on the Earth tides. The values of presented radial acceleration change in the range from $-3.67 \cdot 10^{-7}$ m s^{-2} (towards the Earth's mass centre) to about $3.75 \cdot 10^{-7}$ m s^{-2} (towards the opposite direction with respect to the Earth's mass centre direction). This means that in the satellite motion, an "undulate" component appears. A time interval of sign change of the acceleration is about 22–23 minutes (Fig. 2*d*). After such interval an action direction of this radial component changes.

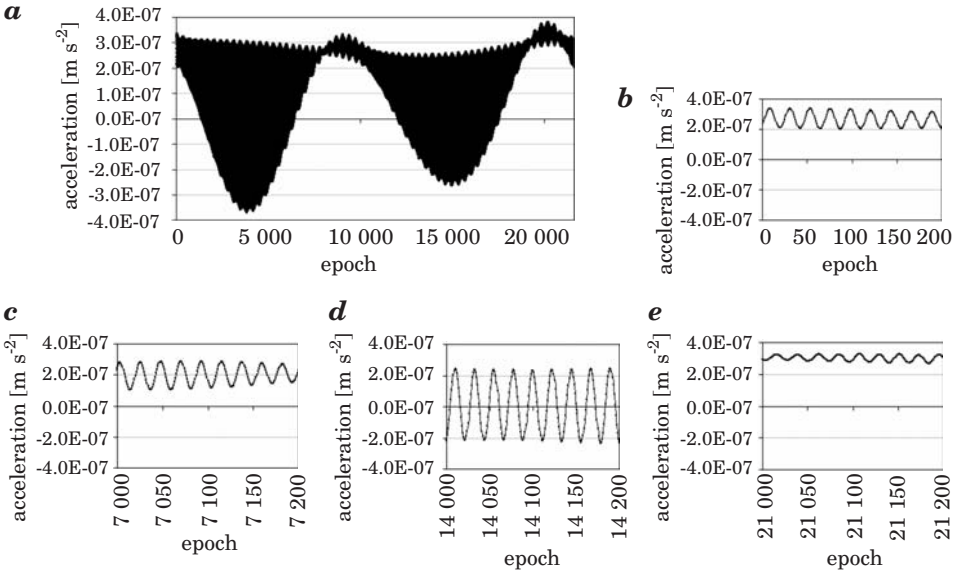

Fig. 2. The radial component of acceleration generated by the Earth's tides along the 30-day orbit with the 2 minute sample interval. The epoch 0 and the last showed epoch correspond to 54313.0 MJD and 54343.0 MJD, respectively. The group of the small graphs presents the parts of the main graph in the chosen epoch ranges

The radial component of the satellite acceleration generated by the ocean tides is given in Figure 3. It is clear visible that it oscillates around zero (Figures 3*a*–3*e*). The values place in the range between – $3.56 \cdot 10^{-7}$ m s^{-2} to about $3.40 \cdot 10^{-7}$ m s^{-2}. Figure 3a shows a faint period of the change of oscillation amplitude. It equals approx. 14–15 days (almost half the Moon's synodic period). However, this period, taking into account the 30-day limitation of the simulated orbital arc, can be a harmonic of the Moon's synodic period (29.5 days) also occurring in the presenting changes. The oscillations given in Figures 3*b*–3*e* seem to be irregular. This oscillation irregularity maybe caused by the "water" nature of ocean tides. A minimum time interval of sign change for the described acceleration is about 4 minutes (Fig. 3*e*), i.e. the action direction of acceleration changes after such interval.

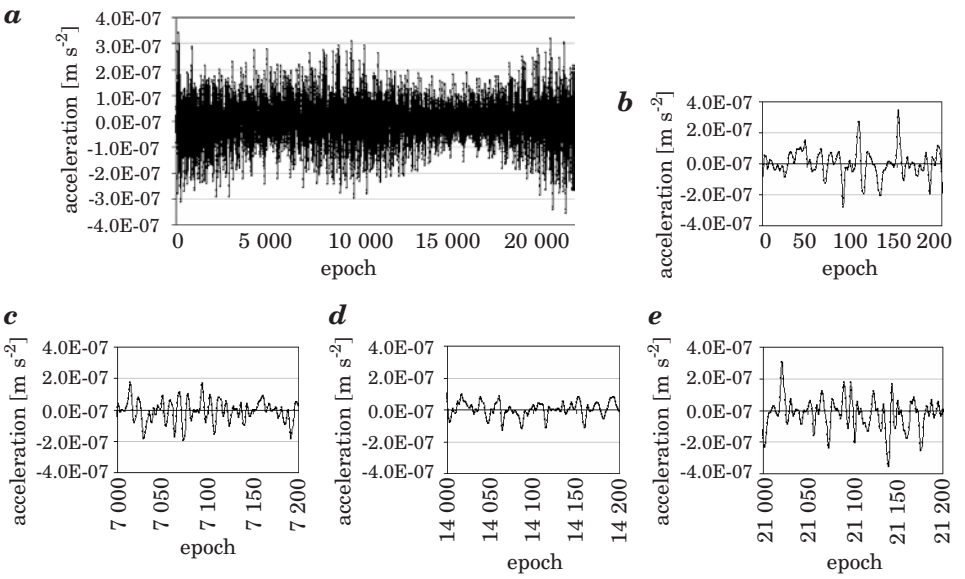

Fig. 3. The radial component of acceleration due to the ocean tides along the 30-day orbit with the 2 minute sample interval. The epoch 0 and the last showed epoch correspond to 54313.0 MJD and 54343.0 MJD, respectively. The small graphs are the parts of the main graph in the chosen epoch ranges

The satellite acceleration due to the gravitation of the Moon is presented in Figure 4. The showed oscillations of the acceleration are very regular here. The visible changes of the oscillation amplitude are in relation with the Moon motion with respect to the satellite orbital plane. Three periods of the oscillating acceleration can be seen in Figure 4. The first period of the changes of the oscillation amplitude is equal to approx. 29–30 days (Fig. 4*a*). The second

period of acceleration changes has the value of about 45 minutes (near half the orbital period, Fig. 4*b* and 4*e*). Finally, the period visible in Figures 4*c* and 4*d* is equal to about 90 minutes. Similarly as for the acceleration generated by the geopotential, the smaller "peaks" occur between the successive larger "peaks" of acceleration value. In this case the difference between the large "peaks" and the small ones is noticeable smaller (Fig. 4*c* and 4*d*). The considered acceleration varies from $4.90 \cdot 10^{-7}$ m s^{-2} to about $1.31 \cdot 10^{-6}$ m s^{-2} (Fig. 4*a*).

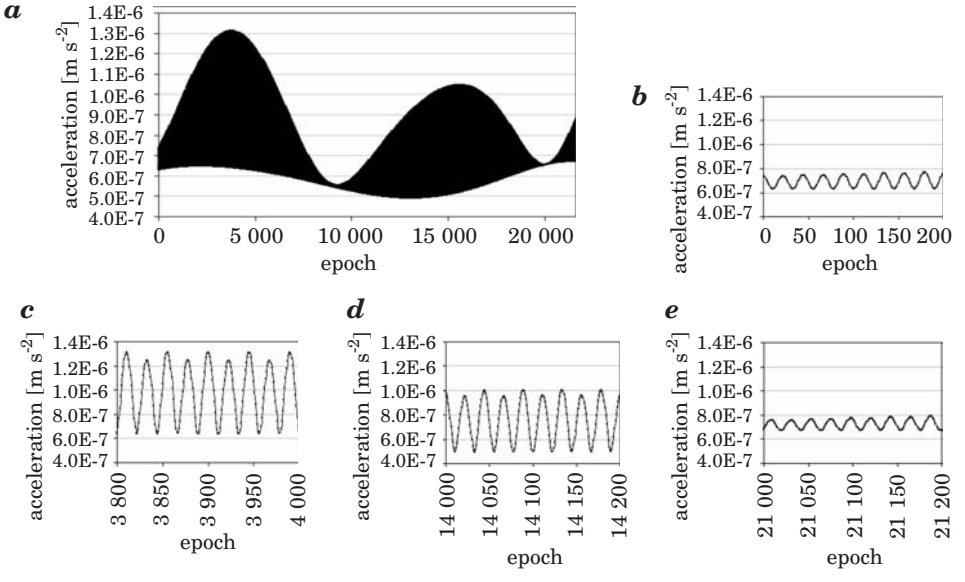

Fig. 4. The acceleration generated by the gravitation of the Moon along the 30-day orbit with the 2 minute sample interval. The epoch 0 and the last showed epoch correspond to 54313.0 MJD and 54343.0 MJD, respectively. The group of the small graphs presents the parts of the main graph in the chosen epoch ranges

The changes of the satellite acceleration under the influence of the gravitation of the Sun are presented in Figure 5. A characteristic feature of these changes is the decreasing oscillation amplitude. This amplitude varies from approx. $1.7 \cdot 10^{-8}$ m s^{-2} (at the start of orbital arc) to about $5.0 \cdot 10^{-9}$ m s^{-2} (at the end of orbital arc). Thus, an angle between the satellite orbital plane and the Earth-Sun direction increases in the whole 30-day interval of the orbit. The showed acceleration is placed between ~ $2.51 \cdot 10^{-7}$ m s^{-2} and ~ $2.68 \cdot 10^{-7}$ m s^{-2}. Similarly as for the acceleration generated by the gravitation of the Moon, two typical periods with the length of ~ 45 minutes and of ~ 90 minutes can be

noticed in Figures 5*b*–5*e*. Unlike the acceleration generated by the Moon, the smaller minimum appears here in the middle of orbital period between successive larger minimums of the acceleration (Fig. 5*d*, 5*e*).

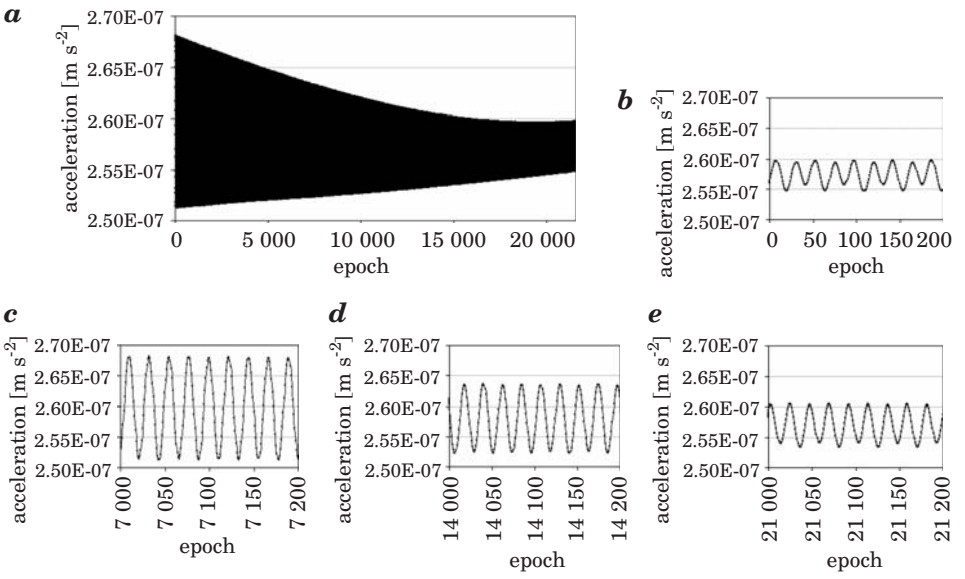

Fig. 5. The acceleration generated by the gravitation of the Sun along the 30-day orbit with the 2 minute sample interval. The first showed epoch and the last showed one correspond to 54313.0 MJD and 54343.0 MJD, respectively. The small graphs present the parts of the main graph in the chosen epoch ranges

Changes in selected orbital elements

Figure 6 shows the semi-major axis for the considered 30-day orbital arc. This orbital element oscillates very regularly with a period of about 45 minutes around the value of about 6624.53 km (Fig. 7*a* and 7*b*). The amplitude of these oscillations is almost constant and equals to approx. 19.54 km. The presence of the 45-minute period of the semi-major axis changes is caused mainly by the satellite orbit perturbation due to the Earth's oblateness. In his orbital motion, the satellite is over the equatorial plane during half the orbital period (just about 45 minutes) and under this plane during half the orbital period, too. The symmetric mass distribution with respect to the equatorial plane (in some approximation) decides about the occurrence of just 45-minute period.

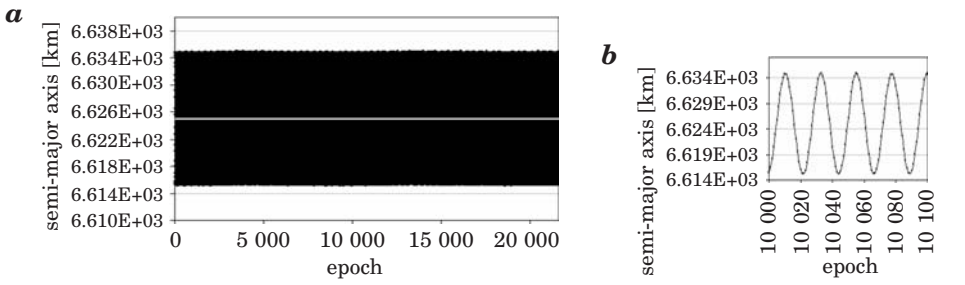

Fig. 6. The semi-major axis of the keplerian osculating orbit along the 30-day orbital arc with the 2 minute sample interval. The epoch 0 – 54313.0 MJD, the last showed epoch – 4343.0 MJD. The small graph gives the part of the main graph in the chosen epoch range. The white line denotes the trend line

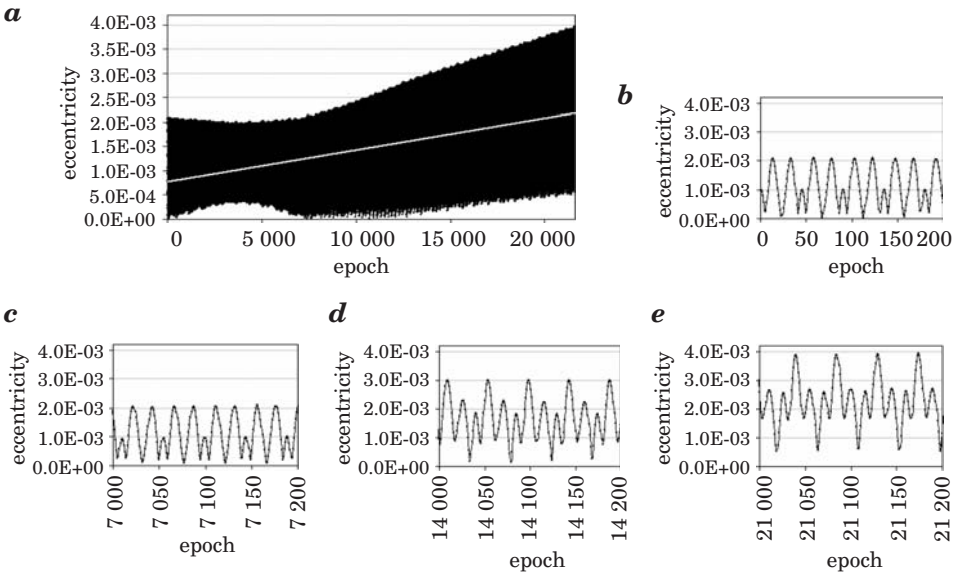

Fig. 7. The eccentricity of the keplerian osculating orbit along the 30 – day orbit arc with the 2 minute sample interval. The epoch 0 and the last showed epoch correspond to 54313.0 MJD and 54343.0 MJD, respectively. The small graphs give the parts of the main graph in the chosen epoch ranges. The white line is the trend line

In the case of eccentricity, the changes are fairly complex (Fig. 7). The oscillation amplitude decreases from about $2.0 \cdot 10^{-3}$ to near $1.6 \cdot 10^{-3}$ at one-fifth of the orbital arc and then it increases to approx. $3.4 \cdot 10^{-3}$ at the end of orbital arc (Fig. 7*a*). The increasing trend occurs in the visible changes. The given values of eccentricity are placed between about $1.81 \cdot 10^{-5}$ to near $3.97 \cdot 10^{-3}$. As it results from Figure 7*a*, the minimum and maximum values of eccentricity changes with about the 1-day period. The period equal to

~ 90 minutes is visible in Figures 7*b*–7*e*. The changing profile of oscillation is given in these figures, too. In this profile, a smaller maximum lies (in the middle of the orbital period) between two the same greater maximums (Fig. 7*b* and 7*c*). Next, the dominant maximum arises from the previous smaller maximum, lying between two smaller maxima (Fig. 7*d* and 7*e*).

The changes of the inclination with its increasing trend are showed in Figure 8*a*. Two periods of the oscillation are visible here. The length of the first period is equal to about 14 days (near half the Moon's synodic period), whereas the second one has the length of near 0.5 day and is connected with the changes of maximum and minimum inclination values. The oscillation amplitude is equal to ~ 0.01 degree and it remains almost constant for the whole orbital arc. From Figure 8, the range of inclination values between 96.499 degrees to 96.526 degrees results. Figures 8*b*–8*e* present the basic oscillations of inclination with the period close to 45 minutes (near half the satellite orbital period). The visible periods and the increasing trend of inclination are caused mainly by the inhomogeneous Earth's gravity field. Additional research showed that the occurrence of the 14 day period is generated also by the gravitation of the Moon and by the tides (mainly by the Earth tides), whereas the increasing trend of inclination is caused, in a less degree, by the gravitation of the Sun, the gravitation of the Moon and the Earth tides.

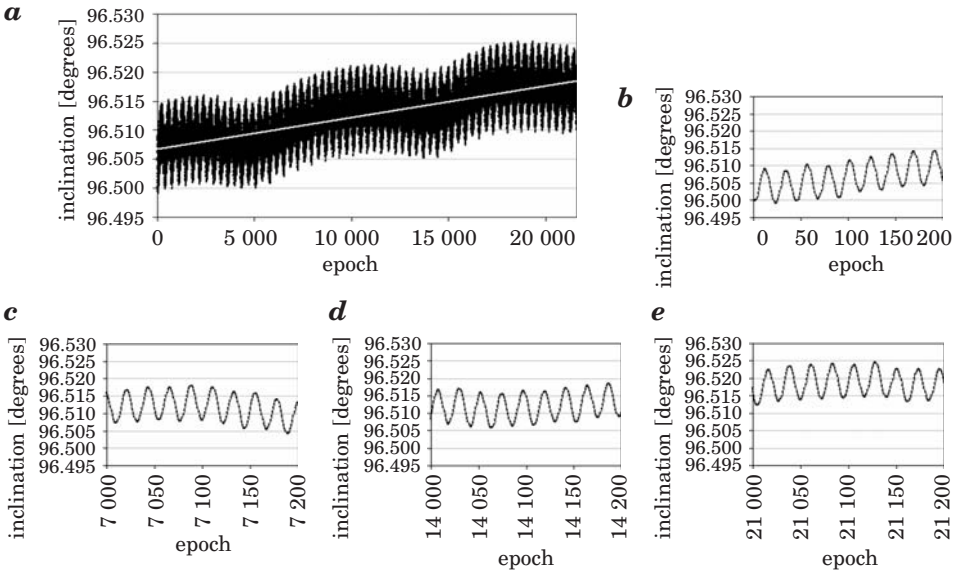

Fig. 8. The inclination of the keplerian osculating orbit along the 30 – day orbit arc with the 2 minute sample interval. The epoch 0 and the last showed epoch correspond to 54313.0 MJD and 54343.0 MJD, respectively. The small graphs contain the parts of the main graph in the chosen epoch ranges. The white line is the trend line

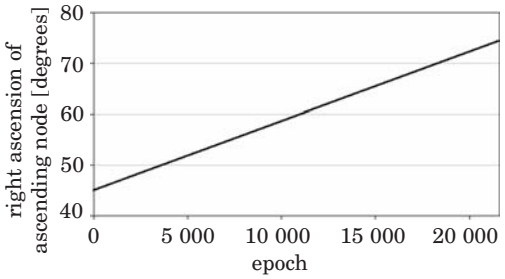

Fig. 9. The right ascension of ascending node of the keplerian osculating orbit along the 30 – day orbit arc with the 2 minutes sample interval. The epoch 0 and the last showed epoch correspond to 54313.0 MJD and 54343.0 MJD, respectively

The characteristic changes of the right ascension of ascending node are given in Figure 9. This orbital element linearly increases from 45 degrees to about 74.4 degrees under the influence of the inhomogeneous Earth's gravity field.

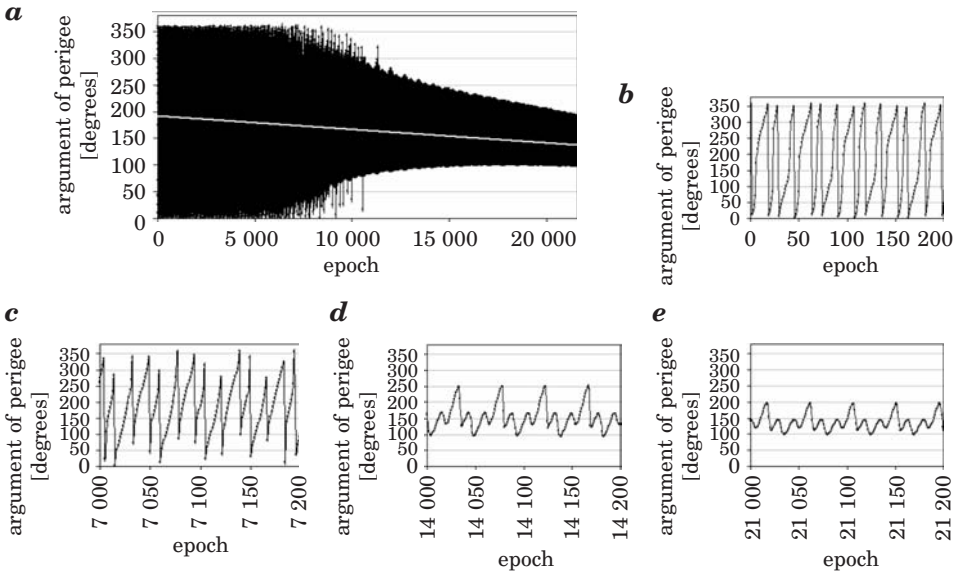

Fig. 10. The argument of perigee of the keplerian osculating orbit along the 30 – day orbit arc with the 2 minutes sample interval. The epoch 0 and the last showed epoch correspond to 54313.0 MJD and 54343.0 MJD, respectively. The small graphs present the parts of the main graph in the chosen epoch ranges. The white line is the trend line

Figure 10 presents the changes of the argument of perigee. These changes are deformed by a numerical noise for about half the orbital arc (Figures 10*a*–10*c*). The aforementioned numerical noise can be connected with the small value of eccentricity (initially – 0.001). After half the orbital arc the

argument of perigee oscillates more regularly with the period of near 90 minutes (Figures 10*d* and 10*e*). Between the successive higher maxima the minimum occurs in the middle of the satellite orbital period. For both part this minimum, two smaller maxima are visible (Fig. 10*d* and 10*e*). The oscillation amplitude decreases to about 100 degrees simultaneously with the decreasing trend of value (Fig. 10*a*).

Summary

The changes of the selected accelerations and orbital elements were determined for the GOCE satellite. In most cases these changes can be characterized by the oscillations with the exception of the right ascension of ascending node, which changes linearly. In two cases, the characteristic profile of the changes of the oscillation amplitude occurred. Namely, the decrease of amplitude from the start of orbital arc to about one-fifth of its length and then the increase to the end of orbital arc. In this way, the oscillation amplitude of the geopotential derived acceleration and of the eccentricity varies. The following approximated periods were noticed in the presented temporary changes:

- 45-minute period (close to half the orbital period) – the changes of: the radial component of acceleration due to the Earth tides, the accelerations due to the gravitation of the Moon and of the Sun, the semi-major axis and the inclination,
- 90-minute period (close to the orbital period) – the changes of: the geopotential derived acceleration, the acceleration due to the gravitation of the Moon and of the Sun, the eccentricity and the argument of perigee,
- 0.5-day period (half the Earth's rotation period) – the changes of: the radial component of acceleration due to the Earth tides (for the minimum and maximum values), the inclination (for the minimum and maximum values, too),
- 1-day period (the Earth's rotation period) – the changes of: the geopotential derived acceleration (for the maximum values), the eccentricity (for the minimum and maximum values),
- 14–15 day period (close to half the Moon's synodic period) – the changes of: the radial component of acceleration due to the ocean tides (for the oscillation amplitude), the inclination,
- 29–30 day period (close to the Moon's synodic period) – the changes of: the acceleration due to the gravitation of the Moon (for the oscillation amplitude), the radial components of acceleration due to the Earth tides and the ocean tides (for the oscillation amplitude; in this case the period of 29–30 days results indirectly from Figures 2, 3, 4.

The basic periods of the showed changes are equal to about 45 and 90 minutes. The longer periods concern usually the changes of the minimum and maximum values or the oscillation amplitude.

The changes of presented orbital elements reflect the combined perturbations mainly coming from the Earth's gravity field. The perturbations in the GOCE orbital elements under the influence of separate forces can be the subject of the another work.

Accepted for print 11.08.2009

References

ANDERSON J.D., LAING P.A., LAU E. L., et al. 2002. *Study of the anomalous acceleration of Pioneer 10 and 11*. Phys. Rev. D65 082004.

BOCK H., JÄGGI A., SVEHLA D. 2007. *Precise Orbit Determination for the GOCE Satellite Using GPS*. Adv. Space Res., 39: 1638–1647.

DITMAR P., KLEES R. 2002. *A Method to Compute the Earth's Gravity Field from SGG/SST data to be Acquired by the GOCE Satellite.* Delft University Press.

DRINKWATER M.R., FLOBERGHAGEN R., HAAGMANS R. et al. 2003. *GOCE: ESA's First Earth Explorer Core Mission.* Space Science Reviews, 00: 1–14.

DROŻYNER A.1995. *Determination of Orbits with Toruń Orbit Processor System*. Adv. Space Res., 16(2).

Gravity Mission – GOCE Brochure (revised). 2006. *ESA's*.

Gravity Field and Steady-State Ocean Circulation Mission, *ESA SP-1233(1)*. 1999. ESA. Report for mission selection of the four candidate Earth Explorer missions.

JOHANNESSEN J.A., BALMINO G., LE PROVOST C. et al. 2003. *The European Gravity Field and Steady-State Ocean Circulation Explorer Satellite Mission Its Impact on Geophysics*. Surveys in Geophysics, 24(4): 339–386.

LAING P.A. 1991. *Implementation of J2000.0 reference frame in CHASMP*. The Aerospace Corporation's Internal Memorandum, 91(6703).

LEMOINE F., KENYON S., FACTOR J. 1998. *The Development of the Joint NASA GSFC and the National Imagery and Mapping Agency (NIMA) Geopotential Model EGM96.* Report No.206861.

MELBOURNE W. 1983. *Project MERIT Standards*. Circ. 167, U.S. Naval Observatory, Washington, D.C.

MÉGIE G., READINGS C. J. 2000. *The Earth Explorer Missions – Current Status*. Earth Observation Quarterly No. 66.

TECHNICAL SCIENCES
Abbrev.: Techn. Sc., No 12, Y 2009

DOI 10.2478/v10022-009-0011-x

ASSESSMENT OF ACCURACY OF EGM08 MODEL OVER THE AREA OF POLAND

Adam Łyszkowicz

Department of Surveying
University of Warmia and Mazury in Olsztyn

Key words: EGM08, quasigeoid heights, ellipsoidal heights, normal heights.

Abstract

The paper presents the evaluation results for the new Earth Gravitational Model (EGM08) that was recently released by the US National Geospatial Intelligence Agency, using GPS and normal heights from precise levelling in the area of Poland. Detailed comparisons of quasigeoid heights obtained from the EGM08 model and other combined global geopotential models with GPS/levelling data have been performed in both absolute and relative sense. The test network covers the entire part of the Poland territory and consists of 360 sites which belong to the Polish national primary triangulation network, with direct levelling ties to the Polish vertical reference frame. The spatial positions of these sites have been determined at cm-level accuracy with respect to ETRF89 during a nation-wide GPS campaign that was organized in the frame of the EUREF activity. Additionally for relative accuracy evaluations of EGM08 model precise GPS/levelling traverse was used. Our results reveal that EGM08 offers a major improvement (more than 80%) in the agreement level among quasigeoidal, ellipsoidal and normal heights over the area of Poland, compared to the performance of previous combined geopotential models for the same area.

OCENA DOKŁADNOŚCI MODELU EGM08 NA OBSZARZE POLSKI

Adam Łyszkowicz

Katedra Geodezji Szczegółowej
Uniwersytet Warmińsko-Mazurski w Olsztynie

Słowa kluczowe: EGM08, odstepy, odstępy quasi-geoidy, wysokości elipsoidalne, wysokości normalne.

Abstrakt

W pracy podano wyniki oceny jakości nowego modelu geopotencjału Ziemi jaki ostatnio udostępnił US National Geospatial Intelligence Agency. Ocenę bezwzględnej i względnej dokładności modelu przeprowadzono przez porównanie odstępów quasi-geoidy wyliczonych z modelu z odstępami uzyskanymi z satelitarnych pomiarów GPS i niwelacji precyzyjnej. Bezwzględna dokładność modelu była testowana na satelitarnej sieci GPS, która pokrywa równomiernie obszar kraju. Sieć ta składa się

z 360 punktów należących do krajowej podstawowej sieci triangulacyjnej. Trójwymiarowe współrzędne kartezjańskie punktów tej sieci wyznaczono w układzie ETRF89 z pomiarów satelitarnych GPS podczas kampanii zorganizowanej w ramach Podkomisji EUREF. Względna dokładność modelu była testowana na precyzyjnym trawersie pomierzonym techniką GPS i dowiązanym do sieci niwelacji precyzyjnej. Uzyskane wyniki pokazują, że model EGM08 daje znacznie lepszą zgodność (ponad 80%) między odstępami quasi-geoidy, wysokościami elipsoidalnymi i wysokościami normalnymi niż poprzednie modele.

Introduction

The earth gravity model EGM08 developed and released by the National Geospatial Intelligent Agency is a significant achievement in global field mapping. For the first time in modern geodetic history, a spherical harmonic model complete to degree and order 2159, with additional spherical harmonic coefficients extending up to degree 2190 and order 2159, is available for the representation of the earth's gravitational potential. This new model make possible with high spatial sampling resolution computation of mean gravity anomalies, geoid ellipsoid separations and other characteristic of gravity field for the entire globe. This model released in April 2008 for the earth science community is attracting interest of geodesists to assess its actual accuracy with different validation techniques and data sets from different part of globe e.g. (KOTSAKIS et al. 2008).

Similar study were conducted for the previous EGM96 model for the territory of Poland. In (ŁYSZKOWICZ 2003) vertical deflections computed from EGM96 model were compared with "observed" astro-geodetic deflections and the agreement on the level 0.5" was achieved. In (KRYNSKI, ŁYSZKOWICZ 2006) six different GGMs: EGM96, EIGEN-CH03S, GGM01S, GGM02S, GGM02, GGM02S/EGM96 were considered. Three kinds of numerical tests with the use of terrestrial gravity data, GPS/levelling height and quasigeoid models obtained from gravity were conducted. It was found that the best suited GGM model for the area of Poland is GGM02S/EGM96 model.

The main purpose of this paper is to present in details the EGM08 evaluation results that has been carried out for the territory of Poland using GPS and normal heights from levelling. In addition to the evaluation test which was carried out in previous studies (ŁYSZKOWICZ 2003), (KRYNSKI, ŁYSZKOWICZ 2006) another series of numerical tests are presented here for the first time.

Data sets

All the evaluation tests and their corresponding results that are presented in the following sections refer to a network of 360 GPS/levelling sites which covers

the entire territory of Poland with a relatively uniform spatial distribution and precise GPS/levelling traverse (see Fig. 1).

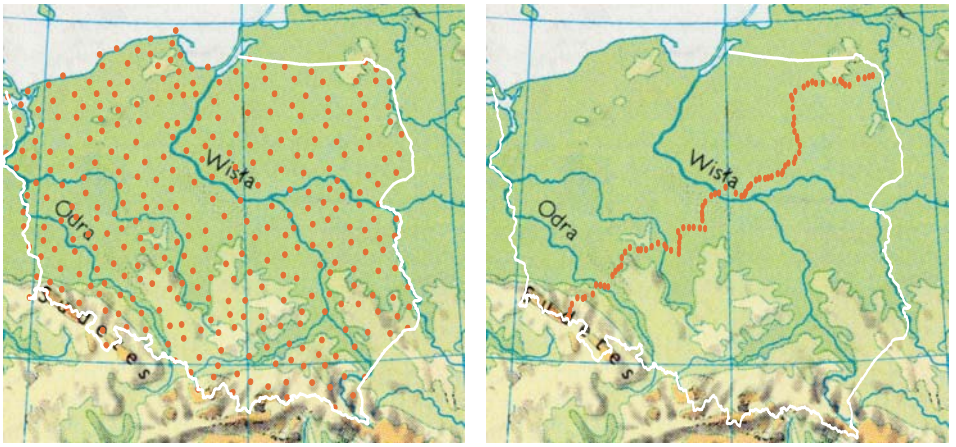

Fig. 1. Spatial distribution of the POLREF (left) and traverse (right) GPS/levelling points over the area of Poland

Ellipsoidal heights. The POLREF network that is a densification of EUREF-POL92 network (11 Polish stations linked in 1993 to ETRF89) consists of 360 sites surveyed in two 4h sessions each, in three campaigns from July 1994 to May 1995 (ZIELIŃSKI et al. 1997). Stations of the POLREF network were located at the sites of primary horizontal control network of Poland and were linked to the national vertical control by spirit levelling (Kronstadt86 datum), with standard deviation of normal height equal to 1.0–1.5 cm (GELO 1994). Standard deviation of ellipsoidal height (GRS80 ellipsoid) is 1.0–1.5 cm (ZIELIŃSKI et al. 1997).

For verification of quasigeoid models developed, as well as for estimation of their relative accuracy, a 868 km long control GPS/levelling traverse across the country has been established (KRYNSKI et al. 2005). The traverse surveyed in 2003 and 2004 in 5 campaigns consists of 190 stations of precisely determined ellipsoidal and normal heights. The stations were located at the benchmarks of the 1st or 2nd order vertical control network, or in their close vicinity. The 49 first order stations of the traverse were surveyed in one or two 24h sessions and remaining 141 stations (as densification points) were surveyed in 4h sessions. The coordinates of 49 the 1st order control stations were determined using the EPN strategy with the Bernese v.4.2 program. Accuracy of the coordinates determined in that way is at the level of single millimeters for majority of stations. The coordinates of densification points were calculated using the

Pinnacle program with the 1st order control stations as reference (KRYNSKI et al. 2005, CISAK, FIGURSKI 2005).

Normal heights. In Poland levelling network was measured three times. Finally levelling network measured in 1974–1982 consists of 135 loops with the average perimeter of about 221 km and total length of levelling lines 17 015 km. The network was connected with neighboring countries and with seven Polish tide gauges.

The levelling lines were measured by automatic levels: Opton Ni 1, Zeiss Ni 002. The following corrections were implemented to the raw data: 1) rod scale corrections, 2) rod temperature corrections, 3) tidal corrections, 4) normal Molodensky corrections. The final adjustment of the entire network was carried out in few versions in 1985. Accepted solution was obtained as a least square approach with stations constrains. Heights of 23 bench marks with their estimated accuracy (from new UPLN solution) was incorporated to the adjustment. After adjustment the standard deviation of height difference is equal ± 0.844 mm $\sqrt{d_{\mathrm{km}}}$ and standard deviation of adjusted heights is between $\pm$ 6.5 mm and $\pm$ 11 mm (WYRZYKOWSKI 1988).

GPS-based quasigeoid height. Based on the known ellipsoidal and normal heights, GPS-based geoid undulations have been computed at the 360 test network POLREF and additionally at 190 points of traverse according to the equation.

$$\zeta^{\mathrm{GPS}} = h - H^n \tag{1}$$

where h is ellipsoidal height from satellite observations and H^n is normal height from levelling. The standard deviation of quasigeoid height ζ^{GPS} computed from GPS observations and normal heights in the case of POLREF network is ± 1.4 – 2.1 cm, and in the case of precise traverse is $\pm$ 1.3 cm.

GGM-based quasigeoid heights. Quasigeoid heights have also been computed at the 360 POLREF GPS/levelling sites and 190 points of traverse using three different geopotential models. For the evaluation results presented herein we consider only the most recent geopotential models, which have been compiled from the combined contribution of various types of satellite data (CHAMP, GRACE, SLR), terrestrial gravity data, and altimetry data; see Table 1.

Table 1
Geopotential models used for the tests at the POLREF and at the traverse GPS/levelling sites

Model	$n_{\max}$	References
EGM08	2190	PAVLIS et al. 2008
EIGEN-5C	360	FÖRSTE et al. 2008
EGM96	360	LEMOINE et al. 1998

The quasigeoid heights were computed from the general formula.

$$\zeta(r,\phi,\lambda) = \zeta_0 + \frac{GM}{r\gamma} \sum_{n=2}^{n_{\max}} \left(\frac{a}{r}\right)^n \sum_{m=0}^{n} (C_{nm} \cos m\lambda + S_{nm} \sin m\lambda)\, P_{nm}\, (\sin\phi) \quad (2)$$

where C_{nm}, S_{nm} are fully normalized spherical harmonic coefficients of degree n and order m, $nmax$ is the maximum degree of geopotential model, GM is product of the Newtonian gravitational constant and mass of the geopotential model, r, ϕ, λ are spherical polar coordinates, a is the equatorial radius of geopotential model and P_{nm} are the fully normalized associated Legendre'a functions.

The term ζ_0 is the zero term due to the difference in the mass of the Earth used in IERS Convention and GRS80 ellipsoid. It is computed according to the well known formula.

$$\zeta_0 = \frac{GM - GM_0}{R\gamma} - \frac{W_0 - U_0}{\gamma} \quad (3)$$

where the parameters GM_0 and U_0 correspond to the normal gravity field on the surface of the normal ellipsoid. For the GRS80 ellipsoid we have $GM_0 = 398\ 600.5000 \times 10^9\ m^3s^{-2}$ and $U_0 = 62\ 636\ 860.85\ m^2s^{-2}$. The Earth's parameter GM used in quasigeoid computation from geopotential models and the constant gravity potential W_0 on the quasigeoid according to IERS Conventions have been set to the following values: $GM = 398\ 600.4415 \times 10^9 m^3s^{-2}$, $W_0 = 62636856.00\ m^2s^{-2}$. The mean Earth radius R and the mean normal gravity γ on the reference ellipsoid are taken equal to 6 371 008.771 m and 9.798 m s^{-2} respectively (GRS80 values). Based on the above conventional choices, the zero degree term from equation (3) yields the value $\zeta_0 = -0.442$ m, which has been added to the quasigeoid heights obtained from the corresponding spherical harmonic coefficients series expansions of all geopotential models.

The numerical computations for the spherical harmonic values of ζ from the various GGMs have been performed with the *geocol* software program that was kindly provided by dr Gabriel Strykowski from Danish National Space Center. The final GGM quasigeoid heights computed from equation (2) refer to the tide free system, with respect to a geometrically fixed reference ellipsoid (GRS80).

Height data statistics. The statistics of the individual height datasets that will be used in our evaluation tests are given in Table 2. Note that the statistics for the GGM quasigeoid heights refer to the values computed from equation (2) at the 360 points of POLREF network sites using full spectral resolution of each model.

Table 2
Statistics of the height datasets over the test network of POLREF GPS/levelling points (in meters)

	Mean	Std dev	Min.	Max
h	220.869	141.889	28.878	1645.515
H	186.763	140.059	-0.372	1601.822
N^{GPS} = h-H	34.106	4.435	27.078	43.733
N_{EGM96}	34.144	4.490	26.841	43.882
N_{EIGEN5}	34.001	4.453	26.948	43.723
N_{EGM08}	33.982	4.435	26.975	43.673

From the following table, it is evident the existence of a discrepancy from -10 up to + 4 cm (second column) between the zero reference surface of the Kronsztad86 vertical datum (which is associated with an unknown W_0 value) and the equipotential surface of the Earth's gravity field that is specified by the conventional value $W_0 = 62\,636\,856.00$ m^2 s^{-2} and realized by the various GGMs over the area of Poland.

Evaluation tests after a simple bias fit

A series of geopotential models evaluation tests was performed based on the point values for the ellipsoidal and normal heights in the test network. The statistics of the differences between the GPS based and the geopotential models quasigeoid heights are given in Table 3. In all cases, the values shown in this table refer to the statistics of the original misclosures h-H-ζ at the 360 POLREF GPS/levelling sites.

Table 3
Statistics of the original residuals $\zeta^{GPS} - \zeta$ at the POLREF GPS/levelling sites (in meters)

	Mean value (bias)	Std dev	Min.	Max
EGM96 (n_{max} = 360)	-0.038	0.190	-0.542	0.572
EIGEN5 (n_{max} = 360)	0.105	0.113	-0.224	0.520
EGM08 (n_{max} = 2190)	0.125	0.036	0.035	0.260

The differences in the estimated bias obtained from each model (Tab. 3) indicate the existence of regional distortions among the various GGM quasigeoids that are likely caused by long and medium wavelength errors in their original spherical harmonic coefficients. Furthermore, the magnitude of the estimated bias between ζ^{GPS} and ζ suggests that there is a visible offset between

– the equipotential surface corresponding to the IERS conventional value $W_0 = 62\,636\,856.00$ $m^{-2}s^{-2}$ and realized by the various geopotential models over the territory of Poland,
– the vertical datum zero height reference surface that is realized through the GPS quasigeoid heights ζ^{GPS}, appears to be located 12 cm (approximately) above the levelling quasigeoid.

From the results given in the Table 3, it is evident that EGM08 offers a remarkable improvement in the agreement among ellipsoidal, normal and quasigeoid heights throughout the territory of Poland. Compared to the two previous geopotential models, the standard deviation of the EGM08 residuals $\zeta^{GPS} - \zeta$ over the entire test network decreases by a factor of 5 from ±19 cm to ±3.6 cm and the major contribution comes from the ultra-high frequency band $360 < n < 2190$ of EGM08 model. Obtained results are remarkably good, because analogous investigations in the area of Greece show the only threefold decrease of the standard error (KOTSAKIS at al. 2008).

Table 4
Percentage of the 360 test points whose absolute values of their adjusted residuals $\zeta^{GPS} - \zeta$ (after a least squares constant bias fit) are smaller than some typical geoid accuracy levels

	< 2 cm	< 5 cm	< 10 cm	< 15 cm	< 20 cm
EGM96 ($n_{max} = 360$)	8.8%	23.3%	43.7%	60.8%	73.5%
EIGEN5 ($n_{max} = 360$)	16.5%	35.1%	64.3%	81.7%	91.7%
EGM08 ($n_{max} = 2190$)	43.7%	89.1%	97.9%	100%	–

In Table 4, we can see the percentage of the GPS/levelling sites in the test network whose adjusted residuals $h\text{-}H\text{-}\zeta$ (after the constant bias fit) fall within some standard quasigeoid accuracy level. The agreement between EGM08 and GPS quasigeoid heights is better than 2 cm for more than 40% of the total 360 test points, whereas for the other GGMs the same consistency level is only reached at 16% or less of the test points. Furthermore, almost 98% of the test points give an agreement between the EGM08 geoid and the GPS/levelling data that is better than 10 cm, compared to 64% (or less) in the case of two other global models that were tested.

Additionally evaluation tests of geopotential models was performed on the sites of precise traverse. The statistics of the differences between the GPS-based and the geopotential models quasigeoid heights are given in Table 5. Investigations were conducted for all (190) points and separately for 44 points being characterizing very high accuracy. The results of calculations are presented in Table 5.

Table 5
Statistics of the original residuals ζGPS – ζ at the 190 and 44 GPS/levelling sites of traverse (all values in meters)

	190 sites				44 sites			
	bias	std dev	Min.	max	bias	std dev	Min.	max
EGM96 (n_{max} = 360)	-0.025	0.115	-0.383	0.213	-0.015	0.115	-0.312	0.213
EIGEN5 (n_{max} = 360)	0.078	0.105	-0.270	0.275	0.086	0.106	-0.202	0.274
EGM08 (n_{max} = 2190)	0.075	0.022	0.027	0.126	0.087	0.019	0.043	0.126

From Table 5 appears that there are no essentials differences in the statistic of the evaluated EGM08 model on the base of all 190 and only 44 sites. Compared to the EGM96 geopotential model, the standard deviation of the EGM08 residuals $\zeta^{GPS} - \zeta$ over the traverse decreases by a factor of 6 from ±11.5 cm to ±1.9 cm. It means, that the existing traverse is the most exact combination of measurements GPS and levelling at present and should recommended to the evaluation of new quasigeoid models in Poland.

The horizontal spatial variations of the EGM08 residuals $\zeta^{GPS} - \zeta$ tested on POLREF network do not reveal systematic pattern within the test network. Both in latitude dependent and longitude dependent scatter plots, as shown in Figure 2 and Figure 3 are free of any sizeable north/south or east/west tilts over the area of Poland. In EGM96, however, some strong localized tilts and oscillations can be identified in their $\zeta^{GPS} - \zeta$ residuals, mainly due to larger systematic errors associated with their spherical harmonic coefficients and significant omission errors involved in the quasigeoid computation.

Evaluation results have also confirmed that EGM08 performs exceedingly better than the other models over the mountainous parts of the Poland test network. A strong indication can be seen in the scatter plots of the residuals $\zeta^{GPS} - \zeta$ (after the least squares constant bias fit) with respect to the normal heights of the corresponding GPS/levelling sites, see Figure 4. These plots reveal a height dependent bias between the GGM and the GPS quasigeoid heights, which is considerably reduced in the case of EGM08. Apparently, the higher frequency content of the new model gives a better approximation for the terrain dependent gravity field features over the area of Poland, a fact that is visible from the comparative analysis of the scatter plots in Figure 4.

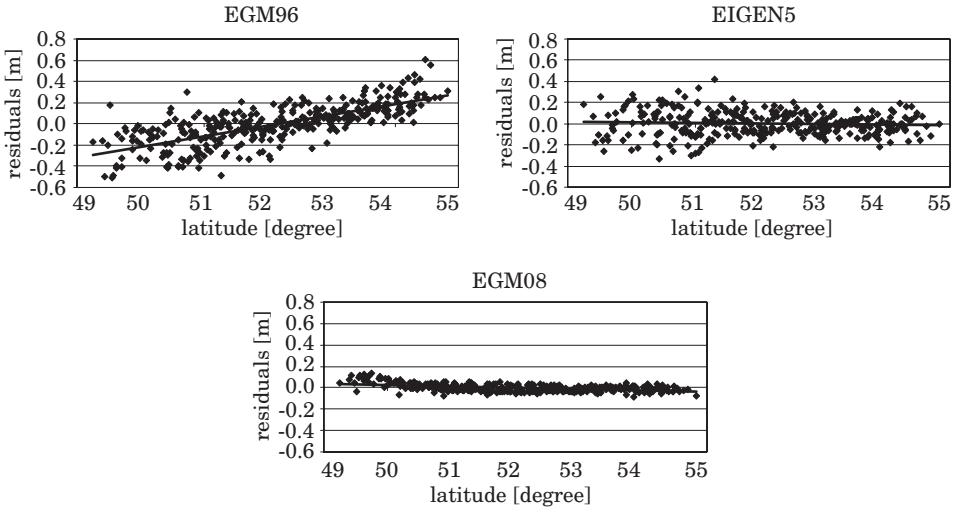

Fig. 2. Latitude dependent variation of the residuals $\zeta^{GPS} - \zeta$ (after a least squares constant bias fit) at 360 points of POLREF network

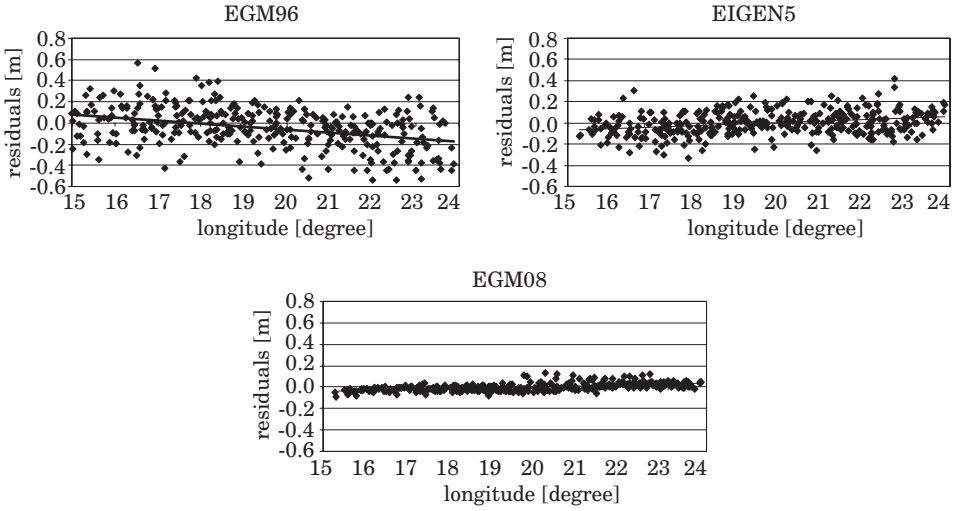

Fig. 3. Longitude dependent variation of the residuals $\zeta^{GPS} - \zeta$ (after a least squares constant bias fit) at 360 points of POLREF network

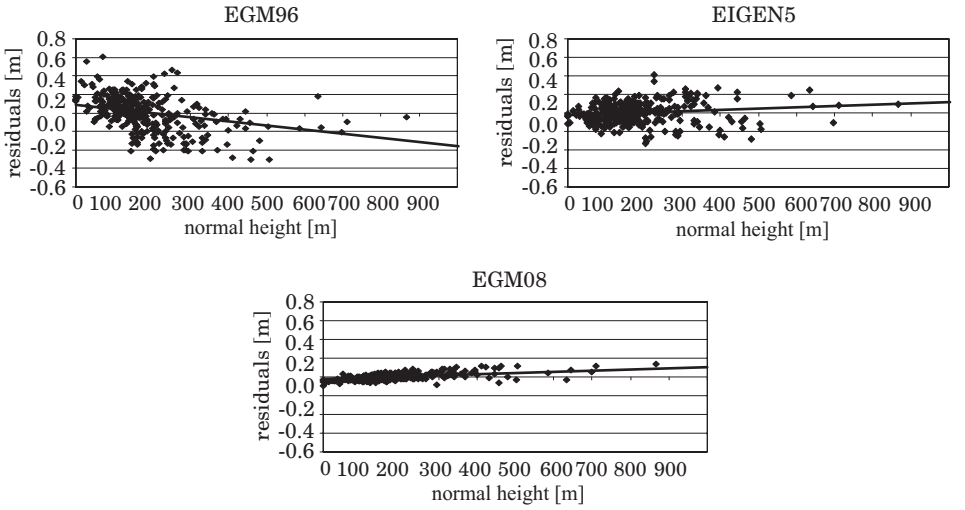

Fig. 4. Height dependent variation of the residuals $\zeta^{GPS} - \zeta$ (after a least squares constant bias fit) at 360 points of POLREF network

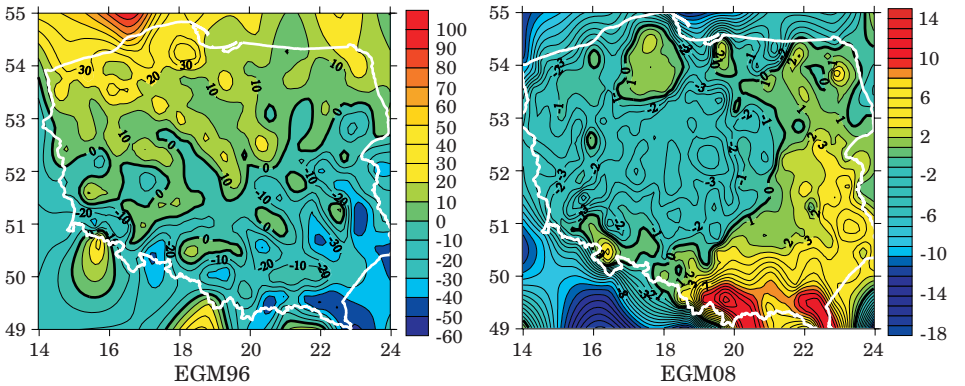

Fig. 5. Geographical distribution of the differences $\zeta^{GPS} - \zeta$ (after a least squares constant bias fit) at 360 sites of POLREF network (in cm)

The spatial distribution of the quasigeoid height residuals for the full resolution model EGM96 and EGM08 is depicted in two separate figures, each with a different color scaling scheme (Fig. 5). From the comparison of the left and right plots, we can verify the overall improvement in the quasigeoid representation over the area of Poland that is achieved with EGM08, compared to the EGM96 model. The achieved improvement is significant i.e. from decimeters to centimeters.

The Figure 5 (right) reveals the remaining inconsistencies with the GPS/leveling data, which are caused by the commission/omission errors of the new model and the systematic local distortions in the normal heights at the test points.

Evaluation tests with different parametric models

The various methods of the fit of gravimetric quasigeoid in Poland to Kronsztadt 86 height datum were study in (KRYNSKI, ŁYSZKOWICZ 2006). The parameters of the model were determined using least squares collocation. In practice, a trend was modelled by a plane function, and the residuals were modelled by a Hirvonen covariance function.

In this paper another series of numerical experiments has been carried out using a number of different parametric models for the least squares adjustment of the differences $\zeta^{GPS} - \zeta$. The motivation for these additional tests was to investigate the fitting performance of some known linear models that are frequently used in geoid/quasigeoid evaluation studies with heterogeneous height data, and to assess their feasibility in modeling the systematic discrepancies between the geopotential models and the GPS based quasigeoid surfaces over the Poland area. These tests were implemented with all three geopotential models that were initially selected for this study.

The various parametric models that have been fitted to the original misclosures h-H-ζ are given in Table 6. Model 1 uses a single constant bias parametric term and it is actually the same model that was employed for all tests of the previous section. Model 2 incorporates two additional parametric terms which correspond to an average north-south and east-west tilt between the geopotential model and GPS quasigeoid surfaces. Model 3 is the usual four parameter model which geometrically corresponds to a 3D spatial shift and an approximate uniform scale change of the geopotential model reference frame with respect to the underlying reference frame of the GPS heights (or vice versa). Finally, models 4, 5 and 6 represent height-dependent linear corrector surfaces that constrain the relation among ellipsoidal, normal and quasigeoidal heights in terms of the generalized equation.

$$h - (1 + \delta_{S_H})H - (1 + \delta_{S_H}) = a_0 \tag{4}$$

The above equation takes into consideration the fact that the spatial scale of the GPS heights does not necessarily conform with the spatial scale induced by the geopotential model quasigeoid undulations and/or the inherent scale of the normal heights obtained from spirit levelling. Moreover, the geopotential model of quasigeoid heights and/or the local normal heights are often affected

by errors that are correlated, to a certain degree, with the Earth's topography (see the results in Figures 4 and 5), a fact that can additionally justify the use of model 4 or 6 for the optimal fitting between ζ^{GPS} and ζ.

Table 6

Various parametric models, (KOTSAKIS 2008)

Number of model	Model
1	$h_i - H_i - N_i = a_0 + v_i$
2	$h_i - H_i - N_i = a_0 + a_1 (\varphi_i - \varphi_0) + a_2 (\lambda_i - \lambda_0) \cos\varphi_i + v_i$
3	$h_i - H_i - N_i = a_0 + a_1 \cos\varphi_i \cos \lambda_i + a_2 \cos\varphi_i \sin \lambda_i + a_3 \sin\varphi_i + v_i$
4	$h_i - H_i - N_i = a_0 + \delta_{S_H} H_i + v_i$
5	$h_i - H_i - N_i = a_0 + \delta_{S_N} H_i + v_i$
6	$h_i - H_i - N_i = a_0 + \delta_{S_H} H_i + \delta_{S_N} + v_i$

The statistics of the adjusted residuals v_i in the test network of 360 GPS/levelling points, after the least squares fitting of the previous parametric models, are given in Table 7 and Table 8 for the case of EGM96 and EGM08, respectively.

Table 7

Statistics of the differences $\zeta^{GPS} - \zeta$ for the EGM96 quasigeoid undulations, after the least squares fitting of various parametric models at the 360 GPS/levelling sites (all values in meters)

Model	Bias	Std dev	Min.	Max
1	-0.038	0.190	-0.504	0.609
2	-0.038	0.117	-0.328	0.424
3	-41.713	0.117	-0.317	0.440
4	0.045	0.180	-0.487	0.923
5	0.406	0.181	-0.546	0.587
6	0.329	0.176	-0.525	0.839

Table 8

Statistics of the differences $\zeta^{GPS} - \zeta$ for the EGM08 quasigeoid heights, after the least squares fitting of various parametric models at the 360 GPS/levelling sites (all values in meters)

Model	Bias	Std dev	Min.	Max
1	0.124	0.036	-0.090	0.136
2	0.125	0.026	-0.068	0.106
3	25.279	0.024	-0.081	0.100
4	0.045	0.180	-0.487	0.923
5	0.119	0.036	-0.090	0.134
6	0.154	0.031	-0.240	0.092

From the above results, it can be concluded that the low order parametric models 2 and 3 which are commonly used in the combined adjustment of GPS, geoid/quasigeoid and leveled heights data offer slight visible improvement in the case of EGM08 model for the territory of Poland. Model 3 gives the best results reducing the standard deviation up to ± 2.4 cm in case of EGM08 model.

Table 9
Statistics of the differences $\zeta^{GPS} - \zeta$ for 44 points of traverse (all values in meters)

	Bias	Std dev	Min.	Max
EGM08 (n_{max} = 2190)	0.000	0.015	-0.035	0.035

In order to check the quality of fitting obtained at POLREF sites the quasigeoid computed from EGM08 was fitted to 44 quasigeoid heights at traverse bechmarks using model 3 from Table 6. The results of the fitting are presented in the Table 9. From the results given in the Table 9 appears, that if we have precise GPS measurements on benchmarks the standard deviation of fitting decrease from ±2.4 cm in the case of the POLREF network to ±1.5 cm in the case of the traverse.

Table 10
Percentage of the 44 test points whose absolute values of their adjusted residuals $\zeta^{GPS} - \zeta$ (after a least-squares constant bias fit) are smaller than some typical geoid accuracy levels

	< 1 cm	< 2 cm	< 3 cm	< 4 cm
EGM08 (n_{max} = 2190)	55%	84%	93%	100%

In Table 10, is given the percentage of the GPS/levelling sites in the test traverse whose adjusted residuals h-H-ζ after the model 3 fit fall within some standard quasigeoid accuracy level. The agreement between EGM08 and GPS quasigeoid heights is better than 1 cm for more than 55% of the total 44 test points, whereas for the POLREF network is 40% only. Furthermore, almost 93% of the test points give an agreement between the EGM08 geoid and the traverse GPS/levelling data that is better than 3 cm and 100% test points do not exceeded 4 cm.

All models which are tested in this section include a common parametric term in the form of a single constant bias. However, the various estimates of the common bias parameter a_0 as obtained from the least squares adjustment of each model, exhibit significant variations among each other (see first column in Table 7 and Table 8). Specifically, the estimated bias between ζ^{GPS} and ζ which is computed from the usual four parameter model appears to be highly

inconsistent with respect to the corresponding estimates from the other parametric models. This is not surprising since the intrinsic role of the bias a_0 in model 3 is not to represent the average spatial offset between the geopotential models and the GPS quasigeoid surfaces, as it happens for example in the case of model 1. In fact, the three additional parametric terms in model 3 are the ones that absorb the systematic part of the differences ζ^{GPS} - ζ in the form of a three-dimensional spatial shift leaving to the fourth bias parameter a_0 the role of a scale-change effect (KOTSAKIS 2008).

Although less inconsistent with each other, the estimates of the bias parameter a_0 from the other parametric models show dm level fluctuations in their values. It should be noted though that the inclusion of additional spatial tilts (model 2) for the fitting between ζ^{GPS} and ζ does not distort the initial estimate of a_0 that was obtained from model 1 over the Poland territory. On the other hand, the use of height dependent scaling terms (models 4, 5 and 6) affects considerably the final estimates of the bias parameter a_0, as it can be easily verified from the results in Table 7 and Table 8.

The realistic estimate for the average spatial offset between a local vertical datum and a quasigeoid from geopotential models seems to have a strong dependence on the parametric model that is used for the adjustment of heterogeneous height data over a test network of GPS/levelling sites. There is strong theoretical and practical arguments that can be stated in favor of the generalized constraint in model 4, the use of the simple model 1 is not necessarily the safest choice for estimating the average spatial offset between a GGM based and a GPS based geoid over a regional network. In view of the frequent absence (or even ignorance) of a complete and reliable stochastic error model for the properly weighted adjustment of the differences $\zeta^{GPS} - \zeta$, a clear geometrical interpretation of the estimated bias a_0 is not always a straightforward task in GGM evaluation studies, (KOTSAKIS 2008).

Baseline evaluation tests

Besides the absolute evaluation tests that were previously presented, an additional set of evaluation results was also obtained through the comparison quasigeoid slopes from geopotential models with GPS/levelling quasigeoid slopes over the Poland territory along the all 190 GPS/levelling benchmarks of traverse (see Fig. 1). For all baselines formed within this traverse, the following differences of relative quasigeoid undulations were computed.

$$\Delta\zeta_{ij}^{GPS} - \Delta\zeta_{ij} = (h_j - H_j - h_i + H_i) - (\zeta_j - \zeta_i) \tag{5}$$

The computation of the above differences took place after the implementation of a least squares constant bias fit between the point values of the EGM08 geopotential model and GPS quasigeoid heights.

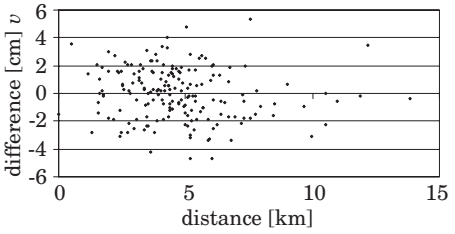

Fig. 6 Differences $\Delta\zeta^{GPS} - \Delta\zeta$ in the test traverse of GPS/levelling 190 benchmarks as a function of baseline length

The residual value computed from equation (5) were sorted in respect to the baseline length and plotted on Figure 6. In our test the baseline length from 0.5 up to 13 km were present for this quasigeoid evaluation scheme. Because of lack appropriate data, differences $\Delta\zeta^{GPS} - \Delta\zeta$ for baselines longer than 10 km were not consider here. The mean value of 190 differences is zero and its standard deviation is ±2 cm. Finally we can assume that for base line up to 10 km standard deviation of quasigeoid slope computed from EGM08 model is constant an equal ±2 cm. It gives the relative accuracy of the order 5×10^{-5}.

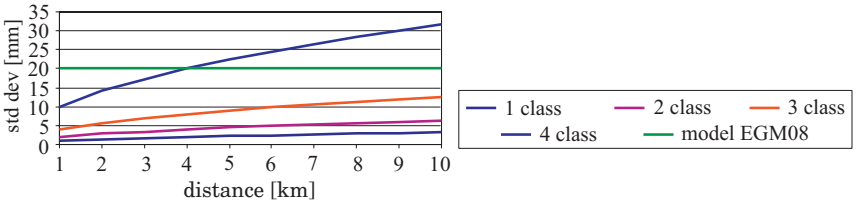

Fig. 7 Expected standard deviation of height differences for first, second, third and fourth class of levelling in Poland and estimated standard deviation (green line) of height differences computed from GPS/EGM08 data

Focusing on the quasigeoid slope evaluation results over short baseline distances up to 10 km can give us an indication for the expected accuracy in GPS/leveling projects when using an EGM08 reference quasigeoid for area of Poland. The preliminary analysis in the test network showed that the agreement between the height differences ΔH_{ij} computed directly from the known normal heights at the GPS/levelling sites and indirectly from the GPS/EGM08

ellipsoidal and quasigeoid heights, can be approximated by the mean error ± 2 cm. Although such a performance cannot satisfy mm level accuracy requirements for first, second and third class of precise levelling it can be satisfied for fourth class (Fig. 7) and provides a major step forward that can successfully accommodate a variety of engineering and surveying applications.

Conclusions

The results of evaluation tests have revealed that the EGM08 model is very accurate over all existing geopotential models for the area of Poland. The accuracy of EGM08 model is comparable with present gravimetric solution which is slightly beneath ± 2 cm. The average inconsistency level between ellipsoidal, normal and EGM08 quasigeoid heights is at the level ± 2.0 cm (Tab. 5) reflecting mainly the regional effects of the remaining commission errors in the models spherical harmonic coefficients, as well as other local systematic errors coming from vertical datum and normal heights. Fitting EGM08 quasigeoid heights to the precise traverse using model 3 slight improvement of accuracy is seen (see Table 9).

In terms of relative geoid accuracy, the EGM08 model evaluated up to 10 km gives value ±2 cm for the standard deviation of the slope residuals $\Delta\zeta^{GPS} - \Delta\zeta$ over all baseline lengths that were considered here and can be satisfied for the fourth levelling class (Fig. 7). It provides a major step forward in variety of engineering and surveying applications.

The results presented here provide a promising evidence for the successful use of EGM08 in future geodetic applications over the area of Poland. However, in view of its possible in the near future using in GPS based leveling projects in Poland, a more detailed analysis with additional interpolation models and "spatial corrector surfaces" for modeling the differences $\Delta\zeta^{GPS} - \Delta\zeta$ is required to achieve cm level consistency for the transformation between GPS/EGM08 and normal heights.

Acknowledgements

The research was financially supported by the Ministry of Science and Higher Education as the research project NN526 2163 33 "*Investigation of the influence of the vertical deviations on the quality of gravimetric quasigeoid on the territory of Poland*". The author desire express thankful to dr Gabriel Strykowski from Danish National Space Center for *geocol* software program

and to prof. Jan Kryński from Institute of Geodesy and Cartography for the GPS/levelling data relating to the traverse.

Accepted for print 26.08.2009

References

CISAK J., FIGURSKI M. 2005. *Control GPS/levelling traverse*, II Workshop on Summary of the project on a cm geoid in Poland, 16–17 November 2005, Warsaw (CD).

FÖRSTE C., FLECHTNER F., SCHMID R., STUBENVOLL R., ROTHACHER M., KUSCHEL J., NEUMAYER H., BIANCALE R., LEMOINE J.M., BARTHELMES F., BRUINSMA S., KÖNIG R., MEYER U. 2008. *EIGEN-5C A new global combined high-resolution GRACE-based gravity field model of the GFZ-GRGS cooperation*. Presented at the 2008 General Assembly of the European Geosciences Union, Vienna, Austria, April 13–18.

GELO S. 1994. Private communication.

KOTSAKIS C. 2008. *Transforming ellipsoidal heights and geoid undulations between different geodetic reference frames,* Journal of Geodesy, 82: 249–260.

KOTSAKIS C., KATSAMBALOS K., AMPATZIDIS D., GIANNIOU M. 2008. *Evaluation of EGM08 in Greece using GPS and levelling heights*, presented at the IAG International Symposium on Gravity, Geoid and Earth Observation, Chania, Greece, June 23–27.

KRYŃSKI J., CISAK J., FIGURSKI M., MAŃK M., BIENIEWSKA H., MOSKWIŃSKI M., SĘKOWSKI M., ZANIMONSKIY Y., ŻAK Ł. 2005. *GPS survey of control traverses and eventual link of the traverse sites to the vertical control with levelling as well as data processing* (in Polish), Institute of Geodesy and Cartography, Report for the Institute of Geodesy and Cartography, Warsaw, pp 27.

KRYŃSKI J., ŁYSZKOWICZ A. 2005. *Study on choice of global geopotential model for quasi-geoid determination in Poland*. Geodezja i Kartografia, 54(1): 17–36.

KRYŃSKI J., ŁYSZKOWICZ A. 2006. *Fitting gravimetric quasigeoid model to GPS/levelling data in Poland*, Proceedings of the 1st International Symposium of The International Gravity Field Service (IGFS), August 28 – September 1, 2006, in Istanbul, Turkey, 231–237.

KRYŃSKI J., ŁYSZKOWICZ A. 2006. *Best suited global geopotential model for quasigeoid modelling in Poland*, poster presented at the 1st International Symposium of The International Gravity Field Service (IGFS), to be held August 28 – September 1, 2006, in Istanbul, Turkey.

LEMOINE F.G., KENYON S.C., FACTOR J.K., TRIMMER R.G., PAVLIS N.K., CHINN D.S., COX C.M., KLOSKO S.M., LUTHCKE S.B., TORRENCE M.H., WANG Y.M., WILLIAMSON R.G., PAVLIS E.C., RAPP R.H., OLSON T.R. 1998. *The Development of the Joint NASA GSFC and the National Imagery and Mapping Agency (NIMA) Geopotential Model EGM96*, NASA Technical Paper NASA/TP1998206 861, Goddard Space Flight Center, Greenbelt, Maryland.

ŁYSZKOWICZ A. 2003. *Gravimetric vertical deflections for the area of Poland, Artificial Satellites*, Journal of Planetary Geodesy, 38(4): 107–118.

PAVLIS N.K., HOLMES S.A., KENYON S.C., FACTOR J.K. 2008. *An Earth Gravitational Model to Degree 2160: EGM2008*; presented at the 2008 General Assembly of the European Geosciences Union, Vienna, Austria, April 13–18.WYRZYKOWSKI T. 1988, *Monograph of precise levelling networks in Poland (in polish)*. IGiK, Warsaw.

ZIELIŃSKI J.B., ŁYSZKOWICZ A., JAWORSKI L., ŚWIĄTEK A., ZDUNEK R., GELO S. 1997. *Polref-96 the New Geodetic Reference Frame for Poland*, Springer, International Association of Geodesy Symposia, Symposium 118: Advances in Positioning and Reference Frames, IAG Scientific Assembly, Rio de Janeiro, Brazil, September 3–9, 1997, 161–166.

TECHNICAL SCIENCES
Abbrev.: Techn. Sc., No 12, Y 2009

DOI 10.2478/v10022-009-0012-9

GEODETIC APPLICATION OF *R*-ESTIMATION – LEVELLING NETWORK EXAMPLES

Robert Duchnowski

Institute of Geodesy
University of Warmia and Mazury in Olsztyn

Key words: *R*-estimation, levelling network.

Abstract

The paper presents geodetic application of *R*-estimation. Proposed method concerns estimation of differences between parameters of two functional models. Such estimation seems very useful in many geodetic problems, e.g., when observations are disturbed with gross errors or when differences mentioned are displacements of geodetic network points. The paper presents general solutions of *R*-estimation but it focuses special attention on its geodetic applications. In particular, it concerns levelling networks. The estimation method proposed here can be applied, for example, to monitoring of reference mark stability. The paper presents particular solution of such problem, based on *R*-estimation principle. Theoretical derivations and analysis are illustrated with some numerical examples.

GEODEZYJNE ZASTOSOWANIA *R*-ESTYMACJI – PRZYKŁADY DLA SIECI NIWELACYJNYCH

Robert Duchnowski

Instytut Geodezji
Uniwersytet Warmińsko-Mazurski w Olsztynie

Słowa klucze: *R*-estymacja, sieć niwelacyjna.

Abstrakt

Praca przedstawia geodezyjne zastosowania *R*-estymacji. Proponowana metoda dotyczy estymacji różnic między parametrami dwóch modeli funkcjonalnych. Taka estymacja wydaje się bardzo użyteczna w rozwiązaniu wielu problemów geodezyjnych, np. kiedy obserwacje są zaburzone błędami grubymi lub kiedy wspomniane różnice są przemieszczeniami punktów osnowy geodezyjnej. Praca przedstawia ogóle rozwiązania *R*-estymacji, ale szczególną uwagę zwrócono na jej geodezyjne zastosowanie, przede wszystkim dotyczące sieci niwelacyjnych. Przedstawiony sposób estymacji może być na przykład stosowany do kontroli stabilności punktów nawiązania. Praca przedstawia sposób takiej kontroli oparty na ogólnych zasadach *R*-estymacji. Przedstawione wyprowadzenia i teoretyczne rozważania zilustrowano kilkoma przykładami numerycznymi.

Introduction

R-estimation is one of the fundamental ways of robust estimation, together with M-estimation and *L*-estimation (HUBER 1981). It is well know and often applied in many scientific researches, e.g., (MUKHERJEE, BAI 2001, ROUSSEEUW, VERBOVEN 2002). The main idea of *R*-estimation is to apply some statistical rank test for example the Wilcoxon one (HUBER 1981, FELTOVICH 2003) to estimate a shift between two samples. For example, from a geodetic point of view, those two samples can be interpreted as two sets of geodetic measurement results or results obtained in two different periods. Then the shift between the samples can be regarded as effect of geodetic point displacement or some non-random error of measurements. On the other hand, *R*-estimation can be also regarded as an estimation of differences between parameters of two different, functional models. Some geodetic applications of *R*-estimators were proposed in the paper (DUCHNOWSKI 2008).

R-estimation, due to its main principles, is robust against outliers and therefore can be an alternative for other robust methods of adjustment, e.g., methods of *M*-estimation class (e.g., HUBER 1981, XU 1989, YANG 1994, DUCHNOWSKI 2005). Robustness is an important property of *R*-estimation but it is not the only advantage. Another one is possibility to apply that estimation class to elimination of some non-random errors from observation sets (DUCHNOWSKI 2008). Presented *R*-estimation properties and applications make the method useful in solving of many geodetic problems. That paper describes application of *R*-estimation within a displacement measurement process. Particular solution concerns leveling networks however their assumptions and principles can also be extended for other kinds of geodetic networks.

Let us consider a leveling network established for deformation or displacement monitoring. Estimation of point heights that change in time is most natural application of *R*-estimation. Such estimation can be regarded as estimation of parameters of two different, functional models (models formulated for two different measurement periods). That application is illustrated later on with the first numerical example. It is also well known that stability of reference marks is essentially important in such problems. Several methods were elaborated to recognize stable reference framework, they are described in many papers and books (PRÓSZYNSKI, KWAŚNIAK 2006). However, those methods sometimes fail, e.g., if a set of measurement results is disturbed with a gross error. Thus it is advisable to have a chance to compare results obtained from different methods. The present paper proposes a new method of mark stability monitoring. That method is of course based on specially modified *R*-estimation. It is very important since its theoretic foundations are different from the classical ones (e.g., HUBER 1981, PRÓSZYNSKI, KWAŚNIAK

2006, DUCHNOWSKI 2008). Another advantage of the method is its robustness which facilitates monitoring of bench marks stability even when an observation set is disturbed with a gross error. The proposed method is also illustrated with numerical example.

R-estimation

Theoretical foundation and basic solutions

Let two independent samples $x_1, x_2, ., x_n$ and $y_1, y_2, .., y_m$ be realizations of random variables X and Y and let $F(x)$ and $G(y) = F(x - \Delta)$ be distributions of X and Y, respectively. Thus both distributions differ from each other in a quantity Δ, which can be regarded as a shift between two samples. The main tusk of R-estimation is to assess the shift Δ. The following test statistic can be formulated for such reason (HUBER 1981).

$$S_{n,m} = \frac{1}{m} \sum_{i=1}^{m} a(R_i) \tag{1}$$

where $a(i)$ are some given scores and R_i is a rank of x_i in the joint sample (containing all elements of two mentioned ones). Usage of a particular function $a(i)$ depends on the kind of assumed rank test (HUBER 1981, FELTOVICH 2003, NARAJDO, MCKEAN 1997). The R-estimation concept is to find such estimator $\hat{\Delta}_R$ of the shift Δ that makes $S_{n,m} = 0$ (or less strictly $S_{n,m} \approx 0$ considering some properties of $S_{n,m} \approx 0$, e.g., discontinuity) i.e., to search for such shift estimator that makes the test (1) unable to detect a difference in locations of two mentioned samples (or to make it least able for such detection).

Let us consider test (1). Scores $a(i)$ are usually generated using a function $J(t)$. For example

$$a(i) = J\left(\frac{i}{m + n + 1}\right) \tag{2}$$

There are several other possibilities for scores $a(i)$, also for the same $J(t)$. They can be found in, e. g., HUBER (1981) or NARAJDO and MCKEAN (1997). If the Wilcoxon test is assumed, i. e., if

$$J(t) = t - \frac{1}{2} \tag{3}$$

then most often used functions $a(i)$ lead to the same test statistic (HUBER 1981). Assuming such form of $J(t)$ function, the following R-estimator of the shift can be formulated

$$\hat{\Delta}^R = \text{med}\ (y_i - x_j) \tag{4}$$

where med (◦) is a median operator and $1 \le i \le m$, $1 \le j \le n$ (HUBER 1981).

Basing on the same assumptions another useful R-estimate can be derived. Consider only one sample $x_1, x_2, \ldots, x_n$ of the variable X. Now, let the expected value $E(X)$ of X be estimated. To solve the problem one can construct a "mirror image" sample, i.e., $2E(X) - x_1$, $2E(X) - x_2$, ., $2E(X) - x_n$, which can stand in for the sample $y_1, y_2, \ldots, y_m$. Then the following estimate (HUBER 1981)

$$\hat{E}^R(X) = \text{med}\left[\frac{1}{2}\ (x_i + x_j)\right] \tag{5}$$

$(1 \le i \le m + n,\ 1 \le j \le m + n)$, , makes $S_{n,m} = 0$ (or at least $S_{n,m} \approx 0$).

The R-estimates presented above are derived basing on the test statistic in Eq.(1) and the $J(t)$ function from Eq.(3). They can be regarded as some variants of the Hodges-Lehmann estimates, too (e.g., HUBER 1981). The estimator Eq.(5) should be used very carefully especially in geodetic applications where number of observations is not very high. It is due to properties of the Hodges-Lehmann estimators. It can be proved that in a very small sample. i.e., when $n < 5$, that estimate is not robust for outliers (ROUSEEUW, VERBOVEN 2002).

Adaptation for geodetic purposes

Both presented estimators can be useful in some geodetic elaborations (DUCHNOWSKI 2008). However, there are some limitations of their applications. The main limitation concerns assumptions of the method, i. e., that all sample elements are identically distributed. If that assumption is taken strictly then geodetic applications of R-estimation is limited to the case when only one quantity is measured and it is measured several times with the same accuracy. As for the second problem, it can be easy overcome if only measurement results are standardized or if one applies other rank test (FELTOVICH 2003). The way how to deal with the first limitation is presented in the paper (DUCHNOWSKI 2008) and it is now shown briefly.

Let $\mathbf{x} \in R^{n\times 1}$ be an observation vector. Generally, that vector consists of realizations $x_1, x_2, \ldots, x_n$ of different random variables, which makes

R-estimators (4) and (5) unable to use. Let us consider the classical functional model of a geodetic network in the form

$$\mathbf{v} = \mathbf{x} - \mathbf{AX} \tag{6}$$

where: $\mathbf{A} \in R^{n \times m}$ is a know, rectangular matrix, $\mathbf{X} \in R^{m \times 1}$ is a vector of unknown parameters and $\mathbf{v} \in R^{n \times 1}$ is a residual vector. Let $\tilde{\mathbf{X}}$ be a "true" or at least initial value of parameter $\mathbf{X}$ and let it be known. Then one can write

$$\tilde{\mathbf{v}} = \mathbf{x} - \mathbf{A}\tilde{\mathbf{X}} \tag{7}$$

and compute a new sample $\tilde{\mathbf{v}} = [\tilde{v}_1, \tilde{v}_2, ..., \tilde{v}_n]^T$, (the notification is simplified for the sake of clarity; formally it is $\tilde{v}_i = [\tilde{\mathbf{v}}]_i$),. Because all residuals $\tilde{v}_1$, (the vector $\mathbf{v}$) can be regarded as identically distributed (assuming the same accuracy or residual standardization) then also $\tilde{v}_i$, (the vector $\tilde{\mathbf{v}}$) can be (e.g., DIONE 1981). It means that $\tilde{\mathbf{v}}$ can be apply in the estimates (4) and (5). Since the true value of the parametric vector $\mathbf{X}$ stays unknown it is very important to find a "good" initial value $\tilde{\mathbf{X}}$. For example, it can be computed on the basis of measurement results $x_1, x_2, ..., x_n$ or can be taken from the previous measurements or adjustments. The second way seems especially useful in deformation or displacement elaborations where current results are compared with the previous, control ones. Despite $\tilde{\mathbf{X}}$ is usually only an assessment of $\mathbf{X}$ and the assumption about identicalness of distributions of the vector $\tilde{\mathbf{v}}$, elements is not satisfied strictly, practically computed $\tilde{\mathbf{X}}$ should be good enough to neglect such nonconformity.

Particular Applications in Leveling Networks

Generally, R-estimation applications in leveling networks are the same like in other kinds of geodetic observational systems. R-estimates can be applied to, e.g., elimination of systematic errors or gross errors from observation sets. The method can be also used during classical least squares adjustment (LS method) for example in the R-LS method (DUCHNOWSKI 2008). This paper proposes applications of R-estimation in leveling networks created for deformation or displacement detection.

The first application is the most natural one and concerns vertical displacement estimation. Consider a leveling network created for such displacement detection. Such network should be measured at least two times resulting in

two observation vectors $\mathbf{x}_1$ and $\mathbf{x}_2$. Basing on assumed functional model Eq. (6) one can write

$$\mathbf{v}_1 = \mathbf{x}_1 - \mathbf{A}\mathbf{X}_1 \tag{8}$$

and

$$\mathbf{v}_2 = \mathbf{x}_2 - \mathbf{A}\mathbf{X}_2 \tag{9}$$

for each epoch, respectively. Usually, heights of the network points are assumed as parameters in such functional models. Thus vectors $\mathbf{X}_1$ and $\mathbf{X}_2$ consist of heights of the same points but in different epochs. Let us now consider a single element $[\mathbf{X}_2]_k$ of the vector $\mathbf{X}_2$ that corresponds with the element $[\mathbf{X}_1]_k$. Then a difference $[\mathbf{X}_2]_k - [\mathbf{X}_1]_k$ can be regarded as a vertical displacement of the respective network point. The formula (5) can be applied to estimate such difference. Since the first measurements are control ones, the estimator $\hat{\mathbf{X}}_2$ (obtained using for example the LS method) can be regarded as a good initial value $\tilde{\mathbf{X}}_2$ for the second measurement set. Thus a sample $\tilde{\mathbf{v}}_2$, for the vector $\mathbf{v}_2$, can be easily created (according to Eq. (7)). One can now consider a limitation of the sample to only such elements that correspond with measurements concerning the parameter $[\mathbf{X}_2]_k$. Such sample can be denoted as $\tilde{\mathbf{v}}_2^k = [\tilde{v}_1^k, \tilde{v}_2^k, ..., \tilde{v}_l^k]^T$ (l is a number of observations concerning $[\mathbf{X}_2]_k$). Without losing generality, one can assume that all l elements of the vector $\mathbf{x}_2$ that were the basis for the computation of $\tilde{\mathbf{v}}_2^k$ are direct measurements of the kth point height. Thus $E([\mathbf{x}_2]_j) = E([\mathbf{X}_2]_j)$ (where $1 \le j \le l$). Since additionally $[\tilde{\mathbf{X}}_2]_k = [\hat{\mathbf{X}}_1]_k$ then

$$\hat{E}^R([\mathbf{X}_2]_k - [\mathbf{X}_1]_k) = \hat{E}^R([\mathbf{x}_2]_k - [\hat{\mathbf{X}}_1]_k) = \hat{E}^R(\tilde{v}^k)$$

can be regarded as an R-estimator of the vertical displacement of the respective network point. The value $\hat{E}^R(\tilde{v}^k)$ can be computed applying the formula (5)

$$\hat{E}^R(\tilde{v}^k) = \operatorname{med}\left[\frac{1}{2}\left([\tilde{\mathbf{v}}]_i^k + [\tilde{\mathbf{v}}]_j^k\right)\right] \tag{10}$$

In theory, such displacement estimator has all properties of R-estimators for example it is robust for outliers (as it was mentioned in the previous section the estimator is robust if $l \ge 5$).

The presented way of estimation is a good solution if reference marks are stable (or if only a few marks are not, taking into account robustness of the method). All reference marks cannot be guaranteed to be stable before such stability is controlled, i.e., before pointing out stable reference framework (what is the main task of monitoring process). Thus, the estimator Eq. (10) is not a good solution for stability monitoring problem. In such problem, it is also better to compare "raw" observation sets from two epochs than to use estimators $\hat{\mathbf{X}}_1$ from the first one (if $\tilde{\mathbf{X}} \neq \hat{\mathbf{X}}_1$ then one can avoid "bad" influences of observations that do not concern a particular reference mark). For such reasons, the estimator Eq. (4) seems to be the best application of R-estimation in a stability monitoring process. Thus one should create two samples $\tilde{\mathbf{v}}_1^k$ and $\tilde{\mathbf{v}}_2^k$ for all particular reference marks and for each epoch, respectively. The initial values $[\tilde{\mathbf{X}}]_k$ can be computed on the base of the first observation set taking into account only observations that correspond to the elements of $\tilde{\mathbf{v}}_1^k$. The shift Δ_k between the mentioned samples, which can be regarded as a vertical displacement of the reference mark, can be estimated applying the formula Eq. (4) written in the more convenient, following form

$$\hat{\Delta}_k^R = \text{med}\ ([\tilde{\mathbf{v}}_2^k]_i - [\tilde{\mathbf{v}}_1^k]_j) \tag{11}$$

where $1 \leq i \leq l$, $1 \leq j \leq l$. Such computed shifts can be a basis for pointing out stabile reference framework. Reference marks can be regarded as stabile if respective estimated shift is inside of the interval assumed for random errors.

Numerical Examples

Example 1

Let us consider a leveling network that consists of three reference marks A, B, C where $H_A = 1000$ [m], $H_B = 2000$ [m], $H_C = 3000$ [m] and one unknown point 1 (it can be also regarded as a part of a bigger leveling network). Let three height differences (between each reference mark and the unknown point) be measured and let the measurement be carried out two times in two different epochs. Let

$$\mathbf{x}_1^T = [2.9990 \quad 1.9997 \quad 1.0013]_{[\text{m}]}$$

be a vector of the first measurement results (it is simulated under assumption that standard deviation of measurement $\sigma = 0.001$ [m] and results are normally distributed). Thus it can be computed $\hat{H}_{1I}^{LS}$. Let now

$$\mathbf{x}_2^T = [3.0140 \quad 2.0155 \quad 1.0158]_{[\mathrm{m}]}$$

be results of the second measurements (it is assumed that the vertical displacement of the point 1 is equal to 0.015 [m]; still $\sigma = 0.001$ [m]). The mentioned vertical displacement can be estimated applying Eq.(10) and one can obtained

$$\hat{E}^R([\mathbf{X}_2]_1 - [\mathbf{X}_1]^1) = \hat{E}^R(\tilde{\mathrm{v}}^1) = 0.0149 \text{ [m]}$$

The value presented here is very close to the true one 0.015 [m]. The displacement can be of course estimated applying the classical LS method. Then it can be calculated $\Delta\hat{H}_1^{LS} = 0.0151$ [m] which is also a good assessment of the true displacement (the difference between those two estimates cannot be big since the sample is very small and the observation sets are free of outliers (ROUSEEUW, VERBOVEN 2002, DUCHNOWSKI 2008)).

Let now the first observation in the vector $\mathbf{x}_2$ be disturbed with a gross error $g_1 = 0.02$ [m]. Then $\mathbf{x}_2^T = [3.0340 \quad 2.0155 \quad 1.0158]_{[\mathrm{m}]}$, and the presented displacement estimators can be computed as $\hat{E}^R(\tilde{\mathrm{v}}^1) = 0.0248$ [m] and $\Delta\hat{H}_1^{LS} = 0.0218$ [m], i.e., they both failed (the R-estimator failed because the sample is too small ($l = 3 < 5$); the LS estimator since that kind of estimates are not robust for outliers in general). However there is another way to estimate the displacement. One can consider the "raw" sets $\mathbf{x}_1$ and $\mathbf{x}_2$ and apply the R-estimator from Eq. (11). Then $\hat{\Delta}_1^R = 0.0165$ [m] which is much better assessment of the displacement (one can mention that for the original, not disturbed, observation set $\mathbf{x}_2$ it is $\hat{\Delta}_1^R = 0.0150$ [m]). What is more, if $g_1 = 0.10$ [m] then it is still $\hat{\Delta}_1^R = 0.0165$ [m] (in contrast, and $\hat{E}^R(\tilde{\mathrm{v}}^1) = 0.0648$ [m] and $\Delta\hat{H}_1^{LS} = 0.0484$ [m].

Example 2

Let us consider a leveling network established for detection of vertical displacements. Let the network contains four reference marks and let stability of those marks be controlled. Let all height differences between the reference marks be assumed as normally distributed with $\sigma = 0.001$ [m] and let they be measured twice. If the first and the fourth reference marks moved vertically and the displacement values are assumed as $\delta_1 = 0.025$ [m] and $\delta_4 = 0.005$ [m] respectively, then two measurement results can be simulated as follows.

$$\mathbf{x}_1 \begin{bmatrix} 0.9984 \\ 1.9994 \\ 0.9983 \\ -0.0001 \\ 1.0002 \\ 0.9999 \end{bmatrix}_{[\mathrm{m}]}, \mathbf{x}_2 = \begin{bmatrix} 0.9742 \\ 1.9716 \\ 0.9742 \\ 0.0008 \\ 0.9959 \\ 0.9965 \end{bmatrix}_{[\mathrm{m}]}, \text{ and } \mathbf{A} = \begin{bmatrix} -1 & 1 & 0 & 0 \\ -1 & 0 & 0 & 1 \\ -1 & 0 & 1 & 0 \\ 0 & 1 & -1 & 0 \\ 0 & -1 & 0 & 1 \\ 0 & 0 & -1 & 1 \end{bmatrix}$$

To find out the stabile reference framework one can eliminate those reference marks which moved vertically. Such movements (displacements) can be estimated with the R-estimator Eq. (11) (the vectors $\tilde{\mathbf{v}}_1^k$ and $\tilde{\mathbf{v}}_2^k$ (for k = 1, 2,..., 4) can be created taking initial values $[\tilde{\mathbf{X}}]_k$ computed, for example, on the basis of the first observation set). Thus it can be computed that

$$\hat{\Delta}_1^R \begin{bmatrix} \hat{\Delta}_1^R \\ \hat{\Delta}_2^R \\ \hat{\Delta}^R \\ \hat{\Delta}_4^R \end{bmatrix} = \begin{bmatrix} 0.0251 \\ 0.0010 \\ -0.0008 \\ -0.0043 \end{bmatrix}$$

The obtained values of displacements are close to the assumed ones (as for the first and the fourth points). Taking into consideration the accuracy of the measurement ($\sigma = 0.001$ [m]) those two points cannot be regarded as stabile. It should be pointed out that also that time the R-estimator (11) shows its robustness (since two network points are assumed to be displaced vertically some results can be regarded as outliers).

The example presented above is rather simple but it illustrates the general idea of R-estimation application to monitoring of reference mark stability itself. The method is intended to be improved by the author.

Conclusions

R-estimation can be a useful statistical tool in some geodetic problems. It can be an alternative for classical approach to geodetic observation elaboration (e. g., for the LS method). Presented R-estimators Eq. (10) and Eq.(11) can be successfully applied to displacement detection herein leveling networks. As for the robustness against outliers the second estimate seems to be more useful (the first one can also be if only the observation number is high enough).

Acknowledgments

The research is supported by the Polish Ministry of Science and Higher Education under the grant "New methods of estimation of parameters in a functional model of geodetic observations (M_{split} estimation)", no. N N526 255 734.

This paper was presented on 13th FIG Symposium on Deformation Measurement and Analysis and 4th Symposium on Geodesy for Geotechnical and Structural Engineering (Lisbon, 2008 May 12–15).

Accepted for print 22.01.2009

References

CHEN Ch. 2001. *Rank estimating equations for random effects models.* Statistics and Probability Letters, 54, 5–12.

DIONNE L. 1981. *Efficient nonparametric estimators of parameters In the general Linear hypothesis.* The Annals of Statistics, 8(2): 457–460.

DUCHNOWSKI R. 2005. *Proposal of robust method of adjustment based on redundancy matrix application (in polish).* Technical Sciences, Supplement 2: 293–300.

DUCHNOWSKI R., WIŚNIEWSKI Z. 2006. *Attenuation Matrix in Robust, Free Adjustment.* Reports on Geodesy, 2(77): 299–306.

DUCHNOWSKI R. 2008. *R-estimation and its application to the LS adjustment.* Bollettino di Geodesia e Scienze Affini, 1: 21–30.

FELTOVICH N. 2003. *Nonparametric Tests of Differences in Medians: Comparison of the Wilcoxon-Mann-Whitney and Robust Rank-Order Tests.* Experimental Economics, 6: 273–297.

HUBER P.J. 1981. *Robust Statistics.* Willey, New York.

MUKHERJEE K., BAI Z.D. 2001. *R-estimation in Autoregression with Square-Integrable Score Function.* Journal of Multivariate Analysis, 81: 167–186.

NARANJO J.D., MCKEAN J.W. 1997. *Rank regression with estimated scores.* Statistics and Probability Letters, 33: 209–216.

PRÓSZYŃSKI W., KWAŚNIAK M. 2006. *Podstawy geodezyjnego wyznaczania przemieszczeń. Pojęcia i elementy metodyki.* Oficyna Wydawnicza Politechniki Warszawskiej.

ROUSSEEUW P. J., VERBOVEN S. 2002. *Robust estimation in very small samples.* Computation Statistics Data Analysis, 40: 741–758.

XU P. 1989. *On robust estimation with correlated observations.* Bulletin Geodesique, 63: 237–252.

YANG Y. 1994. *Robust estimation for dependent observations.* Manuscripta Geodaetica, 19: 10–17.

TECHNICAL SCIENCES
Abbrev.: Techn. Sc., No 12, Y 2009

DOI 10.2478/v10022-009-0013-8

RELATIONAL DATABASE OF THREE PRECISE LEVELLING CAMPAIGNS IN POLAND

Kamil Kowalczyk, Michał Bednarczyk

Department of Surveying
University of Warmia and Mazury in Olsztyn

Key words: data base, levelling network.

Abstract

Four precise levelling campaigns were carried out in Poland: in 1926–1937, 1953–1955, 1974–1982, 1997–2003. The levelling data from these campaigns is stored in printed catalogues, text files and spreadsheets. A comprehensive analysis of this data requires its compilation in a standardized form (a database). First attempts at the standardization of precise levelling data format date back to 2002 at the University of Warmia and Mazury in Olsztyn (ŁYSZKOWICZ et al. 2002). The authors of this paper, in turn, have collected the complete data from the last three precise levelling campaigns in Poland, which gives an opportunity to standardize the levelling database structure. The subject of the paper is to provide a theoretical background and to offer a relational database of the precise levelling network in Poland, with the data from each campaign. The paper describes the data, database schemas and examples of retrieving information with SQL queries.

RELACYJNA BAZA DANYCH SIECI NIWELACJI PRECYZYJNEJ OBSZARU POLSKI Z KOLEJNYCH KAMPANII

Kamil Kowalczyk Michał Bednarczyk

Katedra Geodezji Szczegółowej
Uniwersytet Warmińsko-Mazurski w Olsztynie

Słowa kluczowe: baza danych, sieć niwelacyjna.

Abstrakt

W Polsce przeprowadzono cztery kampanie niwelacji precyzyjnej: 1926–1937, 1953–1955, 1974–1982, 1997–2003. Materiał niwelacyjny z tych prac jest przechowywany w katalogach papierowych, plikach tekstowych oraz arkuszach kalkulacyjnych. W celu przeprowadzania szerszych analiz tych wyników należy zebrać cały materiał w jednolitej formie (bazie danych). Pierwsze próby ujednolicenia formy przechowywania danych z niwelacji precyzyjnej podjęto na Uniwersytecie Warmińsko-Mazurskim w 2002 roku (ŁYSZKOWICZ i inni 2002). Obecnie nadarzyła się okazja ujed-

nolicenia struktury bazy danych niwelacyjnych dzięki zgromadzeniu przez autorów kompletnego materiału z trzech ostatnich kampanii niwelacji precyzyjnej w Polsce. Przedmiotem niniejszego opracowania było przygotowanie teoretyczne i praktyczne relacyjnej bazy danych sieci niwelacji precyzyjnej obszaru Polski z kolejnych kampanii. Praca zawiera opis danych z poszczególnych kampanii niwelacji precyzyjnej oraz schematy budowy tej bazy, a także przykłady uzyskiwania różnych informacji za pośrednictwem zapytań SQL.

Introduction

The analysis of contemporary vertical crustal movements and their forecasting has long been a focus of interest for geodesists, geologists and geophysicists. These movements result from the changes of the Earth's shape, size and location in space. The changes can be determined on the basis of different measurement data (geological, seismic observation, sea level observation, GPS observation, levelling data). The most precise measurement method is geometric precise levelling.

Precise levelling campaigns are carried out rarely, every 20 years on average. In Poland four precise levelling campaigns took place: in 1926–1937, 1953–1955, 1974–1982, 1997–2003. The data obtained in these campaigns is stored in the Centre for Geodesic and Cartographic Documentation (Centralny Ośrodek Dokumentacji Geodezyjnej i Kartograficznej) in the form of catalogues. The catalogues are analog and/or digital, depending on the available recording possibilities during measurement. A comprehensive analysis of this data requires its compilation in a standardized form (a database). First attempts at the standardization of precise levelling data storage date back to 2002 at the University of Warmia and Mazury in Olsztyn (ŁYSZKOWICZ et al. 2002). This database contained very small data sets from three levelling campaigns. The data was not standardized, mainly due to the different numbering of lines and benchmarks, different levelling routes, different types of adjustments and different storage media (printed documents, text files). During the work on a model of vertical crustal movements in Poland (KOWALCZYK 2006a), the complete data from the last two levelling campaigns (unadjusted height differences without normal corrections) was collected and converted to a common digital form (xls format). The data from 1939 (*Katalog* 1939) and 1960 (*Katalog* 1960) catalogues was also digitized, however it only contained adjusted height differences, which, given the analysis method (KOWALCZYK 2006b), did not provide a suitable levelling data for the research on vertical crustal movements.

The model of vertical crustal movements in Poland (KOWALCZYK 2006a) is a static model. To create a kinematic model requires the data from at least three levelling campaigns. Therefore, the goal of the work presented in this paper has been to collect this data, standardize it, and place it in one common

levelling database, as well as to organize the database optimally for the aforementioned purpose.

An important part of the research into crustal vertical movements is data without normal corrections and unadjusted data. Unfortunately, the records from the first and second precise levelling campaigns do not contain such data. In 2008, courtesy of the personnel of the Centre for Geodesic and Cartographic Documentation in Warsaw, unadjusted data from survey logs from the second precise levelling campaign was obtained. This created an opportunity to standardize the database structure of the three campaigns. While merging the data from 1974–1982, 1997–2003 did not constitute a major problem (similar work had been carried out in the Centre (SEKOWSKI 2005)), standardizing all three campaigns was a serious challenge both logistically and in terms of programming. The paper describes the available levelling data, presents the existing source data sets which contain the levelling data and describes the problems faced in the standardization process. As a result, a complete database has been created, containing unadjusted results from three levelling campaigns: 1953–1955, 1974–1982, 1997–2003. This data will allow in a near future to determine a kinematic model of vertical crustal movements in Poland. Currently, work is in progress on augmenting the database with results from the first precise levelling campaign in Poland, which took place before the World War II.

Levelling data

Levelling campaign of 1926–1937

Class I levelling network from 1926–1937 was referenced to a tide gauge in Gdynia, built in 1931. The lines were designed along class I roads, and sometimes along rail road tracks (WYRZYKOWSKI 1988).

Table 1

Geometric specifications of the 1926–1937 network

Line length [km]	Number			Mean length [km]		
10 046	traverses n_F	lines n_L	sections n_R	Loop F	line L	sections R
	36	121	5 907	445	83	1.7

The survey was conducted with Zeiss precise levels, type III, with optical flat, telescope 35× and reversible level 8''–10''/2 mm. 3-metre levelling rods with 2 graduation lines on an invar tape were used (RANIECKI 1932).

The measurements were taken with the telescope in the horizontal position, using "from the middle" method, with aiming line distance 50 m. The results were adjusted using two criteria. The first criterion determined the maximal deviation of height difference between two points in two measurements, the second criterion determined the maximum mean error for 1 km of the levelling line.

Results were adjusted for levelling rods' systematic errors and with normal orthometric corrections. Before adjustments mean error for the whole network was estimated and the results are shown in Table 2.

Table 2

Mean error before adjustment, mean probable errors, mean error after adjustment (survey 1926–1937) [mm/km]

Mean error before adjustment			Mean errors		Mean error after adjustment
			random	systematic	
m_1	m_2	m_3	η	m_0	m
±0.45	±0.73	±1.04	±0.31	±0.05	±1.04

Legend:
m_1 – mean deviation for two measurements between two points, m_2 – mean deviation for two line measurements, m_3 – mean traverse perimeter error, mean probable errors were calculated with Lallemand's formulae.

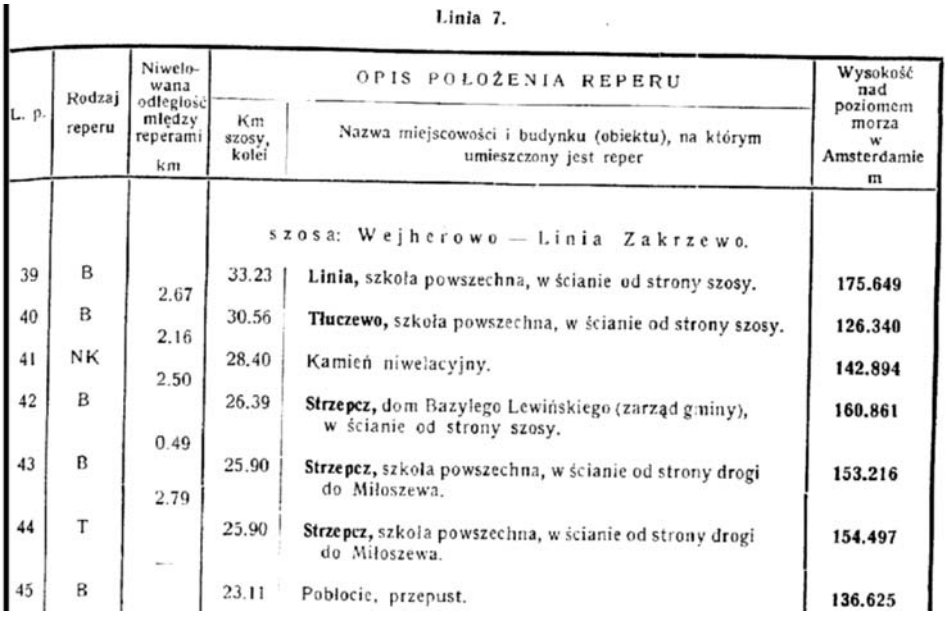

Linia 7.

L. p.	Rodzaj reperu	Niwelowana odległość między reperami km	OPIS POŁOŻENIA REPERU: Km szosy, kolei	OPIS POŁOŻENIA REPERU: Nazwa miejscowości i budynku (obiektu), na którym umieszczony jest reper	Wysokość nad poziomem morza w Amsterdamie m
			szosa: Wejherowo — Linia Zakrzewo.		
39	B	2.67	33.23	**Linia,** szkoła powszechna, w ścianie od strony szosy.	**175.649**
40	B	2.16	30.56	**Tłuczewo,** szkoła powszechna, w ścianie od strony szosy.	**126.340**
41	NK	2.50	28.40	Kamień niwelacyjny.	**142.894**
42	B	0.49	26.39	**Strzepcz,** dom Bazylego Lewińskiego (zarząd gminy), w ścianie od strony szosy.	**160.861**
43	B	2.79	25.90	**Strzepcz,** szkoła powszechna, w ścianie od strony drogi do Miłoszewa.	**153.216**
44	T	—	25.90	**Strzepcz,** szkoła powszechna, w ścianie od strony drogi do Miłoszewa.	**154.497**
45	B		23.11	Pobłocie, przepust.	**136.625**

Fig. 1. Sample page from the 1929 catalogue

Thereafter the network was adjusted using conditional method. The so called Normal-Null (N.N.) datum was selected as the benchmark for the height of network points. The height of network benchmarks was referenced to the so called Normal-Null (N.N) datum, i.e. the Normal Amsterdam Level. For network adjustment, the height of an old first order German benchmark, located on a town hall wall in Torun (m) was selected.

The final results were collected in a catalogue of points in a first order levelling network (*Katalog* 1939). For each line the following were given: type and description of benchmarks' location, distances between them, and their height with an accuracy of 1 mm. The catalogue of the levelling campaign 1926-1937 has a traditional, printed form (*Katalog* 1939). The author obtained a copy (Fig. 1) of this catalogue from the Topography Board of the Polish Army (350 scanned images). 292 pages of the catalogue were converted, resulting in 121 spreadsheet pages (xls).

Levelling campaign of 1953–1955

The main factors considered in the design of this campaign's first order levelling network were good stabilization and the possibility of using the already present network elements. The geometric specifications of the network are shown in table 3. The first order levelling network was initially not referenced to Polish tide gauges on the Baltic coast. This was done several years later, by means of second order levelling lines (WYRZYKOWSKI 1993).

Table 3

Geometric specifications of the 1952–1955 network

Line length [km]	Number			Mean length [km]		
5 778	traverses n_F	lines n_L	sections n_R	Loop F	line L	sections R
	12	60	about 4500	609	96	1.3

Measurements for this network were taken using precise levels such as Aerogeopribor NA – 1, with telescope 44×, reversible level 10''/2 mm, with optical flat and an elevation screw, or Wild N III with similar specifications, telescope 44×, reversible level 6''/2 mm. In both cases 3-metre wooden levelling rods were used, with an invar tape with 2 graduation lines displaced against each other. The measurements were carried out using "from the middle"

method, with the maximum length of the horizontal aiming line 40 m. The measurement results were adjusted for levelling rods' systematic errors and, in the first stage (i.e. preparation for the independent adjustment), normal orthometric corrections. In the second stage, i.e. preparation of Polish data for the joint adjustment of the international network, normal corrections were introduced (WYRZYKOWSKI 1988). Mean error of the network before adjustment was also estimated using Lallemand's formulae and the results are shown in Table 4.

Table 4

Mean error (1953–1955 survey) [mm/km]

Mean probable error		Mean error after adjustment
random	systematic	
η	m_0	m
±0.37	±0.13	±0.78

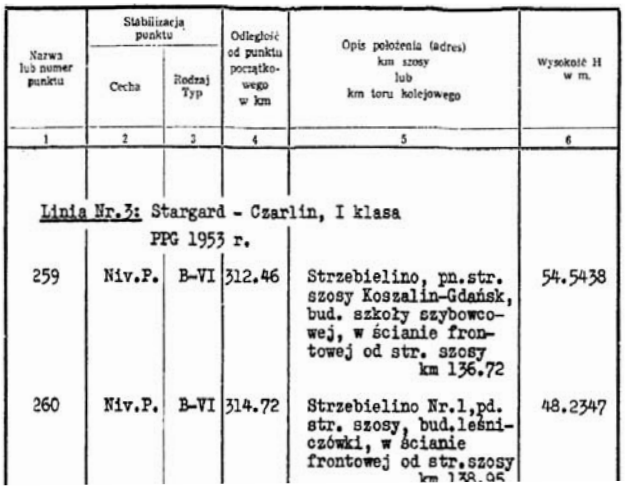

Nazwa lub numer punktu	Stabilizacja punktu: Cecha	Stabilizacja punktu: Rodzaj Typ	Odległość od punktu początkowego w km	Opis położenia (adres) km szosy lub km toru kolejowego	Wysokość H w m.
1	2	3	4	5	6
Linia Nr.3: Stargard - Czarlin, I klasa PPG 1953 r.					
259	Niv.P.	B-VI	312.46	Strzebielino, pn.str. szosy Koszalin-Gdańsk, bud. szkoły szybowcowej, w ścianie frontowej od str. szosy km 136.72	54.5438
260	Niv.P.	B-VI	314.72	Strzebielino Nr.1,pd. str. szosy, bud.leśniczówki, w ścianie frontowej od str.szosy km 138.95	48.2347

Fig. 2. Sample page fragment from the 1960 catalogue

The adjustment was calculated twice. The first adjustment was based on – as in the previous network – the height of Torun – Townhall benchmark, referenced to Normal Amsterdam Level. The second adjustment was based on the zero point of Kronstadt tide gauge (WYRZYKOWSKI 1988). Standard deviation value after adjustment is shown in Table 4.

The results after the second adjustment were accepted as final. The data was collected in a catalogue of levelling points (*Katalog* 1960). The author obtained a copy of this catalogue, about 500 scanned images (Fig. 2) from the Geological Exploration Company in Warsaw, as well as copies of calculation

logs from the archives of the Centre for Geodesic and Cartographic Documentation (about 450 photographs). The data was then digitized into over 60 spreadsheet pages in .xls format, which contain the complete unadjusted levelling data.

Levelling campaign of 1974–1982

The levelling campaign of 1974–1982 was carried out in two stages. The first stage was a survey in 1974–1979, part of the network was then merged with the Unified Vertical Reference Network. The second, complementary survey, took place in 1980-1982. The geometric specifications of the network are shown in Table 5.

Table 5

Geometric specifications of the 1974–1979 network

Line length [km]	Number			Mean length [km]		
10 438	traverses n_F	lines n_L	sections n_R	traverse perimeter F	line L	sections R
	47	173	ok. 9700	354	64	1.1

For the first time the measurements were taken using self levelling levels. Initially, Opton levels type Ni 1, made in West Germany, were used, but in 1977 they were replaced with Zeiss levels type Ni 002, made in East Germany. In the case of Ni 1, 3-metre wooden levelling rods with an invar tape with 1 cm graduation were used, in the case of Ni 002 – similar levelling rods, with 2 graduation lines of 0.5 cm displaced against each other. The following adjustments were made: temperature adjustment and the adjustment for the levelling rods' systematic errors; for daily changes of the vertical caused by the Moon and the Sun; and normal adjustments (I and II). First order levelling network was directly referenced to seven Polish tide gauges: in Swinoujscie, Kolobrzeg, Ustka, Leba, Wladyslawowo, Hel and Gdansk – Nowy Port. Mean error before adjustment and mean error after adjustment are shown in Table 6.

Table 6

Mean error before adjustment, random and systematic mean errors and mean error after adjustment (1974–1979 survey) [mm/$\sqrt{\text{km}}$]

Mean error before adjustment			Mean errors		Mean error after adjustment
			random	systematic	
m_1	m_2	m_3	η	m_0	m
±0.29	±0.55	±0.94	±0.28	±0.09	±0.91

* before levelling correction

A supplemental survey was carried out in the years 1980–1982. The measurement method and the equipment remained the same. Also, the same adjustments were made as in 1974–1979. Specifications of the network are shown in Table 7.

Table 7

Geometric specifications of the 1980–1982 network

Line length [km]	Number			Mean length [km]		
17 015	traverses n_F	lines n_L	sections n_R	traverse perimeter F	line L	sections R
	135	371	15 827	221	46	1.1

Mean error before adjustment, mean probable error and mean error after adjustment are shown in Table 8.

Table 8

Mean error before adjustment, mean probable error, mean error after adjustment (1980–1982 survey) [mm/$\sqrt{\text{km}}$]

Mean error before adjustment			Mean errors		Mean error after adjustment
			random	systematic	
m_1	m_2	m_3	η	m_0	m
±0.29	±0.53	±0.92	±0.28	±0.08	±0.84

* before levelling correction

The data from 1974–1982 campaign are stored in a digital form (Fig. 3). They were obtained from the Centre for Geodesic and Cartographic Documentation in Warsaw andconverted into 376 spreadsheet pages (Fig. 4).

```
==========================================================================
|Lp | Nr punktu |  [R]  |Przew.popr.| PN I  | PN II | Wysokosc |Sr.bl.wys.|
|   |-----------------------------------------------------------------|
|   | Rodzaj    |  Typ  | Kod stab. |Glowica| Grupa |  Wsp. X  ,  Wsp. Y  |
|   |-----------------------------------------------------------------|
|Opis  polozenia  punktu                                                 |
==========================================================================
| 25|   30530022|  22.59|    1.50182|     -4|      1|   28.5995|     0.000|
|   |B          |VIA    |870        |AP 6105|A      | 6132550.0, 3591000.0|
|SWARZEWO,NR 185,BUD.MSZK.A.GAPPA,KM 21.05
|-------------------------------------------------------------------------|
| 26|   30530023|  23.39|   -5.37329|     -2|     -2|   23.2262|     0.000|
|   |BK         | IV    |713        |AB 2807|A      | 6133350.0, 3591050.0|
|WLADYSLAWOWO,KAM.NIW.PODZ.NA MIEDZY J.GALA I STRUGA,KM 21.801
|-------------------------------------------------------------------------|
| 27|   30530024|  24.39|   -7.71709|     -1|     -2|   15.5091|     0.000|
```

Fig. 3. Sample text file with the data from the 1974–1982 campaign

A	B	C	D	E	F	G	H	I	J	K
nr linni	lp	nr punktu	R w km	dh+popr N	popr N 1	popr N 2	dh	H wyrównane	średni błąd	rodzaj stabilizac
1	1	31340032	0	0	0	0	0	20.4037	8.4	F
1	2	31340077	0.62	-2.77415	-1	-5	-2.77409	17.6296	0	B
1	3	31340078	0.81	0.97048	0	2	0.97046	18.6	0	B
1	4	31340079	1.26	-0.203	0	0	-0.203	18.397	0	B
1	5	31340080	1.96	0.56443	0	1	0.56442	18.9615	0	B
1	6	31340081	2.82	-1.13962	-1	-2	-1.13959	17.8218	0	B
1	7	31340082	3.08	1.68817	0	3	1.68814	19.51	0	B
1	8	31320010	3.59	8.00282	-1	16	8.00267	27.5128	0	B
1	9	31320011	5.33	-5.57143	-2	-11	-5.5713	21.9414	0	B
1	10	31320012	5.51	4.21671	0	9	4.21662	26.1581	0	B
1	11	31320013	6.41	15.23723	-2	34	15.23691	41.3953	0	BK
1	12	31320014	6.7	-0.57919	-1	-1	-0.57917	40.8162	0	BK
1	13	31320015	7.5	-11.41717	-2	-27	-11.41688	29.399	0	BK
1	14	31320016	8.52	-3.53707	-2	-8	-3.53697	25.8619	0	BK
1	15	31320017	8.76	-0.28072	0	0	-0.28072	25.5812	0	BK
1	16	31320018	9.6	-6.12983	-1	-15	-6.12967	19.4514	0	B
1	17	31320019	11.63	-1.06308	-1	-3	-1.06304	18.3883	0	BK
1	18	31320020	12.13	4.38638	-1	12	4.38627	22.7747	0	BK
1	19	31320021	12.45	0.78761	-1	2	0.7876	23.5623	0	BK
1	20	31320022	12.49	-0.83638	0	-2	-0.83636	22.7259	0	BK
1	21	31320023	13.43	-6.55388	0	-19	-6.55369	16.172	0	B
1	22	31320024	14.77	-5.6105	-1	-17	-5.61032	10.5615	0	B
1	23	31320025	15.43	7.86364	0	25	7.86339	18.4252	0	BK
1	24	31320026	16.81	-2.67338	0	-8	-2.6733	15.7518	0	B
1	25	31320027	17.86	-9.53487	-1	-33	-9.53453	6.2169	0	B
1	26	31320028	19.33	-4.50539	0	-16	-4.50523	1.7115	0	BK
1	27	31320029	19.37	2.57364	0	9	2.57355	4.2852	0	B
1	28	31320030	20.01	-0.78918	0	-3	-0.78915	3.496	0	B
1	29	31320031	20.05	-0.30177	0	-1	-0.30176	3.1942	9.21	B

Fig. 4. Sample of converted data from the 1974–1982 campaign

Levelling campaign of 1997–2003

The measurements for the 1997–2003 were taken between April 1999 and June 2002. Incorporated into the network was also the line measured in May and June 1997 and October 2003. The measurements were mainly carried out along the same lines as in 1974–1982, with minor modifications. A number of reference benchmarks were stabilized in different places, most of them near Wroclaw, Lublin and Grudziadz. Polish levelling network was connected with the neighbouring countries' networks via 28 reference benchmarks. The network includes 8 Polish EUVN points (European Vertical Reference Network), as well as major tide gauges on the Polish coast: in Swinoujscie, Kolobrzeg, Ustka, Leba and Wladyslawowo. The first order precise levelling network was measured using self levelling Zeiss Ni002 levels (about 66% of the network), and digital self levelling Zeis DiNi11 levels (about 31%) and Topcon levels (about 3%) (ŁYSZKOWICZ, JACKIEWICZ 2005). Network specifications are shown in Table 9.

Table 9

Geometric specifications of the 1997–2003 network

Line length [km]	Number			Mean length [km]		
17 516	traverses n_F	lines n_L	sections n_R	traverse perimeter F	line L	sections R
	138	382	16 150	217	45.8	1.085

Parametric method was used for network adjustment (GAJDEROWICZ 2005). All measurements were carried out in two stages. In the first stage error equations were formed for each line's height differences, with the calculated parameters being heights of nodal points. In the second stage, adjustments were calculated for the heights of benchmarks in each line, separately for every line. The values of mean errors obtained in this way (ŁYSZKOWICZ, LEONCZYK 2005) are shown in Table 10.

Table 10

Mean error before adjustment, mean probable error, mean error after adjustment (survey 1997–2003) [mm/$\sqrt{\text{km}}$]

Mean error before adjustment			Mean probable error			Mean error after adjustment
			random	systematic		
				for lines	for traverses	
m_1	m_2	m_3	η	m_0	σ	m
±0.28	±0.52	±0.83	±0.26	±0.08	±0.10	±0.88

Data structure

In order to standardize the data from the levelling campaigns, the information has been compared with respect to whether it is present in the catalogues available to the author. Each catalogue contains slightly different data. Table 11 shows the structure of the available data from each levelling campaign.

The following measurement dates have been adopted:
- in campaign 4 the table information,
- in campaign 3 mean measurement date, converted to decimal,
- in campaign 2 year of measurement as given in the catalogue, plus half a year (which reduces measurement difference to a maximum of 5 months),
- in campaign 1 year of measurement as given in the catalogue, plus half a year (which reduces the measurement difference to a maximum of 5 months).

Accuracy of the measurement date in campaign 4 was 1 day; in campaign 3 (accuracy 1 month) in the date conversion to decimal the following convention was adopted:

– for even months – 15th day of the month,

– for odd months – 30th day of the month.

Example:

– measurement date between 11.1978 and 12.1978 – adopted date 30.11.1978 = 1978.92,

– measurement date between 10.1978 and 12.1978 – adopted date 15.11.1978 = 1978.88.

Table 11

Content of the catalogues and survey logs

Specification	Campaign 1 1926–1937	Campaign 2 1953–1955	Campaign 3 1974–1982	Campaign 4 1997–2003
Normal correction				
Line number				
Benchmark number				
Benchmark type				
Section length				
Mileage				
Head				
Benchmark height				
Description				
Coordinates		Sporadically		
Adjusted height difference				
Unadjusted height difference plus levelling rod adjustment				
Atrtribute				
Measurement date				
Benchmark ID				
Line ID				
Stabilization code				
Group				

Relational database concept for levelling campaigns

Analog data – converted to a digital form – together with the data from campaign 4 were used to create a standardized relational database. The database created in such a way integrates campaigns 2, 3 and 4. For each campaign the data collected is structured differently. The first version of the database was designed to make comparisons between campaigns possible without major modifications to the structure of the data. The design ensures

scalability as well, so that the database can be expanded in the future with the data from the missing campaign 1, future campaigns or by adding attributes to objects such as points or lines. This gives a data set which makes a wide range of analyses possible and at the same time is easy to modify.

The analysis of the collected data, at the stage of designing entities and determining relationships for the subsequent database design, was based on characteristic properties of these data sets. Topological relationships between nodes and edges, as well as time of measurement, were considered most significant differentiating attributes. However, the way the data from survey logs is recorded directly into database tables makes the nodal points appear in the database several times – depending on how many lines starts and ends at a given nodal point. Moreover, most benchmarks are the shared by different campaigns. A simple arrangement of this data in a common set causes redundancy. So, first of all, some data is redundant – the information related to reference points is unnecessarily repeated. Secondly, this may cause anomalies during modification – a change or an update will necessitate changes in all records related to a given point. On one hand it overworks the system, on the other it may cause loss of data integrity. It may also cause deletion anomalies – the deletion of the line containing a given point will also delete the information about the point.

Based on the above reasoning, the following tables have been designed: points, lines, sections and benchmarks. Table *punkty* (points) contains the data on all the levelled points. Table *linie* (lines) contains the data on the levelling lines. Table *repery* (benchmarks) contains the data on the adjusted heights. Each line consists of a starting point and the end point. Table *odcinki* (sections) contains the data on sections within the lines. Each section has a starting point and the end point, and is assigned to a levelling line. Measurement time is divided between levelling campaigns. Each campaign took place in a certain time span; in the first version of the database this gave rise to three separate tables for lines, sections and heights adjusted in each campaign. Table names include the appropriate campaign number (e.g. *linie2* – lines from campaign no. 2, *sections3* – sections from campaign no. 3, *repery4* – adjusted heights from campaign no. 4). There is one table *points*, common for all the campaigns. This is the first version of the database. By analogy to the object-oriented approach, one can treat *punkty*, *linie* and *odcinki* tables as containing objects. Class names of these objects are identical with the table names. The objects have descriptive attributes, graphic attributes and topology. Descriptive attributes are recorded in the columns, graphic attributes are the points' coordinates and the topology is the aforementioned relationships between lines, sections and points. These relationships have been physically created by assigning each point's identifier to the lines and sections which

contain the point. In the relational model adopted here, these are equivalent to relationships between tables.

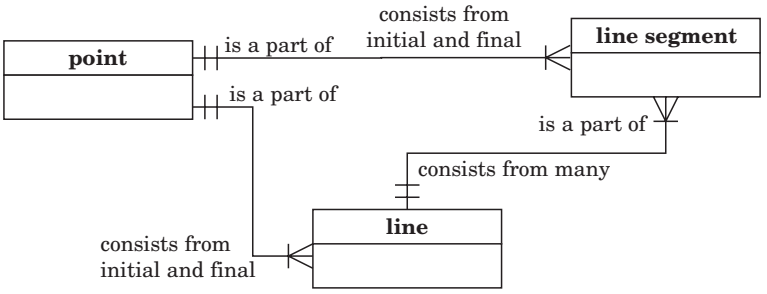

Fig. 5. Relationships between entities

The separation of the data into campaigns, as described above, makes it easier to remove information from data sets without the necessity to modify the original structure, based on the source catalogues. It is a good solution, especially for demonstration purposes – for viewing and analysing the data from each campaign separately. For analyses comprising all the campaigns simultaneously, joining the tables containing objects of the same class may be more practical. This will produce e.g. one table *linie*, by joining three tables for separate campaigns: *linie2*, *linie3*, *linie4*. Tables containing sections should be treated similarly. In order to be able to differentiate the objects from different campaigns, they should be assigned an additional attribute: campaign number. For example, each line, apart from the attributes such as line number, starting point and end point, should also be assigned the number of the campaign during which it was measured. This method has been used to produce the second version of the database.

Table joining gives access to all the campaigns simultaneously with one simple query. In the first version, obtaining information from all three campaigns required at least three queries – for each table, or, in some cases, using a join. It is easier in the first version to add or remove a whole campaign, irrespectively of the data set structure. Only minimal requirements on the data integrity must be met – the proper assignment of point and line identifiers. There are no constraints on other attributes. In the second version, the addition of a new campaign necessitates adding new columns, which contain attributes specific only for a given campaign. In this situation, records from these columns in other campaigns will remain empty. The only solution is to select a set of attributes common to all campaigns. This however entails a loss of some data, which is undesirable.

Generally, the first version is better optimized for performance – the data is divided into smaller parts, which often speeds up searching. There are no

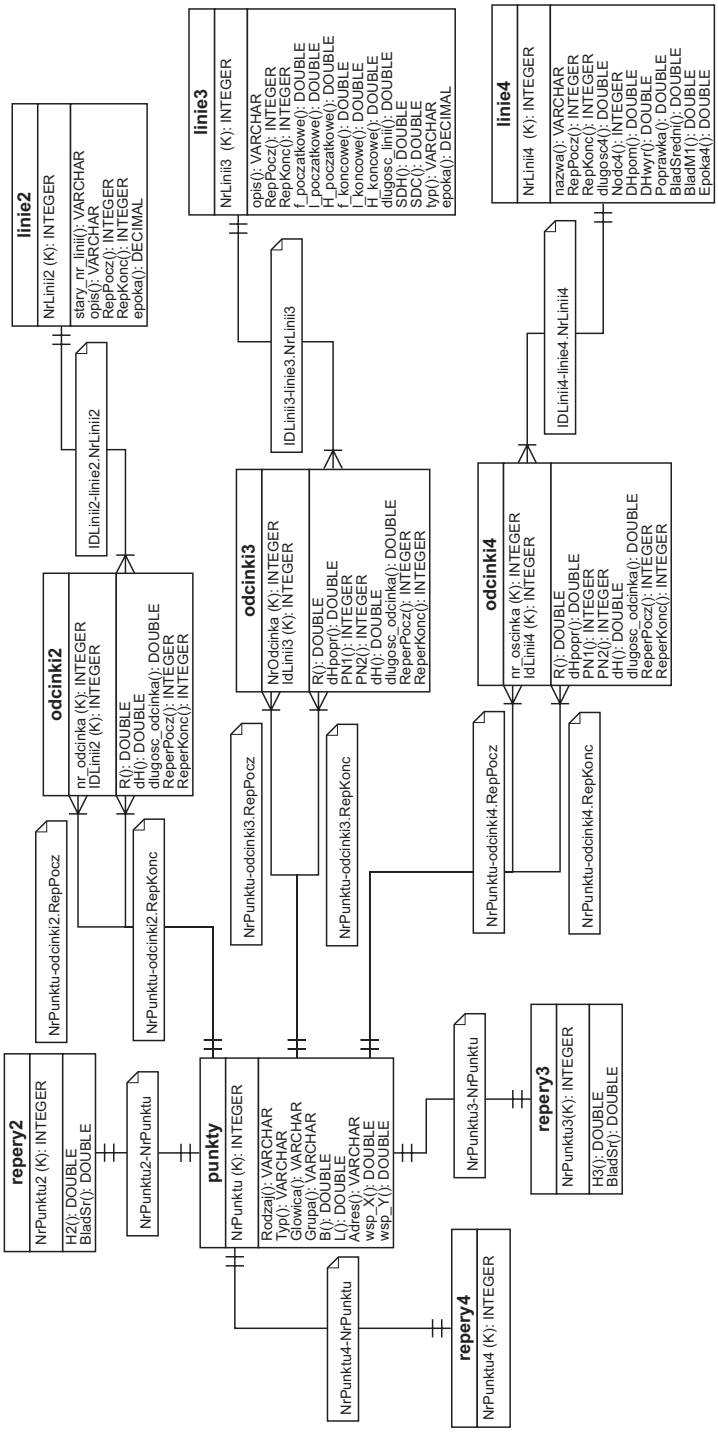

Fig. 6. First version of the database schema

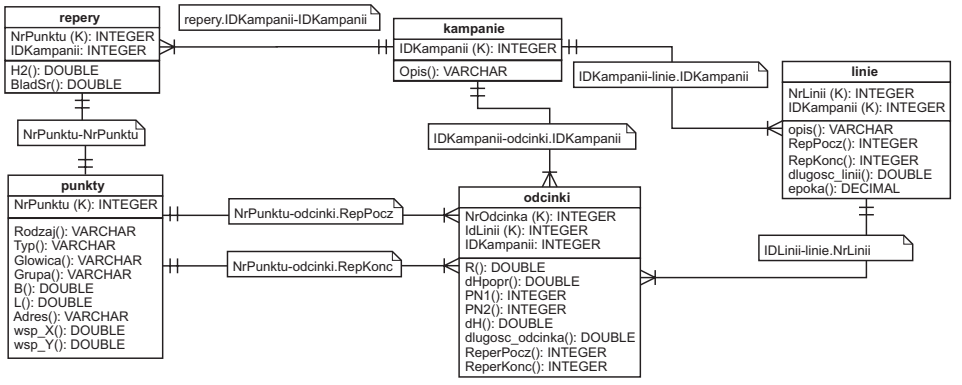

Fig. 7. Second version of the database schema

redundant records and the campaign information can be easily placed in a structure similar to the original. SQL queries for this structure are usually fairly complex, but in some cases (example 2 and 2a in the chapter *Using the database*) they can be simpler than in the second version. The second version of the database is better optimized for functionality. First of all, joining the data in a large set makes it possible to build simpler and more intuitive queries, although examples 2 and 2a below show that it is not always the case. On the other hand, joining the data and the creation of redundant records associated with this procedure (a result of joining sets of different structures), slows down searching, which is also evident in the discussed examples. Both database structures – first and second – have their advantages and drawbacks, which result from technological possibilities and limitations, as well as the limitations of relational databases.

Currently there are two versions of the database schema. The logical division of the data set into entities is identical for both versions. The basic difference in the physical build of the databases is – as described above – joining of benchmark, section and line tables respectively, as well as the introduction of an additional table *kampanie* for campaigns in the second version. Which version is optimal for future vertical movements research is yet to be determined.

Data transfer

The next step after the database design is creating a physical database. The procedure described in this chapter has been applied to the first version of the database schema. The second version was created by conversion of the first version (imported and controlled).

The database schema can be implemented in any relational database management system. At this stage, the most important task was to transform the source data sets to a form which could be used in the schema. the original data was initially digitized and saved as MSExcel files. This involved only campaigns 2 and 3 – campaign 4 had already been saved as MSAccess database file. Due to the formatting of the source data, the conversion was carried out in MSAccess system, using MSOffice programming tools, with MS Visual Basic for Applications as the programming language. All the procedures performed on the database during conversion were automated, which means that the import of data for the schema is a repeatable process.

The first step was the import of data to MSAccess system, for each campaign in the form of two tables: *Kampania* and *linie*. The former contains the information about all the reference points measured during the campaign, placed in lines, according to the mileage – i.e. in the same way as in the survey log or the catalogue. The latter contains the information about the lines themselves, numbered. In the case of campaign 4 the data was practically ready to import. Campaigns 2 and 3 were formatted in such a way, that each line was in a separate MSExcel spreadsheet page. Therefore, it was necessary to unify the data sets with respect to the type of data and to merge the spreadsheets into one table. Own program was used for this purpose, written in MSVBA for Applications.

The second step was to create appropriate tables in the system – SQL queries were used to do that. The next step was to transfer the data from *kampania* table to the structure created. The information on the reference points and sections was transferred to the appropriate tables by means of queries. Table *odcinki* contains additionally section lengths, starting point identifiers, end point identifiers and section numbers within lines. This data was created using a designated program written in MSVBA for Applications.

This stage's work resulted in the database structure described above, filled with the data from each campaign and linked with relationships.

Using the database

The functionality of the database is determined by the possibility to retrieve different information by means of SQL queries. A few examples of such queries are given below. More complex analyses would require dedicated applications utilizing the data from the database.

Example 1. Asking in which lines, of which campaign and in which epochs, point no. 10230015 is a starting point (query for the first version of the database):

```
SELECT nr_punktu, linie2_epoka, linie3_epoka, linie4_epoka,
NrLinii2, NrLinii3, NrLinii4
FROM p_pocz_linii_wszystkie1kampanie
WHERE NrPunktu=10230015;
```

Result:

nr_punktu	linie2.epoka	linie3.epoka	linie4_epoka	NrLinii2	NrLinii3	NrLinii4
10230015		1976,33	2001,55		42	249
10230015		1978	2001,55		180	249
10230015		1976,33	2001,62		42	248
10230015		1978	2001,62		180	248

Fig. 8. Result of SQL query for the first version of the database – example 1

The query is based on the query: *p_pocz_linii_wszystkie_kampanie*, which retrieves the starting points for the lines in all the campaigns. It is a multiple join of table *points* with tables *linie2*, *linie3* and *linie4*:

```
SELECT DISTINCT punkty.*, linie4.epoka, linie2.epoka, linie3.epoka,
linie4.NrLinii4, linie3.NrLinii3, linie2.NrLinii2
FROM ((punkty LEFT JOIN linie4 ON punkty.NrPunktu = linie4.RepPocz)
LEFT JOIN linie2 ON punkty.NrPunktu = linie2.RepPocz)
LEFT JOIN linie3 ON punkty.NrPunktu = linie3.RepPocz
WHERE
(((linie4.epoka) Is Not Null)) OR (((linie2.epoka) Is Not Null))
OR (((linie3.epoka) Is Not Null));
```

Result:

NrPunktu	Rodzaj	Typ	KodStab	Głowica	Grupa	B	L	Adres	wsp_X	wsp_Y	linie2.epoka	linie3.epoka	linie4_epoka
10230015	F	III	700	AA 8920	D	52,25609	19,17286	KROŚNIEWICE	5650150	4506550		1978,13	2001,53
10230015	F	III	700	AA 8920	D	52,25609	19,17286	KROŚNIEWICE	5650150	4506550		1976,92	2001,53
10230015	F	III	700	AA 8920	D	52,25609	19,17286	KROŚNIEWICE	5650150	4506550		1978,13	2001,47
10230015	F	III	700	AA 8920	D	52,25609	19,17286	KROŚNIEWICE	5650150	4506550		1976,92	2001,47
11240014	B	VI	860	AA 8270	D	51,95966	19,3025	OZORKÓW,UL	5616950	4514600		1980,92	2001,55
11240014	B	VI	860	AA 8270	D	51,95966	19,3025	OZORKÓW,UL	5616950	4514600		1978	2001,55
11240014	B	VI	860	AA 8270	D	51,95966	19,3025	OZORKÓW,UL	5616950	4514600		1980,92	2001,55
11240014	B	VI	860	AA 8270	D	51,95966	19,3025	OZORKÓW,UL	5616950	4514600		1978	2001,55
11310027	B	VI	860	AA 7104	D	52,11951	19,95109	ŁOWICZ,UL.AR	5633850	4559450		1976,92	2001,42
11610016	F	II	700	AA 7373	D	52,00105	22,76894	MIĘDZYRZEC I	5621400	4752750	1954,5	1977,33	2001,52
11610016	F	II	700	AA 7373	D	52,00105	22,76894	MIĘDZYRZEC I	5621400	4752750	1954,5	1975,29	2001,52
11610016	F	II	700	AA 7373	D	52,00105	22,76894	MIĘDZYRZEC I	5621400	4752750	1954,5	1977,33	2001,43
11610016	F	II	700	AA 7373	D	52,00105	22,76894	MIĘDZYRZEC I	5621400	4752750	1954,5	1975,29	2001,43
11610016	F	II	700	AA 7373	D	52,00105	22,76894	MIĘDZYRZEC I	5621400	4752750	1954,5	1977,33	2001,52
11610016	F	II	700	AA 7373	D	52,00105	22,76894	MIĘDZYRZEC I	5621400	4752750	1954,5	1975,29	2001,52
11610016	F	II	700	AA 7373	D	52,00105	22,76894	MIĘDZYRZEC I	5621400	4752750	1954,5	1977,33	2001,43
11610016	F	II	700	AA 7373	D	52,00105	22,76894	MIĘDZYRZEC I	5621400	4752750	1954,5	1975,29	2001,43
11620017	F	III	700	AB 1451	D	52,036	23,36788	ZALESIE,PN.S	5626400	4793750		1975,33	2001,55
11710010	F	II	700	AA 7324	D	52,08273	23,61322	TERESPOL,ZA	5632150	4810400	1954,5		
12140013	F	III	700	AA 8158	A			Sieradzul.Sienk	5577600	4474200		1977,33	
12140034	B	VI	860	AJ 4030	D	51,59595	18,73341	SIERADZ,UL.S	5577600	4474200			2001,82
12220037	F	III	700	AA 8449	D	51,73812	19,46392	ŁÓDŹ,PD-WSC	5592050	4525150		1978,04	2001,58
12220037	F	III	700	AA 8449	D	51,73812	19,46392	ŁÓDŹ,PD-WSC	5592050	4525150		1978,62	2001,58

Fig. 9. Result of SQL query *p_pocz_linii_wszystkie_kampanie* – multiple join

Example 1a. This is an example of a query for the second version of the database, which retrieves the same data as in example 1. The query in the second version is much simpler and does not require an additional query joining the data from several tables:

```
SELECT punkty.nr_punktu, linie.IDkampanii, linie.NrLinii, linie.epoka
FROM punkty INNER JOIN linie ON punkty.NrPunktu4 = linie.reppocz
WHERE (((punkty.NrPunktu4)=10230015));
```

Result:

nr_punktu	IDkampanii	NrLinii	epoka
10230015	3	180	1978
10230015	4	249	2001,55
10230015	4	248	2001,62
10230015	3	42	1976,33

Fig. 10. Result of SQL query for the second version of the database – example 1a

Example 2. Retrieval of the points which are present in all the campaigns simultaneously (set intersection) as starting points for lines – query for the first version of the database:

```
SELECT DISTINCT punkty.*
FROM
((punkty INNER JOIN linie2 ON punkty.NrPunktu = linie2.RepPocz)
INNER JOIN linie3 ON punkty.NrPunktu = linie3.RepPocz)
INNER JOIN linie4 ON punkty.NrPunktu = linie4.RepPocz;
```

Result:

NrPunktu	Rodzaj	Typ	KodStab	Glowica	Grupa	B	L	Adres	wsp_X	wsp_Y
11610016	F	II	700	AA 7373	D	52,00105	22,76894	MIĘDZYRZEC PODL.,F.P.W.PRZED WARSZT.SAM.I	5621400	4752750
13430030	F	II	700	AA 7581	D	51,10306	20,8413	SKARZYSKO-KAMIENNA,BZIN,UL.KRAKOWSKA,F.F	5520200	4620050
16330035	F	II	700	AA 6826	D	50,03232	19,9519	KRAKÓW,UL.H.KAMIEŃSKIEGO,F.P.W.PO PN.STR.	5401700	4555950
18310020	F	III	700	AA 9076	D	49,62188	19,95981	RABKA,UL.KRAKOWSKA,F.P.W.OBOK KAPLICZKI,I	5356050	4555829
18310053	F	II	700	AA 6870	D	49,48237	20,03274	NOWY TARG,RYNEK,F.P.W.NA SKWERZE PRZED I	5340459	4560879
18330027	F	II	700	AA 7147	D	49,36551	19,80676	CHOCHOŁÓW,F.P.W.96.3M OD GRANICY PAŃSTW/	5327720	4544285
18410028	F	II	700	AA 7919	D	49,6254	20,94707	GRYBÓW,RYNEK,F.P.W.NA TERENIE ZAKŁADU OF	5355839	4627156
18510012	F	II	700	AA 8286	D	49,6337	21,78654	MIEJSCE PIASTOWE,UL.DUKIELSKA,F.P.W.ZNAK C	5356993	4687793
20230018	F	II	700	AA 7494	D	54,38553	19,83025	BRANIEWO,UL.KRÓLEWIECKA,F.P.W.,NA PLACU F	5961250	4494350
22240019	F	II	700	AA 8096	D	53,77861	20,48704	OLSZTYN,F.P.W.,UL.DĄBROWSZCZAKÓW,NA PLAC	5892900	4536050
26330081	F	I	690	5	D	52,23038	20,95019	W-WA WOLA,UL.WOLSKA,F.P.W.W PARKU IM.SOV	5720300	4565250
32530036	F	II	700	AA 8162	D	54,04825	18,75838	CZARLIN,F.P.W.,PD.STR.SZOSY STAROGARD GDA	6052150	3615600
34140026	B	VI	880	NIV.P.	D	53,33714	15,04798	STARGARD SZCZECIŃSKI,UL.MARIACKA,KATEDRA	5973400	3370450
41140018	B	VI	880	NIV.P.	D	52,59991	15,50315	SKWIERZYNA,RYNEK,BUD.URZĘDU MIASTA I GMIN	5731000	3623800
42440019	F	II	700	AA 7912	D	52,23003	18,23127	KONIN,UL.POZNAŃSKA,F.P.W.,PN.STR.ULICY,PRZ	5690350	3809500
42440034	F	II	703	AA 8089	D	52,20902	18,25615	KONIN,UL.3-GO MAJA,F.P.W.,NA PLACU KOŚCIOŁA	5688050	3811250
43140020	F	II	700	AA 8852	D	51,93925	15,50652	ZIELONA GÓRA,UL.KOSCIELNA,F.P.W.PRZY KOŚC	5657500	3622850
46210014	F	II	700	AA 8086	D	51,05223	16,19153	JAWOR,PLAC WOLNOŚCI,F.P.W.,NA SKWERKU,ZN	5558300	3669300
47240024	B	VI	880	HM	D	50,43919	16,65744	KŁODZKO,PL.B.CHROBREGO,RATUSZ,ŚCIANA WS	5490000	3701950
47330030	B	VI	880	HM	D	50,46342	17,00814	PACZKÓW,UL.KOŚCIELNA,KOŚC.KAT.P.W.ŚW.JAN	5492750	3726850
47330067	B	VI	860	AA 0094	D	50,44662	16,89046	BŁOTNICA NR 52,BUD.LEŚNICZÓWKI NADL.BARDO	5490850	3718500
48410056	F	III	700	AA 8775	D	50,19596	17,83538	GŁUBCZYCE,UL.RACIBORSKA,F.P.W. PRZED BUD.	5463600	3786050
54130024	F	III	700	AA 9145	D	49,75051	18,63571	CIESZYN,PL.LONDZINA,F.P.W.OBOK KOŚCIOŁA	813150	213750
54140041	F	III	700	AA 8682	D	49,6869	19,1863	ŻYWIEC,UL.WESOŁA,F.P.W.OBOK KAPLICZKI	806050	253450

Fig. 11. Result of SQL query for the first version of the database – example 2

Example 2a. Retrieval of the same information as in example 2, but from the second version of the database.

```
SELECT DISTINCT punkty.NrPunktu, punkty.Rodzaj, punkty.Typ,
punkty.KodStab, punkty.Glowica, punkty.Adres
FROM punkty INNER JOIN linie ON punkty.NrPunktu = linie.reppocz
WHERE
punkty.nrpunktu IN (SELECT punkty.NrPunktu
FROM punkty INNER JOIN linie ON punkty.NrPunktu = linie.reppocz
WHERE linie.idkampanii=2)
AND
punkty.nrpunktu IN (SELECT punkty.NrPunktu
FROM punkty INNER JOIN linie ON punkty.NrPunktu = linie.reppocz
WHERE linie.idkampanii=3)
AND
punkty.nrpunktu IN (SELECT punkty.NrPunktu
FROM punkty INNER JOIN linie ON punkty.NrPunktu = linie.reppocz
WHERE linie.idkampanii=4);
```

It is evident that this query is more complex. A set intersection requires calling three sub-queries for the same table. The resulting set is exactly the same as in example 2, but the execution of the query takes considerably longer (a few dozen seconds).

In the nearest future the database will be improved and augmented with more data. One of the first improvements will be to add more data on the localization of reference points. At present, points from campaign 4 have geodesic coordinates (system 42), points from campaign 3 have coordinates in system 65, while only few points from campaign 2 do have coordinates. The addition and standardization of the coordinates will make it possible to create a graphical representation of the data from all the campaigns as well as facilitate spatial analysis and import to other formats.

Summary

The integration of the data from levelling campaigns permits the analysis of the information from several campaigns simultaneously. This has been demonstrated above in the discussion of SQL queries. Additional solutions, such as dedicated computer programs, may further increase the usefulness of the database. Computer technology gives practically unlimited opportunities, from adding new information to the database and recalculating (adjusting) the coordinates, to structure modification depending on the needs. Thus it is possible to tackle diverse analytical problems by easily selecting relevant data

sets. Moreover, the data existing in a relational database can be transferred to any other relational database management system, which makes it independent of the physical storage format. Additionally, the data can be converted to any other format, for example any GIS system format, like the popular ESRI shapefile, or an object or object-relational database.

Undertaking the work of digitizing this data has undoubtedly been well-justified and will help make a better use of the precise levelling data in Poland.

Accepted for print 8.09.2009

References

ŁYSZKOWICZ A., LEWANDOWICZ E., KOWALCZYK K., OGÓREK T. 2002. *Status of the precise levelling data base at the University of Warmia and Mazury in Olsztyn.* International Association of Geodesy / Section I – Positioning; Subcommission for Europe (EUREF), Publication, 12: 151–156

KOWALCZYK K. 2006. *Modelling the vertical movements of the earth's crust with the help of the collocation method.* Reports on Geodesy, 2(77): 171–178.

WYRZYKOWSKI T. 1988. *Monografia krajowych sieci niwelacji precyzyjnej I klasy*. Inst. Geod. i Kart., Warszawa.

Katalog wysokości reperów polskiej podstawowej sieci niwelacji (niwelacji precyzyjnej I-ego rzędu) nad poziomem morza w Amsterdamie. 1939. Ministerstwo Komunikacji, Biuro Pomiarowe, PM-3a.

Katalog punktów niwelacyjnych. Bałtycki system wysokości (zero mareografu w Kronsztadzie). 1960. Główny Urząd Geodezji i Kartografii MSW.

Katalog,1982. Centralny Ośrodek Dokumentacji Geodezyjnej i Kartograficznej, Warszawa.

TECHNICAL SCIENCES
Abbrev.: Techn. Sc., No 12, Y 2009

DOI 10.2478/v10022-009-0014-7

ANALYSIS OF COMPILATION TECHNOLOGY OF DIGITAL TERRAIN MODEL BASED ON SATELLITE, TACHEOMETRIC AND PHOTOGRAMETRIC DATA

Katarzyna Pająk

Department of Surveying
University of Warmia and Mazury in Olsztyn

K e y w o r d s: Digital Terrain Model, GPS, RTK method.

A b s t r a c t

One of the most important, and at the same time, the most difficult task undertaken in complex process of generation geographic information system is generation of Digital Terrain Model. DTM is primary infromation layer used by systems which depict phenomena in qualitative way. It is also basic element in spatial structure of these systems. In literature there is a lot information concern obtaining terrain data to construct DTM by using photogrammetric and classical methods, but there is almost no information about using satellite methods in such purpose. In this article analysis of compilation technology of DTM generation based on data obtained due to various survey methods, including satellite one, are presented.

ANALIZA TECHNOLOGII OPRACOWANIA NUMERYCZNEGO MODELU TERENU NA PODSTAWIE DANYCH SATELITARNYCH, TACHIMETRYCZNYCH I FOTOGRAMETRYCZNYCH

Katarzyna Pająk

Katedra Geodezji Szczegółowej
Uniwersytet Warmińsko-Mazurski w Olsztynie

S ł o w a k l u c z o w e: Numeryczny model terenu, GPS, metoda RTK.

A b s t r a k t

Jednym z najważniejszych, a zarazem najtrudniejszych zadań, jakie są podejmowane w złożonym procesie konstruowania systemów informacji przestrzennej, jest tworzenie numerycznego modelu terenu. NMT jest podstawową warstwą informacyjną wykorzystywaną przez systemy opisujące zjawiska wartościowo i stanowi dla nich podstawę organizacji przestrzennej. W literaturze przedmiotu znajdziemy wiele informacji dotyczących pozyskiwania danych terenowych do budowy NMT metodami fotogrametrycznymi i klasycznymi, mało jest natomiast informacji o wykorzystaniu do tego celu metod satelitarnych. W artykule przedstawiono analizę technologii powstania NMT z wykorzystaniem danych z różnych metod pomiarowych, w tym również metody satelitarnej.

Introduction

Digital terrain model can be define as the collection of the points and approximate surfaces which are necessary to define relief features and to enable to determine any point of this terrain surface with given accuracy. At traditional maps information about relief features in form of contours was addition to primary map content. Nowadays DTM is stand-alone product with wide spectrum of applications. Usually it is operating as one of the layers of Geographic Information System. Co-operating with others layers it is used to conduct complex analyses in selected area.

Given area with its land development and traffic intensity is basic element significantly influence road and highway projects. Digital terrain descriptions are integral part of road and highway geometric design system. Using DTM one has following advantages:

– enables to gather terrain data in acceptable form to processing and storing,
– enables to show existing or design surface in almost any form:
  a) traditional, like contour scheme, profiles and sections,
  b) pictoral view, such as grid model.
– enables to conduct earth mass calculation.

Naturally, using DTM created some problems, the most important ones are cost- and time-consuming process of gathering data to creation DTM.

Elevation data to create DTM can be obtained by means of:

– direct measurement method (tacheometry or GPS survey),
– cartographic method (processing of existing analog maps),
– photogrametric method (processing of aerial photos or satellite images)
– aerial laser scanning method
– radar interferometry method.

Experiments description

In order to gather necessary data for creation digital terrain model surveys were conducted by following methods:

– direct GPS RTK/OTF survey,
– direct tacheometric survey,
– photogrammetric method.

Direct satellite survey

First survey was the direct satellite measurement. The terrain survey was done using a quad type vehicle (Fig. 1) on which necessary equipment for field

data collection was installed. The survey equipment consisted of two precise geodesic receivers Ashtech, two navigation receivers Thales Mobile Mapper with post-processing option, GPS anntenas: geodesic and navigation and the GPRS terminal. There was also, typical for RTK survey, anntena (L1, L2) on frame construction and receiver Thales Mobile Mapper (PAJĄK 2008).

Fig. 1. The vehicle with necessary equipment for field data collection

For precise navigation survey profiles were needed. These profiles were designet on MicroMap and subsequently were converted to receiver Thales Mobile Mapper. It enabled to keep sustain vehicle in correct course during data collection (Fig. 2).

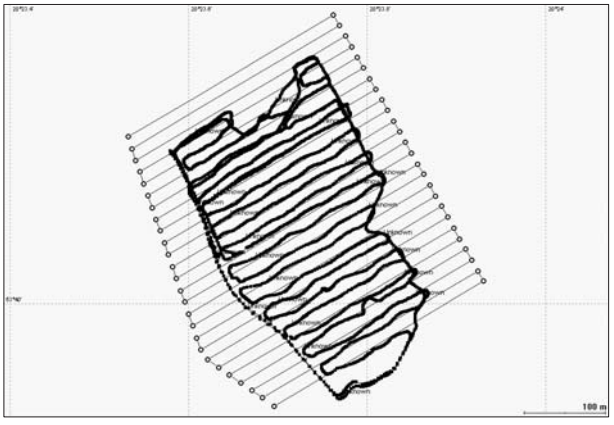

Fig. 2. Designed survey profiles in MikroMap and paths of actual navigation along them

Using real-time method during survey, coordinate were obtained in real time, corrections were transmitted using GPRS technology. They were also took into account in real time during registration to mobile receiver. Raw data were also registered and used in calculation in post-processing mode.

In RTK survey corrections transmmitted by GPRS were used what resulted in high accuracy. Mean errors of coordinate *X, Y, H* for the whole survey amounted eventually to:

m_X = 0.096 m, m_Y = 0.064 m, m_H = 0.198 m (PAJĄK et al. 2006).

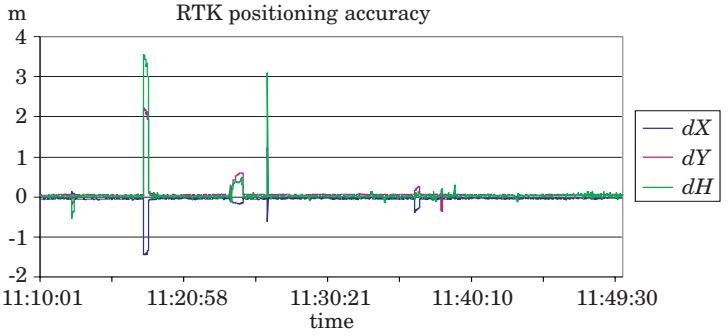

Fig. 3. Accuracy of coordinate by RTK method

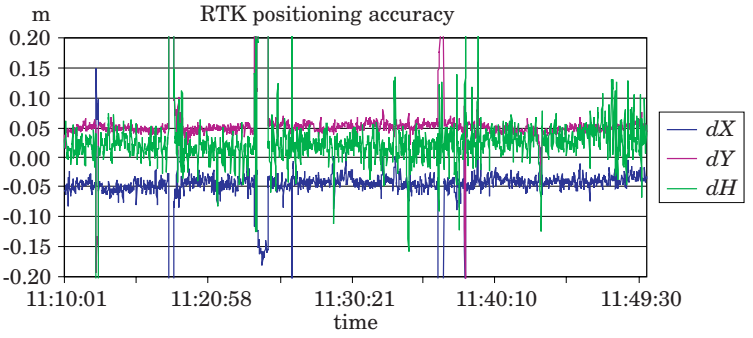

Fig. 4. Accuracy of coordinate by RTK method (zoomed)

Obtained results enabled to generate digital terrain model.

Tacheometric direct survey

During direct tacheometric survey first stage of task was static GPS measurement at three points because of the lack of national network. Obtained coordinate were used in following tacheometric calculation in Winkalk. One

point was established as the station, with electronic tacheometer Leica, and two others as reference points. Distance and elevation measurements between station and reference points were taken for control. Measured distance was congruent with distance calculated from coordinate, angular discrepancy was only 0g,0010, and elevation difference was only 4 mm. After such orientation of the instrument and its control terrain point measurment began. Obtained data were used to generate digital terrain model (PAJĄK 2008).

Photogrammetric measurements

Photogrammetric method consisted of photogrammetric processing of aerial photos. In photogrammetric measurement digital photogrammetric station were used. All measurements were manual and included various point and form lines which depicted relief features as:
– scattered point in regular grid,
– form lines (brow, water-course),
– breaklines (banks, precipices),
– extreme points (summits, bottoms).

Measurements of photogrammetric model took place at Okręgowe Przedsiębiorstwo Geodezyjno-Kartograficzne in Olsztyn. Area study was located in one stereogram. Measurements were done with digital photogrammetric station Intergraph using:
– aerial photos, colour negative form 1995, scale 1:26 000,
– scanned images of aerial photos in scale 1:26 000, pixel = 30 μm, 24 bpp, format Intergraph TIFF, then images were converted to Intergraph TIFF with compression JPEG, quotient Q = 10,
– photogrammetric network consisted of control points, whose coordinate were estimated by means of GPS survey.

High accuracy of correlated measurements of fiducial coordinates in digital image was guaranteed. Sigma error did not exceed 8 μm. Digital terrain model was generated manually. Coordinates were collected for over 800 points in area of about 5 ha, with spatial distribution in regular grid 10 m – 10 m. form lines, breaklines-banks, extreme points were also measured (PAJĄK 2008).

Statistical analyses

These analyses are based on examination of surfaces GRID created by using data obtained with three various methods: tacheometric, satellites and photogrammetric. For surface interpolation kriging method was used. In order

to test difference between GRID surfaces, size for grid was selected as 4 m × 4 m and 8 m × 8 m,. Neither breaklines nor extreme lines were taken into account. Analyses included also TIN surfaces, which was presented in other article.

In statistical evaluation of GRID surface following parameteres were considered:

– variance and standard deviation of GRID surface – it describes dispersion of data around arithmetic mean.

$$dH_{\text{śr}_{\text{TACH-RTK,FOT}}} = \frac{(H_{1_{\text{TACH}}} - H_{1_{\text{RTK,FOT}}}) + \ldots + (H_{n_{\text{TACH}}} - H_{n_{\text{RTK,FOT}}})}{n}$$

$$V(H) = \frac{[(dH_{1_{\text{TACH-RTK,FOT}}} - dH_{\text{śr}_{\text{TACH-RTK,FOT}}})]^2 + \ldots +}{n-1}$$

$$\frac{+ \ldots + [(dH_{n_{\text{TACH-RTK,FOT}}} - dH_{\text{śr}_{\text{TACH-RTK,FOT}}})]^2}{n-1}$$

$$\delta(H) = \sqrt{V(H)}$$

where:

$dH_{1\ldots n_{\text{TACH-RTK,FOT}}} = dH_{1\ldots n_{\text{TACH}}} - dH_{1\ldots n_{\text{RTK,FOT}}}$ – values of successive differences between elevations in GRID surfaces based on data from satellite (photogrammetric) survey and tacheometric one.
$dH_{\text{śr}}$ – mean value of difference in elevation of GRID surfaces based on data from satellite (photogrammetric) survey and tacheometric one.
n – number of points,

– RMS- Root Mean Square.

$$\text{RMS} = \sqrt{\frac{(dH_{1_{\text{TACH-RTK,FOT}}})^2 + \ldots + (dH_{n_{\text{TACH-RTK,FOT}}})^2}{n}}$$

where:

$dH_{1\ldots n_{\text{TACH-RTK,FOT}}} = dH_{1\ldots n_{\text{TACH}}} - dH_{1\ldots n_{\text{RTK,FOT}}}$ – values of successive differences between elevations in GRID surfaces based on data from satellite (photogrammetric) survey and tacheometric one.
n – number of points.

Analyses of GRID surfaces based on data used for DTM generation, obtained by means of three survey methods

Using three survey methods terrain data were collected, and their spatial distributions are presented in Figure 5.

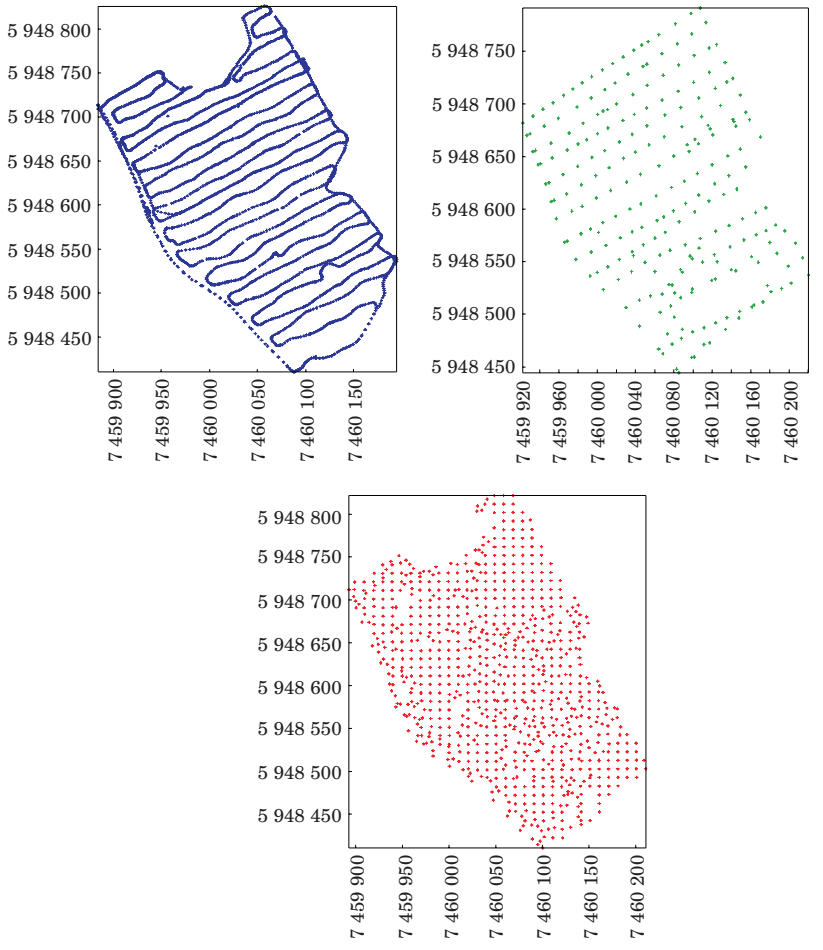

Fig. 5. Spatial distribution of data obtained from satellite RTK, tacheometric and photogrammetric methods

After superimposition of data obtained from three survey methods, overlap area was determined and became the object of subsequent analyses (Fig. 6) (on account of small size of overlap area the area study was limited).

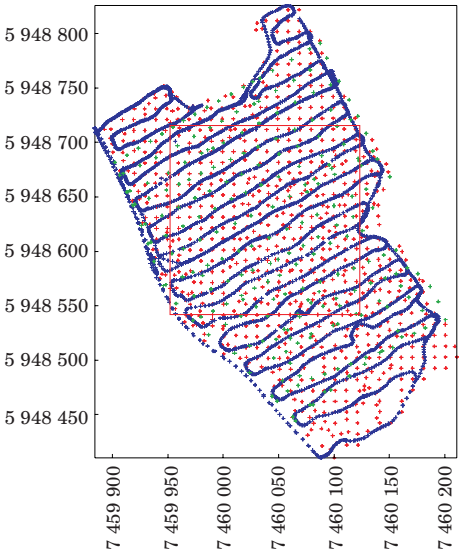

Fig. 6. Spatial distribution of superimposed data obtained from three survey methods and determination of overlap area for subseqent analyses

Obtained data enables to interpolate GRID with step size 4 m × 4 m and 8 m × 8 m.

Analysis included calculation of elevation differences in common points of GRID surfaces constructed with data from direct tacheometric and direct satellite surveys and also calculation of variance, standard deviation, RMS and minimal, maximal and mean difference between elevations for these surfaces.

– For search radius of 60m, and GRID with steps 4 m × 4 m and 8 m × 8 m mentioned values amounted to:

Table 1

Analyses of GRID surfaces

Specification	GRIDTACH-RTK (4 m × 4 m)	GRIDTACH-RTK (8 m × 8 m)
Variance (m)	0.046	0.039
Standard deviation [m]	0.215	0.198
RMS [m]	0.219	0.200
Min [m]	-0.507	-0.395
Mean [m]	0.038	0.031
Max. [m]	2.096	1.376

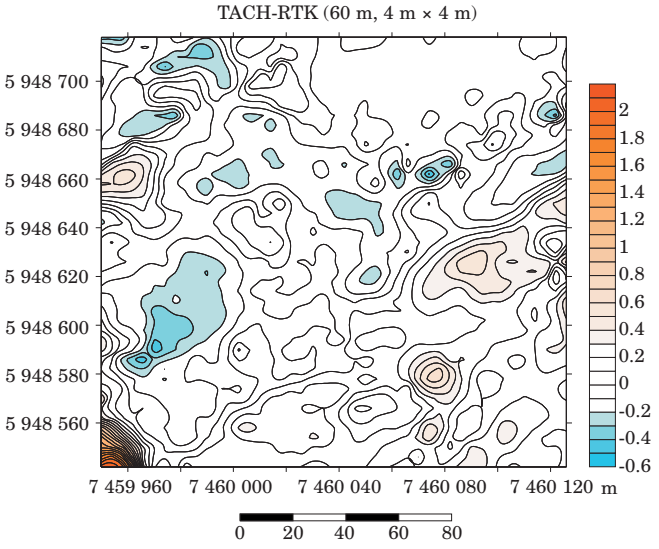

Fig. 7. Map of distribution of elevation differences on surface GRID 4 m × 4 m

Analysing results of calculation, analyses and comparison in the table it can be observed that for differential surface GRID$_{\text{RTK-TACH}}$ 4 m × 4 m with searching radius of 60 m RMS was 0.219 m, standard deviation 0.215 m, mean difference of elevation for this surface is 0.038 m. For differential surface GRID$_{\text{RTK-TACH}}$ 8 m × 8 m with the same searching radius mentioned parameters amounted 0.200 m, 0.198 m, 0.031, respectively. Distribution of differences in elevation for differential surface GRID$_{\text{TACH-RTK}}$ 4 m × 4 m is presented in Figure 7.

In Figure 8 distribution of elevation differences in differential surface GRID$_{\text{TACH-RTK}}$, 8 m × 8 m, resulted from comparison surfaces GRID created with data from direct tacheometric and direct satellite surveys.

After analysing data obtained from two survey methods, for GRID 4 m × 4 m and GRID 8 m × 8 m digital models with searching radius of 60 m were generated.

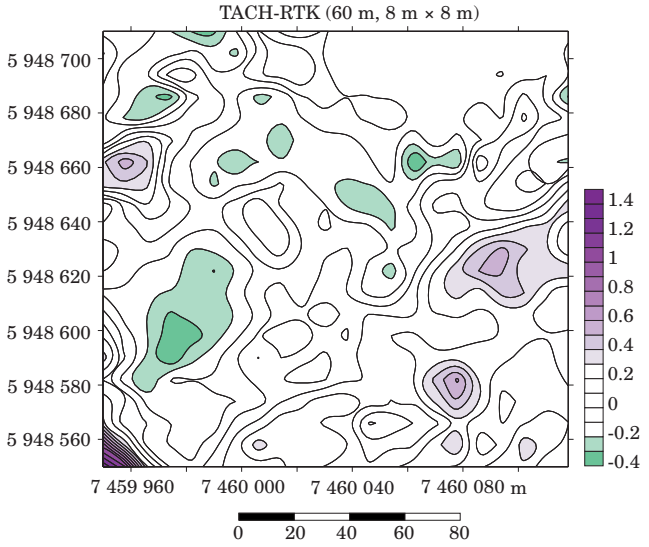

Fig. 8. Maps of distribution of elevation differences on surface GRID 8 m × 8 m

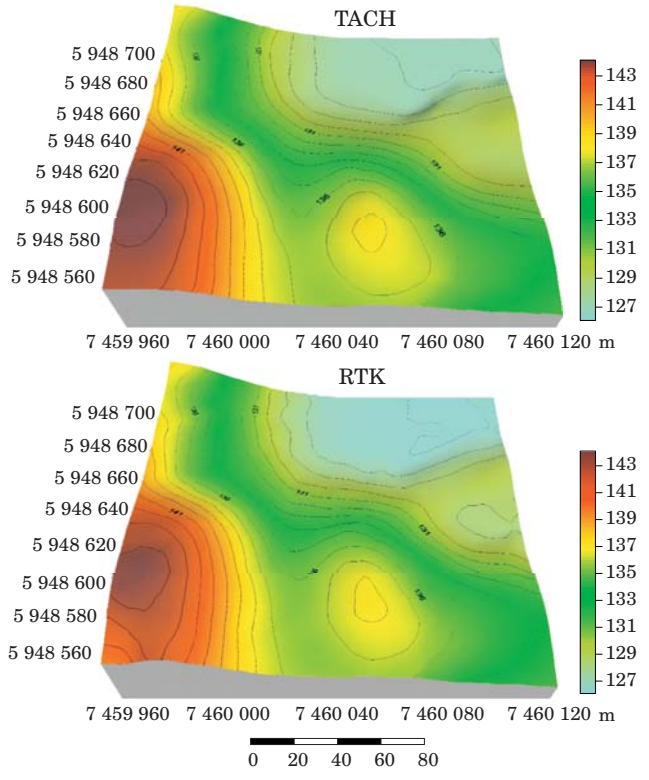

Fig. 9. DTM with contours, grid 4 m × 4 m, searching radius 60 m

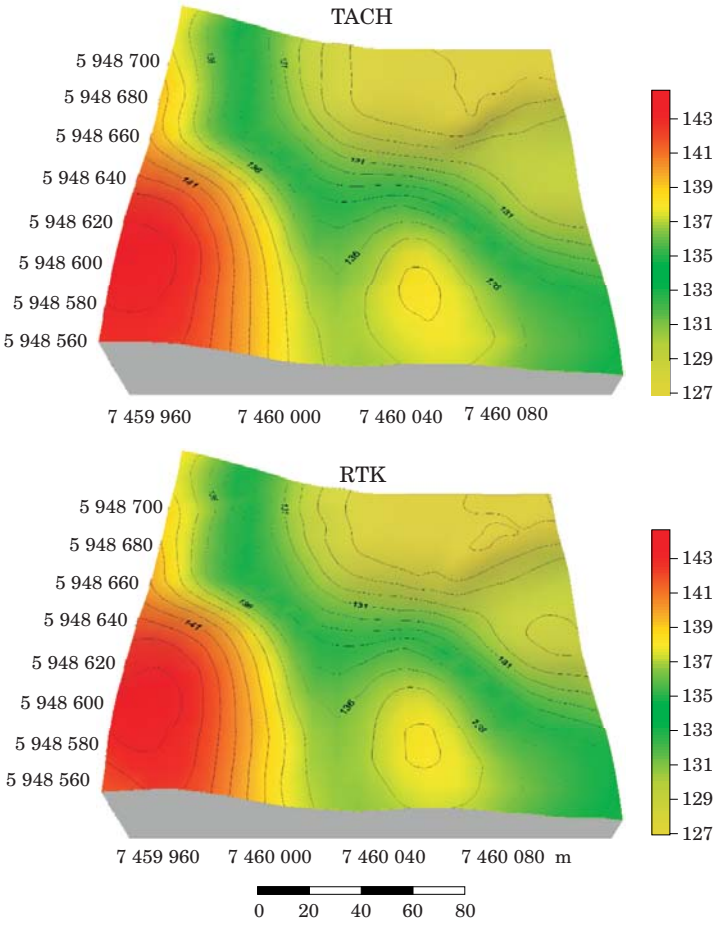

Fig. 10. DTM with contours, grid 8 m × 8 m, searching radius 60 m

Analysing presentations in Fig. 9 and 10, showing digital model generated from data collected by means of direct tacheometric and satellite surveys. It is seen that there is neither disturbances in elevations nor in spatial characterics of study area. Interpretation of contours presented in figure allow us to conclude that there is no significant difference between models based on direct tacheometric and direct satellite surveys.

Second analysis included calculation of elevation differences at common points of GRID surfaces generated from data gathered by using direct tacheometric survey and photogrammetic method. Variance, standard deviation, RMS, minimal, maximal and mean difference between elevation for these surfaces were also objects of interest.

– For search radius of 60 m, and GRID with steps 4 m × 4 m and 8 m × 8 m mentioned values amounted to:

Table 2

Analyses of GRID surfaces

Specification	GRIDTACH-RTK (4 m × 4 m)	GRIDTACH-RTK (8 m × 8 m)
Variance (m)	0.090	0.086
Standard deviation [m]	0.301	0.292
RMS [m]	0.430	0.426
Min [m]	-0.559	-0.559
Mean [m]	0.307	0.311
Max. [m]	2.422	1.908

Like in previous analysis, and with the same condition about searching radius for differential surface GRIDRTK-TACH 4 m × 4 m RMS was 0.403 m, standard deviation 0.301 m. Mean difference of elevation for surface GRIDTACH-FOT 4 m × 4 m was 0.307 m. For differential surface GRIDRTK-FOT 8 m × 8 m mentioned parameters were 0.426 m, 0.292 m, 0.311, respectively. Distribution of differences in elevation for differential surface GRIDTACH-FOT 4 m × 4 m is presented in Figure 11.

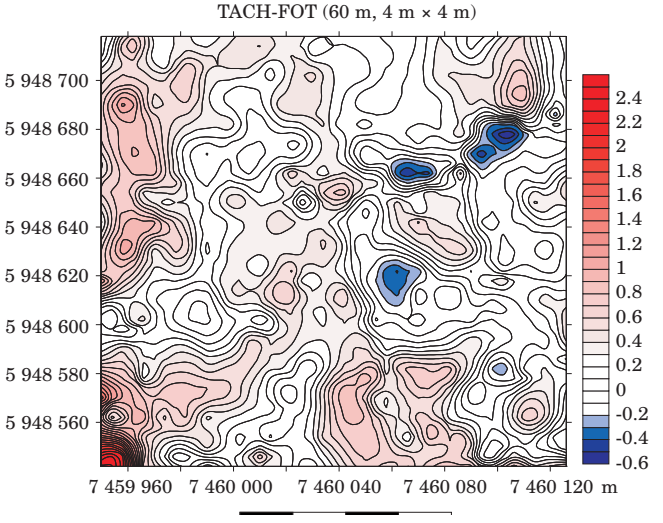

Fig. 11. Map of distribution of elevation differences on surface GRID 4 m × 4 m

Distribution of differences in elevation for differential surface GRIDTACH-FOT 8 m × 8 m is presented in Figure12.

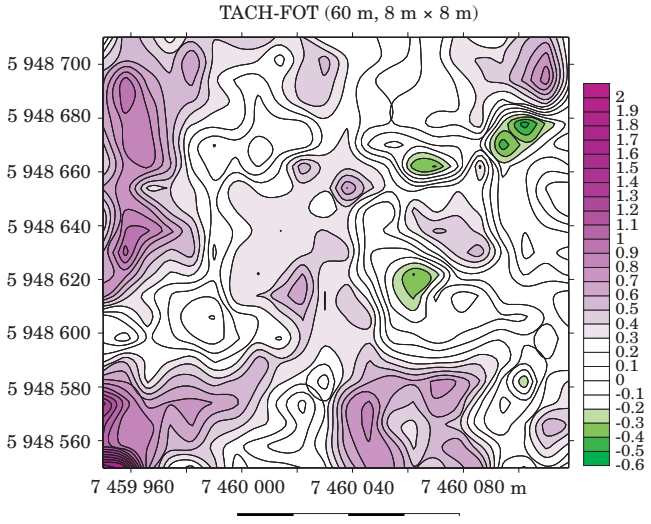

Fig. 12. Map of distribution of elevation differences on surface GRID 8 m × 8 m

After analysing data obtained from two survey methods, for GRID 4 m × 4 m and GRID 8 m × 8 m digital models with searching radius of 60 m were generated (Fig. 13, 14).

Analysing presentations in Fig. 13 and 14, showing digital model generated from data collected by means of direct tacheometric and photogrammetric methods there is neither disturbances in elevations nor in spatial characterics of study area. Interpretation of contours presented in figure allow us to conclude that there are places on model, generated by using photogrammetric methods, where contours in comparison to theirs respective location on model based on direct tacheometric survey diverged (PAJĄK 2008).

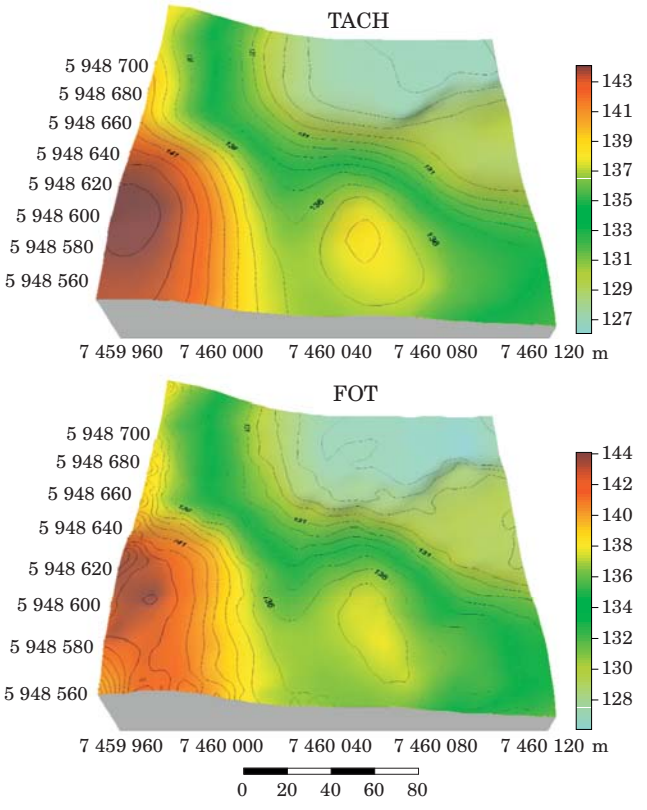

Fig. 13. DTM with contours, grid 4 m × 4 m, searching radius 60 m

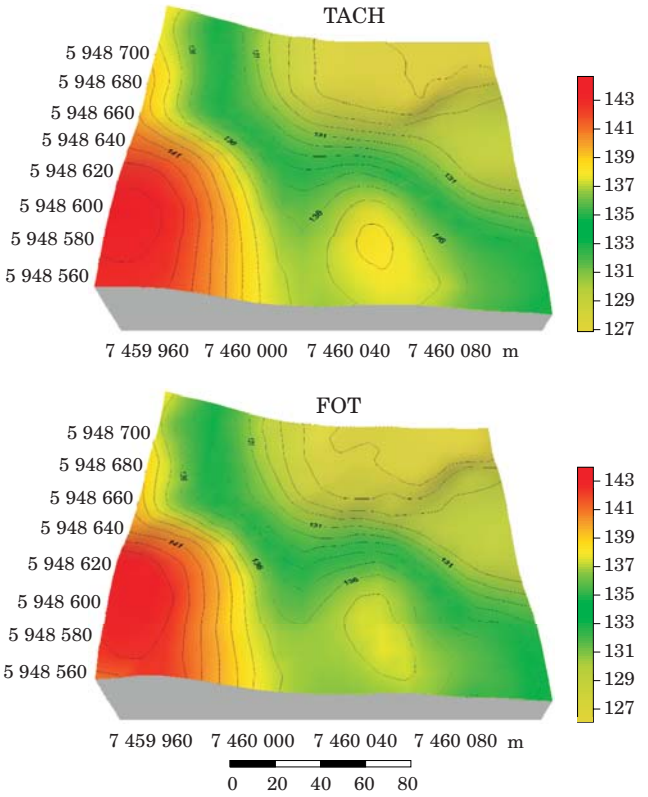

Fig. 14. DTM with contours, grid 8 m × 8 m, seeking/searching radius 60 m

Conclusions

Direct satellite surveys RTK GPS/OTF enabled to collect a lot of measurement points in relatively short time, in cheap, fast and safe way.

In comparison to tacheometric method, mean difference in elevation is 3 cm, and standard deviation 20 cm for surfaces created as GRID.

GPS method for measurement of terrain data used for DTM generation is fast method with high accuracy. However, despite of high class equipment used in experiments it can be stated that there is a significant influence of any changes in satelite configuration on survey accuracy.

There is one leading factor arguing for satellite technology, namely efficiency seen as reducing time of acquisition of accurate data required to DTM creation. The evidence of reducing time-consuming aspect of gathering data is 90 minutes when area of 5 ha were measured, and there was only one person in vehicle. Others methods needed much more time.

Analyses which took into account various models, confirmed that model generated from data obtainted by satellite methods gives better result in comparison to photogrammetric method.

The final results of the following study is function describing.

Accepted for print 8.10.2009

References

CIECKO A., OSZCZAK B., OSZCZAK S. 2003. *Determination of Accuracy and Coverage of Permanent Reference Station (DGPS/RTK) in Gdynia.* 7th Bilateral Geodetic Meeting Italy-Poland, Bressanone, Italy, 22–24 May, Published in Reports on Geodesy, 2(65).

PAJĄK K., CIEĆKO A., OSZCZAK S. 2006. *Analyses of Different Methods used for Creation of Digital Terrain Model (DTM).* 8th Bilateral Geodetic Meeting Poland–Italy, Wrocław, Poland, Reports and Geodesy, 2(77).

PAJĄK K. 2008. *Research and analyses of technology for creation Digital Terrain Model with using satellite, classic and photogrammetric methods.* Ph.D. Thesis, Olsztyn.

TECHNICAL SCIENCES
Abbrev.: Techn. Sc., No 12, Y 2009

DOI 10.2478/v10022-009-0015-6

ENTERPRISE ARCHITECT AND MAGIC DRAW UML – COMPARING THE ABILITIES OF CASE TOOLS

Halina Tańska

Department of Multimedia and Computer Graphics
University of Warmia and Mazury in Olsztyn

K e y w o r d s: UML, CASE tools, the process of creating software, the criteria of evaluating CASE tools.

A b s t r a c t

Creating information systems is complicated and involves finding solutions for analytic-design problems and for that reason using new programming languages and CASE tools is necessary. The author tries to evaluate two items chosen from a group of many tools available on the software market. For that reason the author pointed out few criteria connected to quality and quantity parameters. The specific character of the product influences the decision about the type of tool made by analytic-design team.

ENTERPRISE ARCHITECT A MAGICDRAW UML – PORÓWNANIE MOŻLIWOŚCI NARZĘDZI CASE

Halina Tańska

Katedra Multimediów i Grafiki Komputerowej
Uniwersytet Warmińsko-Mazurski w Olsztynie

S ł o w a k l u c z o w e: język UML, narzędzia CASE, proces tworzenia oprogramowania, kryteria ocen narzędzi CASE.

A b s t r a k t

Tworzenie systemów informatycznych ze względu na złożoność i konieczność rozwiązywania wielu problemów analityczno-projektowych wymaga stosowania nowoczesnych języków modelowania oraz narzędzi CASE. Autorka podejmuje próbę oceny użyteczności dwóch spośród wielu narzędzi obecnie spotykanych na rynku oprogramowania. W tym celu przyjęła kilka kryteriów uwzględniających parametry ilościowe i jakościowe. Decyzja o wyborze narzędzia zależy od specyfiki tworzonego projektu i jest podejmowana przez zespół analityczno-projektowy.

Introduction

Using tools which allow to identify complex problems, preparing proposals of a solution and the choice of a solution which is the best in particular situation by analytic-design teams is a common phenomenon in the process of creating information systems. The usage of CASE – Computer Aide Software Engineering allows to make some changes in the project in a systematic way as well as to monitor other stages of creating software.

CASE tools perform a number of important functions such as supporting the authors and creators of software during conceptual and implementation work. Their usage increases the level of communication between specialists from different branches of science, makes the bond with the client stronger and makes the documentation and its modification more legible. As a result, the issue is formulated in a correct way (the specification of requirements) and it is better understood which helps to define the criteria of accepted assumptions verification in a more detailed way.

Present-day CASE tools market is very diverse[1] which means that one can choose such tools to perform the process of creating the software in a flexible and optimal way. Simple classification of CASE tools consists of commercial and non-commercial tools[2]. Commercial tools, absolutely professional, support all lifecycle phases of the system (the analysis of requirements, designing, programming, testing, modification). Enterprise Architect in Corporate version is a tool of this type. The second group includes commercial tools which support only selected phases of designing. MagicDraw UML in Personal version is a tool of this type.

The author tries to compare selected CASE tools – EA and MD. She pointed out a list of different features which are used to evaluate the tools (the criteria of evaluation) to illustrate in a better way the differences connected to the quality and abilities of tools. Among them there are the features connected to unified modeling language, the quality of graphic, technical quality, the ease of modification and verification of models. Obtained results are presented in a synthetic way by using the tabular form (Tables 1–5).

Selected quantity parameters

Many producers of CASE tools don't point out any particular methods of creating information system, they only give a number of conceptual and

[1] Authors who write about the diversity of tools: Wrycza et al. 2005, H. Tańska 2005, Pirjanowicz 2008.

[2] A different division was presented in this book: Fuglewicz et al. 1995. They point out three levels: Lower, Middle, Upper CASE.

implementation models as well as different techniques of modeling. Unified Modeling Language makes specifying analytic, design and implementation decisions easier and they must be made while creating and adjusting information system[3]. Table number 1 presents differences in the way of reproducing UML[4] while creating the system. Selected 12 features allow to state that the difference in activities connected to business analysis, database designing, import of database schemes, creating schedules, creating non-standard types of diagrams required by the user. According to this comparison Enterprise Architect offers more possibilities.

Table 1

The abilities of CASE tools and Unified Modeling Language (UML)

Feature	Enterprise Architect	Magic Draw UML
UML version	UML 2.0	UML 2.0
Types of UML diagram	All included in UML 2.0 standard	It is possible to make 9 from 13 UML diagrams
Support for business analysis diagrams	Yes	No
Diagram Completeness	Diagrams contain all objects and relations defined in the standard	Diagrams contain all objects and relations defined in the standard
Standard UML Stereotypes	Yes	Yes
Stereotypes defined by the user	Yes	Yes
Database designing	Yes	No
Import of database schemes	Yes	No
Creating schedules	Yes	No
Possibility of creating non-specific type of diagram by the user	Yes	No
Possibility of using elements from a diagram in another diagram	Yes	Yes
Adding elements to diagrams from model browser	Yes	Yes

Source: my own analysis based on: MagicDraw User Manual.pdf and Enterprise Architect User Guide.pdf and technical and usable documentation of the producer (www.sparxsystem.com.au, www.magicdraw.com 30.06.2008)

Processes which make performing a number of tasks in a project automatic play an important role in evaluating CASE tools. The designer can create

[3] P. Graessle, H. Baumann, Ph. Baumann underline that UML "can by used to modeling different systems: information, business or other systems". Graessle et al. 2006.

[4] Unified Modeling Language is a graphic language for presenting, specifying, designing and documenting the elements of information application. It allows to unify the process of preparing the system section including conceptual objects like the functions of the system as well as specific objects like classes, database schemes and programming components which can be used again.

a framework of source code for particular elements of application in a programming language selected by the modeler, among other things to generate DDL code[5] of the database with is modeled. What is more, these tools allow to generate the documentation of the system in an automatic way according to the needs of the designer and system user. The documentation created in this way consists of system architecture and a detailed description of all components. Complete documentation becomes a source of knowledge for analysts, designers, programmers and system users.

Table number 2 presents 6 features which are connected to the processes which are performed automatically in CASE tools (Enterprise Architect and MagicDraw UML).

Table 2

Comparison of automatic generation processes

Feature	Enterprise Architect	Magic Draw UML
Generating documentation in HTML format	Yes	Yes
Generating documentation in RTF format	Yes	No[a]
Generating DDL	Yes[b]	No
Generating the framework of source code	Yes[c]	No
Control of correctness	Yes	No
Reverse engineering	Yes[d]	No

[a] Generating only the pattern of documentation.
[b] DB2, InterBase, MS Access, MySQL, Oracle 9i, PostgreSQL, SQL Server 2000, SQL Server 7, Sybase Adaptive Server Anywhere, Sybase Adaptive Server Enterprise
[c] ActionScript, C, C#, C++, Delphi, Java, PHP, Pyton, VBnet, Visual Basic
[d] For the same languages as in the case of generating source code

Source: my own analysis based on: MagicDraw User Manual.pdf and Enterprise Architect User Guide.pdf

Selected features point out poor support of generating documentation (only HTML format) by MagicDraw. Other processes like generating DDL, generating the framework of source code, the control of correctness, reverse engineering are not used by this tool.

Selected quality parameters

Tools like CASE are often used in big software companies. In these companies work is divided between few or even more people. Quite often

[5] Date Definition Language (DDL) allows to operate on structure which contain data. It involves adding, modifying and deleting tables or bases.

different elements are made in completely different rooms, buildings or even cities. For that reason the possibility of working on a project from many places and by using the net is crucial. It is connected with keeping information confidential as well as the safety of information which is sent. Table number 3 presents the possibilities of work by using MagicDraw UML and Enterprise Architect in an environment which involves one as well as many posts. The ability of these two tools to move created models, diagrams or elements made by using these tools to other tools or modeling environment while keeping the cohesion and integration of data was compared.

Table 3

Technical quality comparison

Feature	Enterprise Architect	Magic Draw UML
Work from many posts	Yes	No
Creating XML schemes[a]	Yes	No
Transformation of models to XMI format	Yes	Yes
Transformation of models to CSV format[b]	Yes	No
Reading of other models made by using other tools	Yes[c]	Partly[d]
Creating hyperlink from UML diagrams to URL	Yes	Yes
Version control	Yes[e]	No
Exporting diagrams to other applications	Yes	Yes
Ability to create a diagram picture	Yes[f]	Yes[g]

[a] Extensible Markup Language (XML)
[b] Comma Separated Values (CSV)
[c] Testing with MagicDraw UML, Rational Rose Enterprise
[d] Only saved in XML Metadata Interchange (XMI)
[e] Uses CVS
[f] In: BMP, PNG, JPG, TGA, GIF, WNF, EMF format
[g] In EMF, EPS, JPG, PNG, SVG, WNF format

Source: my own analysis based on: MagicDraw User Manual.pdf and Enterprise Architect User Guide.pdf

It is worth mentioning that CASE tools support team work much more often and moving created models from one tool to another one is an important criterion of evaluating their functionality. Table number 3 presents 9 features which are connected to technical aspects and to the export of diagrams to other applications. Only three features (transformation of models to XMI format, creating hyperlinks from UML diagrams to URL, creating diagram picture) which occur in both tools; only Enterprise Architect possess other 6 features.

Visual-usability aspects also influence the evaluation of CASE tools. Often applications with too complicated user interface or too difficult navigation are

rejected even though they have good project parameters. It is caused by the fact it is difficult to master the ability to use tools effectively by the teams which create software in a short period of time. Additionally it is worth pointing out the possibility of adjusting visual parameters of the tool to user's habits.

Graphic quality of application is another feature which has been compared. Quality aspects were evaluated such as possible adjustment of elements appearance and tools background to the individual habits of the user. Moreover, the settings of application interface appearance according to the user's expectations were taken under consideration (Tab. 4) which makes working with the tool easier and using the application more convenient. The change of interface appearance as well as the arrangement of different elements influence the way the tool is used and makes it less time-consuming.

Table 4

Graphic quality comparison

Feature	Enterprise Architect	Magic Draw UML
Adding symbols to diagram space	Yes	No
Changing the size of symbols and connections	Yes	Yes
Changing the colours of diagram background	Yes	Yes
Changing the colours of diagram elements	Yes	Yes
Possibility of adding icons and symbols by the user	Yes	No
Possibility of choosing the type of interface	Yes	Yes
Possibility of changing elements arrangement	Yes	Yes

Source: my own analysis based on: MagicDraw User Manual.pdf and Enterprise Architect User Guide.pdf

MagicDraw application doesn't allow the user to add new symbols and icons which can especially discourage experienced users. Among 7 features, 5 of them connected to changing the size of symbols and icons, colours of diagram background and its elements, arranging these elements and choosing interface are not very different in two tools which have been compared.

The author who teaches information systems designing, software engineering and the basics of information system managing evaluated selected tools by using subjective opinions of students. Table 5 presents non-technical features which influence general evaluation of CASE type application.

Enterprise Architect, according to the opinions of 100 students from the 3rd year of information science who took part in this research, has intuitive user interface and good arrangement of tools which allows to make very professional diagrams, generating the code and preparing documentation fast and quite easily. According to many students EA tool allows to use UML in

Table 5

Other aspects of comparison

Feature	Enterprise Architect	Magic Draw UML
The ease of tool usage	intuitive	intuitive
The ease of diagram modification	intuitive	intuitive
The ease of finding necessary information in the diagram	intuitive	intuitive
Size and complexity of the tool	Very complex with a huge number of options	Simple tool to create diagrams
Time needed to get to know the abilities of the tool	Very long (to master all possible abilities)	Short
The quality of tool's technical documentation	Very rich	Good

Source: my own analysis based on: MagicDraw User Manual.pdf and Enterprise Architect User Guide.pdf

more complex way. As a result it guarantees good support in a full system lifecycle from analyzing requirements, creating diagrams, generating the code till testing and preparing final technical documentation of model software. The tool makes team work easier and guarantees the safety of designing. It allows the usage of different programming languages (however Java platform is the most recommended format by company called Sparx System) and database according to the needs. Enterprise Architect is mainly dedicated to Windows platform although distribution for Linux platform have appeared recently. To sum up, it is a tool which requires time to master all its abilities.

MagicDraw UML (MDU) is a simple tool and less complex than Enterprise Architekt so it is easier to master. Many users will appreciate its simplicity and intuitiveness. MagicDraw UML is a tool which can by use by anyone who is interested in UML and has experience in programming and designing objects. MDU has an intuitive user interface. The arrangement of tools is clear and as a result it is easier to find a necessary tool, it takes less time and makes the process of creating diagrams easier. The price often influences the choice of a tool. It is important for the decision-maker when he or she makes decision about the purchase. One can check the current prices of EA and MDU tools on their producers' web pages[6].

[6] Data can be obtained from these web pages: www.sparxsystem.com.au and www.magic-draw.com

Conclusion

CASE tools are poorly described in the literature despite their growing popularity (there is a small number of items). Items available on the market are not directly devoted to CASE tools, they are only elements which the descriptions of other issues consist of. The necessity of mastering the tool which the design team hasn't used before must be taken under consideration before starting the production. Mastering these tools takes much time during the process of creating the system because there are many modules, elements and options. Deepened knowledge of UML is necessary.

Establishing the list of features (the criteria of evaluation) was required to compare these tools. The features, which allow to make the quality of software and documentation better, amass the knowledge of design team in repository (system encyclopedia), make information more available (among other things different models, documentation, data) and a faster flow of information between project groups or tools as well as the automation of many other activities, were chosen.

Enterprise Architect in Corporate version is a perfect tool for big companies producing software because they need a tool to support analysts, programmers, managers and application kontrolers. On the other hand MagicDraw UML in Personal version is a great tool supporting a single designer at the initial phases of system lifecycle.

To sum up, Enterprise Architect in Corporate version is a tool which offers better functionality (better and more abounding functionality than MagicDraw UML). If the fact that the systems are seldom created by a single designer and more often by a specialized design teams is taken under consideration, it is reasonable to use tools which support production. Then good tools are needed to support analysts and designers so the process of creating application would be more efficient and complex, the verification of the work progress done by project managers would be easier and kontrolers would obtain mechanisms necessary to perform the tests. No doubt, Enterprise Architect and MagicDraw UML are CASE tools of this type. These tools satisfy most needs of many companies which design and produce information systems. However it is the team leader who makes the final decision which tool to choose.

Accepted for print 25.09.2009

References

GRAESSLE P., BAUMANN H., BAUMANN PH. 2006. *UML 2.0 w akcji. Przewodnik oparty na projektach.* Helion, Gliwice.

FUGLEWICZ P., STĄPOR K., TROJAN A. 1995. *CASE dla ludzi.* Lupus, Warszawa.

PIRJANOWICZ W. 2008. *Podstawy programowania.* Wydawnictwo Uniwersytetu Warmińsko-Mazurskiego, Olsztyn.

TAŃSKA H. 2005. *Wykorzystanie narzędzi CASE do modelowania systemu informatycznego.* W: *Kompiutiernyje tiechnołogii pri modielirowanii, w uprawlenii i ekonomikie*. XVI Mierzdunarodnyje Konfieriencji "Nowyje tiechnołogii w maszynostrojenii". Charkow – Rybaczie.

WRYCZA S., MARCINKOWSKI B., WYRZYKOWSKI K. 2005. *Język UML 2.0 w modelowaniu systemów informatycznych.* Helion, Gliwice.

MagicDraw User Manual.pdf, http://www.sparxsystem.com.au

Enterprise Architect User Guide.pdf, http://www.magicdraw.com

TECHNICAL SCIENCES
Abbrev.: Techn. Sc., No 12, Y 2009

DOI 10.2478/v10022-009-0016-5

NUMERICAL ASPECTS OF A PNEUMATIC TYRE MODEL ANALYSIS

Józef Pelc

Chair of Mechanics and Machine Design
University of Warmia and Mazury in Olsztyn

Key words: tyre, computational code, finite element method, block diagram, deformation, strength.

Abstract

This paper presents a method of axisymmetric analysis of a pneumatic tyre model, based on the finite element method. A brief characterisation has been provided of a heterogeneous tyre model, which consists of three groups of materials: cord-rubber composite, physically nonlinear rubber and bead wire steel. The system is also geometrically nonlinear. This is all reflected in a detailed block diagram of the author's in-house code intended for analysis of deformation and strength of pneumatic tyres. The results of exemplary calculations made with the use of this code are presented.

NUMERYCZNE ASPEKTY ANALIZY MODELU OPONY PNEUMATYCZNEJ

Józef Pelc

Katedra Mechaniki i Podstaw Konstrukcji Maszyn
Uniwersytet Warmińsko-Mazurski w Olsztynie

Słowa kluczowe: opona, program obliczeniowy, metoda elementów skończonych, schemat blokowy, deformacja, wytrzymałość.

Abstrakt

W pracy przedstawiono sposób analizy obrotowo-symetrycznego modelu opony pneumatycznej bazującego na metodzie elementów skończonych. Podano krótką charakterystykę modelu niejednorodnej opony, w której wyróżniono trzy grupy materiałów: kompozyt kord-guma, fizykalnie nieliniową gumę i stal drutówek. Układ charakteryzuje się również nieliniowością geometryczną. Wszystko to ma swoje odbicie w szczegółowo przedstawionym schemacie blokowym programu autorskiego przeznaczonego do analizy deformacji i wytrzymałości opon pneumatycznych. Zamieszczono wyniki przykładowych obliczeń wykonanych za pomocą tego programu.

Introduction

Currently, the production of new commercial models of pneumatic tyres does not start until its geometric parameters and dimensions have been tested, the tyre has been mounted onto a rim and inflated, its strength, shape and distribution of pressure in the area of static contact with the ground have been examined and even the behaviour of the tyre under operation conditions has been checked. A future product is therefore tested and improved at the design phase, which requires a reliable computer model. Due to a considerable progress in computer methods in solid mechanics and power of computers, a number of commercial FEM codes are currently available which provide extensive analytic capabilities for even the most complex problems of the mechanics of a deformable body. Hence, a problem arises as to whether an analysis of deformation and strength of a pneumatic tyre can be performed directly with an FEM code, even if it is one of the most advanced software code. It is possible with one tyre; however, this is unacceptable to tyre designers due to the time needed to prepare a computational model. The fundamental difficulty lies in the fact that due to the technology of tyre formation, the density and angle of cords depend on the distance of a finite element from a tyre axis of rotation. For example, the cord density in the ply of a truck tyre decreases by ca. 50% between the tyre bead to the apex (PELC 1995c). Therefore, when preparing data which describe the mechanical properties of a tyre material, one should specify them separately for each finite element. This is why the author has spent years developing a tyre computational model based on the finite element method (PELC 1992, 1995a, 2000, 2002), followed by algorithms and a computer code intended for analysis of pneumatic tyre deformation analysis, in which data are generated from the properties of a raw layer of cord-rubber composite (wound on a tyre building drum) and the position of an element in a formed tyre. Moreover, a tyre is characterised by complex geometry and heterogeneity.

Loads acting on a tyre may cause considerable displacements and some materials, such as rubber, behave as nonlinear-elastic elements. Therefore, a tyre model is a nonlinear model and determination of an equilibrium path for such a system requires an incremental-iterative technique. All these issues are reflected in a block diagram of the author's code, intended for pneumatic tyre model axisymmetric analysis.

Characterisation of an axisymmetric tyre model

A pneumatic tyre has a complex structure and must be regarded as a heterogeneous system (Fig. 1). Three types of materials can be distinguished in a tyre:
– cord-rubber composite (ply layers, belts and chafer),

– rubber (e.g. tread, sidewall, etc.),
– steel (bead wire).

In the case of simulation of a tyre mounting on a rim or inflation, one can assume that a tyre is an axisymmetric system, *i.e.* that its points are not moving circumferentially. In such a case, only a cross section of a tyre can be considered (Fig. 2a) and only this area undergoes discretization. Although the finite elements seem to be plane, in fact they are rings with a triangular or rectangular cross-section.

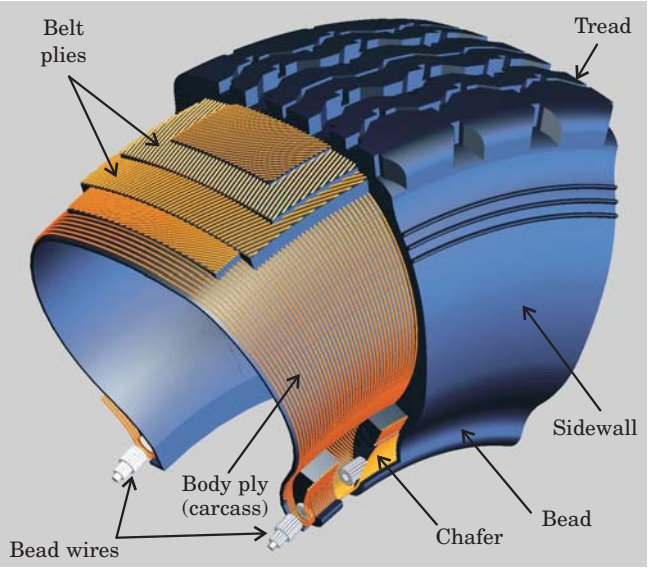

Fig. 1. The structure of a pneumatic radial truck tyre

Unlike a plane problem (2D), this one is classified as a 2.5D problem, *i.e.* there are non-zero circumferential stresses. The finite element mesh, fixing of the tyre bead and the action of internal pressure are presented in Fig. 2b. Nodes situated in the tyre plane of symmetry (yz) can move only in the radial direction.

The angle of the cord to the parallel line of the layer in a formed tyre (θ) can be calculated from the so-called "panthograph role" (HOFFERBERTH 1956):

$$\cos\,\theta = \frac{r}{r_0}\cos\,\theta_0 \tag{1}$$

where:
r_0/r – the radius of a point of a layer on a drum/in a tyre,
θ_0 – angle of a cord in a green layer.

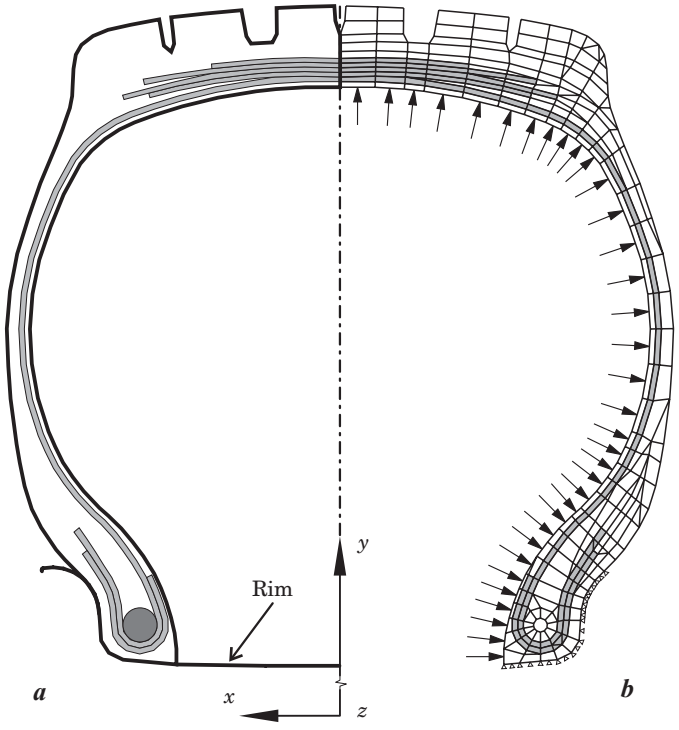

Fig. 2. An axisymmetric model of a truck tyre: *a* – cross section with layers, *b* – mesh of finite elements and boundary conditions

The cord density in a tyre layer depends on the density in a green layer placeed on a drum e_{p0}:

$$e_p = e_{p0} \frac{r_0 \sin \theta_0}{r \sin \theta} \tag{2}$$

and it allow to determine the ply cord volume fraction based on the cross section area of a cord (A_c) and the layer thickness (t):

$$v_c = \frac{e_p A_c}{t} \tag{3}$$

The fraction value provides the basis for calculation of effective material constants for a cord-rubber composite layer. Assuming that the shear modulus for cords is greater than it is for rubber, HALPIN and TSAI (1969) formula yields:

$$\begin{aligned} E_1 &= E_c v_c + E_r (1 - v_c) \\ E_2 &= \frac{E_r(1 + 2v_c)}{1 - v_c} \\ \nu_{12} &= \nu_c v_c + \nu_r(1 - v_c) \\ G_{12} &= G_r \frac{1 + v_c}{1 - v_c} \end{aligned} \tag{4}$$

where:
letters $E/G/\nu$ – denote Young and Kirchhoff moduli and Poisson ratio, respectively, and the c/r indices denote cord and rubber, respectively. Axis 1 is parallel to cord, while axis 2 denotes one that is perpendicular to it, lying on the layer plane.

In a displacement formulation of FEM, assumed in the axisymmetric tyre model, it is convenient to describe rubber properties as if it was a nearly incompressible material, as proposed by BLATZ and KO (1962).

Having determined the tangent constitutive tensor for the material (${}_0\mathbf{D}$), one can calculate the second Piola-Kirchhoff stress tensor (${}_0\mathbf{S}$) based on the known increment of Green-Lagrange strain tensor (${}_0\mathbf{E}$):

$${}_0\mathbf{S} = {}_0\mathbf{D}\,{}_0\mathbf{E} \tag{5}$$

Defining the tensor as (BROCKMAN 1986)

$${}^t_0\mathbf{H} = \frac{\partial I_3}{\partial\, {}^t_0\mathbf{C}} \tag{6}$$

where:
${}^t\mathbf{C}$ denotes Cauchy-Green deformation tensor, and I_3 – its third invariant, and taking into account the strain energy density function in the Blatz-Ko model for a nearly incompressible material, the second Piola-Kirchhoff stress tensor can be written:

$${}^t_0\mathbf{S} = \frac{\partial W}{\partial\, {}^t_0\mathbf{E}} = \mu\,[\mathbf{I} - I_3^{-0.5(\alpha+2)}\,{}^t_0\mathbf{H}] \tag{7}$$

For a rubber-type elastomer, regarded as a hyperelastic material,

$$ {}_0\mathbf{D} = \frac{\partial^2 W}{\partial\, {}^t_0\mathbf{E}\, \partial\, {}^t_0\mathbf{E}} = \frac{d\, {}^t_0\mathbf{S}}{d\, {}^t_0\mathbf{E}} \tag{8} $$

Additionally introducing a tensor of the fourth order

$$ {}^t_0\mathbf{Q} = \frac{\partial\, {}^t_0\mathbf{H}}{\partial\, {}^t_0\mathbf{C}} \tag{9} $$

yields a tensor of incremental constitutive relationship (tangent)

$$ {}_0\mathbf{D} = \mu(a + 2) I_3^{-0.5(a+4)}\, {}^t_0\mathbf{H}\, {}^t_0\mathbf{H} - 2\mu I_3^{-0.5(a+2)}\, {}^t_0\mathbf{Q} \tag{10} $$

Material constants μ and a are determined from the results of experiments performed for each type of rubber. In axisymmetric problems – ${}^t_0C_{31} = {}^t_0C_{32} = 0$ and ${}^t_0C_{33} = 1$.

Material constants matrix (constitutive matrix) is constructed in accordance with the principles of composite material mechanics (JONES 1975).

Node displacements in the finite element axisymmetric tyre model are determined by the incremental method with iterations, based on a matrix equation (BATHE 1982):

$$ ({}^t_0\mathbf{K}_L + {}^t_0\mathbf{K}_{NL})\, \mathbf{u}^{(i)} = {}^{t+\Delta t}\mathbf{R} - {}^{t+\Delta t}_0\mathbf{F}^{(i-1)} \tag{11} $$

where:
$\mathbf{u}^{(i)} = {}^{t+\Delta t}\mathbf{u}^{(i)} - {}^{t+\Delta t}\mathbf{u}^{(i-1)}$, ${}^{t+\Delta t}\mathbf{u}^{(0)} = {}^t\mathbf{u}$, ${}^{t+\Delta t}_0\mathbf{F}^{(0)} = {}^t_0\mathbf{F}$, whereas ${}^{t+\Delta t}\mathbf{R}$ represents a vector of nodal external forces which act on a tyre. The index in brackets denotes the number of iteration.

A linear stiffness matrix ${}^t_0\mathbf{K}^L$, non-linear stiffness matrix ${}^t_0\mathbf{K}_{NL}$ and a vector of internal forces ${}^t_0\mathbf{F}$ are calculated from a matrix (linear – ${}^t_0\mathbf{B}_L$ and non-linear – ${}^t_0\mathbf{B}_{NL}$) which occurs in strain-displacement relations, incremental constitutive matrix ${}_0\mathbf{D}$ as well as matrix ${}^t_0\mathbf{S}$ and vector ${}^t_0\hat{\mathbf{S}}$, made up of the components of the second Piola-Kirchhoff stress tensor. It must be stressed that matrix ${}^t_0\mathbf{B}_L$ is the sum of two components: ${}^t_0\mathbf{B}_{L0}$ with constant terms and ${}^t_0\mathbf{B}_{L1}$ with the terms dependent on the level of displacements, *i.e.* which change during the incremental-iterative process.

Block diagram of the author's code

The code intended for analysis of axisymmetric models of pneumatic tyres has been developed by the author over many years. Due to the complicated structure of pneumatic tyres, the code is considerably large, with ca. 4000 lines in the FORTRAN language (excluding comment lines). An input data file for the author's code is generated with preprocessing tools, described by PELC (1995b). The data are grouped in sections with specific names (numbers of elements and nodes, node coordinates, types of elements, materials assigned to elements, boundary and load conditions) and have a structure typical for FEM codes, except a significant difference in description of the model material parameters. The data constitute a section in an input data file and contain: name of the material, thickness of the layer (t), cord cross section area (A_c), density of cord in a layer on the drum (e_{p0}), angle of cord to the parallel line of the tyre building drum (θ_0), the layer radius on the drum (r_0), the Young modulus of the cord (E_c), Poisson ratio for the layer rubber or the a parameter for the Blatz-Ko rubber model (ν_r, a), shear modulus for the layer rubber or parameter μ for the Blatz-Ko rubber model (G_r, μ). (*cf.* PELC 2007). Unlike commercial FEM codes, data for the author's code do not contain the values of cord-rubber layer effective constants because for a specific tyre composite they depend on the distance of a layer point from the tyre axis of rotation. The values of those constants are calculated in the relevant subroutine for consecutive elements and material parameter matrices are constructed.

Due to the three selected types of materials in tyre, the code block diagram (Fig. 3) is divided into three paths, with that related to the cord-rubber composite being the most complex. A bimodular characteristic of the cord was assumed with a high value of the Young modulus for stretching and an extremely small value for compression. Therefore, two matrices of material constants are prepared and which of them will be used depends on the state of the current stress in cord, observed during the tyre incremental loading. Due to the assumed rotational symmetry of the problem (i.e. zeroing of deformations E_{xz} and E_{yz}), 4×4 matrices are obtained from full constitutive matrices **D** and **D'**.

An non-inflated tyre has a very low stiffness. Therefore, load increments during the initial phase of simulation must be very small for the iteration process to be convergent. With increasing internal pressure, the system becomes increasingly stiff and load increments may be increased. The author's computation code employs the arc-length control method as presented by CRISFIELD (1981), which makes it possible to automatically match the length of the load step with the degree of non-linearity of the equilibrium path and helps pass through so-called "limit points" (BADUR 1979). The load level in the

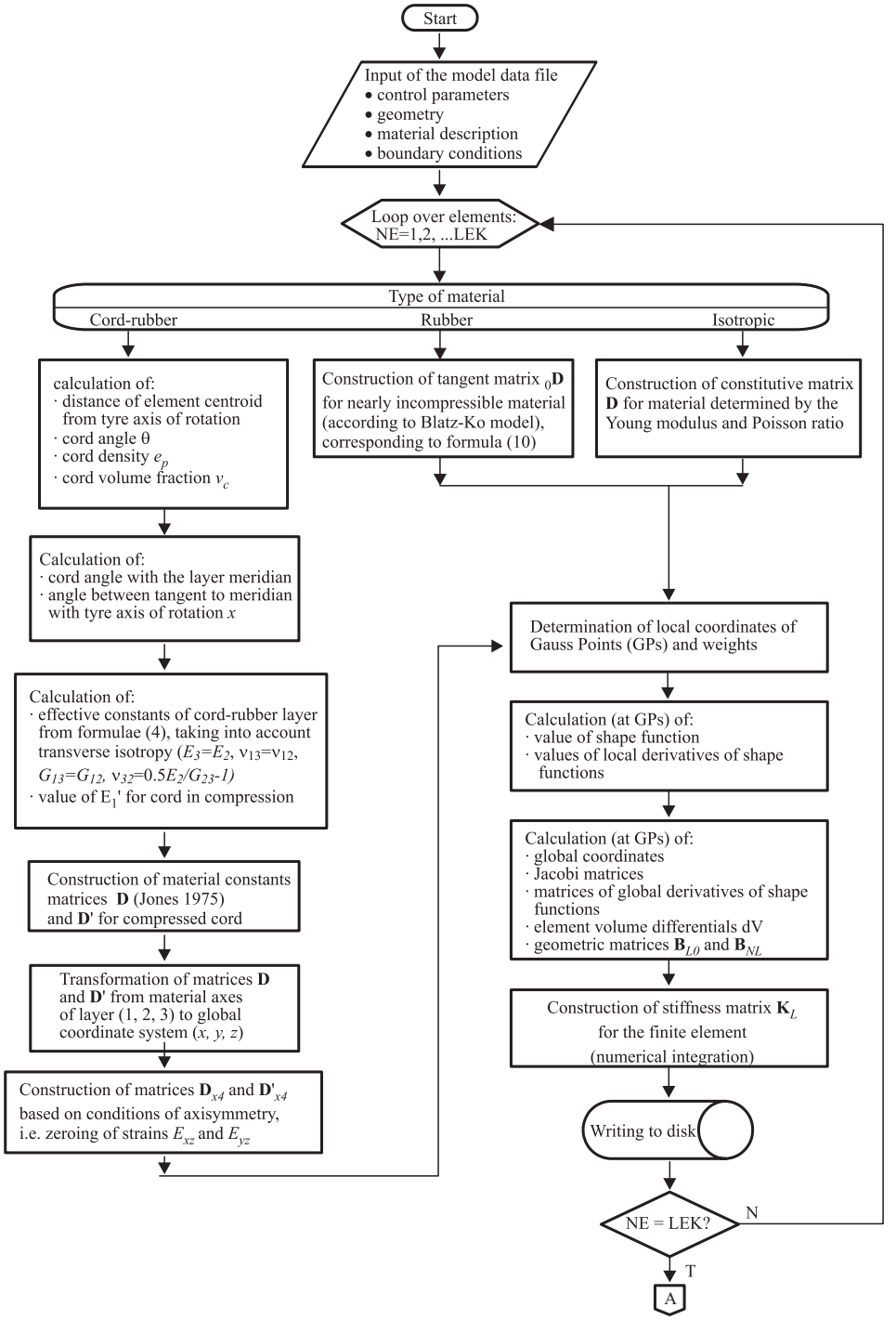
Start
Input of the model data file
• control parameters
• geometry
• material description
• boundary conditions
Loop over elements:
NE=1,2, ...LEK
Type of material
Cord-rubber
Rubber
Isotropic
calculation of:
· distance of element centroid from tyre axis of rotation
· cord angle θ
· cord density e_p
· cord volume fraction v_c
Construction of tangent matrix ${}_0\mathbf{D}$ for nearly incompressible material (according to Blatz-Ko model), corresponding to formula (10)
Construction of constitutive matrix **D** for material determined by the Young modulus and Poisson ratio
Calculation of:
· cord angle with the layer meridian
· angle between tangent to meridian with tyre axis of rotation x
Calculation of:
· effective constants of cord-rubber layer from formulae (4), taking into account transverse isotropy ($E_3=E_2$, $\nu_{13}=\nu_{12}$, $G_{13}=G_{12}$, $\nu_{32}=0.5E_2/G_{23}-1$)
· value of E_1' for cord in compression
Construction of material constants matrices **D** (Jones 1975) and **D'** for compressed cord
Transformation of matrices **D** and **D'** from material axes of layer (1, 2, 3) to global coordinate system (x, y, z)
Construction of matrices $\mathbf{D}_{x4}$ and $\mathbf{D}'_{x4}$ based on conditions of axisymmetry, i.e. zeroing of strains E_{xz} and E_{yz}
Determination of local coordinates of Gauss Points (GPs) and weights
Calculation (at GPs) of:
· value of shape function
· values of local derivatives of shape functions
Calculation (at GPs) of:
· global coordinates
· Jacobi matrices
· matrices of global derivatives of shape functions
· element volume differentials dV
· geometric matrices $\mathbf{B}_{L0}$ and $\mathbf{B}_{NL}$
Construction of stiffness matrix $\mathbf{K}_L$ for the finite element (numerical integration)
Writing to disk
NE = LEK?
N
T
A

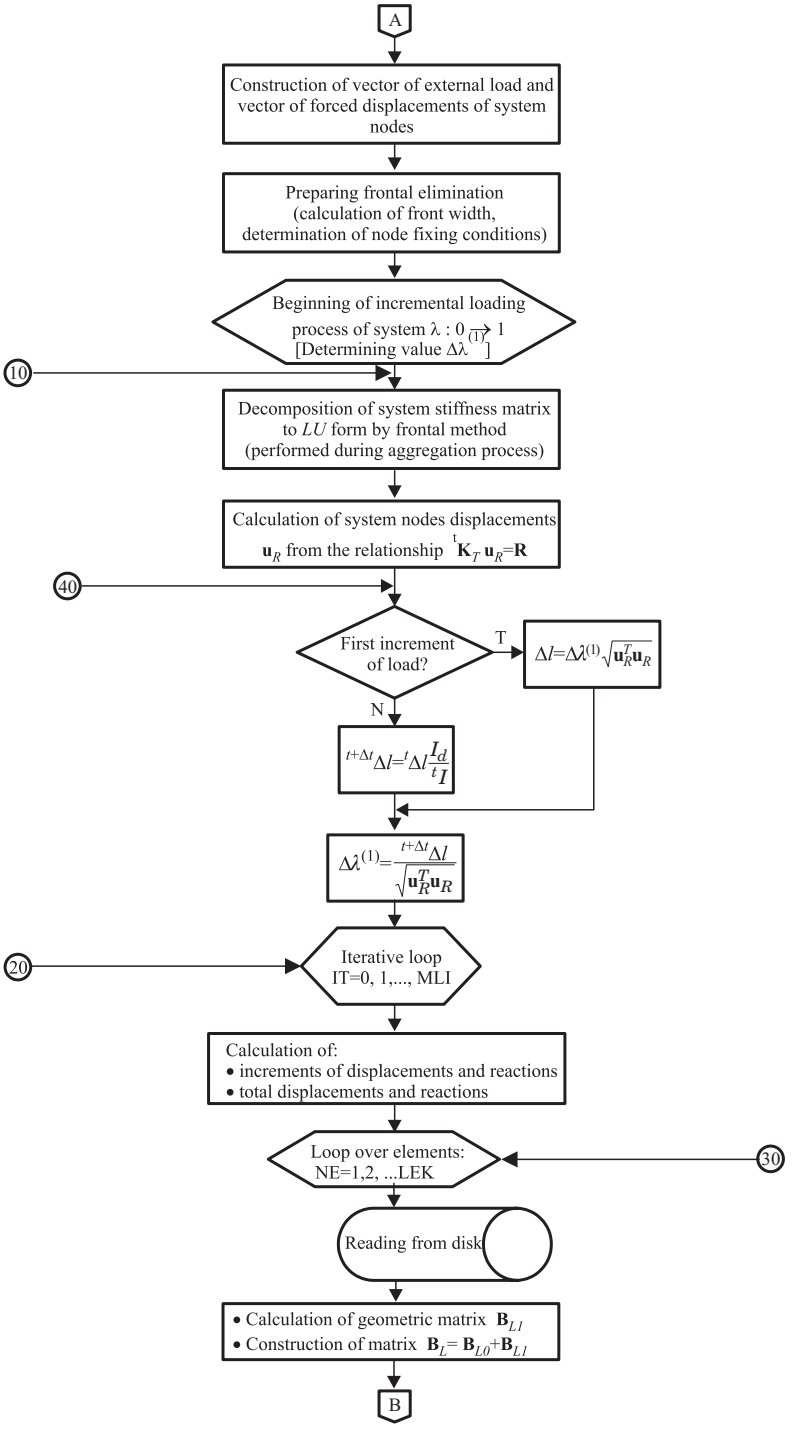
A
Construction of vector of external load and vector of forced displacements of system nodes
Preparing frontal elimination (calculation of front width, determination of node fixing conditions)
Beginning of incremental loading process of system λ : 0 (1) 1 [Determining value Δλ(1)]
10
Decomposition of system stiffness matrix to LU form by frontal method (performed during aggregation process)
Calculation of system nodes displacements $\mathbf{u}_R$ from the relationship ${}^{t}\mathbf{K}_T\,\mathbf{u}_R=\mathbf{R}$
40
First increment of load?
T
$\Delta l=\Delta\lambda^{(1)}\sqrt{\mathbf{u}_R^T\mathbf{u}_R}$
N
${}^{t+\Delta t}\Delta l={}^{t}\Delta l\frac{I_d}{{}^{t}I}$
$\Delta\lambda^{(1)}=\frac{{}^{t+\Delta t}\Delta l}{\sqrt{\mathbf{u}_R^T\mathbf{u}_R}}$
20
Iterative loop IT=0, 1,..., MLI
Calculation of:
• increments of displacements and reactions
• total displacements and reactions
Loop over elements: NE=1,2, ...LEK
30
Reading from disk
• Calculation of geometric matrix $\mathbf{B}_{L1}$
• Construction of matrix $\mathbf{B}_L=\mathbf{B}_{L0}+\mathbf{B}_{L1}$
B

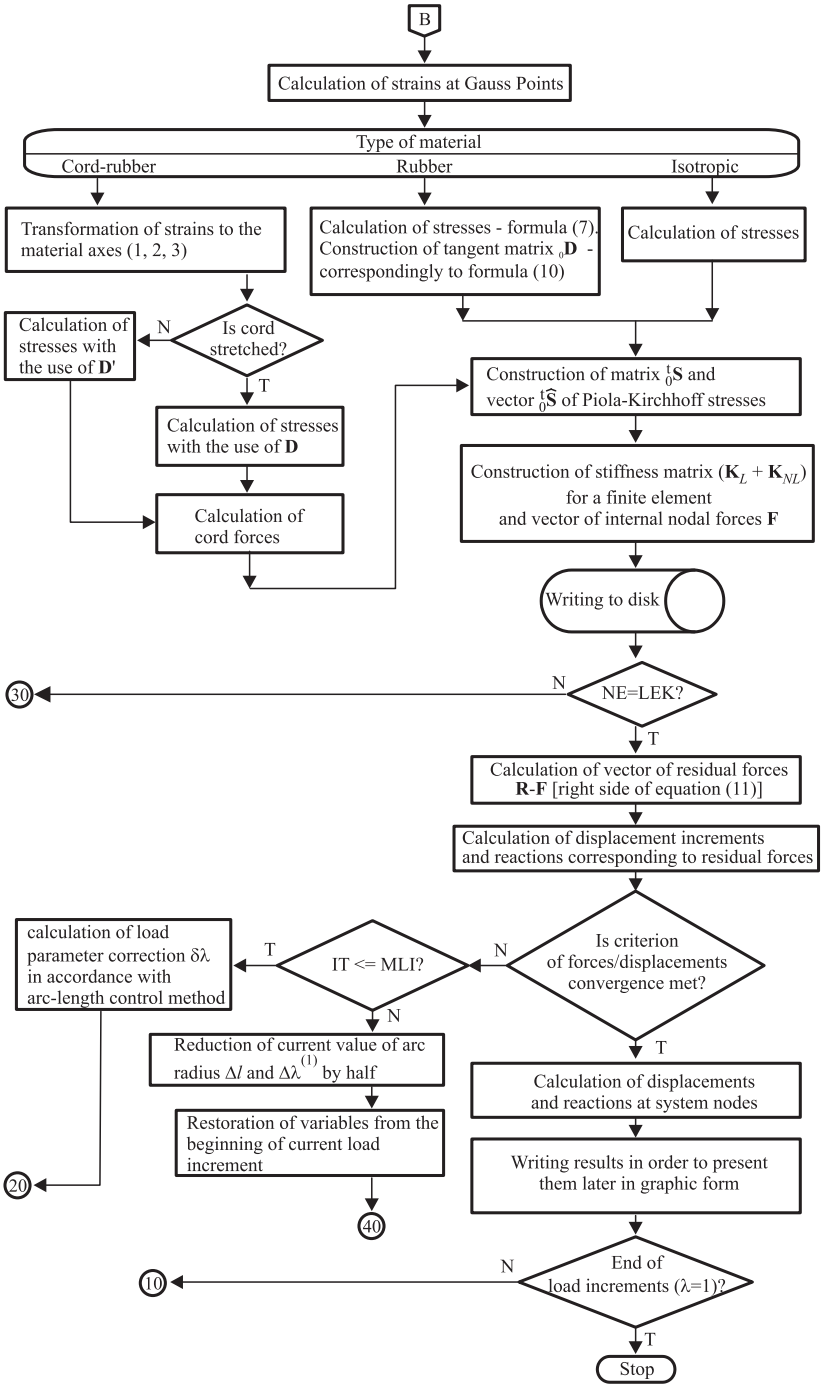

Fig. 3. Block diagram of the code for analysis of axisymmetric deformations of pneumatic tyres

method is controlled by a dimensionless parameter λ, which is equal to zero at the beginning of the incremental process and equal to one at its end. At the beginning of the first load increment, the value of load increment $\Delta\lambda^{(1)}$ is set arbitrarily. The radius of arc Δl, which leads to the path of equilibrium, is calculated with the use of displacement vector of all the nodes of the system ($\mathbf{u}_R$) and the information on the number of iterations performed in the previous increment ${}^tI$, whereas I denotes the desired number of iterations. Matrix ${}^t\mathbf{K}_T$ denotes the tangent matrix of the system. It is possible in the subprogram which performs the iteration process to apply two criteria of the process convergence. One of them is based on the Euclidean norm of the nodal residual force vector and the other is related to the iterative displacement increment.

Illustrative calculation results

The author's code can be used to analyse a tyre under axisymmetric loading (internal pressure, centrifugal force of inertia). It is also possible to apply an axisymmetric displacements of a tyre bead nodes. The necessity for axial displacement of the bead nodes towards the tyre's plane of symmetry (y,z) results from a greater spacing of beads in the vulcanisation form than after the tyre has been mounted on a rim. Radial displacements stem from the necessity of the tyre clamping on the rim during the mounting process in order to create the proper friction necessary to transfer the moment of force from the drive and braking and to ensure air-tightness in the contact area between the bead and rim.

By using post-processing tools (PELC 1995b), the author's code can generate the following results in a graphic form:
– a tyre profile before and after deformation,
– element mesh after deformation,
– history of displacement of two characteristic points of a tyre,
– diagrams of force values in cords,
– diagrams of elastic strain energy density in layered materials,
– elastic strain energy distribution in a tyre cross section,
– a map of maximal values of shear strain in a tyre cross section,
– a map of maximal Cauchy stress in sections perpendicular to the tyre profile.

The values presented in diagrams and maps are calculated at the centroids of a finite elements based on the respective values in Gauss points.

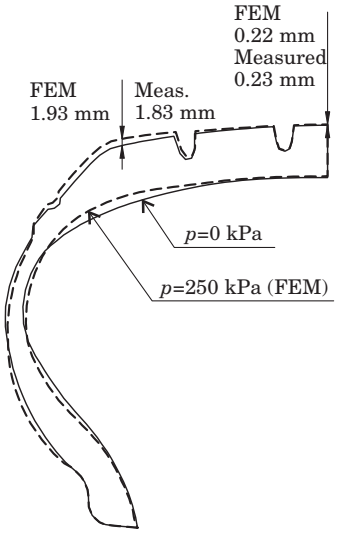

Fig. 4. A passenger car tyre. Initial profile and after inflating to the pressure of 250 kPa

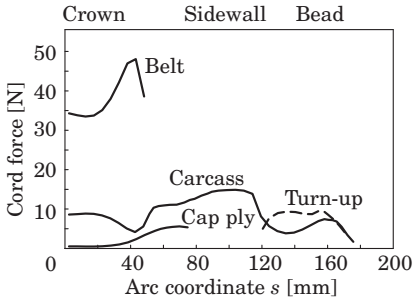

Fig. 5. A passenger car tyre. A diagram of forces in layer cords caused by a pressure of 250 kPa

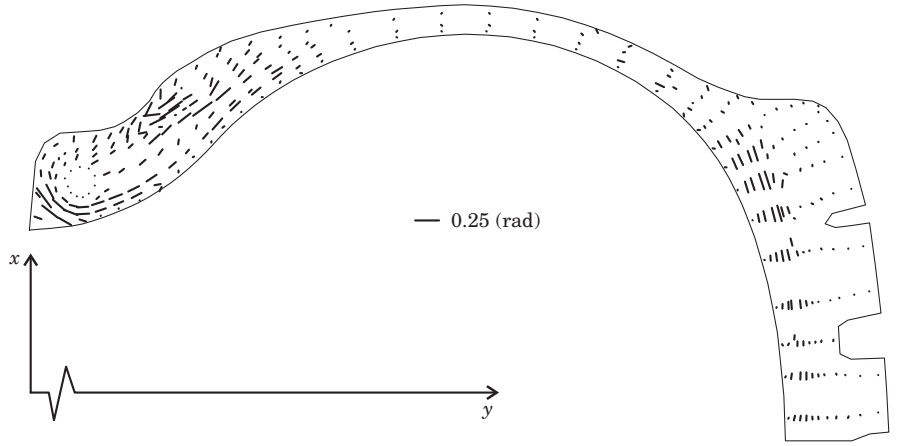

Fig. 6. A truck tyre: a map of extreme values of shear strain in an inflated tyre (p = 800 kPa)

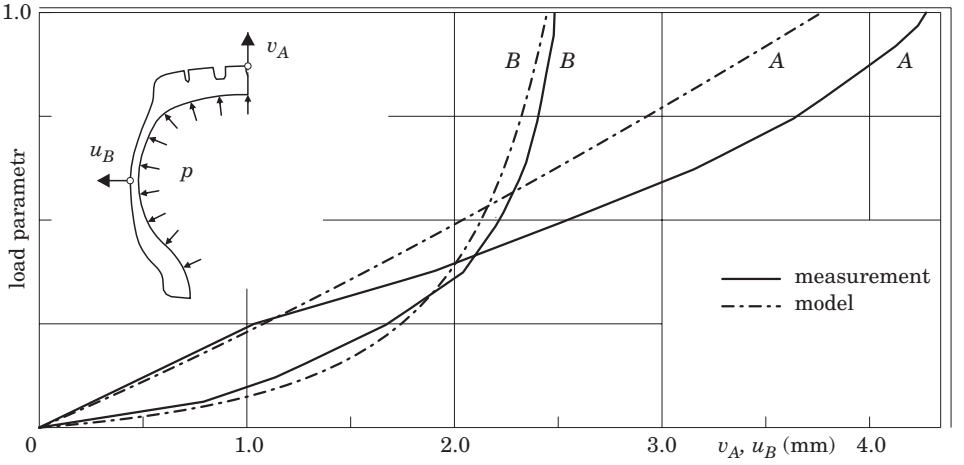

Fig. 7. A truck tyre. A diagram of displacements of characteristic points of a tyre as a function of internal pressure

Summary and conclusions

Pneumatic tyre deformation modelling and strength analysis is a complex issue due to the heterogeneity and non-linear nature of the system. In this case, the method of finite elements seems to be the only tool for reliable modelling of the behaviour of such a system. Due to the heterogeneous structure of a tyre, the block diagram of a code for an axisymmetric tyre model analysis has a complex structure resulting from the distinguishing of three types of materials: cord-rubber composite, nearly incompressible rubber and steel. The geometric non-linearity of a tyre and physical non-linearity of rubber requires that the stiffness matrix of the system should be updated during the process of loading; the incremental-iterative procedure, visible in the block diagram, is linked with it. The author's computer code enables analysis of both passenger tyres and truck tyres.

Accepted for print 25.09.2009

References

BADUR J. 1979. *Efektywne wyznaczanie punktów granicznych w nieliniowej mechanice konstrukcji.* IV Konf. Metody Komputerowe w Mechanice Konstrukcji, tom II. Koszalin, kwiecień, s. 203–209.

BATHE K.J. 1982. *Finite element procedures in engineering analysis*. Prentice-Hall, Englewood Cliffs, N.Y.

HALPIN J.C., TSAI S.W. 1969. *Effects of environmental factors on composite materials*. AFML-TR, pp. 67–423.

HOFFERBERTH W. 1956. *Zur Festigkeit des Luftreifens*. Kautschuk u. Gummi. 9: 225–231.
JONES R.M. 1975. *Mechanics of composite materials*. McGraw-Hill London
PELC J. 1992. *Large displacements in tire inflation problem*. Engineering Transactions, 40(1): 103–113.
PELC J. 1995a. *Pomiary i analiza metodą elementów skończonych opony całostalowej do samochodów ciężarowych podczas pompowania*. Acta Acad. Agricult. Tech. Olst. Aedificatio et Mechanica, 26: 15–27.
PELC J. 1995b *Pre-Processing and Post-Processing in Pneumatic Tire Analysis by the Finite Element Method*. Acta Acad. Agricult. Tech. Olst. Aedificatio et Mechanica, 26: 29–36.
PELC J. 1995c. *Orthotropic material model in pneumatic tire analysis*. Proceedings of the XII Polish Conference on Computer Methods in Mechanics, Warsaw–Zegrze, Poland, 9–13 May 1995, pp. 271–272.
PELC J. 2000. *Material Modelling in Cord-Rubber Structures*. Kautsch., Gummi Kunstst. 53(10): 561–565.
PELC J. 2002. *Static three-dimensional modelling of pneumatic tyres using the technique of element overlaying*. Proc. Instn Mech. Engrs, Part D: J. Automobile Engineering, 216(9): 709–716.
PELC J. 2007. *Modelowanie skończonych deformacji opon pneumatycznych,* Rozprawy i Monografie 134, Wyd. UWM.

TECHNICAL SCIENCES
Abbrev.: Techn. Sc., No 12, Y 2009

DOI 10.2478/v10022-009-0017-4

ALGORITHMS APPLIED IN TURBOMACHINE MODELING WITH VARIABLE INPUT DATA

Paweł Pietkiewicz

Chair of Mechanics and Machine Design
University of Warmia and Mazury in Olsztyn

K e y w o r d s: modeling, heuristic, rotor, bearing.

A b s t r a c t

The idea of the allowance method for the input data uncertainties in the turbo-machines rotor-bearings systems modelling are contained in the paper. The author presents selected calculation results, when two different generation algorithms of the random variability course of the shear force, that imposes the rotor shaft loading, have been applied. The initial numerical research results displayed in this paper allow for acknowledge of such tools' kind usability, however they also signal the difficulties occuring in the interpretation of the alanysed systems answers, received this way.

ALGORYTMY STOSOWANE W MODELOWANIU MASZYN WIRNIKOWYCH Z UWZGLĘDNIENIEM ZMIENNOŚCI DANYCH WEJŚCIOWYCH

Paweł Pietkiewicz

Katedra Mechaniki i Podstaw Konstrukcji Maszyn
Uniwersytet Warmińsko-Mazurski w Olsztynie

S ł o w a k l u c z o w e: modelowanie, heurystyka, wirnik, łożyskowanie.

A b s t r a k t

Artykuł opisuje ideę uwzględniania niepewności danych wejściowych w modelowaniu układów wirnik-łożyska w maszynach wirnikowych. Przedstawiono wybrane rezultaty obliczeń z zastosowaniem dwóch różnych algorytmów generowania losowego przebiegu zmienności siły poprzecznej obciążającej wał wirnika. Wyniki wstępnych badań numerycznych pozwalają na potwierdzenie przydatności wykorzystywanych narzędzi, jednak sygnalizują także występujące trudności w interpretacji otrzymywanych tą drogą odpowiedzi analizowanych układów.

Introduction

In view of the ongoing progress in calculation technology, numerical calculations are popularly applied in various types of scientific research. Despite a very high level of advancement, further development is needed due to the following reasons:

- difficulties are encountered in the process of building mathematical models that describe physical phenomena with sufficient accuracy,
- the selection of an adequate model from the range of the existing models and the models proposed by engineering software designers is a difficult process,
- as a calculating machine, a computer operates based on deterministic algorithms, and every time the performed calculations are replicated, a single, identical result is produced for the same set of input data,
- as regards various models and numerical tools, the results are unknown when input data are modified during calculations.

In view of the above problems, the results of numerical calculations are often difficult or impossible to compare with the outcome of experiments carried out on a real object where the results of successive replications often differ not only due to the inaccuracy of measurements but also due to the variability of experimental conditions. This paper discusses the existing algorithms for generating stochastic variable input data used in numerical calculations. The objective of this long-term study was to validate the suitability of the analyzed algorithms for turbomachine modeling and to bring the results of numerical calculations closer to experimental data.

The analyzed model and the scope of the study

Figure 1 presents the model analyzed in this paper. It is a single-mass, inboard rotor with a journal bearing. Concentrated mass is found in the mid-length of the rotor in the form of a disc. The rotor is subjected to a single

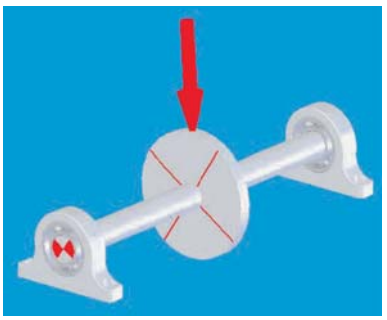

shaft length:	1.4 m
shaft diameter:	0.1 m
disc diameter:	0.4 m
disc thickness:	0.1 m
rotor weight:	179 kg

Fig. 1. The analyzed model of a rotor subjected to rotating transverse force

variable transverse force which rotates at a set rotational speed when applied at the mid-length of the rotor. The known ratio of the rotational speed of that force to the rotor's rotational speed is marked with the symbol x. This study presents the results for $x = 1$.

The objective of the performed calculations was to determine the effect of changes in transverse force during the calculations on the trajectory of the rotor shaft axis and its properties, mostly the direction of rotation, shape, angle of inclination and the effect on the frequency and amplitude of rotor axis vibrations. The observed trajectories will apply to the rotor axis in the cross-section of the applicable transverse force.

As regards physical phenomena applicable to turbomachines, the effect of changes in force value on resonance and the loss of rotor-bearing stability had to be determined. The objective of the experiment was to:

- determine the effect of stochastic variability in transverse force on the trajectory of the rotor shaft axis (PIETKIEWICZ 2007),
- investigate the response of the rotor-bearing system in the form of rotor vibrations, subject to the shaft's rotational speed, at variable transverse force, and to evaluate the compatibility of the resulting functions with the functions mapped for constant force values (PIETKIEWICZ 2007),
- compare resonance phenomena occurring at constant and variable transverse force (PIETKIEWICZ 2007),
- compare the phenomena accompanying the loss of rotor-bearing stability (PIETKIEWICZ 2008),
- model the location where the rotor's moving parts rub against the fixed components of the modeled object (PIETKIEWICZ 2009) (in an actual object, e.g. against the housing).

The applied algorithms for generating stochastic processes

Numerical calculations were performed with the use of tools developed and applied by the Szewalski Institute of Fluid-Flow Machinery of the Polish Academy of Sciences in Gdańsk. The solver was the NLDW software described in many publications on turbomachine modeling (KICIŃSKI 2005, PIETKIEWICZ et al. 2006, PIETKIEWICZ 2007), adapted to account for changes in external load applied to a moving rotor. The post-processor were Matlab applications for processing and visualizing calculation results. To account for the stochastic variation of transverse force during rotor operation, a pre-processor had to be build to generate successive values of the load applied to the rotor in accordance with various algorithms. The program generated a series of numbers corresponding to the stochastic variation of the transverse force applied to the rotor at preset rotor operating parameters:

– rotational speed n,
– nominal force P,
– scope of possible changes in transverse force $|\Delta P|$,
– maximum change in force value in the successive stage of generating the force function $|\delta_{max}P|$,
– ratio of the rotational speed of the applied force to rotor speed x,
– angle of shaft rotation $\Delta\alpha$ which leads to a change in force value P.

Transverse force functions were generated according to two types of algorithms. The first algorithm concept is presented in Figure 2. The algorithm generating stochastic variations "without limitations" accounts for random changes in value in the preset range of $-\Delta P$ to ΔP in each calculation step. Figure 2 presents a situation in which nominal force value $P = 500$ N changes in the range of ± 20%, starting at rotational angle $\alpha = 7.5^{o}$. According to the described algorithm, a change in force value, e.g. from maximum to minimum, is possible (but not necessary) within one step (a section of one shaft revolution) equal to $\Delta\alpha$. In Figure 2, the above can be observed when the angle of rotation changes from 15° to 17.5°.

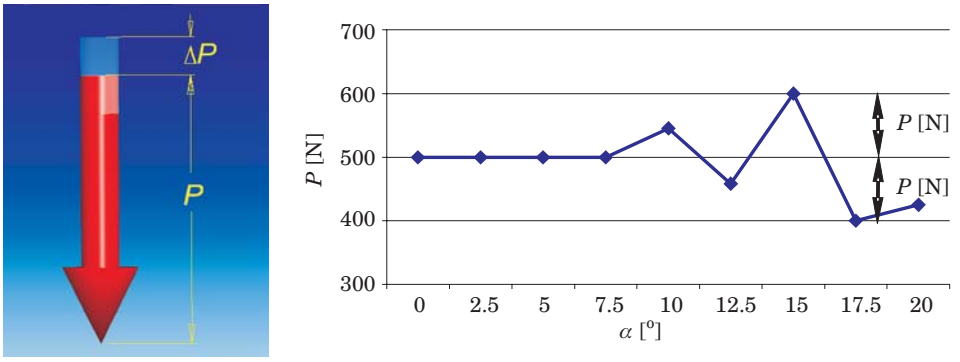

Fig.2. Conceptual algorithm generating a transverse force function "without limitations"

Figure 3 illustrates an algorithm generating a stochastic process "with additional limitations". The additional value $\delta_{max}P$ denotes the maximum scope of the successive change in the transverse force value when the shaft is rotated by angle $\Delta\alpha$. Any changes in the function value, from the maximum value limited by $P + \Delta P$ to the minimum value determined by $P - \Delta P$, are impossible when the shaft rotates only by angle $\Delta\alpha$. In the example shown in Figure 3, the algorithm becomes applicable starting with angle $\alpha = 2.5^{o}$, and the value of the force changes from maximum to minimum within the range of 7.5° to 17.5°. Owing to its stochastic nature, the illustrated example is purely theoretical and improbable.

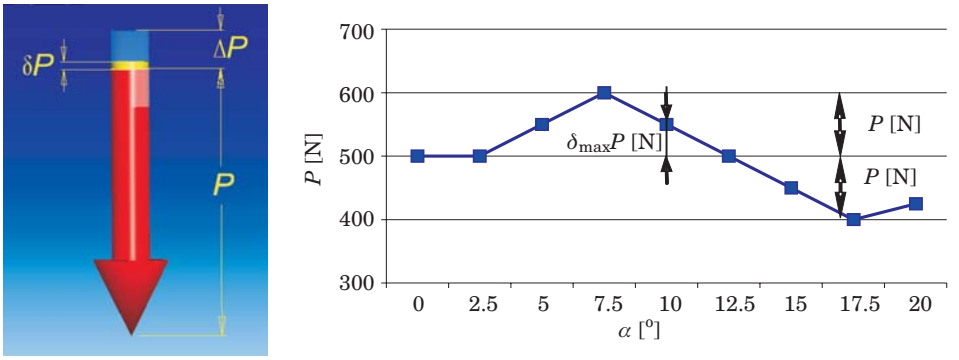

Fig. 3. Conceptual algorithm generating a transverse force function "with additional limitations"

A minimal number of steps in pre-processor operation, designed to change the transverse force value from maximum to minimum, is expressed by the following relationship (1):

$$k = \frac{2 \cdot \Delta P}{\delta_{\max} P} \tag{1}$$

The limitation to a single change in the transverse force value was introduced to account for the physical possibility of change in the force value when the rotor moves by angle $\Delta\alpha$. In calculations applicable to high rotational speeds and small angles $\Delta\alpha$, which determine the frequency of change in the value of the force applied to the rotor, a physical explanation could be difficult to formulate for a model "without limitations".

A close correlation exists between the described algorithms. If the algorithm generating a stochastic process "with additional limitations" permits a change in the value of the transverse force from maximum to minimum in one step ($k = 1$), the relationship (1) may be transformed to that shown in (2), which corresponds to an algorithm "without limitations":

$$\delta_{\max} P = 2 \cdot \Delta P \tag{2}$$

In view of relationship (2), the algorithm generating the transverse force function "without limitations", which allows for a single-step change in the value of force P from minimum to maximum (or the reverse), will be referred to as algorithm K-1 in subsequent parts of this study. Since the algorithm "with

additional limitations" sets the m number of steps required to change the force value from minimum to maximum (or the reverse), this algorithm will be referred to as K-m, where m indicates the minimum number of generator steps needed to change the force value between its extremes, and m is an integer that satisfies the condition $m > 1$.

Results

The use of numerical calculations with deterministic algorithms (e.g. in the form of an NLDW program) for modeling a rotor subjected to a transverse force, as shown in Figure 1, produces results in the form illustrated in Figure 4.

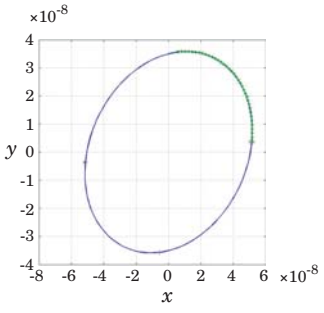

Fig. 4. Model trajectory of the rotor axis at the cross-section where the force is applied

The trajectory of the rotor's axis of symmetry in a horizontal plane is a clearly defined ellipse or, in special cases, a different plane figure (KICIŃSKI 2005, PIETKIEWICZ 2007). The effect of changes in the transverse force applied to the rotor may be described with the use of the existing numerical methods only as regards the determination of the modeled system's response in the form presented in Figure 5.

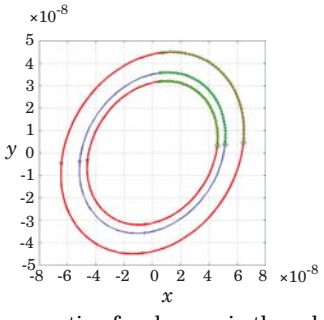

Fig. 5. A quasi-static approach to accounting for changes in the value of the transverse force applied to the rotor

Assuming that the system is subjected to a force in the range of F_{min} to F_{max}, when changes in the value of the force applied to the rotor are taken into account, the system's probable response to the load should be within the range marked by two red trajectories (Fig. 5). They correspond to the system's response to load which varies subject to a preset range of values. This hypothesis does not account for changes in load value during the calculations which correspond to the motion of the rotor shaft. The results accounting for changes in the value of the transverse force during the modeled rotation are presented below. The relevant calculations were performed on the following assumptions:

- the rotor is ideally balanced,
- the rotational speed of the shaft equals n = 3000 rpm,
- the value of the force applied at node 8 is P = 500 N,
- the maximum deviation of force P is ΔP = 100 N (20%),
- the angle of the force change interval is $\Delta\alpha$ =2.5°,
- the ratio of angular velocity of the transverse force to the shaft is x = 1; 2; 0.5,
- oil viscosity is constant.

Calculations using algorithm *K*-1 for generating variable value of force *P*

For the needs of the presented calculations, it has been assumed that a force with a nominal value of P = 500 N, variable in a range of $\Delta P = \pm 100$ N, rotates in accordance with the rotor as regards rotational speed. At the assumed speed of n, the rotor moves at the speed of 50 revolutions per second, producing vibration frequency of 50 Hz. This case will be regarded as the base case in subsequent calculations, and it is presented in Figure 6. In the generated figure drawings, the post-processor registers the results of the rotor's last 6 rotations for which the calculations have been performed.

A hodograph of the transverse load applied to the rotor at mid-length is presented in the top left corner of the table. Changes in the projection of the vector of force P, in one of the adopted directions of the coordinate system, are shown in the top right corner. The rotor-bearing system's response to load is presented in the center in the form of a trajectory of the rotor shaft axis in a transverse plane where force P was applied. Changes in shaft displacement projection in one of the directions of the coordinate system are also illustrated in the center of the table. The third row contains the results of a spectrum signal analysis (fft) of vibrations at a point shared by the rotor axis and the transverse plane where force P rotates. The system's response is marked by an

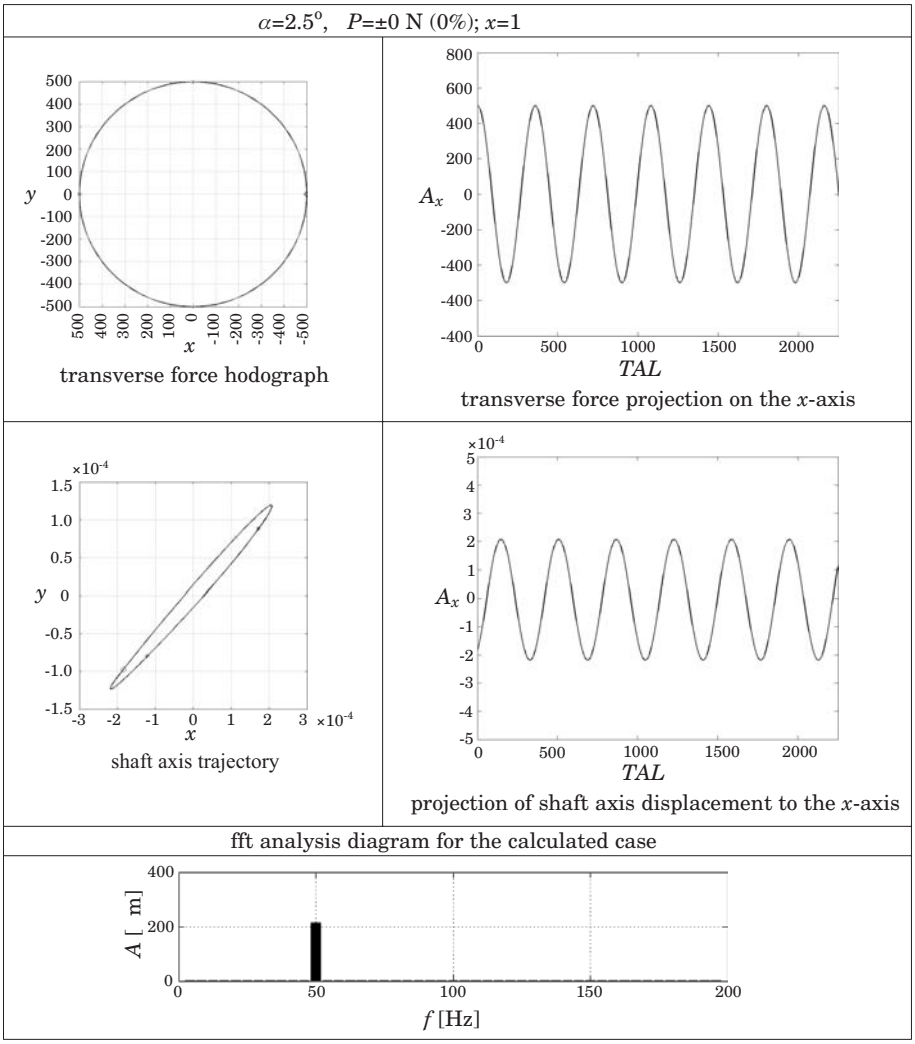

Fig. 6. Calculation results for the base case

ellipse with a clearly defined contour. The lines generated by the calculations of 6 rotor revolutions overlap, pointing to highly stable results, a correct model and its deterministic character.

Figure 7 presents the results of identical calculations performed on the assumption that force P changes its value within the range of 10% of its nominal value, as per algorithm K-1. The force vector hodograph in Figure 7 clearly indicates that the value of force P changes during rotation. The projection

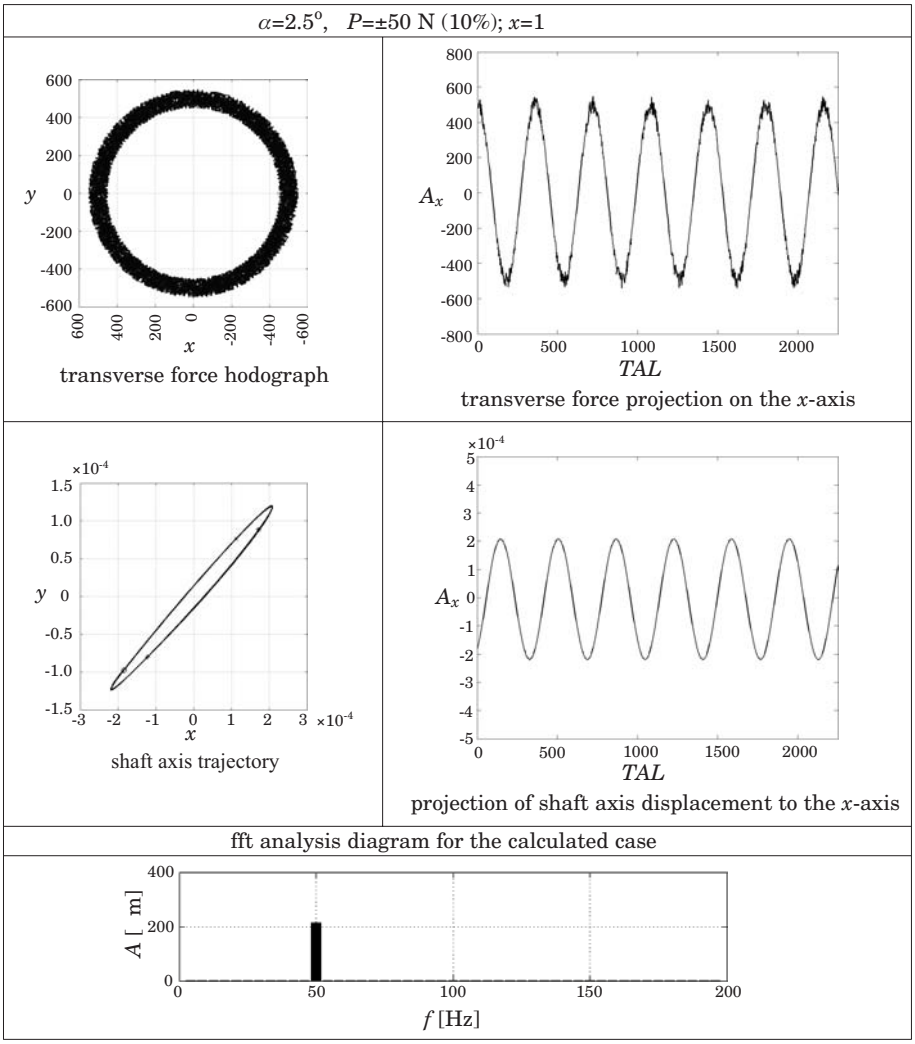

Fig. 7. Calculation results for $\Delta P = \pm 50$ N (10%)

of force on the x-axis shows "disturbances" in the sinusoidal pattern of the curve in the area of the relative extremum. The contour of the trajectory of the rotor shaft axis is visibly thicker in comparison with the base case. The above is due to the fact that the trajectory of the observed point is not repeated in the transverse plane in the successive 6 revolutions. The displacement between the ellipses is negligent, and the resulting changes are not noticeable in the diagram of vibration projections on the x-axis. The vibration component, drawn as the

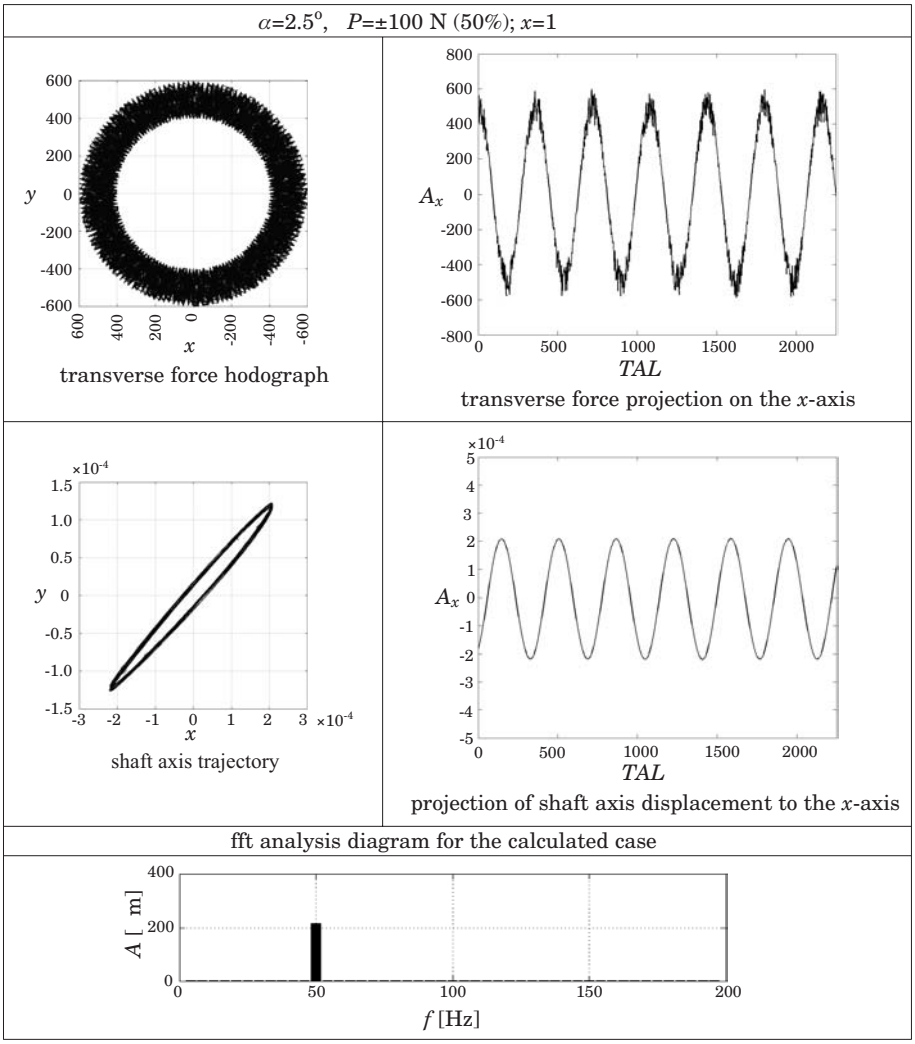

Fig. 8. Calculation results for $\Delta P = \pm 100$ N (20%)

spectrum of vibration signals, is maintained at a frequency of 50 Hz. A different frequency of rotor axis vibrations is not revealed.

In Figure 8, which lists calculation results for case $\Delta P = \pm 100$ N, the value of force P clearly varies during revolution in comparison with case $\Delta P = \pm 50$ N. In the projection on the x-axis, the disturbances in the sinusoidal pattern are visible not only in the area of the relative extremum, but also on the edges of the harmonic function. The above implies that the range of random changes in the value of force P in the direction of the x-axis is comparable with the change

resulting from the harmonic function. The system's response is an ellipse with a clearly displaced contour. The projection of the displacement on the x-axis and the fft analysis are not sufficiently sensitive to deviations in the value of force P for the changes to become observable to the naked eye.

Calculations using algorithm *K-m* for generating variable force *P*

The experiment was carried out for algorithms K-2, K-4, K-10 and K-20. The applied symbols indicate the minimum number of steps required to change the value of force P from minimum to maximum, or the reverse (point 2).

Figure 9 presents sample hodographs of transverse force vectors obtained with the use of set algorithms for generating stochastic variations in the value of force P. The maximum value has been adopted at $|\Delta P| = 0.2P$. $|\delta_{\max} P|$ values were determined by the value of m in each algorithm.

As demonstrated by the hodographs of force P, the diagrams produced with the application of algorithms K-10 and K-20 differ in "structure". As regards the system's response to the applied variable load according to algorithm K-10, the trajectory of the rotor axis clearly differs from the remaining trajectories.

Additional calculations were performed to generate stochastic variations in the value of force P according to algorithms K-10 and K-20. Selected results are presented in Figures 10-11.

Every replication of the process generating stochastic variations in the value of force P produces completely different results. The hodographs of the transverse force applied to the rotor, as presented in Figure 10, are apparently identical, yet a spectrum analysis of the results produced by one of the calculations shows noise introduced by the random variability of the transverse force. The hodographs of force vectors generated in three successive replications, as presented in Figure 11, show a completely different pattern of variations in the value of the transverse force. In the first process generating the diagram of force P values, a cluster of values was noted in the area of the highest allowable value of force P, while the second replication produced a more event distribution of stochastic values. In the third replication, the contour of the force diagram was even more clearly defined in the area of both extreme values. The trajectories of the modeled system's response to load are completely different. Disturbances in the shape of the ellipse are visible in the third replication. The above could suggest that the variability of input data over time has a significant effect on calculation results.

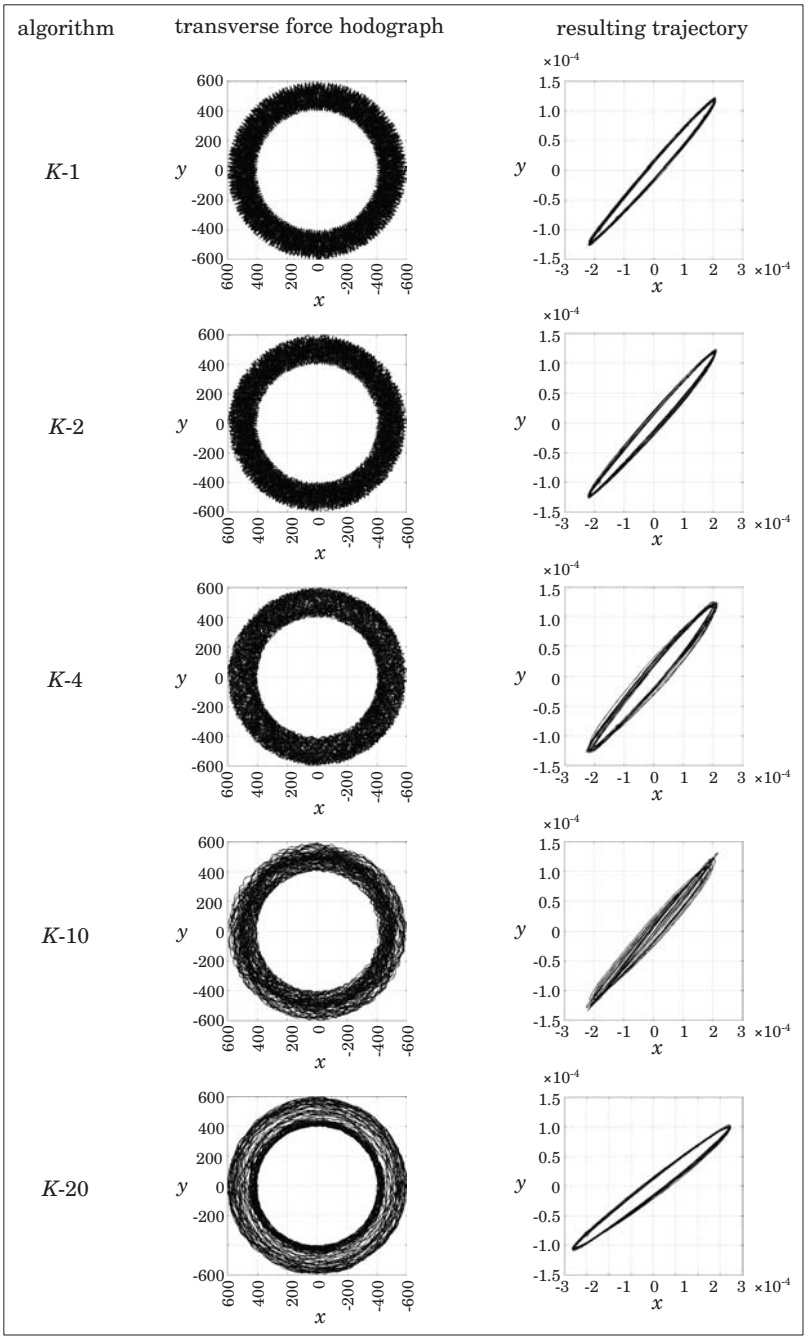

Fig. 9. A comparison of hodographs of stochastically varied transverse forces according to K-m algorithms at different values of n, $\Delta P = 0.2\ P$

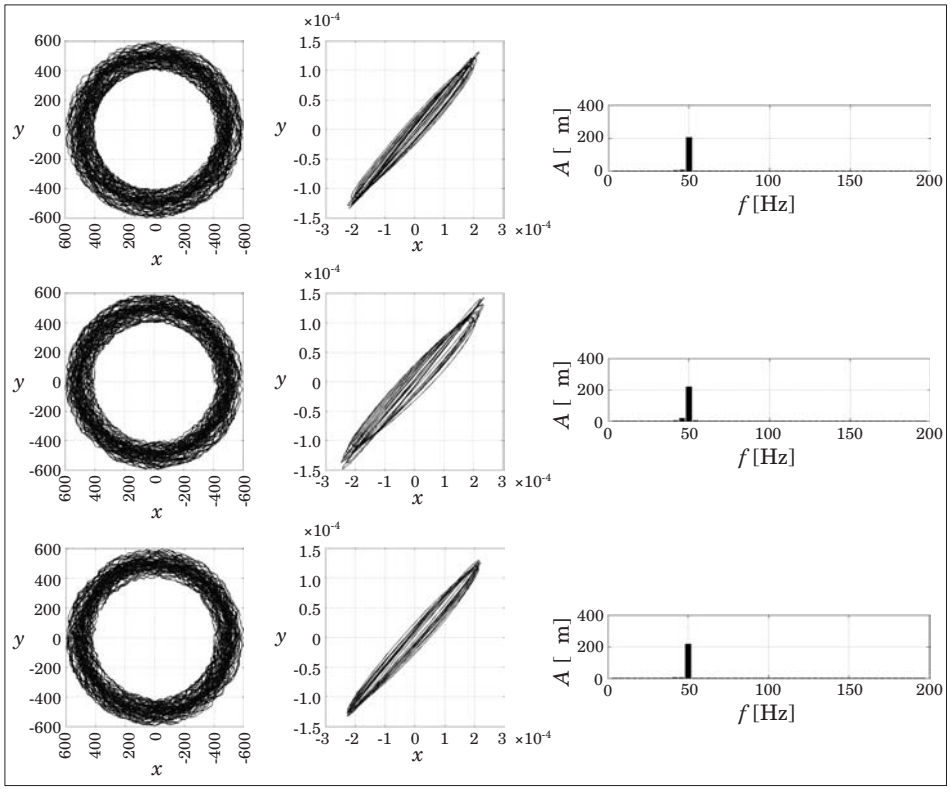

Fig. 10. Results of additional calculations using algorithm *K*-10

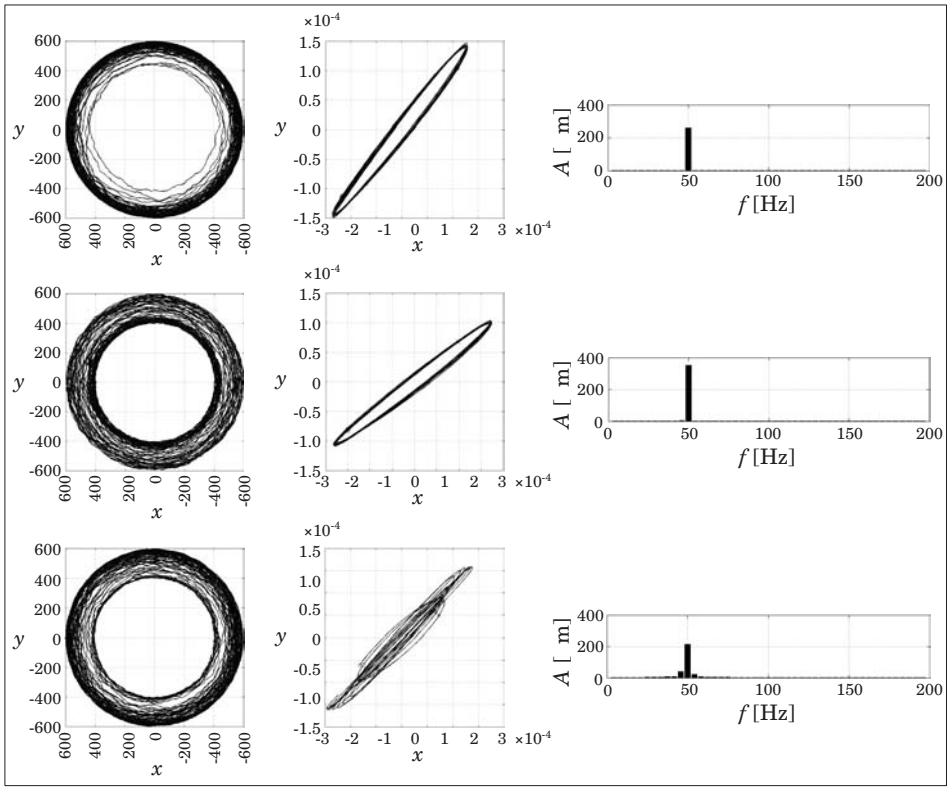

Fig. 11. Results of additional calculations using algorithm *K*-20

Conclusions

The findings of this study point to problems in the process of obtaining reliable results with the use of deterministic algorithms in engineering software. The use of variable input data in numerical calculations and simulations produces a number of probable results rather than a single repeatable result. The above leads to significant inconsistencies in the interpretation of the results.

The presented results concern a model of a rotor-bearing system to which a single force variable over time has been applied. If various forces and their variability are taken into account, the produced results would require a highly accurate and complex interpretation.

A quasi-static approach to accounting for variations in input data does not support the recognition of the non-linearity of correlations that describe the phenomena occurring in the rotor-bearing system. The results of calculations involving stochastic processes that account for variations in the value of the radial force applied to the rotor indicate that the use of the relevant algorithms

in numerical calculations accurately reflects the dynamics of the phenomena observed in the studied systems.

According to the author, the absence of full repeatability of the obtained results as well as their form – sets rather than specific values or processes – are more characteristic of experiments replaced by numerical calculations. Similarly to the hitherto practice of interpreting the results of experiments performed on actual objects, the results of many numerical calculations are much more prone to error and difficult to interpret.

Accepted for print 4.08.2009

References

KICIŃSKI J. 2005. *Dynamika wirników i łożysk ślizgowych.* IMP PAN, Gdańsk.

Modelowanie i diagnostyka oddziaływań mechanicznych, aerodynamicznych i magnetycznych w turbozespołach energetycznych. 2005. Red. J. KICIŃSKI. IMP PAN, Gdańsk.

PIETKIEWICZ P., KICIŃSKI J., CZOSKA B., MARKIEWICZ A. 2006. *Opracowanie modelu defektów z uwzględnieniem niepewności danych wejściowych.* Opr. wew. IMP PAN, Gdańsk.

PIETKIEWICZ P. 2007. *Niepewność danych wejściowych w obliczeniach numerycznych.* Biuletyn WAT, LVI.

PIETKIEWICZ P. 2008. *Modelowanie utraty stabilności układu wirnik-łożyska przy stochastycznej zmienności danych wejściowych.* Biuletyn WAT, LVII (2).

PIETKIEWICZ P. 2009. *Modelowanie otarć wirników o elementy nieruchome.* XIII Szkoła Komputerowego Wspomagania Projektowania, Wytwarzania i Eksploatacji, Jurata, s. 277–282.

TECHNICAL SCIENCES
Abbrev.: Techn. Sc., No 12, Y 2009

DOI 10.2478/v10022-009-0018-3

TYPICAL FAILURES OF GEAR PUMPS. DEFECTS CLASSIFICATION

Paweł Pietkiewicz

Chair of Mechanics and Machine Design
University of Warmia and Mazury in Olsztyn

K e y w o r d s: gear pumps, symptom, defect, diagnostic relations.

A b s t r a c t

The paper comprises research results of the gear pump typical failures and their connection with symptoms observed during the pump working. Worked out criteria and their boundary values allowed the defect classes creation and the defect-symptom diagnostics relation building.

TYPOWE USZKODZENIA POMP ZĘBATYCH. KLASYFIKACJA DEFEKTÓW

Paweł Pietkiewicz

Katedra Mechanizacji i Podstaw Konstrukcji Maszyn
Uniwersytet Warmińsko-Mazurski w Olsztynie

S ł o w a k l u c z o w e: pompa zębata, symptom, defekt, relacje diagnostyczne.

A b s t r a k t

Artykuł zawiera wyniki badań nad typowymi uszkodzeniami pomp zębatych oraz ich powiązaniami z symptomami obserwowanymi w czasie pracy pomp. Opracowane kryteria oraz ich wartości graniczne pozwoliły na stworzenie klas defektów i budowę relacji diagnostycznych symptom--defekt.

Introduction

Transfluent liquid energy utilization is very common nowadays. Despite of passing time and new technical solutions, which are still rising in many fields, hydraulic and pneumatic systems are the most preferable systems for the machinery drive. A pump, that acts as the pressure and flow rate generator is

the basic unit of the hydraulic system. The main job of the pump is the high working pressure generation with as high efficiency as possible. Since the higher the working pressure is, the greater the stream density of the transported energy is, so the higher is the efficiency of the whole system.

Present science endeavours do not focus on the new appliances designing, but on making a study of changes occurring in the existing elements and whole systems during their exploitation. For various reasons one aims at the prediction of the failure states generation, which the most often are preceded by every part or sub-assembly wear symptom occurrence. Possibility of the breakdown occurrence prevention is connected with the correct interpretation of the wear diagnostic. Necessary requirement of such possibility is the knowledge of the most often occurring device defects and definition of the relations between symptoms and defects of each device and whole systems. Symptom-defect relation definition, that occur in the technical object allows construction of the model, which by the modern inference methods application, for example heuristic methods, enables the break-down anticipation, that were not found as yet.

This work is dedicated to the defects, that occur in one of the basic pump types, which the gear pump with the external gear is (Fig. 1). Gear pumps are used for all liquids of a little contamination (ICKIEWICZ 1995a, 1995b, KOLLEK 1996), and the high work pressure generation possibility is their advantage.

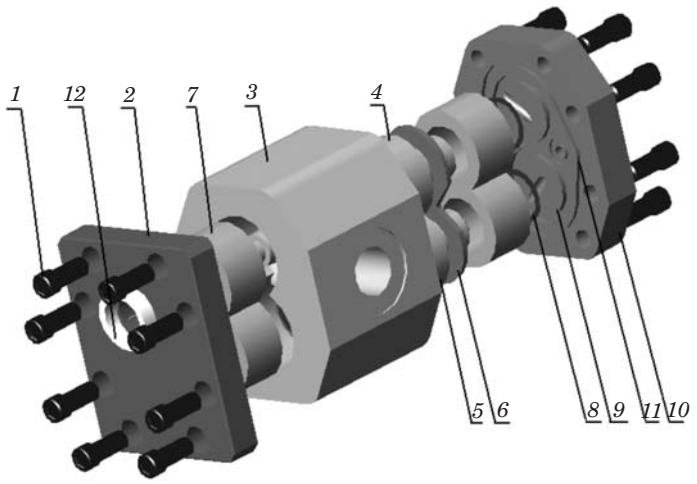

Fig. 1. Demonstrative drawing of the PZ2 type gear pump structure: *1* – bolts, *2* – front end plate, *3* – casing, *4* – driving wheel (drive gear), *5* – driven wheel (idler gear), *6* – resistance filler (compensation), *7* – bearing sleeve, *8* – thrust ring, *9* – seal under the driven wheel, *10* – rear end plate, *11* – large seal (stadium), *12* – Shaft end seal

Source: own study.

In the pump casing 3 two identical gear wheels: driving 4 and driven 5, are rotating. The gear pump functioning is based on the working liquid transportation along the wheel circumference and forcing out the certain liquid batch from the suction space to the pressure space owing to the gear wheels rotation. Considering the finite volume of the pressure chamber, under the influence of the generated pressure, the liquid surplus is forced out through the outlet plot, into the fed hydraulic system.

The tight separation of the suction chamber from the pressure one is the condition of the proper functioning of that device. Pumping assembly leaktightness is an important factor in the correct pump and the whole system functioning. It is acquired by the resistance fillers 6 application (Fig. 1). The axial compensation, that increases the pump efficiency by the internal leaktightness improvement, is their principal task. The radial clearance compensation is the complement of the axial compensation and is rarely applied at the present time (KOLLEK 1996).

Domain of research

Research, comprising observations and failures measurements, that occur in the tested pump pieces, were conducted in the Chair of Mechanics and Basis of Machinery Design of the University of Warmia and Mazury in Olsztyn. They referred to the selected components, the wear of which have a very distinct influence on the pump functioning and their output parameters.

In case of the **seals** applied in such type pumps, the subjects to assessment were:

- outer seal – so-called stadium – responsible for the external tightness of the pump from the side of its rear end plate,
- gear wheel seals – responsible for the proper axial forces compensation, that exist during the pump working,
- rubber-spring seal on/of the pump shaft – responsible for the external tightness from the side of the power drive feed to the pump.

The mechanical or thermal damage degree was estimated in all mentioned seal components, distinguishing the following seal wear states:

- new seal – soft material, section according to the design,
- worn out seal – hard inflexible material, flattened section,
- damaged seal -the seal continuity break off, the surface defect, melting in consequence of too high working temperature.

In case of the resistance (compensation) fillers – responsible for the proper axial forces compensation, which occur during the pump working and reduction of the differential pressure on the suction and pressure sides of the pump beyond the oil transport zone – the following quantities were estimated:

– R_{max} of the compensation filler from the side, which cooperates with the end face of the gear wheel,
– compensation filler deflection,
– percentage part of the seized or torn off from the compensatory filler surface,
– filler scorch traces occurrence.

During the tests and measurements realization it was found, that some quantities measurements would be encumbered with an error, which would not allow conclude properly upon the element wear relations as well as on the pump output parameters change. Quantities, which do not have a direct influence on the pump working parameters, were not submitted to the precise measurements.

– trace of the material acquired from the inner casing surface, which mates with the gear wheels,
– wear out scale/ratio/rate attrition rate of the needle bearings races,
– the noise generated by the working device.

Research results

Defects observed together with the pumps number weight, in which failures have been observed with reference to the overall number of tested pumps, are placed in Table 1. Specified failures have created a defects set S (failure states) of elements $\{s_1, s_2, ..., s_n\}$.

Table 1

Failures occurring in the tested pumps. Elements of the defects set S (failure states)

Id	Defect	Part in test
s_{01}	Resistance filler scratches over 16 μm	74.0%
s_{02}	Resistance filler flexure over 0.1 mm	67.7%
s_{03}	Resistance filler scorch	45.2%
s_{04}	Copper resistance filler surface defect	32.3%
s_{05}	Torn gear wheel seal off /broken	32.3%
s_{06}	Regular seals wear	29.0%
s_{07}	Resistance filler scratches 16 μm and below	26.0%
s_{08}	Resistance filler flexure up to 0.1 mm	26.0%
s_{09}	Gear wheel sealing rings fusion	22.6%
s_{10}	Seized surface of the resistance filler	19.4%
s_{11}	Lack/failure of the shaft end seal	9.7%
s_{12}	Resistance filler surface tear off/break	6.5%
s_{13}	Torn off/broken big seal „stadium”	6.5%
s_{14}	Incorrect/abnormal shaft end seal assembly	3.2%
s_{15}	Case crack	3.2%

Element s_{15} was recognized as accidentally occurring. During the research it was found, that the pump specimen, which was characterized by the failure state s_{15}, did not show the distinct wear symptoms related to the stated failure. In this consequence the s_{15} element was not taken into consideration in the subsequent research results analysis. Exemplary pictures of the selected seal failures and resistance fillers in the tested pumps, are shown in Figs. 2÷3.

Fig. 2. Gear pump seal failures: *a* – torn gear wheel seal off, *b* – fused sealing rings, *c* – torn big seal on the rear end plate ("stadium")

Source: own research.

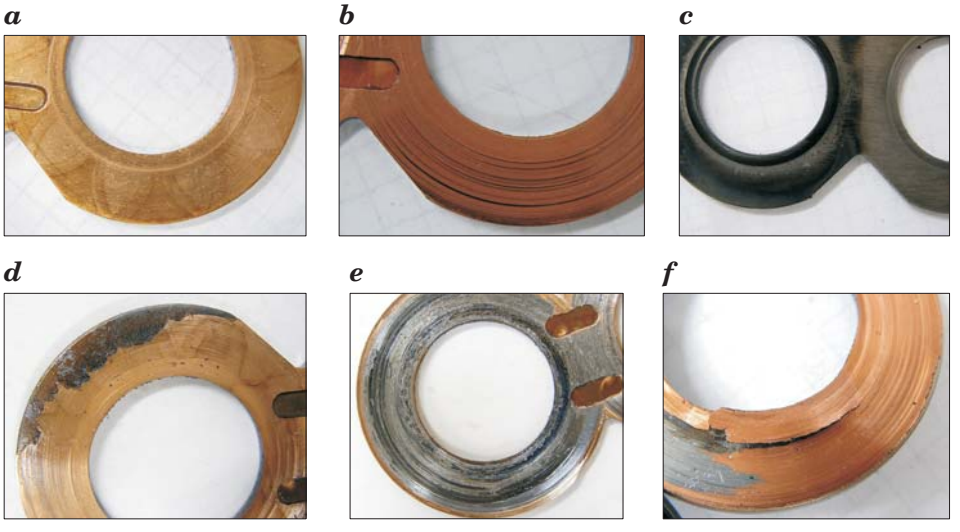

Fig. 3. Resistance filler seals failures: *a* – resistance filler scratches under 16 μm, *b* – scratches over 16 μm, *c* – resistance filler scorch, *d* – torn filler surface off, *e* – seized surface of the resistance filler, *f* – copper coating defect

Source: own study.

Relation of the occurring failure states and observed symptoms

The gear pump failure states, that occurred most often, were identified in chapter 3. Criterial quantities providing the wear symptoms identification of tested pumps, were separated during the pump characteristics empirically obtained analysis.

- maximum pump working pressure Δp_{max} at the minimum and nominal rotational speed,
- maximum pump total efficiency in the working point at the minimum and nominal rotational speed,
- slope of a flow characteristic at the nominal rotational speed.

The symptom groups were formed and presented in Table 2.

Table 2

Elements specification of the set of gear pump wear symptoms A

Id	Verbal description of the symptom	Criterial quantities boundary values
a_1	Pump efficiency reduction from several to over a dozen per cent compared to a new device of the same type. Acquired maximum working pressure equal to the nominal in the whole rotational speed range. Slightly decreasing flow characteristic towards the increasing working pressure.	$\Delta p_{max} = \Delta p_{nom}$ (160 at) $0.74 < \eta \leq 1.00$ $10^{-7} \leq \text{tg}\ \theta \leq 4 \cdot 10^{-6}$
a_2	A device total efficiency exceeding 74%. Maximum forcing pressure varying according to the rotational speed, not lower than a half nominal value at the nominal rotational speed. Flow characteristic considerably sloped in the direction of the pressure increase.	$0.5\ \Delta p_{nom} < \Delta p_{max} \leq \Delta p_{nom}$ $0.50 < \eta \leq 0.73$ $4 \cdot 10^{-6} \leq \text{tg}\ \theta \leq 10^{-5}$
a_3	A device total efficiency exceeding 50%. Maximum forcing pressure up to 50% of the nominal value at the nominal rotational speed, at the lower speeds the lower pressure value. Flow characteristic considerably and very sloped.	$\Delta p_{max} \leq 0.5\ \Delta p_{nom}$ $0.00 < \eta \leq 0.50$ $\text{tg}\ \theta \geq 10^{-5}$
a_4	A device efficiency equal to zero. Pump load inability, slope coefficient/factor of the flow characteristic determination impossibility. Very abundant outflow of the working medium through the device shaft sealing.	$\Delta p_{max} = 0$ $\eta = 0$ tg θ value determination impossibility

The attempt to find a relation among them was undertaken in the subsequent order (CEMPEL, TOMASZEWSKI 1992, PIETKIEWICZ 2004a, 2004b, RZADKOWSKA, PIETKIEWICZ 2004, PIETKIEWICZ, RZADKOWSKA 2004). For that purpose the trial to compose a binary symptom-defect diagnostic matrix was taken up. The received binary matrix (Tab. 3) defines, if there is any relation between specific symptoms and defect, which were noticed during tests.

Table 3

Binary symptom-defect diagnostic matrix

a_i	Failure state s_j													
	s_{01}	s_{02}	s_{03}	s_{04}	s_{05}	s_{06}	s_{07}	s_{08}	s_{09}	s_{10}	s_{11}	s_{12}	s_{13}	s_{14}
a_1	1	1	0	0	0	1	1	1	0	0	0	0	0	0
a_2	1	1	1	1	1	1	0	1	0	1	0	1	1	0
a_3	1	1	1	1	1	1	1	1	1	1	0	1	1	1
a_4	1	1	1	1	1	1	0	1	1	1	1	0	0	0

Analyzing values of the matrix placed in the form of the Table 3, one can notice, that the majority of symptoms are likely to be generated by a number of specific failures. The symptom a_4 can be an example as well as the failure states s_{01}, s_{03} and s_{11}. It means, that one symptom may be caused by different defects. Further probability analysis of the failure occurrence in the tested unit trial indicated a high probability of such cases.

Classification of the occurring failures. Defects classification

The diagnostic matrix, placed in chapter 4, presents the relations between the observed gear pumps wear symptoms and their specific defects. Once the structure and gear pump principle of operation is known, an attempt at the failure states groups creation, also called as the defects classes, was made. Failures of the gear pump structure pieces, which are the members of the defects set (failure states) S with $\{s_1, s_2, ..., s_n\}$ elements, were grouped into the defects classes, thus making a set of defects classes K with $\{k_1, k_2, ..., k_n\}$elements.

The defects classes description and information on which failure states were assigned to a particular defects classes, were placed in table 4. The failure classes were created as sets of defects, which in a different manner perturb the gear pump functionality.

Defects, which arise during the regular gear pumps exploitation by loading some elements of their structure, are contained in k_1 class.

Defects generating a total loss of axial compensation are included among the k_2 class. The loss of this property by the gear pump is a ground to a large maximum pressure reduction, which the pump is likely to generate. Defects numbered among the k_2 class most often arise in consequence of the system overloading, its overheating and as the result of the compensation fillers damage and often by tearing the gear wheel seals off.

Table 4

Defects classes created on the basis of the carried gear pump research out

k_l	Class description	s_j
k_1	Exploitation wear of sealing and responsible for the axial compensation elements	s_{06} s_{07} s_{08}
k_2	Total loss of axial compensation	s_{05} s_{09}
k_3	Total loss of pump leak-tightness	s_{11}
k_4	Pump leak-tightness reduction/failure	s_{13} s_{14}
k_5	Axial compensation failure – excessive elements wear responsible for the axial compensation	s_{01} s_{02} s_{03} s_{04} s_{10} s_{12}

In case of the defect denoted as s_{11} the separate defect class k_3, which consists of only one failure, was created. The rubber-spring seal on the pump shaft destruction as well as its absence results in the total loss of pump leak-tightness. An oil; led to the device; flows outside through the gap at the driving shaft very often even before the pump start-up.

The defects class k_4 contains failure states related to the pump outer seals failure, which however do not generate the entire hold-up of the hydraulic system. The reason of this class failure arising, may be a considerable pump overloading or an irregular sealing assembly.

The most numerous class of the failure states is the k_5 class, to which defects considerably reducing the axial compensation effectiveness of the forces related to the working medium pressure, were included. Failures related to the frequent device overload, incorrect working medium application, its high impurity or else foreign matters getting inside the pump, belong to them.

Table 5

Binary symptom-defect class diagnostic matrix for the tested pumps sample

a_i	Defects classes k_l				
	k_1	k_2	k_3	k_4	k_5
a_1	1	0	0	0	1
a_2	1	1	0	1	1
a_3	1	1	0	1	1
a_4	1	1	1	0	1

Creation of the failure states classification, which occur in a pump, enabled to define a relation between the observed symptoms and defect classes (CEMPEL, TOMASZEWSKI 1992, PIETKIEWICZ, 2004b, PIETKIEWICZ, RZADKOWSKA 2004) in the form of the symptom-defect class matrix (Tab. 5).

Based on the table 5 it is possible to conclude about the interrelation existence between the observed wear symptoms of the tested devices and the defects classes, which may come out in the particular specimen.

Summary

The research, conducted for the gear pumps, allowed to establish failures occurring the most often and their relation to the observed wear symptoms. Similar research may be conducted for any technical device or machine. In case of the complex mechanical systems such experiment may be hard to carry out. Therefore, before the research project of the whole system is constructed, tests of each element entering into its composition should be executed. Gear pump always is a part of more complex hydraulic system, which drives a material system, and is the example of this. The failure states of the whole hydraulic system may be the results of subsystems failure states or of its elements (i.e. the pump). Therefore the observed symptoms may be very ambiguous and may signal failure states of different elements of the entire system.

Diagnostic matrices, which arose as a result of the research and exhibit symptoms to the occurring diagnostic states relation, allow the technical devices models to be constructed. The proper symptom-defect relations structure may be helpful in the break down anticipation of the simple material systems as well as the complex machines. The diagnostic models construction requires the precise identification concerning probable failure states. This is not always possible in case of complex material systems.

One may make an attempt at the models construction of machines and systems based on heuristic inference algorithms, owing to an adequate unification methods application and analysis of the obtained results. Unlike the classic algorithms, which require the knowledge of all variables, heuristics allows a continuous adaptation of the inference algorithms to arisen situation. In case of new, not encountered before symptoms or failure states occurrence, heuristic models partially based on the "experiment", make additions to a base of knowledge on the analysing object, simultaneously developing or aiding the development of new procedures when the failure not observed up to now occurs.

Accepted for print 31.08.2009

References

CEMPEL CZ., TOMASZEWSKI F. 1992. *Diagnostyka maszyn. Zasady ogólne. Przykłady zastosowań.* Międzyresortowe Centrum Naukowe Eksploatacji Majątku Trwałego, Radom.

ICKIEWICZ J. 1995. *Zagadnienia zanieczyszczenia cieczy roboczych i ich wpływ na zużycie elementów układu hydraulicznego.* Materiały kongresowe „Hydropneumatica '95", s. 26–34.

ICKIEWICZ J. 1995. *Zagadnienia pulsacji cieczy w układach hydraulicznych z pompami zębatymi.* Materiały kongresowe „Hydropneumatica '95", s. 35–41.

KOLLEK W. 1996. *Pompy zębate konstrukcja i eksploatacja,* Zakład Narodowy imienia Ossolińskich, Wrocław – Warszawa – Kraków.

PIETKIEWICZ P. 2004a. *Modelowanie relacji diagnostycznych. Pompy zębate*. W: *Diagnostyka maszyn roboczych. Detekcja, relacje, wnioskowanie hybrydowe*. Red. R. Michalski, Wyd. UWM, Olsztyn.

PIETKIEWICZ P. 2004b. *Relacje diagnostyczne w pompach zębatych.* XXXI Ogólnopolskie Sympozjum Diagnostyka Maszyn. Węgierska Górka 1.03–6.03. (wyd. CD).

PIETKIEWICZ P., RZADKOWSKA W. 2004. *Zastosowanie diagnostycznego eksperymentu czynno-biernego przy badaniu relacji „symptom-defekt" w pompach zębatych. Badanie, konstrukcja, wytwarzanie i eksploatacja układów hydraulicznych*. XIV Ogólnopolska konferencja CYLINDER 2004, Ustroń.

RZADKOWSKA W., PIETKIEWICZ P. 2004. *Zmiana parametrów roboczych pompy zębatej w zależności od występujących uszkodzeń.* VIII Szkoła Komputerowego Wspomagania Projektowania, Wytwarzania i Eksploatacji, Jurata, s. 191–199.

TECHNICAL SCIENCES
Abbrev.: Techn. Sc., No 12, Y 2009

DOI 10.2478/v10022-009-0019-2

DEVELOPMENT OF THE FOIL BEARING TECHNOLOGY

***Krzysztof Nalepa*[1], *Paweł Pietkiewicz*[2], *Grzegorz Żywica*[3]**

[1] Chair of Power Engineering
[2] Chair of Mechanics and Machine Design
University of Warmia and Mazury in Olsztyn
[3] Institute of Fluid-Flow Machinery Polish Academy of Sciences in Gdańsk
Rotor Dynamics and Slide Bearing Department

K e y w o r d s: foil bearings, journal bearings, bearing systems, microturbines.

A b s t r a c t

Development of the bearing technology with deformable elements of the bearing sleeve utilization are presented in the paper. Foil or a set of foils with the viscoelastic properties comprise the deformable element. Foil bearing technology is utilized mostly in the high-speed turbo machines, such as the energetic microturbines. This results the bearing operating regime: high rotational speed, high temperature, work in the friction conditions during machine start-up and rundown. Three foil bearing generations, which differ in the structure and properties with regard to load capacity, stiffness and undesirable variation damping, were distinguished in such bearing development. Technical solutions of the foil journal and thrust bearings were shown.

ROZWÓJ TECHNOLOGII ŁOŻYSKOWANIA FOLIOWEGO

***Krzysztof Nalepa*[1], *Paweł Pietkiewicz*[2], *Grzegorz Żywica*[3]**

[1] Katedra Elektrotechniki i Energetyki
[2] Katedra Mechaniki i Podstaw Konstrukcji Maszyn
Uniwersytet Warmińsko-Mazurski w Olsztynie
[3] Instytut Maszyn Przepływowych Polskiej Akademii Nauk w Gdańsku
Zakład Dynamiki Wirników i Łożysk Ślizgowych

S ł o w a k l u c z o w e: łożysko foliowe, łożyskowanie maszyn szybkoobrotowych.

A b s t r a k t

W artykule przedstawiono rozwój technologii łożyskowania z wykorzystaniem odkształcalnych elementów panwi łożyska. Element odkształcalny stanowi folia lub zespół folii o właściwościach lepko-sprężystych. Technologia łożysk foliowych jest wykorzystywana głównie w szybkoobrotowych

maszynach wirnikowych, jak mikroturbiny energetyczne. Wynikają z tego warunki pracy łożyska: duża prędkość obrotowa, wysoka temperatura, praca w warunkach tarcia podczas rozruchu i wybiegu maszyny. W rozwoju tego typu łożyskowania wyróżniono trzy generacje łożysk foliowych, które różnią się konstrukcją i właściwościami pod względem nośności, sztywności oraz zdolności tłumienia niepożądanych drgań. Przedstawiono rozwiązania techniczne łożysk foliowych poprzecznych i wzdłużnych.

Introduction

In view of the requirements set by rapid technological advancement, technical equipment undergoes constant minimization, while ensuring the right operating parameters, in particular the power output. As regards turbomachines, this requirement implies increased rotational speed. This generates a number of problems. One of the most important considerations is the choice of bearing capable of operating at high speeds. In recent years, foil bearings, a sub-category of journal bearings (Fig. 1), began to receive widespread

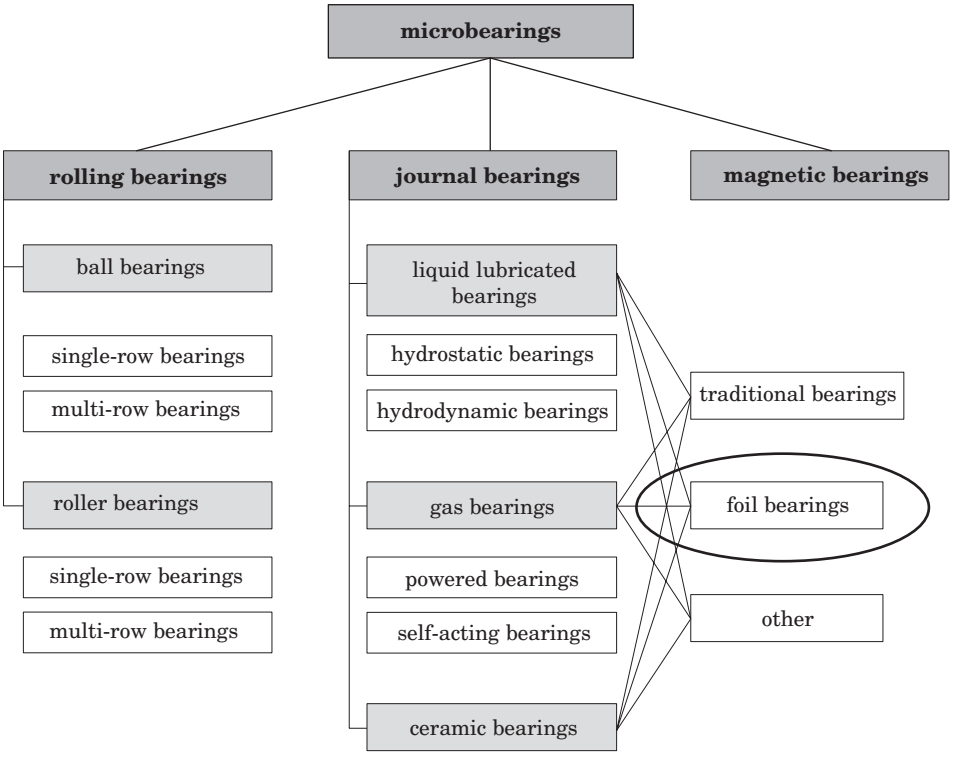

Fig. 1. Microbearing classification in view of bearing structure and operating principle. Position of foil bearings in the classification of microbearings

Source: Żywica (2007).

coverage in scientific publications. The foil bearing concept first appeared in the mid 20th century, yet the required manufacturing technology was developed much later.

A variety of turbomachines are presently on offer, including microturbines with the output of 25-250 kW. Microturbines deliver many advantages, in particular in distributed small-scale power plants. A small number of rotating and moving elements, compact structure, small size and weight facilitate assembly and maintenance. Most microturbine rotors operate at rotational speeds higher than 40 000 rpm with frequent operational interruptions. The temperature inside microturbines usually reaches several hundred degrees Centigrade. For this reason, rotor support bearings in microturbines have to meet stringent requirements as regards:

– allowable rotational speed,
– load capacity,
– allowable operating temperature,
– life and reliability,
– bearing precision and stiffness,
– vibration damping and silent running.

In view of the above requirements, foil bearings are a highly recommended solution and the associated manufacturing technology is becoming more available with time. The operating principles of a foil bearing and a traditional journal bearing are compared in Figure 2, where the structure of a traditional

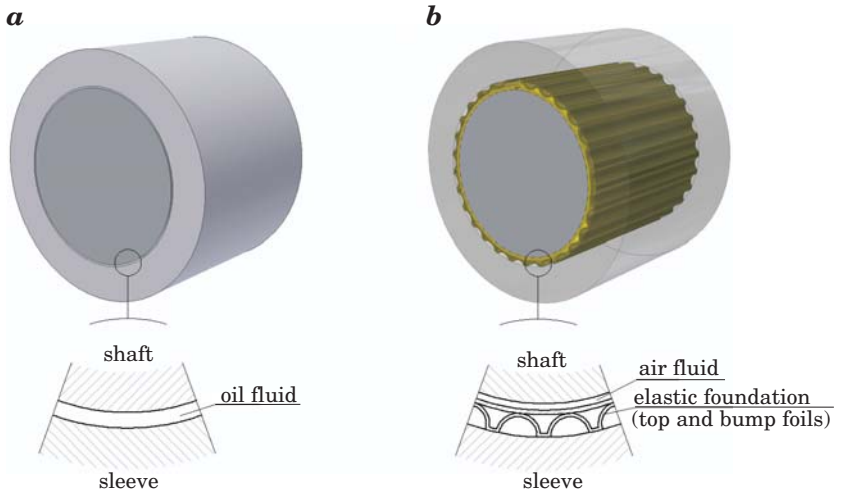

Fig. 2. Comparison of the operating principles of a liquid-lubricated journal bearing and a gas foil bearing

Source: Own work.

bearing is shown on the left, and that of a foil bearing – on the right. The bearing's subsequent layers in the radial direction are presented at the bottom. Despite structural similarities, the main differences are clearly manifested. In a traditional bearing, liquid is the only carrier medium, and the co-acting surfaces are made of alloys resistant to pressure and friction in overloaded bearings. During normal operation, gas is the lubricating medium in foil bearings. During start-up, rundown and overloading of the rotor, the resulting forces are distributed by a set of foil elements whose chemical composition, shape and thickness is determined by the bearing structure (DELLACORTE 2003).

Foil bearings are classified into several generations, of which three will be discussed in subsequent parts of this article. The first foil bearing concept dates back to 1953. Since then, various structural solutions based on the original concept have been developed.

In recent decades, many foil bearing structures were developed together with advancements in the relevant technology, mainly in the area of materials science. In view of the required operating parameters and the geometry that determines operating parameters, foil bearings have been classified into three generations.

First generation foil bearings

First generation foil bearings are bearings whose load-carrying structure comprises only viscoelastic foil or a foil set whose properties are fixed in all directions. Such bearings are fit for use only in very small devices that are subject to small load, such as fans. Owing to their limited load capacity, they are not suited for turbocompressors or microturbines.

In its simplest structural form, a foil bearing comprises a foil element which overlays the internal surface of the bearing sleeve (HOU et al. 2004). This solution is illustrated in Figure 3.

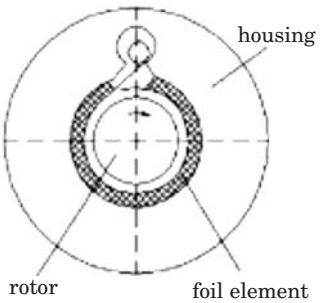

Fig. 3. The structure of a foil bearing with a single viscoelastic foil element
Source: HOU et al. 2004.

The viscoelastic foil overlay is fitted in the bearing sleeve at a single point along the sleeve's circumference. During normal operation, the bearing's functional behavior is similar to that of a traditional gas bearing. During overload, the journal hits the foil surface. Owing to its viscoelastic properties, the foil absorbs the energy displaced in the radial direction. This simple solution does not differ significantly from traditional journal bearings. Various structural improvements have been developed, one of which is shown in Figure 4. One layer of viscoelastic foil has been replaced with a second foil level which is fitted in a similar manner, but the foil element is long enough to wrap the internal diameter of the sleeve several times, creating a foil spiral inside the bearing. The foil is made of beryl bronze (in both cases). Spiral layers are separated with numerous copper wires. The resulting bearing can operate at the speed of around 220 000 rpm. The structure comprising several foil elements is presented on the right side of Figure 4. There are several points for fixing foil elements along the sleeve circumference. The length of foil elements is around 2/3 of the internal circumference of the sleeve, creating two active foil layers which are separated by thin copper wires.

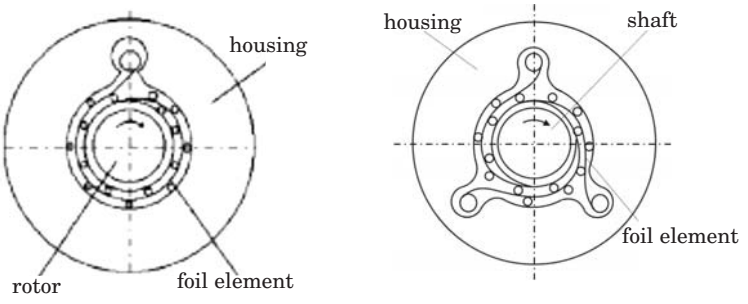

Fig. 4. Foil bearing with spiral foil (Hou et al. 2004) and several spirally-overlaid foil elements
Source: On the basis of Xiong et al. 1997.

The structure of a bearing comprising several foil elements without clearance between particular layers is presented in Figure 5.

During the operation of the bearing shown in Figure 5, the foil element supported by spacing wires is not deflected, and the load is absorbed by the successive foil elements. The length of every foil leaf is designed to overlay half of the length of the successive layer. When load is applied to any part of the foil element, some energy is absorbed by deflecting the element subjected to load, while some energy is distributed to the layer found directly beneath it. Since every terminal part of the element is supported by the most elastic fragment of the element found directly beneath it, the bearing retains its elasticity in the radial direction along the entire circumference of the sleeve.

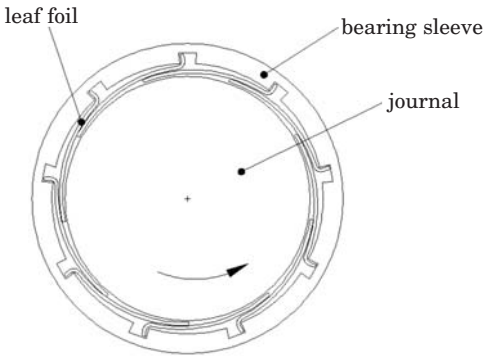

Fig. 5. Structure of a multi-layer foil bearing
Source: Based on DELLACORTE 2003.

The use of first generation foil bearings is limited by, among others, the properties of materials applied in foil production. In addition to delivering a high level of elasticity, foil elements have to be resistant to friction wear at high loads and speeds as well as to extreme temperatures. There are practically no materials that meet all of the above requirements.

Bump foil offers new structural possibilities. The structural model of a foil bearing with an additional foil element is presented in Figure 6.

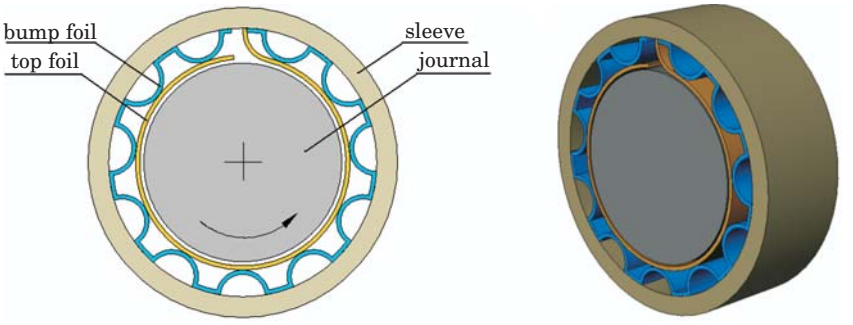

Fig. 6. Bump foil bearing
Source: Own work.

The top foil layer which directly co-acts with the rotating journal remains smooth, and it carries the distributed load to the bump foil layer found underneath. Owing to its shape and material properties, bump foil is subject to local elastic deflections, and it absorbs the energy generated by, for example,

overloading. The structure of a bearing where smooth foil has been separated into two separate layers is presented in Figure 7.

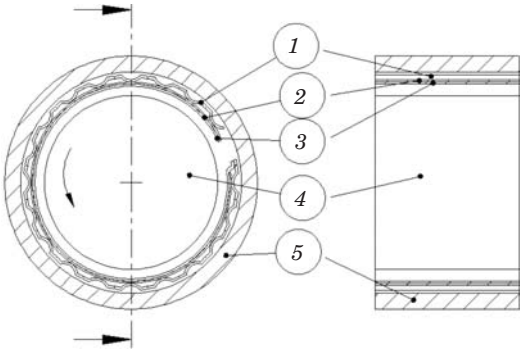

Fig. 7. Structure of a foil bearing with a separate viscoelastic foil layer. *1* – bump foil, *2* – viscoelastic foil, *3* – top foil, *4* – journal, *5* – bearing sleeve
Source: On the basis of LEE et al. 2004.

In the structure shown in Figure 7, top foil is made of tempered molybdenum sulfate. Top foil is wrapped around the bearing sleeve at the angle of 355°. The second layer is made of viscoelastic acrylic polymers resistant to the temperature of 150°C. Prior to assembly, bump foil is formed in the bearing sleeve. A foil leaf identical to the first layer co-acting with the journal is additionally interfaced with the sleeve surface (LEE et al. 2004).

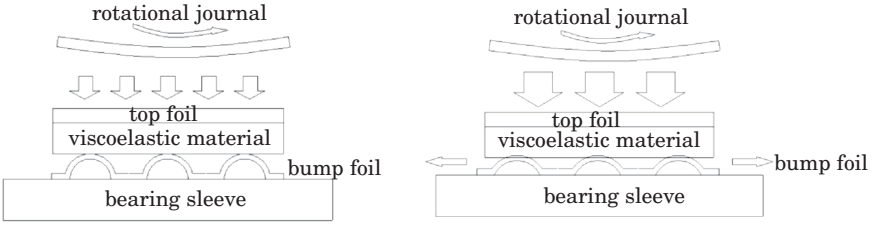

Fig. 8. Operating principle of bump foil bearings
Source: Based on LEE et al. 2004.

The operating principle of bump foil bearings is presented in Figure 8. The bearing operating under normal conditions is shown at the top. The gas or fluid film exerts pressure on the top foil. The top foil is deflected, carrying the load to the viscoelastic layer which absorbs most of the energy. Under higher loads, the excess energy deflects both foil layers, and it exerts pressure on the

bumps of adequately shaped foil. The load applied to foil bumps deflects the entire structure of bump foil. In the absence of a separate viscoelastic layer, the top foil takes over its function, and any excess load is carried to the adequately shaped bump foil.

Bump foil delivers a variety of new structural solutions for bearings. A structural diagram of a multi-layer bump foil bearing is presented in Figure 9. Its structure has been modified in such a way that top foil fragments do not overlap and they do not form an elastic layer. The applied foil plays the role of the elastic layer.

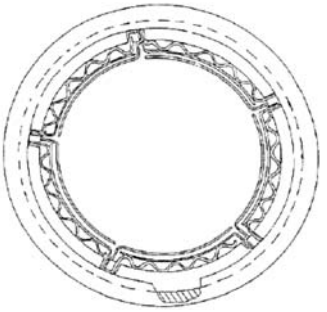

Fig. 9. Multi-layer bump foil bearing

Source: AGRAWAL 1997.

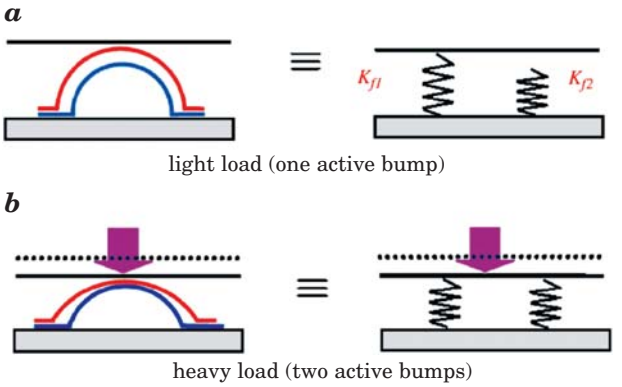

Fig. 10. The operating principle of a double bump foil layer

Source: KIM, SAN ANDRES 2007.

The solution presented in Figures 6 and 7 may be deployed to protect the shaft journal and the supporting bearing against critical load with the use of a double bump foil layer. The first layer is more elastic, while the second layer delivers greater stiffness. The operating diagram of a double bump foil element

is presented in Figure 10. The upper foil layer is activated at the initial stage of applying the load. The upper layer is deflected to discharge the load. If a heavier than designed load is applied, the second, stiffer layer is activated.

Similar structural solutions may be applied in foil thrust bearings. The bearing surface is divided into several sections. Each section is covered by a petal. The leading edge is fixed to the bearing surface, and the top foil petal rises gradually above the surface to which it is fixed. Bump foil is placed under the top foil layer. The top foil petal is inclined in the circumferential direction, and lubricating film is produced during rotational movement (DellaCorte 2004).

Second generation foil bearings

The 1980s witnessed the onset of bearings which are suitable for use in turbocompressors and turbopumps. In second generation bearings, the geometry of the support structure changes in one of the directions. Variability in the axial direction is most frequently noted. It eliminates edge leaks caused by the gas lubricant, thus significantly increasing the bearing's load capacity. Structural models of second generation bearings are presented in Figures 11 and 12.

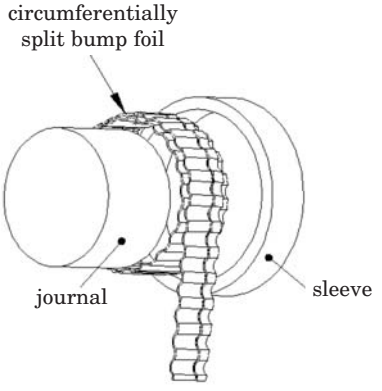

Fig. 11. Structural model with variable pitch of bump foil in the axial direction
Source: On the basis of DellaCorte 2000.

A model with a variable load-carrying structure in the circumferential direction is presented in Figure 12. Bump foil deflections were compacted in places where the upper foil layer was marked by the lowest stiffness.

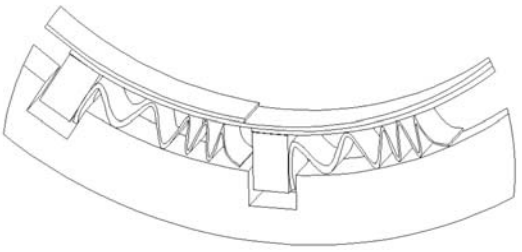

Fig. 12. Structural model with variable-pitch bump foil in the circumferential direction
Source: Own work.

Second generation foil bearings paved the way to the development of more complex structures that combine the physical properties of the available materials with variable bump foil geometry in all directions.

Third generation foil bearings

In third generation foil bearings, changes in the properties of the load-carrying structure are observed in minimum two directions. Third generation bearings feature several bump foil layers where, subject to load and deflection, the elastic properties of the load-carrying structure vary in the radial direction. Third generation bearings also include any combinations of second generation foil bearings. A structural model of a third generation foil bearing is presented in Figure 13.

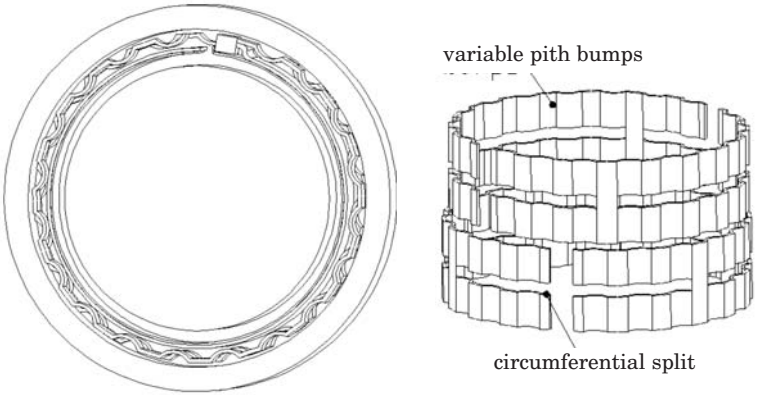

Fig. 13. Structural model using variable pitch bump foil in the circumferential and axial direction
Source: Based on DellaCorte 2003.

Due to their high load capacity, third generation bearings are used in micro-power plants, microturbines and devices in which first and second generation bearings could not be applied due to heavy load constraints.

The load capacity of different generation bearings can be compared based on the results of research studies investigating specific solutions, as shown in Figure 14.

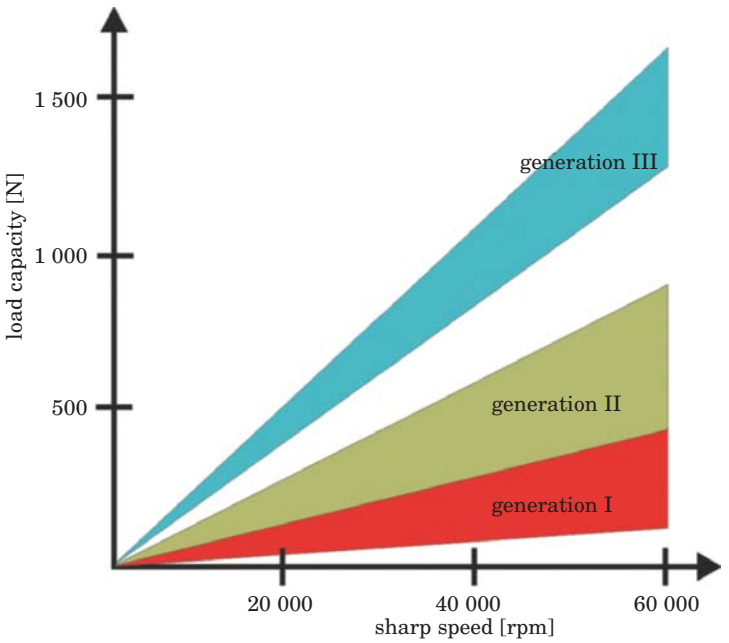

Fig. 14. A comparison of the load capacity of three generations of foil bearings
Source: On the basis of DELLACORTE 2003.

Conclusions

The presented overview of the structural solutions deployed in bearings in microturbines and other devices of the type illustrates the great variety of technical solutions supporting the operation of contemporary rotor machines. The greatest advantages delivered by traditional rolling bearings are the stiffness of the structural support and low sensitivity to sudden load change. Foil bearings guarantee stable rotor operation at high speed and small loads. Except for overload, start-up and rundown, moving parts do not come into contact with stationary parts. Gas and foil bearings do not require the use of

lubricants harmful to the environment. Owing to those properties, state-of-the-art foil bearings deliver rotational speed of 2 million rpm at operating temperatures as high as 800°C. Regardless of the strengths and weakness of different support solutions for microturbines and other technical devices, the knowledge and practice of building and diagnosing microbearings is undergoing rapid expansion world-wide. Research studies are initiated in various areas that range from material technology to modeling support structures in foil bearings. New technologies supporting the production of structural elements, new research methods and testing equipment need to be developed to verify the properties of the processed materials and finished elements.

Accepted for print 31.08.2009

References

AGRAWAL G.L. 1997. *Foil air/gas bearing technology – an overview*. The American Society of Mechanical Engineers, 97-GT-347.

BRUCKNER R.J. 2004. *Simulation and Modeling of the Hydrodynamic, Thermal, and Structural Behavior of Foil Thrust Bearings.* Department of Mechanical and Aerospace Engineering, Case Western Reserve University.

DELLACORTE C., PINKUS O. 2002. *Tribological Limitations in Gas Turbine Engines:A Workshop to Identify the Challenges and Set Future Directions.* Glenn Research Center, Cleveland, Ohio.

DELLACORTE CH. 2000. *Load Capacity Estimation of Foil.* Air Journal Bearings for Oil-Free Turbomachinery Applications.

DELLACORTE CH. 2004. *Future Issues and Approaches to Health Monitoring and Failure Prevention for Oil-Free Gas Turbines.* NASA Glenn Research Center, Cleveland, Ohio.

DELLACORTE CH., VALCO M.J. 2003. *Oil-free turbomachinery technology for regional jet, rotorcraft and supersonic business jet propulsion engines.* NASA Glenn Research Center, Cleveland, Ohio.

DELLACORTE CH., ZALDANA A.R., RADIL K.C. 2002. *A Systems Approach to the Solid Lubrication of Foil Air Bearings for Oil-Free Turbomachinery*. NASA Glenn Research Center, Cleveland, Ohio.

HOU Y., ZHU Z.H., CHEN C.Z. 2004. *Comparative test on two kinds of new compliant foil bearing for small cryogenic turbo-expander*. Cryogenics 44, 69–72.

TAE HO K., SAN ANDRES L. 2007. *Analysis of advanced gas foil bearings with piecewise linear elastic supports*. Tribology International 40, 1239–1245.

XIONG L.Y. WU G., HOU Y. 1997. *Development of aerodynamic foil journal bearings for a high Speer cryogenic turboexpander.* Cryogenics, 37, 221–230.

ŻYWICA G. 2007. *Analiza rozwiązań konstrukcyjnych mikrołożysk dostępnych w literaturze i katalogach firm.* Opr.wew. IMP PAN, Gdańsk.

TECHNICAL SCIENCES
Abbrev.: Techn. Sc., No 12, Y 2009

DOI 10.2478/v10022-009-0020-9

MODELING FOIL BEARINGS

***Wojciech Miąskowski*[1], *Paweł Pietkiewicz*[1], *Grzegorz Żywica*[2]**

[1] Chair of Mechanics and Machine Design
University of Warmia and Mazury in Olsztyn
[2] Institute of Fluid-Flow Machinery Polish Academy of Sciences in Gdańsk
Rotor Dynamics and Slide Bearing Department

Key words: foil bearing, modelling foil bearings.

Abstract

This paper presents selected numerical models of foil bearings developed in a few research centres around the world. The development of reliable foil bearing numerical models still poses many problems. Such difficulties are encountered mainly due to foil bearings' complex structure. In addition to elements found in conventional journal and sleeve bearings, elastic-plastic elements as a foil complex occur. Foil bearing models have to account for the structural base, the fluid lubricating film as well as the interactions between the two factors. A reliable foil bearing models would significantly contribute to bearing design At present, such bearing modeling process requires time-consuming and costly experiments.

MODELOWANIE ŁOŻYSK FOLIOWYCH

***Wojciech Miąskowski*[1], *Paweł Pietkiewicz*[1], *Grzegorz Żywica*[2]**

Katedra Mechaniki i Podstaw Konstrukcji Maszyn
Uniwersytet Warmińsko-Mazurski w Olsztynie
Instytut Maszyn Przepływowych Polskiej Akademii Nauk w Gdańsku
Zakład Dynamiki Wirników i Łożysk Ślizgowych

Słowa kluczowe: łożysko foliowe, modelowanie łożysk foliowych.

Abstrakt

W artykule przedstawiono wybrane modele numeryczne łożysk foliowych opracowane w kilku ośrodkach badawczych na świecie. Opracowanie wiarygodnych modeli numerycznych takich łożysk wciąż sprawia wiele trudności. Wynika to przede wszystkim ze złożonej budowy łożysk foliowych, gdyż oprócz elementów znanych z klasycznych łożysk ślizgowych, występują elementy sprężysto-podatne w postaci zespołu folii. Modelując łożyska foliowe, oprócz strukturalnej oraz przepływowej warstwy nośnej, należy również uwzględnić ich wzajemne oddziaływanie. Wiarygodne modele łożysk foliowych znacznie ułatwiłyby proces projektowania. Obecnie opracowywane konstrukcje takich łożysk wymagają bowiem przeprowadzania bardzo czasochłonnych i kosztownych badań eksperymentalnych.

Introduction

Foil bearings applied in high-speed machines are complex structures as regards the applied materials and structural characteristics. In functional terms, they are similar to hydrodynamic bearings where the dynamically formed lubricant with adequate dynamic pressure is responsible for the bearing's load capacity. There are, however, several differences between foil bearings and bearings with a stiff sleeve. The sleeve elements of a foil bearing are subjected to complex load which deforms the foil layer. This type of bearings cannot be adequately described with the use of the classic theory of modeling hydrodynamic and aerodynamic bearings. New modeling methods have to be developed to design the required solutions in foil bearings.

This paper presents selected approaches to modeling the operating parameters of foil journal bearings and foil thrust bearings. The discussed models highlight the main trends in research studies investigating foil bearings.

Modeling the effect of bearing structure on the load capacity of foil bearings

Foil bearings have been applied for many years, yet the development of reliable numerical models still poses many problems. Such difficulties are encountered mainly due to foil bearings' complex structure. In addition to elements found in conventional journal and sleeve bearings, foil bearings feature a foil complex (bump foil and top foil layers). Owing to this solution, rotors equipped with foil bearings are characterized by a much higher stability reserve than conventional journal bearings. Excess energy is dispersed through foil deformation and friction between the co-acting foil elements, and the shape of the lubricating gap adapts to the operating environment. The structure of a typical foil bearing is presented in Figure 1. The foil complex

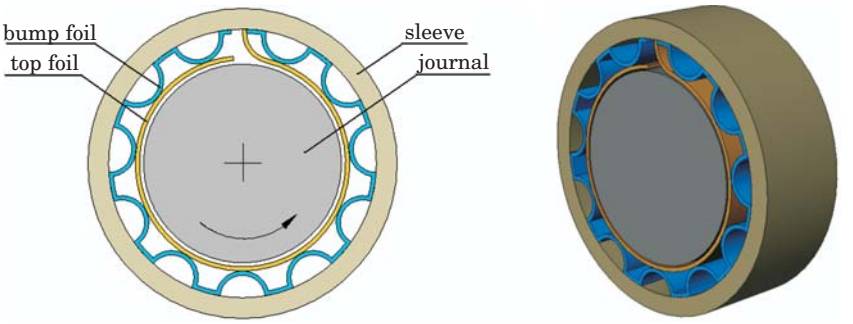

Fig. 1. A typical foil bearing

Source: Own work.

forms the bearing's structural base which, together with the fluid lubricating film, determines the dynamic properties of bearing systems.

Foil bearing models have to account for the structural base, the fluid lubricating film as well as the interactions between the two factors. During machine start-up and shut-down, the journal and the top foil layer come into direct contact. This creates additional problems as fluid friction requires a different modeling approach than that applicable to stable rotor operation. It should also be noted that the properties of materials used in the production of bearing elements are largely dependent on temperature. In typical applications, the working temperature of foil bearings can change within a very wide range (several hundred ^{o}C). In view of the above, the modeling of foil bearing operation requires complex fluid-structural numerical analyses that account for thermal phenomena. Owing to the complexity of the discussed problem, the discrepancies in the published numerical calculations and experimental results can reach up to 500% (AGRAWAL 1997).

The problem of developing foil bearing models is investigated by various research teams around the world. A reliable operating model would significantly contribute to bearing design. At present, the modeling process requires time-consuming and costly experiments. The use of reliable models could significantly simply this procedure.

The most popular methods in foil bearing modeling rely on the Reynold's equation to describe the lubricating fluid film base (LEZ et al. 2007, SUDHEER KUMAR REDDY 1997, KIM, SAN ANDRES 2007). Algorithms of the finite difference method or the finite volume method are usually applied in the numerical model. The interactions between the foil complex and the sleeve surface are usually simulated with the finite element method (LEZ et al. 2007, SUDHEER KUMAR REDDY 1997, BRAUN 1997). Some authors propose to replace bump foil with a single stiffness-damping element (RUBIO, SAN ANDRES 2006). The entire foil bearing is modeled by coupling the fluid film model and the structural model. Some references suggest he use of analytical formulas (HESHMAT et al.1983, KU, HESHMAT 1992, WELOWIT, ANNO 1975, LEE et al. 2006). According to the authors of this study, such formulas are developed based on highly simplified theoretical models and their usefulness is debatable.

Research studies into foil bearings are carried out by the Szewalski Institute of Fluid-Flow Machinery of the Polish Academy of Sciences (IMP PAN) in Gdańsk in collaboration with the research team of the University of Warmia and Mazury in Olsztyn. The main objective of those efforts is to design a foil bearing suitable for use in micro-turbines operating in the ORC cycle. A special bearing structure is required to match the operating parameters of such machines. In this case, the key advantages delivered by foil bearings are: high rotational speeds, operability in a wide range of temperatures, excellent

vibration damping, long working life, easy maintenance and compatibility with a variety of lubricants.

To facilitate the design process, the research team of IMP PAN in Gdańsk developed a numerical model supporting the preliminary selection of bearings. The proposed method combines customized solutions with commercially-available software. MESWIR-series applications developed by IMP PAN was used to describe non-linear phenomena in the lubricating gap and the dynamic characteristics of the rotor. Foil complex deformations were analyzed with the application of the MES – ABAQUS package. A complete model of a foil bearing integrated with the rotor model was developed by combining the strengths of both software applications (KICIŃSKI, ŻYWICA 2008). The model was partially validated in an experiment which confirmed its suitability for predicting the properties of bearing-rotor systems (KICIŃSKI et al. 2008).

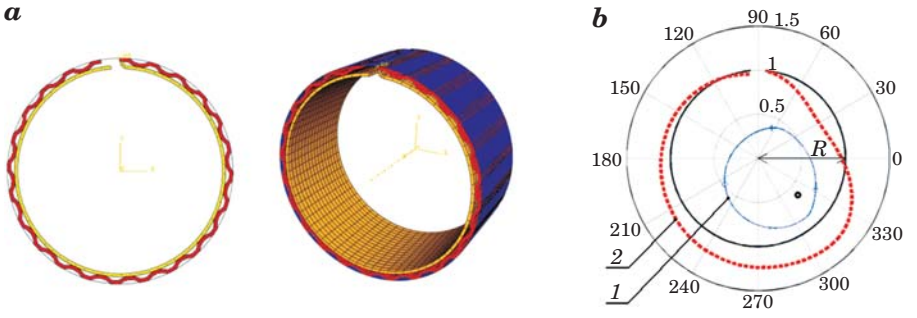

Fig. 2. MES model of a foil bearing's structural base (*a*) and selected calculation results (*b*) (*1* – trajectory of journal vibration, *2* – shape of deformed foil complex)
Source: Own work.

The bearing model and the results of calculations determining the deformation of the foil complex and the trajectory of journal vibrations are presented in Figure 2. The calculations were performed for the rotor-foil bearing system with dimensions corresponding to a 3 kW micro-turbine. The rotor diameter was 10 mm and the rotor length – 140 mm. The lubricating fluid was isobutane, a low-boiling medium. The calculations were performed for a speed range of 10 000 – 100 000 rpm (Fig. 3). The obtained results validated the system's stability in the majority of the tested speed ranges. The models developed by IMP PAN support the analysis of practically every rotor-foil bearing system, and the achieved results facilitate the design of new structures and the optimization of the existing designs.

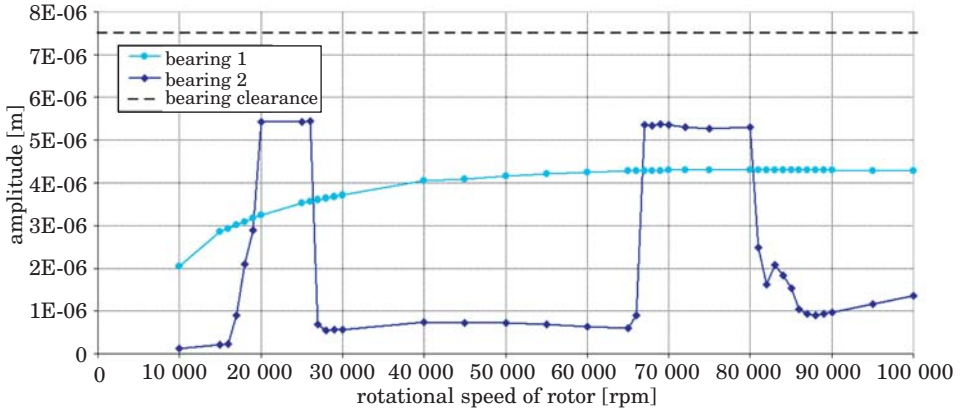

Fig. 3. Amplitude of relative journal-sleeve vibrations in the speed range of 10 000 – 100 000 rpm
Source: Own work.

Modeling the wear of structural elements during foil bearing operation

Since foil bearing elements come into direct physical contact during operation, models supporting the analyses of surface friction in the bearing's structural base during start-up, rundown and overload need to be developed. A numerical analysis of the above was carried out by Bruckner in a study of thrust bearings. The thrust bearing with eight bearing pads of a foil complex uniformly placed around the bearing perimeter is a subject of his study (BRUCKNER 2004). The tested bearing's diagram is show in Figure 4 and its basic technical data are presented in Table 1.

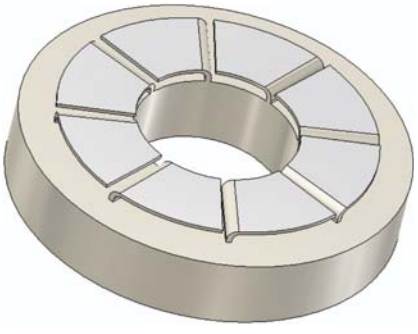

Fig 4. Structural diagram of a foil thrust bearing with eight bearing pads of foils
Source: Own work.

Table 1

Technical data of a foil thrust bearing

Radius inner	23 mm
Radius outer	45 mm
Azimuthal extent of one foil set	43 deg
Characteristic speed	40 000 rpm
Midspan speed	148 m/s
Lubricant	Air at see level conditions
Top foil material	Inconnel X-750
Top foil thickness	0.13 mm

Source: Own work.

The objective of the study was to simulate and validate the results of foil wear during the operation of a foil thrust bearing. Visible wear of the mating surfaces begun with the midspan of all foils sets even during low load tests. The top foil layer was divided into two regions (outboard and inboard) when the numerical model of a foil thrust bearing developing. According to model, different inclination angle of the outboard region and the bearing disc plane were assumed. The calculations also took temperature changes and the thickness distribution of lubricating film on mating surfaces into account. The pressure distributions on the top foil surface was determined inter alia on the basis of such models development. A comparison of simulation and experimental results confirms the model's usability to predict areas, where one may deal with the substantial friction wear. Despite the bump foil substitution with the stiffness coefficients, determined in the numerical calculations, such way model development allowed the reliable results of the biggest wear of the top foil regions occurrence prediction, to be attained.

Conclusions

This paper presents selected models of foil bearings. One should notice, that the present state of art and available software supporting engineering calculations do not allow entire representation of all phenomena, that occur in such type bearings. Despite those difficulties, discussed, simplified models allowed analysis and particular properties prediction of the foil bearings, according to current needs of the research teams. At the present knowledge and computer techniques state, the numerical models development, which describe the most important properties with regard to the present research conduction, is the reasonable attempt to the complex systems modelling, as the

foil bearings are. Models' development requires an intensive team-work of scientists, who deal with the modelling as well as with the experiments. The suitable technical abilities, which mean a high-efficiency computer working station with the adequate software and dedicated test stands, are also essential.

Research on subjects, discussed in this paper, are conducted by the recently established research team of the Szewalski Institute of Fluid-Flow Machinery of the Polish Academy of Sciences in Gdańsk and the University of Warmia and Mazury in Olsztyn. Besides the formulation of a simulation model, which considerably simplify and speed up the design process, the final foil bearing construction solution, anticipated for the application in the low power micro-turbines, become the result of this cooperation. The task requires a number of the research work, such as the adequate structural materials for the bearing elements selection, development of their manufacturing process and the specialized test stands construction (necessary for close to the reality conditions tests), to be conducted. Research findings will support the validation of the existing, as well as simplify the new numerical models of the foil bearings development. All those issues will be a subject of the further publications.

Accepted for print 03.07.2009

References

AGRAWAL G.L. 1997. *Foil Air/Gas Bearing Technology – An Overview*. International Gas Turbine & Aero engine Congress & Exhibition, Orlando (USA) June 1997.

BRAUN M., CHOY F., DZODZO M., HSU J. 1997. *Two-dimensional dynamic simulation of continuous foil bearing*. Tribology International, 29(1): p. 61–68.

BRUCKNER R.J. 2004. *Simulation and Modeling of the Hydrodynamic, Thermal, and Structural Behavior of Foil Thrust Bearings*. Department of Mechanical and Aerospace Engineering, Case Western Reserve University.

HESHMAT H., WALOWIT J., PINKUS O. 1983. *Analysis of Gas-Lubricated Foil Journal Bearings*. ASME Journal of Lubricate Technology. 105: 647–655.

KICIŃSKI J., ŻYWICA G. 2008. *Metody łożyskowania wysokoobrotowych wirników mikroturbin stosowanych w układach kogeneracyjnych*. Archiwum Energetyki, XXXVIII (2): 137–145.

KICIŃSKI J., ŻYWICA G., BANASZEK S. 2008. *Modelling the Elastic Strains of Foil Bearing Bush*. 7th EDF & LMS Poitiers Workshop: "Operational Limits of Bearings: Improving of Performance through Modelling and Experimentation" – FUTUROSCOPE, Poitiers (France) 2 October 2008.

KICIŃSKI J., ŻYWICA G., RZĄDKOWSKI R., DREWCZYŃSKI M. 2008. *Modelowanie strukturalnej warstwynosnej łozyska foliowego*. Acta Mechanica et Automatica, 2(1): 45–50.

KIM T.H., SAN ANDRES L. 2007. *Analysis of Advanced Gas Foil Bearings with Piecewise Linear Elastic Supports*. Tribology International, 40: 1239–1245.

KU R., HESHMAT H. 1992. *Compliant Foil Bearing Structural Stiffness Analysis:* Part I – *Theoretical Model Including Strip and Variable Bump Foil Geometry*. ASME Journal of Tribology, 114: 394–400.

LEE Y.B., PARK D.J., KIM CH. 2006. *Numerical Analysis for Bump Foil Journal Bearing Considering Top Foil Effect and Experimental Investigation*. 7th Conference on Rotor Dynamics IFToMM, Austria, paper ID-229.

LEZ S., ARGHIR M., FRENE J. 2007. *Static and Dynamic Characterization of a Bump-Type Foil Bearing Structure.* ASME Journal of Tribology, 129: 75–83.

MIĄSKOWSKI W., NALEPA K., PIETKIEWICZ P. 2008. *Charakterystyka prac prowadzonych w światowych ośrodkach naukowych i przemysłowych zajmujących się mikrołożyskami.* IMP PAN, Arch. 24/2008, Gdańsk.

MIĄSKOWSKI W., NALEPA K., PIETKIEWICZ P. 2008. *Opracowanie koncepcji układu pomiarowego dla stanowiska badawczego dynamiki wirników. Przegląd aparatury pomiarowej*. IMP PAN, Arch. 169/08, Gdańsk.

RUBIO D., SAN ANDRES L. 2006. Bump-Type Foil Bearing Structural Stiffness: Experiments and Predictions. ASME Journal of Engineering for Gas Turbines and Power, 128: 653–660.

SUDHEER KUMAR REDDY D., SWARNAMANI S., PROBHU B. 1997. *Analysis of Aerodynamic Multileaf Foil Bearings.* Wear, 209: 115–122.

WELOWIT J., ANNO J. 1975. *Modern Development in Lubrication Mechanics.* Applied Science Publisher, London.

ŻYWICA G. 2008. *Kształtowanie własności strukturalnej warstwy nośnej łożyska foliowego.* XXXV Sympozjum DIAGNOSTYKA MASZYN, Węgierska Górka, 3–8 marca.

TECHNICAL SCIENCES
Abbrev.: Techn. Sc., No 12, Y 2009

DOI 10.2478/v10022-009-0021-8

FOIL MICRO-BEARING TESTS

***Wojciech Miąskowski*[1], *Krzysztof Nalepa*[2], *Grzegorz Żywica*[3]**

[1] Chair of Mechanics and Machine Design
[2] Chair of Power Engineering
University of Warmia and Mazury in Olsztyn
[3] Institute of Fluid-Flow Machinery Polish Academy of Sciences in Gdańsk
Rotor Dynamics and Slide Bearing Department

K e y w o r d s: foil bearing, high-speed machines bearings, bearing systems testing.

A b s t r a c t

Selected methods of testing applied in the research centres dealing with foil bearings technology are overviewed in this paper. Tests analyzing foil bearings require special test rigs and a testing methodology that simulates the bearings' actual working conditions. Test rigs should allow factors, that influence on a bearing's exact operating environment. For this reason, most tests investigate selected key parameters Tribological tests under extreme bearing operating temperatures and with the effect of lubricants make a separate group of tests. Another tests group is focused on the optimal bearing stiffness determination through the choice of adequate structural solutions and manufacturing technologies. Foil bearing test methods presented in this paper do not exhaust the study domain, in which new constructions may be tested. They only overview basic test methods used for the foil bearing systems.

BADANIE ŁOŻYSK FOLIOWYCH

***Wojciech Miąskowski*[1], *Krzysztof Nalepa*[2], *Grzegorz Żywica*[3]**

[1] Katedra Mechaniki i Podstaw Konstrukcji Maszyn
[2] Katedra Elektrotechniki i Energetyki
Uniwersytet Warmińsko-Mazurski w Olsztynie
[3] Instytut Maszyn Przepływowych Polskiej Akademii Nauk w Gdańsku
Zakład Dynamiki Wirników i Łożysk Ślizgowych

S ł o w a k l u c z o w e: łożysko foliowe, łożyskowanie maszyn szybkoobrotowych, badania systemów łożyskowania.

A b s t r a k t

W artykule przedstawiono wybrane metody badań stosowane w ośrodkach badawczych zajmujących się technologią łożysk foliowych. Badania eksperymentalne łożysk foliowych wymagają opracowania specjalnych stanowisk badawczych i tworzenia metod badań, które pozwoliłyby na

odtworzenie warunków, w jakich będą pracować badane łożyska. Stanowiska badawcze powinny uwzględniać czynniki, które mają wpływ na warunki pracy łożyska. Badania są prowadzone w kilku głównych kierunkach. Jedną gałąź stanowią badania tribologiczne w ekstremalnej temperaturze, w jakiej będą pracować łożyska, a także z użyciem mediów smarnych. Inna gałąź badań jest skierowana na zapewnienie optymalnej sztywności łożysk przez odpowiednią konstrukcję i dobór technologii wykonania elementów konstrukcyjnych. Przedstawione w artykule metody badań łożysk foliowych nie wyczerpują zakresu badań, jakim mogą być poddawane nowo opracowywane konstrukcje. Stanowią jedynie przegląd podstawowych metod badań stosowanych w systemach łożysk foliowych.

Introduction

The contemporary demand for energy requires solutions that rely on the latest technological advancements. New concepts are increasingly often evaluated based on criteria such as environmental protection, cost effectiveness and comprehensiveness of application. As a result, power equipment undergoes constant minimization, while ensuring the right operating parameters, in particular the power output. The reduction in the size of elements responsible for energy processing increases the speed of moving parts. Their operating speed is controlled by bearings supporting the working elements. In principle, the theoretical premises for conventional bearing solutions also apply to micro-turbines and other devices of the type. Yet new impediments are encountered at high rotational speeds. The main problem is the choice of structural materials which are resistant to high temperatures and guarantee the required structural precision. This, in turn, necessitates the development of new bearing designs.

A wide variety of micro-bearings are described in scientific publications, and their usefulness has to be analyzed in view of numerous criteria. Based on the available sources, the following key criteria for the selection of micro-bearings are applied (Żywica 2007):
– allowable rotational speed,
– load capacity,
– allowable operating temperature,
– working life and reliability, ease of repair,
– bearing precision and stiffness,
– vibration damping,
– resistance to external factors.

In view of the rapid advancement of the micro-bearing technology, in particular magnetic and foil bearings, the published sources describe various experiments, numerical analyses and analytical calculations that aim to optimize the structure of micro-bearings. This study overviews selected micro-bearing tests which evaluate the key properties of the analyzed foil bearings.

Measuring the vibration of rotors equipped with foil bearings

Operating vibration is one of the key working parameters of every rotor-bearing system. Tests measuring the vibration level of rotor journals are performed for every type of bearings, in particular journal bearings. In view of the specific structure of foil bearings, their geometry varies subject to working conditions. For this reasons, tests measuring the vibration of rotors equipped with foil bearings are of special significance.

Since foil bearings operate at very high speeds and temperatures, they have to be analyzed in test rigs consisting of a real object equipped with the tested bearings (XIONG et al. 1996, HOU et al. 2004). Figure 1 presents a photograph of a turboexpander applied in a test rig. Figure 2 shows the structural diagram of two bearing variants applied in the turboexpander rotor with bearing diameter of 12 mm, weight of 90 g and rotational speed of approximately 230 000 rpm.

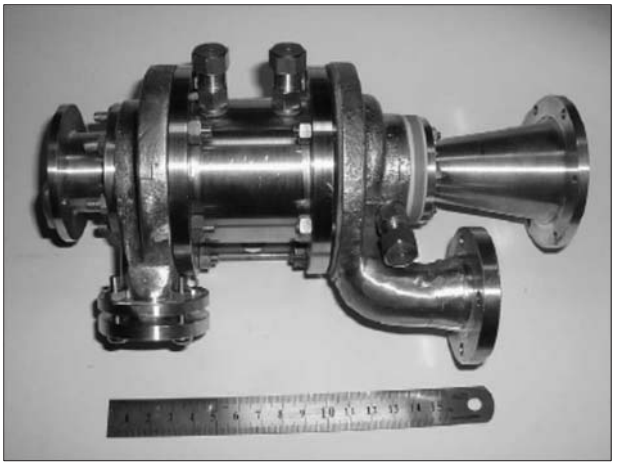

Fig. 1. Turboexpander applied in the study
Source: HOU et al. (2004).

The bearing's rotational speed was measured with the use of fiber optic probes. Rotor vibrations were measured in two mutually perpendicular directions with probes inserted in the stationary part of the device. Tests were carried out for two bearing types in several variants:

– spiral bearings where foil is supported with the following number of copper wires: n = 15, 17, 19, 21, 23

– multileaf bearings with the following number of foil elements: n = 6, 7

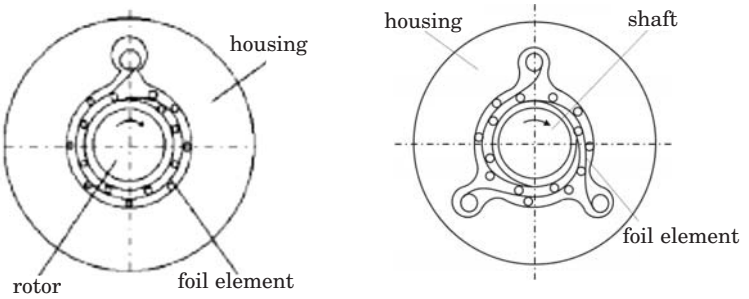

Fig. 2. Structural diagram of the tested bearings. On the left – a spiral foil bearing (HOU et al. 2004); on the right – a multileaf bearing
Source: On the basis of XIONG et al. (1997).

Figures 3 and 4 present selected experimental results.

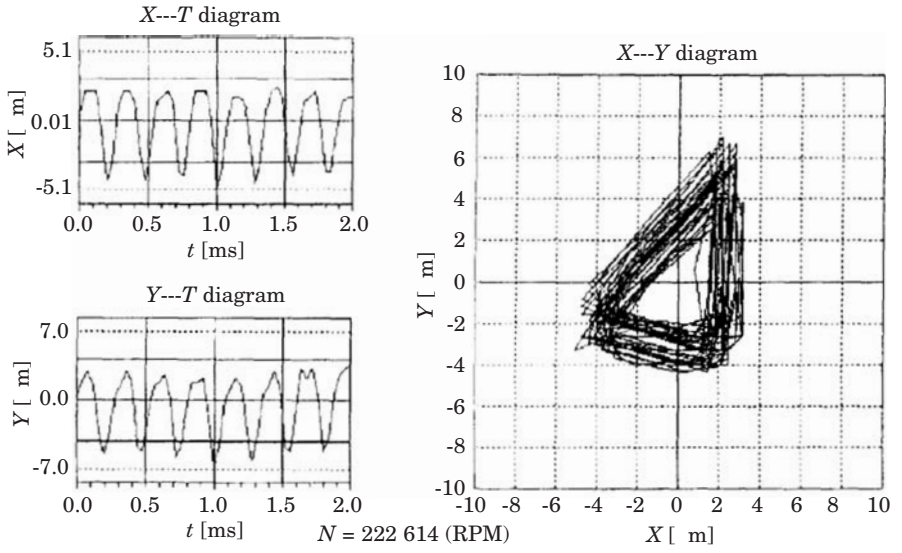

Fig. 3. The results of vibration measurements in a rotor equipped with a spiral foil bearing where the foil element is supported by 15 copper wires with a diameter of 0.2 mm. Rotational speed: 222 614 rpm
Source: HOU et al. (2004).

Bearings with a more complex structure (multileaf and bump foil bearings) were subjected to similar tests. The author of the study measured rotor shaft displacement in two directions as well as working temperatures (DELLACORTE 2004). Owing to the high operating temperature of foil bearings, optical displacement probes were applied (devices based on the resistance of the structural material lose their properties at temperatures higher than 400°C,

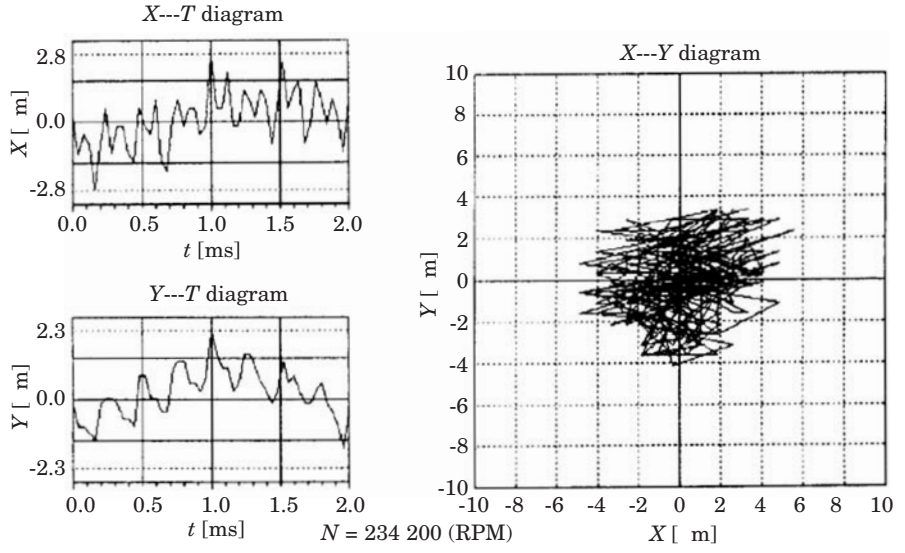

Fig. 4. The results of vibration measurements in a rotor equipped with a multileaf foil bearing with 6 foil elements. Rotational speed: 234 200 rpm

Source: HOU et al. (2004).

and the correlation between temperature and resistance cannot be determined).

The sensor comprises a fiber optic unit with two functions. Some fibers emit light with a set frequency. The emitted light beam is reflected from the moving rotor shaft. Subject to the shaft's location, reflected light is channeled to a different fiber which intercepts the reflected beam. Based on the results of specific calculations, the probe determines the location of the rotor surface in the measured direction.

The rotor surface has to be adequately prepared for the optical measurement of rotor displacement. Having tested various chemical compounds, a platinum-based surface was chosen due to its ability to withstand operating temperatures higher than 600°C. This measurement method was selected due to the following factors:

– the light reflecting properties of the tested materials changed with temperature and rotational speed (e.g. silver becomes softened and the shaft coating layer changes its thickness with speed),

– the coating layer has to demonstrate stable and high light reflecting parameters. At high temperatures, many compounds become coated with an oxide layer or change their color.

Temperature was measured with temperature sensors placed on the "rear" side of the foil element. The detailed distribution of sensors was not described

Testing foil bearing stiffness

The stiffness of every bearing type is one of its main operating parameters. Model test rig with the rotor weight of around 5 kg, its diameter of 35 mm and total length of 594 mm is presented in YONG-BO et al. 2004. The turbine was installed at the end of the rotor. The rotor was equipped with two bearings on both ends in the axial direction.

Two mutually perpendicular displacement sensors were installed in the midspan of the rotor. A rotational speed sensor was also used.

The rotor has a diameter of 60 mm, and it is supported by two ball bearings. The tested bearing is placed in the midspan of the rotor. The bearing has the inside diameter of 61.45 mm, the length of 60 mm and the weight of 5.3 kg. Displacement was measured with the use of 4 displacement sensors placed in mutually perpendicular directions on both sides of the tested bearing. Each ball bearing was equipped with two accelerometers measuring acceleration in mutually perpendicular directions.

The test was carried out for two foil bearing structural variants (foil bearings with Cu coated viscoelastic foil and bump foil).

The effect of double bump foil on the properties of foil bearings (TAE HO KIM, 2007)

The properties of a foil bearing, in particular the bearing's overload resistance, can be improved through the use of a double bump foil element where one foil layer is characterized by higher stiffness. Under normal operating conditions, the bearing relies on the properties of the inside foil layer. During overload, the rotating journal comes into direct physical contact with bump foil. The foil layer is deformed, yet it does not damage the bearing because the external foil layer absorbs some of the overload energy. The discussed tests involved a numerical analysis of the Reynold's equation. The structural diagram of the bearing and the model bearing with a double bump foil layer are presented in Figure 5.

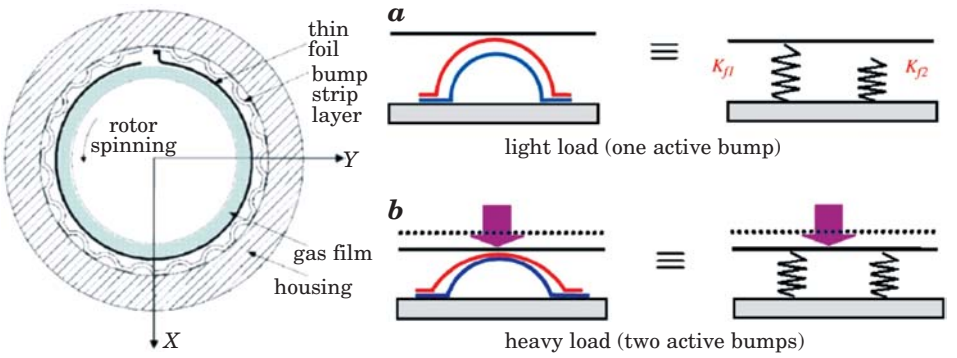

Fig. 5. A schematic diagram of a bump foil bearing and a model bearing with a double bump foil layer
Source: KIM, SAN ANDRES (2007).

The results of simulation tests are presented in Figures 6–8.

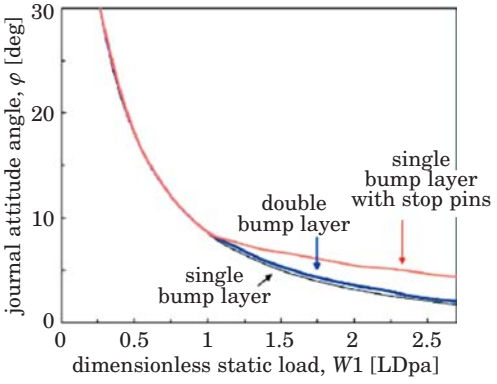

Fig. 6. Measurement of relative eccentricity subject to static load in three bearing variants
Source: KIM, SAN ANDRES (2007).

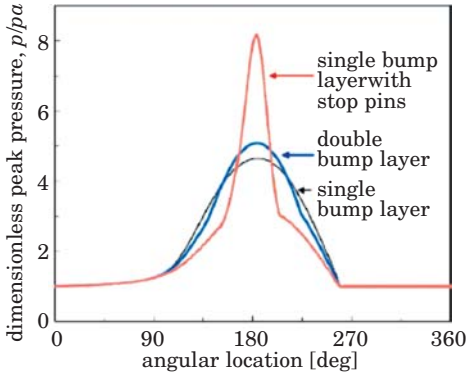

Fig. 7. The effect of bearing overload on three types of foil elements
Source: KIM, SAN ANDRES (2007).

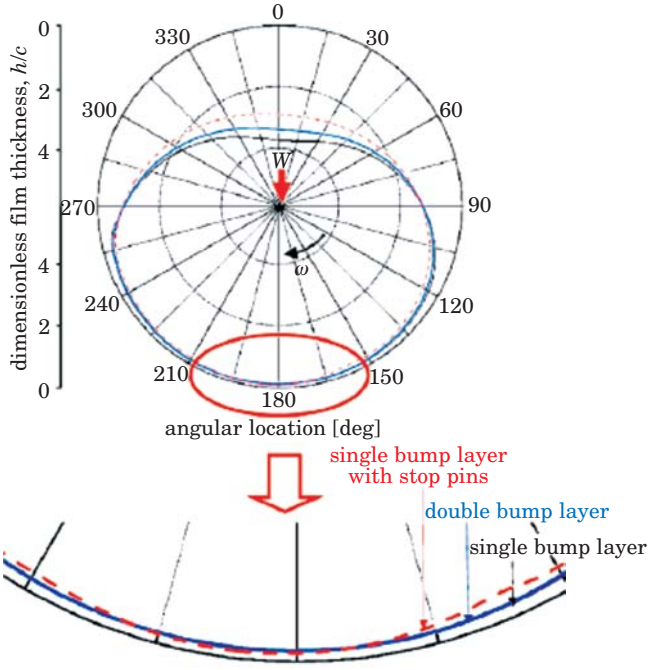

Fig. 8. Thickness distribution of lubricating film in three bearing variants
Source: Kim, San Andres (2007).

Testing micro-bearing surface wear caused by high temperature and friction

The properties of structural materials applied in bearings' working elements are investigated separately owing to foil bearings' very high rotational speed, small size and high operating temperature. The choice of materials which retain their elastic properties in a wide range of temperatures and which are resistant to friction wear during the start-up, rundown and overload of machines equipped with foil bearings is a very important consideration. A model test rig for analyzing the tribological wear of materials applied in the production of bearing foil is presented in MITI commercial materials (MiTi® Tribometers for Friction, Wear and Lubrication Testing).

The device supports tests within the speed range of up to 10 000 rpm and working temperatures of up to 900°C. The operating radius of the torque measuring rod is 3.18 to 79.4 mm. The load applied to the tested element ranges from 100 to 500 g.

The effect of high temperatures on bearing operation is analyzed in a test rig shown in MITI commercial materials. The test rig investigating normal

bearing operation is placed in the proximity of the heat source. This solution supports the evaluation of changes in the bearing's operating parameters and its fitness for use in an environment simulated by the device.

Conclusions

Tests analyzing foil bearings require special test rigs and a testing methodology that simulates the bearings' actual working conditions. A bearing's exact operating environment is very difficult to recreate, and such tests are performed by very few research centers around the world. For this reason, most tests investigate selected key parameters. Tribological tests have to account for extreme operating temperatures as well as the effect of lubricants which are often highly chemically active substances. Tests aiming to determine the optimal bearing stiffness through the choice of adequate structural solutions and manufacturing technologies should be preceded by simulations which significantly reduce experimental costs.

In recent years, a research team pooling the resources of the University of Warmia and Mazury in Olsztyn, the Szewalski Institute of Fluid-Flow Machinery of the Polish Academy of Sciences in Gdańsk and other research centers was created to further research into the development of foil bearings, the appropriate testing methodology and the use of foil bearings in power microturbines.

Accepted for print 31.08.2009

References

BANG K.G., LEE D.G. 2002. *Thrust bearing design for high-speed composite air spindles*. Composite Structures, 57: 149–160.

BAUMAN S. 2005. *An Oil-Free Thrust Foil Bearing Facility Design,Calibration, and Operation*. NASA.

BELFORTE G., COLOMBO F., RAPARELLI T., TRIVELLA A., VIKTOROV V. 2006. *An experimental study of high-speed rotor supported by air bearings: test RIG and first experimental results*. Tribology International, 39: 839–845.

BRUCKNER R.J. 2004. *Simulation and Modeling of the Hydrodynamic, Thermal, and Structural Behavior of Foil Thrust Bearings*. Department of Mechanical and Aerospace Engineering, Case Western Reserve University.

CHANGQING B., QINGYU X. 2006. *Dynamic model of ball bearings with internal clearance and waviness*. Journal of Sound and Vibration, 294: 23–48.

CHUANG-CHIA LxIN, GHODSSI R., AYON A.A., DYE-ZONE CHEN, JACOBSON S., BREUER K., EPSTEIN A.H., SCHMIDT M.A. 1999. *Fabrication and Characterization of a Micro Turbine/Bearing Rig*. Massachusetts Institute of Technology, Cambridge, MA 02139, USA.

DELLACORTE K. 2004. *Future Issues and Approaches to Health Monitoring and Failure Prevention for Oil-Free Gas Turbines*. NASA Glenn Research Center, Cleveland, Ohio.

HAGIU G.D., GAFITANU M.D. 1997. *Dynamic characteristics of high speed angular contact ball bearings.* Wear, 211: 22–29.

HARRIS T.A. 2001. *Rolling bearing analysis*. New York, Wiley.

HOU Y., ZHU Z.H., CHEN C.Z. 2004. *Comparative test on two kinds of new compliant foil bearing for small cryogenic turbo-expander.* Cryogenic, 44: 69–72.

JUNG-KOO P., KYUNG-WOONG K. 2004. *Stability analyses and experiments of spindle system using new type of slot-restricted gas journal bearings.* Tribology International, 37:451–462.

KUROKI J., SHINSHI T., LI L, SHIMOKOHBE A. 2006. *A micro-magnetic bearing using capacitive axial displacement sensing.* Precision Engineering, 30: 54–62.

KWAN Y.B.P., CORBETT J. 1998. *A simplified method for the correction of velocity slip and inertia effects in porous aerostatic thrust bearings*. Tribology International, 31: 779–786.

MASLEN E. 2000. *Magnetic Bearings*. University of Virginia, Department of Mechanical, Aerospace, and Nuclear Engineering, Charlottesville, Virginia, Revised June 5.

MING Z., FENGXIANG W., YIDAN S., JIQIANG W. 2006. *Stability Analysis of Magnetic Bearing with Resonance Circuit.* Power Electronics and Motion Control Conference, 2006. IPEMC 2006. CES/IEEE 5th International, vol. 2, 1–5.

MIZUMOTO H., ARII S., KAMI Y., GOTO K., YAMAMOTO T., KAWAMOTO M. 1996. *Active inherent restrictor for air-bearing spindles.* Precision Engineering, 19: 141–147.

MORALES W., FUSARO R., KASCAK A. 2003. *Permanent Magnetic Bearing Spacecraft Applications.* NASA/TM – 2003–211996.

QINGCHANG T., WEI L., XUEJUN X. 2002. *Investigations on a magnetic-hydrodynamic hybrid thrust bearing*. Tribology Letters, 12(1): 61–66.

RADIL K.C., DELLECORTE CH. 2002. *The Effect of Journal Roughness and Foil Coatings on the Performance of Heavily Loaded Foil Air Bearings.* Tribology Transactions, 45(2): 199–204 (13 ref.).

SCHWEITZER, G. 2005. *Safety and Reliability Aspects for Active Magnetic Bearing Applications – a Survey*. Journal of Systems and Control Engineering, Proc. of the Institution of Mechanical Engineers (IMechE), Part I, 219: 383–392.

SU JERRY C.T., LIE K.N. 2003. *Rotation effects on hybrid air journal bearings*. Tribology International, 36: 717–726.

SUDHEER KUMAR REDDY D., SWARNAMANI S., BRABHU B.S. 1997. *Anaysis of multileaf foil journal bearings.* Wear, 209: 115–122.

TAE HO KIM, LUIS SAN ANDRES 2007. *Analysis of advanced gas foil bearings with piecewise linear elastic supports.* Tribology International, 40: 1239–1245.

TAN Q., LI Q., LIU B. 2002. *Investigations on a permanent magnetic-hydrodynamic hybrid journal bearing.* Tribology International, 35: 443–448.

XIE Z., ZHU H., SUN Y. 2005. *Structure and Control of AC-DC Three-degree-of-freedom Hybrid Magnetic Bearing.* Electrical Machines and Systems, 2005. ICEMS 2005. Proceedings of the Eighth International Conference on, 1801–1806 Vol. 3.

XIONG L.Y., WU G., HOU Y. I inni. 1997. *Development of aerodynamic foil journal bearings for a high Speer cryogenic turboexpander.* Cryogenic, 37, 221–230.

YANLIANG X., YUEQIN D., XIUHE W., YU K. 2006. *Analysis of Hybrid Magnetic Bearing With a Permanent Magnet in the Rotor by FEM*. Transactions an Magnetics, 42(4): 1363–1366.

YONG-BO L., TAE-HO K. I inni. 2004. *Dynamic characteristics of a flexible rotor system supported by a viscoelastic foil Bearing (VEFB).* Tribology International, 37: 679–687.

KANG Y., SHEN P.C., HUANG C.C., SHYR S.S., CHANGY P. 2006. *A modification of the Jones-Harris method for deep-groove ball bearings.* Tribology International, 39: 1413–1420.

MiTi® Tribometers for Friction, Wear and Lubrication Testing - http://www.miti.cc/images/products-services/tribometer/Tribometer.pdf – 1.04.2009

TECHNICAL SCIENCES
Abbrev.: Techn. Sc., No 12, Y 2009

DOI 10.2478/v10022-009-0022-7

NUMERICAL ANALYSIS OF FLOW BIFURCATIONS IN A CLOSED-OFF CHANNEL

Wojciech Sobieski

Chair of Mechanics and Machine Design
University of Warmia and Mazury in Olsztyn

K e y w o r d s: bifurcation, fluid flow, CFD.

A b s t r a c t

This article describes the results of numerical simulations of fluid flow in a closed-off channel with a plain nozzle. Simulations were performed with the application of the Finite Volume Procedure in the Multi Flower 2D non-commercial application. The main objective of the study was to determine the effect of channel geometry on flow structure. A total of 27 system configurations were analyzed for nine geometry variants and three pressure variants in the feed nozzle. Based on the obtained results, five main flow types were determined, including Hopf bifurcation structures. This paper presents simulation results and it analyzes the observed flow types in view of general bifurcation conditions. The final section of this paper describes the attempts at repeating numerical simulations with the use of the FLUENT commercial application. This simulation makes a reference to an earlier experiment carried out by DYBAN et al. (1971), and it is a continuation of previous research described in detail by BADUR, SOBIESKI (2001).

NUMERYCZNA ANALIZA ZJAWISKA BIFURKACJI W PRZEPŁYWIE PŁYNU PRZEZ ŚLEPO ZAKOŃCZONY KANAŁ

Wojciech Sobieski

Katedra Mechaniki i Podstaw Konstrukcji Maszyn
Uniwersytet Warmińsko-Mazurski w Olsztynie

K e y w o r d s: bifurcation, fluid flow, CFD.

A b s t r a k t

Artykuł przedstawia badania numeryczne przepływu płynu przez ślepo zakończony kanał z umieszczoną wewnątrz prostą dyszą zasilającą. Symulacje wykonano metodą objętości skończonych z zastosowaniem niekomercyjnego pakietu Multi Flower 2D. Podstawowym celem badań było określenie wpływu geometrii kanału na strukturę przepływu. Badania wykonano dla 27 konfiguracji układu – dziewięciu wariantów geometrii i trzech wariantów ciśnień w dyszy zasilającej. Analiza

wyników doprowadziła do wytypowania pięciu głównych struktur przepływowych, w tym również struktur o charakterze bifurkacji Hopfa. W pracy zestawiono wyniki symulacji w formie zbiorczej, a także przeanalizowano zaobserwowane typy przepływów pod kątem ogólnych uwarunkowań bifurkacji. W końcowej części opisano próby powtórzenia symulacji numerycznych za pomocą komercyjnego pakietu FLUENT. Badania symulacyjne nawiązują do eksperymentu (DYBAN et al. 1971) i są kontynuacją wcześniejszych prac, opisanych szczegółowo w artykule (BADUR, SOBIESKI 2001).

Introduction

There are various examples of devices and sites with suddenly expanded parts (pipelines, channels, orifices, valves, gates, faults and many others) which perturb fluid flow and obstruct the bifurcation process. The new, post-bifurcation flow types may be divergent or oscillating in nature (BADUR, SOBIESKI 2001, KURNIK 1997). The flow type observed after the active bifurcation parameter has been exceeded (in most cases, the Reynolds number or the Mach number) is firstly determined by geometry and secondly – by velocity (DYBAN et al. 1971, CHIANG et al. 2001).

Various published sources describe experimental studies and numerical bifurcation simulations in suddenly expanded channels or ducts (Fig. 1). The first group is inclusive of a study carried out by DYBAN et al. (1971) which inspired the simulation analyses presented in this article. The experiment described in the cited study will be discussed in subsequent sections of this paper. The experiments and simulations carried out by CHIANG et al. (2001) are also a highly valuable source of data. They present detailed measurements of basic flow types which were modeled with the use of simulation techniques at a very high level of consistency. Similar experimental and numerical simulation studies have been described by MULINA et al. (2003). The most noteworthy papers in the second group include the work of BATTAGLIA et al. (1997) which delivers a detailed account of a numerical analysis of an expanded channel at various geometry and Reynolds number configurations. A similar study was carried out on a smaller scale by MANICA, DE BORTOLI (2003) to investigate an analogous flow system with the use of a non-Newtonian fluid model. Numerical bifurcation analyses were also performed by Polish researchers, including BADUR et al. (1999).

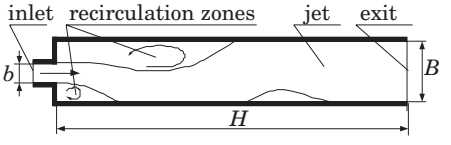

Fig. 1. Bifurcation in a two-dimensional planar channel
Source: BATTAGLIA (1997)

Author investigating numerical modeling of flow structures in suddenly expanded channels or ducts focus mainly on the determination of the critical Reynolds number at which the system is destabilized or bifurcation is observed. DYBAN et al. (1971) is the only researcher to have discussed in detail the forms and structures observed in a flow system following changes in geometry and flow parameters. The absence of in-depth studies investigating the above inspired the author to conduct the experiment presented in this paper, whose main objective was to classify the possible range of bifurcation forms in closed-off channels with a plain feed nozzle. This geometry was applied to compare simulation results with the above cited experiment. Basic numerical analyses of the same experiment were discussed by BADUR and SOBIESKI (2001), including an extensive introduction to the bifurcation theory, a description of the mathematical simulation model and the resulting software application. In the conclusions section, the author compared the results of the experiments and simulations, noting the reported similarities and differences. For this reason, the above aspects were intentionally omitted or only briefly indicated in this article. Detailed information can be found in the above cited study by BADUR and SOBIESKI (2001).

Laboratory experiment

The test stand, as described in the study by DYBAN et al. (1971), for the simulation model developed in this paper is presented in Figure 2. It comprises a closed-off channel with a moving rear wall (*4*) and a feed nozzle through which the fluid is supplied. The nozzle inlet b was adjustable in a range of 5 to 27 [mm]. The maximum channel length H, controlled with the movement of the rear wall, was 191 [mm]. Fluid was evacuated from the device via two symmetrical exits (*2*). The casing (*3*) was fixed, and the authors set up two variants of the test stand with the width of the main channel chamber equal to 25 and 51 [mm]. The working medium was air and water with aluminum particles. Flow was observed through the channel's top, transparent lid. Geometry was determined with the use of geometric indicators defined by the b/B and H/B ratios.

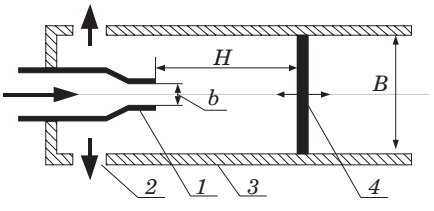

Fig. 2. Test stand: *1* – nozzle (inlet), *2* – exits, *3* – fixed casing, *4* – moving wall
Source: DYBAN et al. (1971)

The authors observed two main types of flow reversal: stationary symmetric flow and non-stationary, asymmetric flow occurring in several variants (Fig. 3). Flow characteristics were determined based on the geometric dimensions of the channel chamber and on the width of the nozzle inlet. The experiment has been discussed in detail and compared with simulation results by BADUR and SOBIESKI (2001).

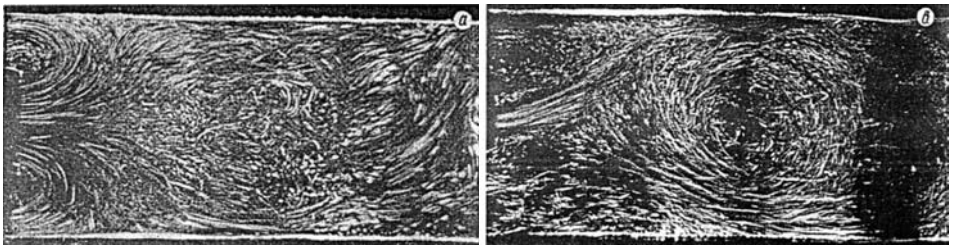

Fig. 3. Symmetric flow (on the left) and asymmetric flow (on the right)
Source: DYBAN et al. (1971)

Computer modeling

Computer-aided simulations involved a series of numerical computations for characteristic cases of channel geometry. The following assumptions were made prior to modeling:

- numerical computations will be performed for three channel lengths and three nozzle widths in a dimensionless system (for H/B = 1.4, 2.8, 4.4; b/B = 0.16, 0.24 and 0.32),
- all numerical computations will be performed for three sets of input parameters (p_c = 0.12, 0.15 and 0.2 [MPa]). The authors of the experiment identified only the range of parameters, not their values,
- the discussed phenomena can be mathematically described with the use of simplified, two-dimensional equations. This assumption was made in view of the experiment's clearly two-dimensional character,
- the numerical experiment will account for only one channel width of B = 25 [mm] to limit the number of simulations,
- the effect of viscosity will be emphasized. The effect of viscosity was computed with the use of the Fluent commercial CFD code.

Three different pressure levels were set at the nozzle inlet for every geometric case: 120000 [Pa], 150 000 [Pa] and 200 000 [Pa]. Pressure at the exits was roughly equivalent to atmospheric pressure at 100000 [Pa]. System temperature was constant at 293 [K]. The working medium was air.

Numerical simulations were carried out with the use of the Multi Flower 2D package (SOBIESKI 2008) developed based on the Finite Volume Procedure and used previously in modeling flows with bifurcations (CUDAKIEWICZ 2005, PUCHALSKI 2008). The following balance equations for mass, momentum, energy and component proportions (BADUR and SOBIESKI 2001, SOBIESKI 2006) were solved during the calculations:

– mass balance: $\frac{\partial}{\partial t}\rho + \nabla(\rho\vec{v}) = 0$, (1)

– momentum balance: $\frac{\partial}{\partial t}(\rho\vec{v}) + \nabla(\rho\vec{v} \otimes \vec{v}) = \nabla(-p\overleftrightarrow{I} + \overleftrightarrow{\tau})\,\rho\vec{s}_b$, (2)

– energy balance: $\frac{\partial}{\partial t}(\rho e) + \nabla(\rho e\vec{v}) = \nabla((-p\overleftrightarrow{I} + \overleftrightarrow{\tau})\,\vec{v} + \vec{q}) + \rho s_e$, (3)

– component balance: $\frac{\partial}{\partial t}(\rho Y_k) + \nabla(\rho Y_k\vec{v}) = \nabla(\vec{J}_k) + \rho s_k$, (4)

where: ρ – density of mixture [kg m^{-3}], $\vec{v}$ – average velocity of mixture [m s^{-1}], $\overleftrightarrow{\tau}$ – total stress tensor [Pa], $\vec{s}_b$ – source of mass forces [N m^{-3}], e – total energy [J], p – pressure of mixture [Pa], $\overleftrightarrow{I}$ – unit tensor [-], $\vec{q}$ – total heat flux [J/(m^{2}s^{-1})], s_e – source of energy [J/(m^{3}s^{-1})], Y_k – mass share of the k$^{\text{th}}$ component [-], $\vec{J}_k$ – total diffusion flux [mol/(m^{2}s^{-1})], s_k – mass source [kg/m^{3}s^{-1}], n_s – number of mixture components. The subscript in the equation (4) may be from 1 to n_s.

Second-order Godunov-type scheme was applied to reconstruct convective fluxes on balance cell walls. Time discretization was based on an explicit scheme at CFL equal to 5. The time step was fixed for all finite volumes. The number of grid cells reached, subject to case, from 43 300 to 85 200. 50 000 iterations were performed for each case. The time required to compute each case was determined by grid size, and it ranged from several to more than ten hours. Balance equations were solved by the relaxation method. The above parameters were selected experimentally at the stage of initial simulations which are not discussed in this paper.

Simulation results

Five principal flow types (Fig. 4) were determined based on an analysis of numerical results obtained with the use of the Multi Flower 2D application:

1) TYPE *A* (e.g. for $b/B = 0.16$, $H/B = 2.8$ and $p_c = 0.2$ [MPa]) – the jet oscillates along the entire channel, it is bifurcated and returns symmetrically in the direction of the side channels. This type of bifurcation is encountered in relatively long channels and at low nozzle width.

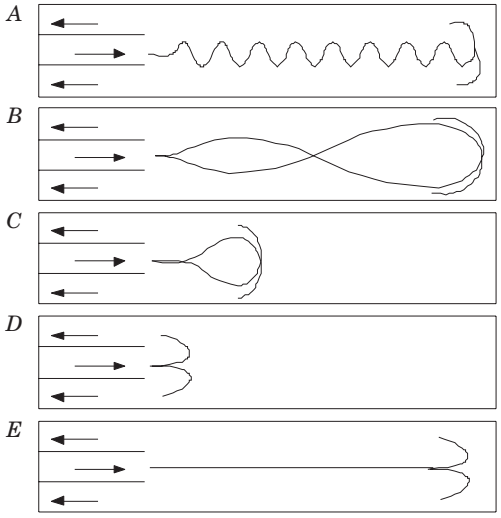

Fig. 4. Types of flow structures observed in numerical simulations

2) TYPE *B* (e.g. for $b/B = 0.16$, $H/B = 4.4$ and $p_c = 0.12$ [MPa]) – in the downstream end of the channel, the jet returns non-symmetrically in the direction of the side channels, alternating between the channels during flow. This type of bifurcation is encountered in very long channels and at low nozzle width.

3) TYPE *C* (e.g. for $b/B = 0.24$ and $H/B = 4.4$ and $p_c = 0.15$ [MPa]) – non-symmetrical jet recovery in the channel. The main jet impinges on a channel wall and, consequently, the attachment point moves along the channel to the opposite side. The flow from one side to the other is irregular. There are no disturbances in the downstream end of the channel which leads to the formation of a dead zone. This type of bifurcation is encountered in relatively long channels and at higher nozzle widths. This flow structure proved to be most sensitive to the value of inlet pressure. At higher pressure (0.2 [MPa] in this experiment), bifurcations were noted along a wide range of H/B and b/B indicators. As inlet pressure decreased (for $p_c = 0.15$ and 0.12 [MPa]), bifurcations disappeared, and a stable flow, classified as type D, was noted.

4) TYPE *D* (e.g. for $b/B = 0.32$ and $H/B = 1.2$ and $p_c = 0.15$ [MPa]) – symmetrical jet recovery, the main jet is dispersed and bifurcated at a distance of around 1 – 1.5 nozzle width b from the nozzle exit. Vortices were not reported in the remaining parts of the channel. The observed flow was highly stable. This type of flow occurs at a high b/B ratio regardless of channel length.

5) TYPE *E* (e.g. for $b/B = 0.16$ and $H/B = 1.2$ and $p_c = 0.12$ [MPa]) – the main jet is observed all the way down to the cut-off wall after which it recirculates symmetrically. The flow is symmetrical or quasi-symmetrical, subject to the pressure applied at the nozzle inlet. This type of bifurcation is encountered in short channels.

Tables 1, 2 and 3 present the flow structures for the three investigated pressure values and 50 000 iterations. It was found very difficult to interpret the results and classify them into particular flow types. Stationary flow types (*E* or *D*) were the easiest to classify, although transitory forms were evidently present. An example of the above is the solution for $b/B = 0.16$, $H/B = 1.2$ and $p_c = 0.2$ [MPa] which displays a visible transition trend from type *E* to type *A* flow. Other transition trends in a stationary system are noted in cases where $b/B = 0.32$. The system is stationary (type *D*) at low and medium pressure, but when pressure is increased at the inlet, a transition to another stationary form (type *E*) or oscillating form (type *C*) is reported, subject to the H/B indicator. Non-stationary cases are even more difficult to classify, especially as regards type *B* and type *C* flows where all efforts to ascertain whether the nozzle jet reaches the rear wall are highly subjective.

In the analyzed geometric system, there are at least three parameters responsible for bifurcation points: two geometric indicators and the inlet/outlet pressure ratio. Those points were not captured due to low geometry resolution and initial parameters of the system. The above could have been achieved if it were possible to model wall movements in the simulation model (self-adopting grids would have to be applied for such a broad range of changes) and to set initial conditions in the form of functions. The current version of the Multi Flower 2D model does not provide the above options.

Despite certain interpretation difficulties, Tables 1, 2 and 3 support the determination of the bifurcation type based on the system's geometric indicators. To validate the usefulness of table data, an additional simulation was carried out for $b/B = 0.16$, $H/B = 2.0$ and total pressure at the inlet $p_c = 130\,000$ [Pa]. It was assumed that type *A* or type *E* flow or a combination of the two flow types would be observed. Simulation results supported the above assumption (Fig. 5). A transitory type was noted. The flow was stable after passing through the nozzle, but oscillations with a growing amplitude appeared as the flow approached the cut-off wall. The loss of flow stability, propagating from the cut-off wall to the nozzle exit, is probably a transitory form between flow types *A* and *E*. Transitory forms between other flow types can be deduced in a similar manner without additional simulations. This problem is analyzed below in reference to the general bifurcation conditions.

Table 1

Flow structures for p_c = 0.2 [MPa]

	b/B = 0.16	b/B = 0.24	b/B = 0.32
H/B = 1.2	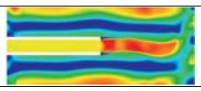	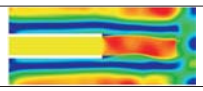	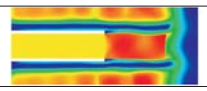
H/B = 2.8	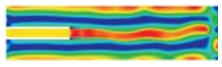	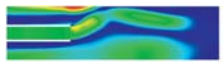	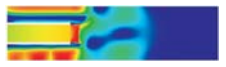
H/B = 4.4	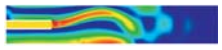	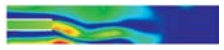	

Table 2

Flow structures for pc = 0.15 [MPa]

	b/B = 0.16	b/B = 0.24	b/B = 0.32
H/B = 1.2	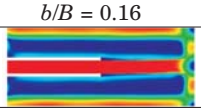	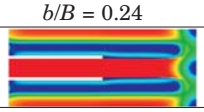	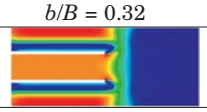
H/B = 2.8		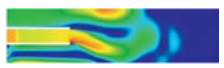	
H/B = 4.4	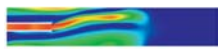		

Table 3

Flow structures for pc = 0.12 [MPa]

	b/B = 0.16	b/B = 0.24	b/B = 0.32
H/B = 1.2	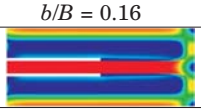	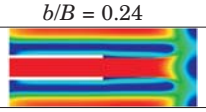	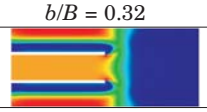
H/B = 2.8		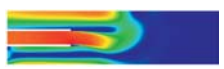	
H/B = 4.4			

Bifurcation theory defines two basic requirements which must be fulfilled for bifurcation to take place (BADUR and SOBIESKI 2001). The first requirement is that the system has to be relatively "lean" with a dominant parameter working in one direction. In line with the second requirement, there must be a "free area" perpendicularly to the dominant direction. The present research validates both requirements. For example, if b/B = 0.32, and H/B = 1.2, the flow emerging from the nozzle is wide, and the channel is short. The resulting system is not "lean", bifurcations do not take place and the entire flow

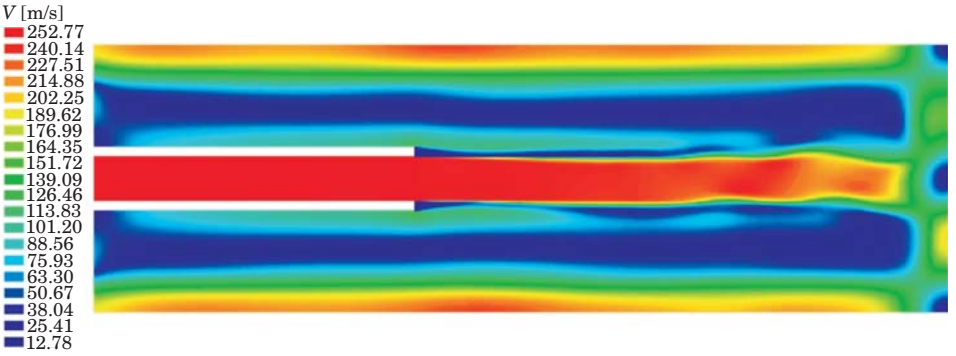

Fig. 5. Total velocity distribution for $b/B = 0.16$, $H/B = 2.0$ and $p_c = 130000$ [Pa]

is stationary. There is clearly no "free area" perpendicular to the dominant direction. With an improvement in the "leanness" criterion (e.g. for $b/B = 0.16$, $H/B = 1.2$ and $p_c = 0.2$ [MPa]) through a decrease in fluid jet width, the system displays a bifurcation trend (shown in Figures as a minor flow asymmetry). A further narrowing of the width of nozzle b would probably result in type B flow. A similar situation is observed as regards flow types C and B. The narrowing of the width of nozzle b improves the "leanness" criterion and clearly supports the development of an oscillating flow form.

When the investigated system is analyzed in view of bifurcation requirements, it can be generally concluded that as indicator H/B approaches unity, bifurcations do not take place because the "leanness" criterion is not met, and as the b/B ratio increases, the "free area" criterion deteriorates, leading to jet "rigidity" and loss of bifurcation. Flow velocity (in this case, modified by total pressure at nozzle inlet) is also an important consideration. The higher the flow velocity, the more likely the transition from a divergent to an oscillating regime, which supports the findings of other authors.

Bifurcation-sensitive parameters

Two complementary methods were employed to determine whether a given flow belongs to a divergent or oscillating bifurcation category. The first method involved an observation of changes in fluid parameters (mostly pressure) in a selected cell of the numerical grid (Fig. 6). The cell was positioned minimally below the lower nozzle edge, at a distance of approximately 1b from the exit cross-section. Pressure changes as a function of time were monitored to determine which of the observed cases could be classified as Hopf bifurcations.

Classical Hopf bifurcations with uniform and periodic changes in flow structure were noted only in types *A* and *B*. Type *D* was completely stationary, and the remaining flow types, although non-stationary, were not marked by clear periodicity.

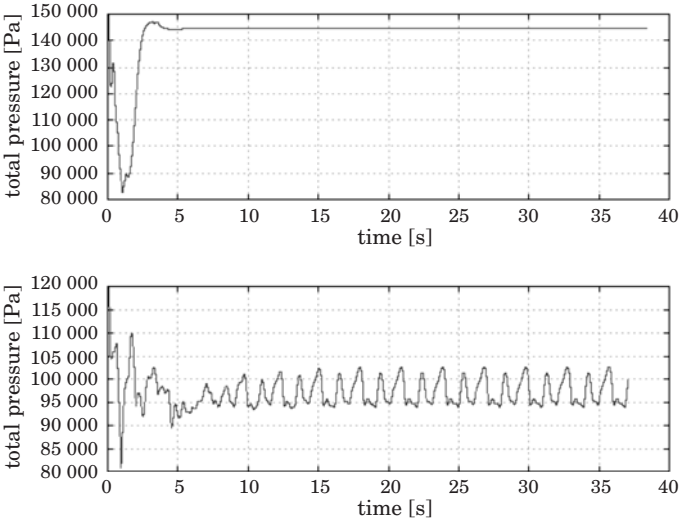

Fig. 6. Total pressure observations in a selected cell: type *D*: $b/B = 0.32$ and $H/B = 1.2$, p_c= 150 000 [Pa] (top); type *B*: $b/B = 0.16$ and $H/B = 4.4$, $p_c = 120\ 000$ [Pa] (bottom)

The second method applied to determine bifurcation type relies on a diagram of convergence of calculations. As previously noted, the solution to linear equations (the ultimate objective of the computation problem) is produced in the Multi Flower 2D application by the relaxation method. In stationary cases, the solution (values of the simple variable vector) is constant over time and an asymptotic result is established at a given level of accuracy. The above is not possible in stationary cases because the searched unknown vector values are subject to change regardless of the degree of flow nonstationarity. Since Hopf bifurcation nonstationarities are cyclical, this periodicity should also be manifested in the equation solving process. This is the case, as demonstrated by the convergence process in Figure 7 (which also illustrates the nonstationary case presented in Fig. 6). The time of one cycle determined in the discussed case was 1.4804 [s]. This method seems to deliver a higher degree of accuracy than the first method due to more pronounced changes in parameter values. The diagram of changes in parameter values in a selected computational cell has a local character in space (which could give rise to doubts as to the method's

effectiveness), while the residue process represents flow on a global scale. It should also be noted that flow type cannot be determined based on the distribution of scalar and vector fields due to difficulties in interpreting their similarities and differences.

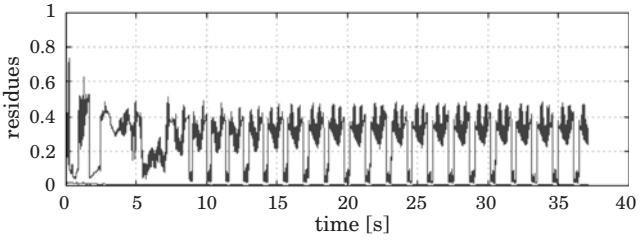

Fig. 7. Convergence process for $b/B = 0.16$; $H/B = 4.4$; $p_c = 120\ 000$ [Pa] (type *B*)

In subsequent parts of the experiment, the FLUENT commercial application was used to determine the effect of viscosity on changes in bifurcation type. Although various efforts were made to ensure that both simulation models are identical (as regards the mathematical model and the applied numerical techniques), satisfactory results were not achieved in the FLUENT application with respect to non-stationary flows. Identical results were reported only in stationary cases. Significant discrepancies in the flow structure as well as in the computed ranges of physical quantities were observed even in the case of small bifurcations. In view of the above, it was concluded that the FLUENT application lacks an appropriate solver for modifying flows with Hopf bifurcations. Perhaps, better results could have been achieved with a different configuration of the simulation model, however, it was not the objective and further investigations were not performed. It should be noted that the FLUENT application supports the modeling of other types of bifurcation, such as the Taylor-Couette bifurcation (DOMAŃSKI 2006).

Conclusions

The following conclusions can be drawn from the experiment:

– computer-aided simulations proved to be consistent with experimental results at the qualitative and, partly, at the quantitative level. A detailed quantitative comparison could not have been carried out due to the absence of the required experimental data (distribution of flow scalar and vector fields). Similar flow structures with a corresponding range of b/B and H/B geometrical indicators were noted in numerical simulations;

– a new type of flow, not described by the authors of the experiment, was discovered during numerical simulations. Type *E* flow is observed in short channels (which are deficient in the "leanness" parameter) and at low values of the *b*/*B* ratio (high availability of "free area" perpendicularly to the dominant direction). Presumably, this is a theoretical flow type which is possible, but difficult to achieve in reality due to imperfections which are almost always encountered (disruption of the ideal flow state);

– estimated areas of oscillating bifurcation, with a division into types, were proposed based on numerical simulations. In view of the analyzed conditions of the bifurcation process, it could be assumed that the main flow types which are possible in the investigated model have been identified in the study. The performed simulations illustrate the transition process between various bifurcation points and the encountered flow structures;

– once again, this experiment confirmed the usefulness of the Multi Flower 2D application for modeling flows with bifurcations. The applied mathematical models and computational algorithms support the propagation of nonstationary bifurcations and the modeling of relevant systems. The mathematical model found in the Multi Flower 2D application does not comprise any options making a reference to the bifurcation theory – this is a characteristic feature of the application which reflects the method of implementing mathematical models and the applied numerical techniques and methods;

– a method for determining the oscillation frequency of Hopf bifurcations based on the calculation process was developed in the study. This method was applied in simulations performed in the Multi Flower 2D package.

Accepted for print 15.12.2008

References

BADUR J., SOBIESKI W. 2001. *Numerical simulation of Hopf bifurcations in a turning off flow*. Research of the Chair of Mechanics and Machine Design, p. 63–98, Olsztyn.

BADUR J., YERSHOV S., RUSANOV A., KARDAŚ D., KUDRYŃSKI A., OCHRYMIUK T. 1999. *An imperfected time marching method for Hopf bifurcation in inviscid flow*. Research Report PAN, 298/97, Gdańsk.

BATTAGLIA F., TAVENER S.J., KULKARNI A.K., MERKLE C.L. 1997. *Birfurcation of low Reynolds number flows in symmetric channels*. AIAA Journal, 35(1): 99–105.

CHIANG T.P., SHEU T.W.H., HWANG R.R., SAu A. 2002. *Spanwise bifurcation in plane-symmetric sudden-expansion flows*. Phys. Rev. E, 65, 16306.

CUDAKIEWICZ M. 2005. *Numerical Modelling of the Work of Jet Pump Devices concerning Flügel-Cunningham Method*. MSc Thesis, UWM WNT, Olsztyn.

DOMAŃSKI J. 2006. *Determination of the parameters of fluid motion in Taylor-Couette flow*. Technical Scienties, 9: 73–78.

DYBAN E.P., MAZUR J., EPIK E.J. 1971. *Osobennosti istieczenja plaskoj vozduščnoj striu v tupik*. Teplofizyka i teplomechanika, 19: 41–45.

KURNIK W. 1997. *Bifurkacje dywergentne i oscylacyjne*. Wydawnictwo Naukowo-Techniczne, Warszawa.

MANICA R., DE BORTOLI A.L. 2003. *Simulation of incompressible non-Newtonian flows through channels with sudden expansion using the power-law model*. TEMA, 4: 333–340.

MULLINA T., SHIPTONA S., TAVENERB S.J. 2003. *Flow in a symmetric channel with an expanded section*. Fluid Dynamics Research, 33: 433–452.

SOBIESKI W. *Projekt Multi Flower 2D*. http://moskit.uwm.edu.pl/~wojsob/ (2008-06-14).

ŚWIĄTECKI A. 2004. *Numerical Analysis of Hopf bifurcations in a 2D geometry*. MSc Thesis, WNT UWM, Olsztyn.

PUCHALSKI E. 2008. *Numerical Analysis of Hopf Bifurcations In The Channel With Extension*. MSc Thesis, WNT UWM, Olsztyn.

TECHNICAL SCIENCES
Abbrev.: Techn. Sc., No 12, Y 2009

DOI 10.2478/v10022-009-0023-6

NUMERICAL AND EXPERIMENTAL ANALYSES OF HOPF BIFURCATIONS IN A LOCALLY EXPANDED CHANNEL

Wojciech Sobieski

Chair of Mechanics and Machine Design
University of Warmia and Mazury in Olsztyn

Key words: Hopf bifurcations, CFD.

Abstract

This article discusses Hopf bifurcations in fluid flow through a locally expanded channel. The first part presents the simulation model and computation results that investigate the possibility of oscillatory bifurcations in the analyzed system at given geometry configurations and parameters. Simulations were performed with the application of the Finite Volume Procedure in the Multi Flower 2D non-commercial package. The second part attempts to supplement simulation results with the use of FLUENT and FlowWorks commercial applications. The last part of the paper describes a laboratory experiment validating the results of numerical computations at the qualitative and, partly, the quantitative level. The described experiments investigate the usefulness of CFD applications and simulation techniques in predicting and analyzing bifurcations under real flow conditions.

ANALIZA NUMERYCZNA I EKSPERYMENTALNA BIFURKACJI HOPFA W KANALE Z LOKALNYM ROZSZERZENIEM

Wojciech Sobieski

Katedra Mechaniki i Podstaw Konstrukcji Maszyn
Uniwersytet Warmińsko-Mazurski w Olsztynie

Słowa kluczowe: bifurkacje Hopfa, CFD.

Abstrakt

Artykuł zawiera rozważania dotyczące występowania bifurkacji Hopfa w przepływie płynu przez kanał z lokalnym, występującym tylko na pewnym odcinku, rozszerzeniem. W pierwszej części przedstawiono model symulacyjny oraz wyniki obliczeń, wskazujące na możliwość występowania w rozważanym układzie bifurkacji oscylacyjnych przy pewnych konfiguracjach geometrii i parametrów. Symulacje wykonano za pomocą niekomercyjnego pakietu Multi Flower 2D, opartego na metodzie objętości skończonych. W części drugiej podjęto próbę uzupełnienia wyników symulacji z zastosowaniem komercyjnych pakietów FLUENT oraz FlowWorks. Ostatnia część artykułu przed-

stawia oryginalny eksperyment laboratoryjny, potwierdzający na poziomie jakościowym i częściowo ilościowym wyniki obliczeń numerycznych. Opisane w pracy badania przedstawiają możliwości wykorzystywania aplikacji CFD i technik symulacyjnych do przewidywania bądź analizowania zjawisk bifurkacyjnych w rzeczywistych układach przepływowych.

Introduction

Nonlinear differential equations can be used to describe various physical phenomena in nature. The equilibrium stability of nonlinear systems has a local character in reference to initial conditions as well as disturbances. The above implies that the effect is not proportional to the parameter describing the cause. Even minor changes in the initial conditions of a system may produce large variations in the long-term behavior of the system. This phenomenon has been referred to as the "butterfly effect" following the publication of Edward Lorentz's article entitled "Can the flap of butterfly's wing stir up a tornado in Texas?". Research efforts are made to investigate whether the processes observed in various systems (physical, chemical, biological, economic, demographic, etc.) are steady, i.e. minimally sensitive to perturbations, and predictable. Due to unpredictable events, a system's equilibrium may be altered to reach an unacceptable or even an undesirable state. Many catastrophes occur when a system shifts from a static to a dynamic equilibrium, such as buckling of rod structures, vibration of suspended bridges or the flatter of airplane wings. Those changes and transitions are related to bifurcation.

In mathematical terms, bifurcation occurs when a minor change in parameters causes the properties of a model to change (MARDSEN 1976, HARB 1996, BADUR, SOBIESKI 2001, LEINE 2006, RODRIGUES 2007). In practice, it implies a splitting of the equilibrium solution branch when a given active (bifurcation) parameter reaches its critical value. In mechanics, bifurcation is defined as the emergence of new momentum, heat and mass transfer components as external conditions change. Two principal bifurcation conditions have been determined in both mechanical and thermal systems (BADUR, SOBIESKI 2001, SOBIESKI 2006):

– the existence of a dominant flow direction, i.e. a direction in which the values of parameters such as velocity, displacement or temperature gradient are much higher than in the remaining (perpendicular) directions,

– the existence of a "free area" perpendicular to the dominant direction, i.e. the possibility of solution branching.

An example of bifurcation in fluid mechanics is thin, stationary fluid flow through an expanded (locally or permanently) channel. The expansion creates a "free area", and the convective part of the momentum flux is responsible for the loss of stability. The active parameter in this case is the Mach number or the Reynolds number.

Other types of bifurcation behavior are also encountered in flow systems, including Taylor-Couette flow between two rotating cylinders (DOMAŃSKI 2006) or Rayleigh-Bènard cells in selected types of convective flow (Elmer Tutorials 2007).

Two types of bifurcations are possible in the analyzed expanded (locally and permanently) channel. The first type is divergent (stationary) bifurcation in which the system initially undergoes a sudden change, after which it stabilizes and takes up a new, stationary form. The second type is oscillatory bifurcation where the permanent solution loses stability and is replaced by a periodic solution that develops with an active parameter increase in the supercritical area (KURNIK 1997, SOBIESKI 2006). In real physical systems, the above corresponds to the loss of equilibrium point stability and the occurrence of self-excited vibrations. Cases with periodic vibrations are referred to as Hopf bifurcations.

There are very few published sources investigating flow structures in locally expanded channels (expanded along a given section). One of the most noteworthy examples is the work of MULLIN et al. (2003) which describes the experiment and presents the results of numerical simulations. The authors of the study identified two basic types of structures: symmetrical and asymmetrical, and concluded that the type of bifurcation is determined mostly by the system's geometry relations. Similar studies have been carried out in reference to permanently expanded channels (an expansion from a set point to the end of the investigated flow area) (BATTAGLIA et al. 1997 MANICA BORTOLI DE 2003), but the conducted experiments were purely simulational. There are several experimental studies investigating flows through permanently expanded channels (ESCUDIER 2002, POOLE 2005, CHIANG et al. 2001), but they make a partial reference to non-Newtonian fluids and flows at a low Reynolds number.

The above cited studies have been carried out based on a classical approach: an experiment is performed and further attempts are made to repeat it virtually with the involvement of a simulation model. The author of this study attempted to reverse this classical approach. The study began with the development of a simulation model and the relevant assumptions. A test stand was then set up based on the results of the simulation phase. This approach naturally gave rise to two key experimental objectives. The first goal was to model the previously investigated bifurcation phenomena observed in locally expanded channels. The second objective was to determine to what extent Hopf bifurcations can be predicted in a real system based on a simulation model.

Computer model

The geometry of the investigated flow structure is presented in Figure 1. The system comprised a plain channel with a symmetrical, local expansion in the center.

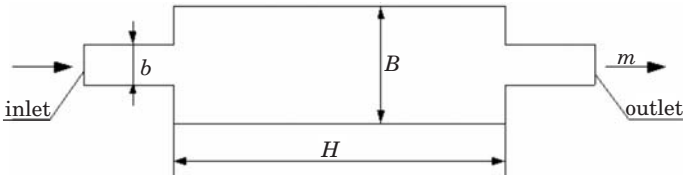

Fig. 1. Flow system geometry

The basic model was defined and the following assumptions were made prior to modeling:

– the experiment analyzes a single-component flow of a medium whose properties resemble those of water (the liquid cannot be directly defined in the applied computational program due to the need to account for the compressible fluid equation),

– the Mach number should be less than 0.3 to maintain medium parameters at the level of near real-event parameters (which follows directly from the previous assumption),

– computation will take place in two-dimensional space (DYBAN 1971, BADUR, SOBIESKI 2001, ŚWIĄTECKI 2004, CUDAKIEWICZ 2005, SOBIESKI 2006),

– the effect of turbulence and viscosity is considered to be negligibly small (BADUR 1999, ŚWIĄTECKI 2004, CUDAKIEWICZ 2005, SOBIESKI 2006),

– outlet pressure is constant and equal to atmospheric pressure at 1013 [hPa],

– static input pressure is constant and equal to 1025 [hPa],

– inlet velocity is controlled by modifying total inlet pressure values,

– inlet and outlet width is identical and constant at 25 [mm],

– total channel length is constant at 280 mm [mm],

– total expansion length H is constant at 200 [mm],

– basic channel width in the expanded section is 50 [mm],

– the result is positive, i.e. a Hopf bifurcation occurs, when the flow is asymmetrical and cyclical changes in flow type are observed. The result is negative when the flux impinges on a side wall and becomes detached only at the outlet.

Following system analyses and preliminary simulations, the following numerical parameters were adopted in the study (PUCHALSKI 2008):

– type of grid: structural, total number of cells: 48 000,
– convective flux reconstruction method: TVD (Total Variation Diminishing),
– time-stepping scheme: implicit, with constant time step for all cells,
– CFL number (Courant-Friedrich-Levy condition): 10,
– minimum number of iterations: 20 000.

The flow simulation model was developed with the use of the Multi Flower 2D v. 3.0.6 non-commercial package (SOBIESKI 2006, SOBIESKI 2008). The package combines applications for developing computer simulations in compressible fluid mechanics and features the following options: modeling two-dimensional flows with every type of geometry relations (internal and external), modeling stationary and non-stationary flows, modeling subsonic, supersonic and transonic flows, modeling multicomponent flows. The Multi Flower 2D package relies on the Finite Volume Procedure (FV) and the Mixture Model. The FV procedure supports multiple balancing of different values (mass, momentum, energy, etc.) in every computational cell and at every time step.

The general system of balance equations found in the Multi Flower 2D solver is as follows (BADUR, SOBIESKI 2001, SOBIESKI 2006):

– mass balance: $\frac{\partial}{\partial t}\rho + \nabla(\rho\vec{v}) = 0$ (1)

– momentum balance: $\frac{\partial}{\partial t}(\rho\vec{v}) + \nabla(\rho\vec{v}\otimes\vec{v}) = \nabla(-p\overleftrightarrow{I} + \overleftrightarrow{\tau}) + \rho\vec{s}_b$ (2)

– energy balance: $\frac{\partial}{\partial t}(\rho e) + \nabla(\rho e\vec{v}) = \nabla((-p\overleftrightarrow{I} + \overleftrightarrow{\tau})\vec{v} + \vec{q}) + \rho s_e$ (3)

– component balance: $\frac{\partial}{\partial t}(\rho Y_k) + \nabla(\rho Y_k\vec{v}) = \nabla(\vec{J_k}) + \rho s_k$ (4)

where: ρ – density of mixture [kg m^{-3}], $\vec{v}$ – average velocity of mixture [m s^{-1}], $\overleftrightarrow{\tau}$ – total stress tensor [Pa], $\vec{s_b}$ – source of mass forces [N m^{-3}], e – total energy [J], p – pressure of mixture [Pa], $\overleftrightarrow{I}$ – unit tensor [-], $\vec{q}$ – total heat flux [J/(m^{2}s^{-1})], s_e – source of energy [J/(m^{3}s^{-1})], Y_k – mass share of the kth component [-], $\vec{J_k}$ – total diffusion flux [mol/(m^{2}s^{-1})], s_k – mass source [kg/m^{3}s^{-1}], n_s – number of mixture components. The subscript in the equation (4) may be from 1 to n_s.

Equations (1)–(4) present the Mixture Model (or the Homogenous Model) for describing homogenous mixes of any number of different phases: gases, fluids and solids. In this model, all phases are regarded as a mixture and have a single balance equation system. The mixture is described with the use of Euler approach (SOBIESKI 2008). The discussed simulations did not require the use of the multicomponent flow modeling option.

The Multi Flower 2D package solver does not contain all elements featured in equations (1)–(4). It does not list stress tensors or source terms. Despite

those simplifications (and taking into account the previous assumptions), the Multi Flower 2D package seems to be an appropriate tool for the needs of this study. Its usefulness has been validated in an earlier study on the modeling of bifurcations in a closed-off plain channel based on a previous experiment carried out by DYBAN (1971) and described by BADUR and SOBIESKI (2001). A high level of qualitative consistence and a satisfactory level of quantitative consistence were reported in that study. The suitability of the Multi Flower 2D package for modeling non-stationary processes with bifurcations has also been confirmed by other authors (ŚWIĄTECKI 2004, CUDAKIEWICZ 2005, PUCHALSKI 2008).

Simulation results

The first phase of the numerical simulation process involved the determination of an area with Hopf bifurcations. Such bifurcations were observed in geometry relations later referred to as the basic model at a total pressure of 105 000 [Pa] (Fig. 2). The maximum computational velocity was 3.85 [m s^{-1}], and the value of the Mach number was below the set limit of 0.3. The first phase ended with the determination of the parameter range for further computations, i.e. channel width B of 40 to 60 [mm], at intervals of 5 [mm], and a total input pressure of 103 000 to 107 000 [Pa], at intervals of 250 [Pa].

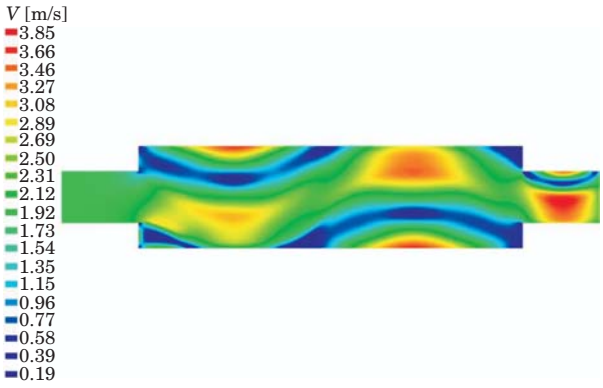

Fig. 2. Basic flow with Hopf bifurcations – total velocity distribution

The second simulation series began with channel width B = 50 [mm] to identify the range at which bifurcations occur. A positive result was reported in a pressure range of 104 500 to 105 000 [Pa]. Width B was changed to 45 [mm] and subsequent efforts were made to determine the range at which Hopf

bifurcations appear. This procedure was repeated for all of the set channel widths. In the case with the lowest analyzed width, a positive result was noted within the range of 104 000 to 120 000 [Pa], but some of the results were disregarded in view of the assumed Mach number; therefore, the maximum total pressure was deemed as correct at 10 600 [Pa].

The Mach number minimally exceeded the threshold value at channel width $B = 45$ [mm] and a pressure of 104 250 and 104 500 [Pa]. Those results were not rejected, but were regarded as less reliable. A positive result was not reported for width $B = 60$ [mm] at any range of input pressure values.

At channel width $B = 55$ [mm] and a pressure of around 103 000 [Pa], a new type of flow was observed, but it was not classified as bifurcation and was subsequently disregarded. The results of this experimental phase are presented in Table 1. Basic model results are highlighted with a different background color.

Table 1

Hopf bifurcation areas

B [mm]	Total pressure [hPa]												
	103	103.25	103.5	103.75	104	104.25	104.5	104.75	105	105.25	105.5	105.75	106
40				X	V	V						V	V
45					X	V	V		V	V	V	V	X
50	X				X	X	V	X	V	X		X	
55		X	X	X	X			X	X	X	X	X	
60								X	X				

The objective of the next stage of the study was to verify whether the observed bifurcations were Hopf bifurcations. For this purpose, total pressure values at a characteristic flow point were registered during the computational process. The selected point was situated minimally outside the flow axis at an adequate distance from the beginning of the expansion (at around 1/4 length of the entire expanded section). Calculations were repeated for $B = 50$ [mm] and a total inlet pressure of 105 000 [Pa] because oscillating flow characteristics were clearly manifested in the investigated case. The pressure change diagram is shown in Figure 3. The regularity of pressure changes after the equations have been expanded proves that the observed process is a case of oscillatory bifurcations.

Flow periodicity is also manifested in the convergence diagram (Fig. 4). The system solution follows the pattern of a periodically changing flow throughout the computation process, but it never reaches a stationary state. It should be noted that the frequency of the residue cycle is twice higher than the frequency

of pressure changes. The above indicates that the computational process expands in the same way after every "reversal" of the flow structure (which takes place twice in each bifurcation cycle).

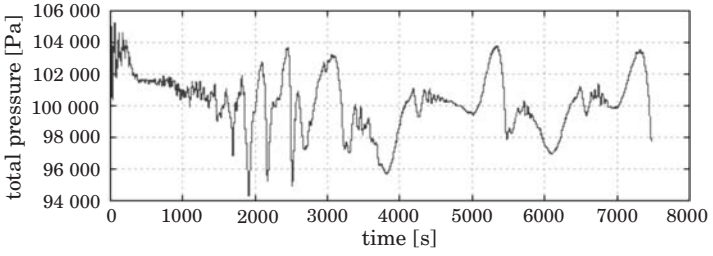

Fig. 3. Diagram of changes in total pressure in a selected cell

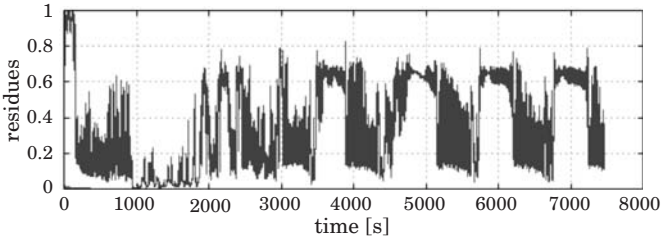

Fig. 4. Convergence process for the basic model

Simulations of prebifurcation flow

Attempts were made to replicate the above results with the use of different software. Simulation models were developed in the FLUENT (based on the Finite Volume Procedure) and the FlowWorks (based on the Finite Elements Procedure) commercial packages. A 3D model was applied in both cases to verify the effect of the number of parameters on computation results. Two computational grids (30 200 and 244 000 cells) and several initial conditions were analyzed in the FLUENT package. Only the basic model with around 25 000 grid cells was analyzed in the FlowWorks package. It should be noted that the authors were unable to precisely replicate the model generated in the Multi Flower 2D package in either of the commercial programs. The reported deviations concerned the definition of the working medium. An incompressible medium was applied in FLUENT and FlowWorks packages, while the Multi Flower 2D relied on a compressible medium described by the ideal gas law.

In general, it was found that the computational algorithms in the FLUENT and FlowWorks packages, which are highly complex and guarantee computational stability for a very broad range of values, suppress bifurcation and produce results that are completely inconsistent with expectations. The results of the basic model simulation, achieved with the use of the above commercial packages, are presented in Figures 5 and 6. Special attention should be paid to the range of total velocity values which are similar in Multi Flower 2D and FlowWorks packages, but are significantly different in the FLUENT application. The causes of the above were not identified.

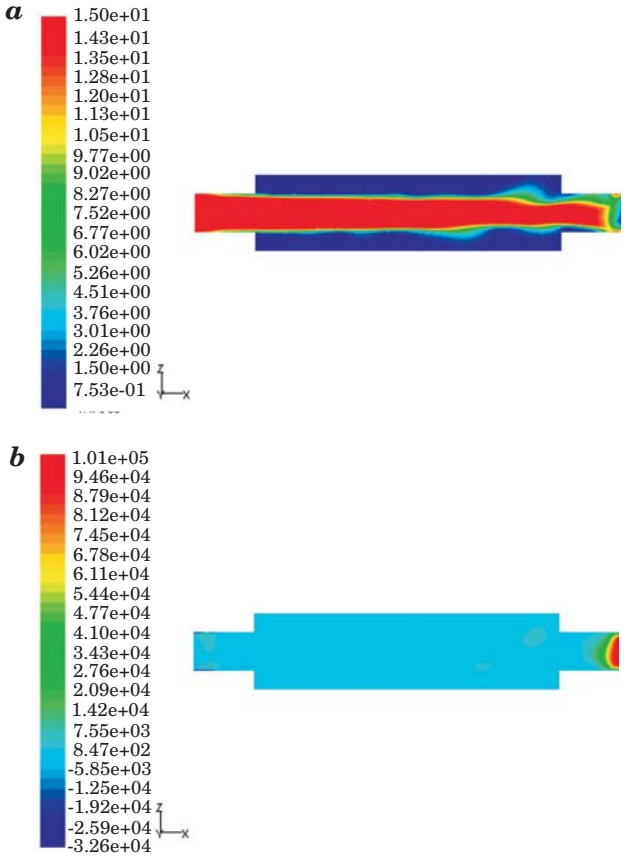

Fig. 5. Distribution of total velocity and static pressure produced in the FLUENT package for the basic model

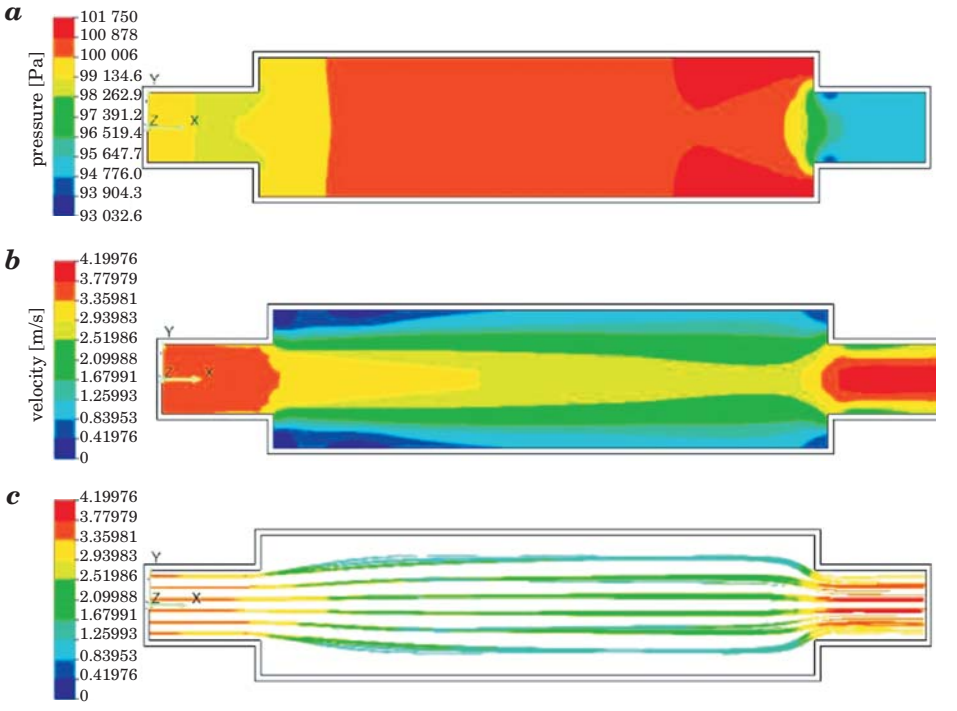

Fig. 6. Distribution of static pressure, total velocity and stream line course observed in the FlowWorks package for the basic model

Laboratory experiment

Since previous experiments were highly general in nature and were carried out at the qualitative level, the author of this study set out to investigate whether simulation results could be applied to predict bifurcations in real systems. A test stand was set up to determine the above. The author assumed that the key factor determining bifurcations was the geometry of the flow system, namely the b/B width ratio. Secondary importance was attached to the type of medium and its parameters.

The set-up of the test stand is presented in Figure 7. The main part comprises two plexiglass panels enclosing partially mobile metal walls. Channel dimensions conform to the dimensions of the previously described basic model. Channel width (in the third spatial dimension) was 20 [mm], and it was deemed sufficient to minimize flow disturbances caused by the viscosity effect. A greater width was not applied to ensure adequate flow intensity. The test stand was supplied from the local water mains.

Fig. 7. Laboratory test stand

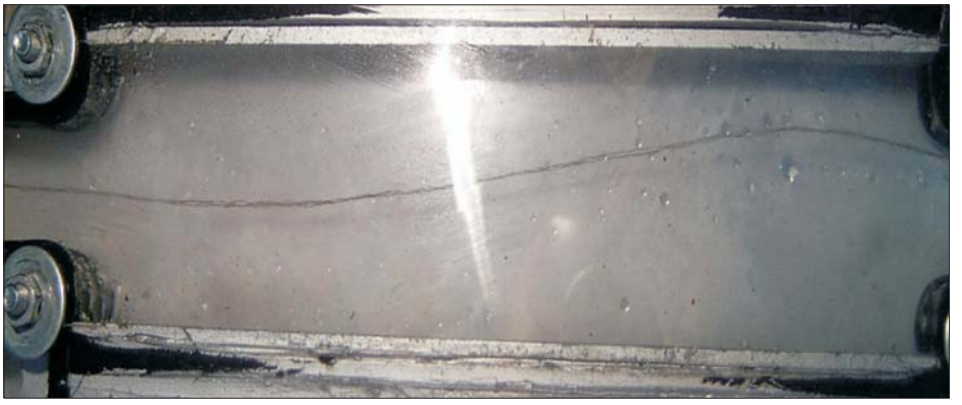

Fig. 8. Flow visualization at an intensity level of 0.72 [l s^{-1}]

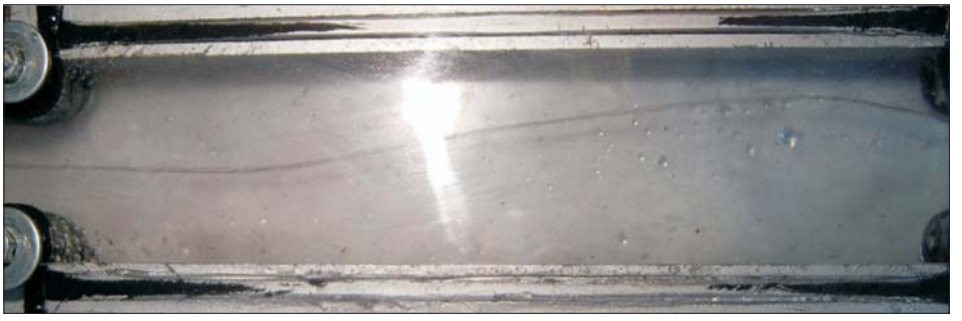

Fig. 9. Flow visualization at an intensity level of 0.97 [l s^{-1}]

The behavior of the water jet was observed upon reaching the expanded channel section at different flow intensity values. A dye was initially introduced into the system together with the liquid for the purpose of visualization, but it failed to achieve the set objective in turbulent flows. The dye became mixed

with water too early, and it did not reflect the movement of the water jet. As part of the second attempt to visualize the flow structure, a thin thread was introduced into the system and attached symmetrically at the channel inlet. The experiment was performed at four flow intensity levels Q = 0.08, 0.33, 0.72, 0.97 [l s^{-1}] to produce the following average flow velocity values at the inlet c = 0.16, 0.65, 1.44, 1.93 [m s^{-1}]. In the first two instances, flow intensity was too low and the thread rested loosely in the channel. At higher flow intensity levels, the thread clearly oscillated and took up the anticipated shape. The above is presented in Figures 8 and 9. Flow velocity was roughly consistent with the values computed in the Multi Flower 2D simulation. Higher intensity flows could not be investigated for technical reasons which prevented the determination of the upper intensity limit at which oscillations occur. It should also be noted that jet oscillations were clearly manifested in the experiment, but the flow was not ideally symmetrically reversed in relation to the axis. The above could be attributed to insufficient accuracy or the manner of thread attachment: the thread had a greater tendency to become reversed in a single direction. The needle placed inside the channel was not ideally centered which also affected measurement precision. The frequency of flow reversal could not be determined with a high degree of accuracy, but according to estimates, it ranged from around 0.2 [Hz] to around 1.5 [Hz]. The above observation is not consistent with the results of the numerical simulation where the computational time per cycle was much longer.

Conclusions

The conducted experiment enabled to formulate the following final conclusions:

– bifurcation flows (including Hopf bifurcations) can be predicted and analyzed with the use of simulation techniques developed as part of Numerical Fluid Mechanics. In view of scant publications addressing this problem, the reported results render this experiment a success;

– the available numerical codes, FLUENT and FlowWorks, do not feature solvents for analyzing bifurcation flows. The above could be due to the high level of complexity of the applied computational algorithms which maximally protect the computational process from the loss of stability. The solver of the Multi Flower 2D package is less stable and less versatile, but it is incapable of suppressing system disturbances with equal efficiency, thus supporting the propagation of bifurcation phenomena. This theory has not been validated, but it has been postulated by the author as a possible explanation;

– the experiment validated the assumption that the b/B width ratio is the key factor responsible for bifurcations in expanded channels. The fact that bifurcations were produced in a real system designed solely in view of previous numerical analyses is a success. Although it was impossible to precisely verify each computational case, the validation of the basic model proved the efficiency of simulation methods and could be a venture point for future research. Follow-up experiments are needed to determine the range of values at which Hopf bifurcations occur in a real system and to compare this range of values with the results of simulations. A study to determine the effect of expansion length H (or dimensionless quantity H/B) on the nature of non-stationary phenomena would also greatly contribute to our understanding of the problem;

– the experiment confirmed the assumption that the type of medium plays a secondary role in the bifurcation process. These findings are supported by the experiment involving a completely different medium than that applied in the simulations (due to the limitations of the simulation program) which produced similar results;

– a satisfactory quantitative conformity of flow parameters was nor achieved. In a real system, bifurcations were observed at a much higher inlet pressure than in numerical simulations (where even minor pressure differences resulted in bifurcations). The above could be due to the specific nature of the applied mathematical model, in particular the equation of state which is more suitable for gas than liquid. This assumption is validated by velocity values which, despite significant differences in inlet pressure, are similar. Total velocity in basic model simulations ranged from 0.19 to 3.85 [m s^{-1}] regardless of the place in space (for the time horizon presented in Fig. 2). In a real system, similar flow values were noted at average inlet velocity equal to 0.72 and 0.98 [m s^{-1}]. The observed velocity values cannot be directly compared due to the absence of data on minimum and maximum velocity in a real system (whose determination requires the use of specialist measurements, such as the PIV method) and changes in these values over time. It is possible that the temporal moment presented in Figure 2 is not the best indicator of the velocity field (minimum and maximum velocity values varied for different temporal moments);

– the analysis of the effect of flow velocity, partially discussed in the previous point, validates reference data according to which in addition to geometry relations, velocity (the Reynolds number in the dimensionless form) is the second most important factor (active parameter) affecting the occurrence and character of bifurcations.

Accepted for print 15.12.2008

References

BADUR J., SOBIESKI W. 2001. *Numeryczne symulacje bifurkacji Hopfa w przepływie z nawrotem*. Badania Naukowe Katedry Mechaniki i Podstaw Konstrukcji Maszyn, s. 63–98, Olsztyn.

BADUR J., YERSHOV S., RUSANOV A., KARDAŚ D., KUDRYŃSKI A., OCHRYMIUK T. 1999. *An imperfected time marching method for Hopf bifurcation in inviscid flow*. Raport badawczy PAN, nr arch. 298/97, Gdańsk.

BATAGLIA F., TAVENOR S.J., KULKARNI A.K., MERKLE CH.L. 1997. *Bifurcation of Low Reynolds Numbers Flow in Symmetric Channel*. AiAA Journal, 35(1).

CUDAKIEWICZ M. 2005. *Numerical Modelling of the Work of Jet Pump Devices concerning Flügel-Cunningham Method*. MSc Thesis, UWM WNT, Olsztyn.

DOMAŃSKI J. 2006. *Determination of the parameters of fluid motion in Taylor-Couette flow*. Technical Scienties, 9: 73–78.

DYBAN E.P., MAZUR J., EPIK E.J. 1971. *Osobennosti istieczenja plaskoj vozduščnoj striu v tupik*. Teplofizyka i teplomechanika, 19: 41–45.

Elmer Tutorials. CSC, the Finnish IT Center for Science, February 9, 2007. URL: <http://www.csc.fi/english/pages/elmer> (2008.06.24).

ESCUDIER M.P., OLIVEIRA P.J., POOLE R.J. 2002. *Turbulent flow through a plane sudden expansion of modest aspect ratio*. Physics of Fluids, 14: 3641–3654.

HARB A.M. 1996. *Application of Bifurcation Theory to Subsynchronous Resonance in Power Systems*. PhD Thesis, Virginia Polytechnic Institute and State University. Blacksburg, Virginia, December.

KURNIK W. 1997. *Bifurkacje dywergentne i oscylacyjne*. Wydawnictwo Naukowo-Techniczne. Warszawa.

LEINE I., CAMPEN D.H. VAN. 2006. *Bifurcation phenomena in non-smooth dynamical systems*. Eur. J. Mech. A/Solids, 25: 595–616.

MARSDEN J.E., MCCRACKEN M. 1976. *The Hopf Bifurcation and Its Applications*. Applied Mathematical Sciences, 19. Springer-Verlag, New York, NY.

MULLIN T., SHIPTON S., TAVENER S.J. 2003. *Flow in a symmetric channel with an expanded section*. Fluid Dynamics Research, 33: 433–452.

POOLE R.J., ESCUDIER M.P., OLIVEIRA P.J. 2005. *Laminar flow of a viscoelastic shear-thinning liquid through a plane sudden expansion preceded by a gradual contraction*. Proc. Royal Society of London, Series A: Mathematical, Physical and Engineering Sciences, 461: 3827–3845.

PUCHALSKI E. 2008. *Analiza numeryczna bifurkacji Hopfa w kanale z rozszerzeniem*. MSc Thesis. Uniwersytet Warmińsko-Mazurski, Wydział Nauk Technicznych, Olsztyn.

RODRIGUES A.M. 2007. *Bifurcation of Dynamical Systems with Symmetry*. Departamento de Matemática Pura, Faculdade de Ciências da Universidade do Porto. Setembro.

SOBIESKI W. 2008. *Influence of Selected Eulerian Multiphase Model Parameters on the Simulation Results for a Spouted Bed Grain Dryer*. TASK QUARTERLY, 12(1–2).

SOBIESKI W. 2006. *Mass exchange model in flows with cavitation*. TASK QUARTERLY, 10(4): 401–416.

SOBIESKI W. *Projekt Multi Flower 2D*. http://moskit.uwm.edu.pl/~wojsob/ (2008.06.14).

SOBIESKI W. 2006. *Zjawisko bifurkacji oscylacyjnych w układach przepływowych*. Seminarium Katedry Mechaniki i Podstaw Konstrukcji Maszyn. Olsztyn.

ŚWIĄTECKI A. 2004. *Numerical Analysis of Hopf bifurcations in a 2D geometry*. MSc Thesis, UWM WNT, Olsztyn.

Reviewers

Janusz Badur, Józef Beluch, Jarosław Bosy, Stefan Cacoń,
Romana Cielątkowska, Marek Fidali, Jarosław Frączek, Roman Kadaj,
Zdzisław Kowalczyk, Danuta Leśniewska, Marek Łagoda,
Bogusława Łapczyńska-Kordon, Artur Olszewski, Leszek Osiecki,
Janusz Podleśny, Leonard Runkiewicz, Bogdan Stefanowicz,
Edwin Wnuk, Jerzy Zielnica